

The University of Nottingham

UNITED KINGDOM • CHINA • MALAYSIA

Additive Manufacturing of Electrochemical Systems and their Application in Bioelectronic Medicine

---

Paola Sanjuán Alberte, MPharm.

Thesis submitted to the University of Nottingham for the degree of Doctor of Philosophy

January 2019

“Si me caí es porque estaba caminando.
Y caminar vale la pena, aunque te caigas”

Eduardo Galeano

Abstract

Bioelectronic medicine is a growing field where a combination of electronic and biological systems are used to induce a therapeutic response. Despite the advancements achieved in the area with the production of retinal and cochlear implants, vagus nerve stimulators and wearable biosensors, there are some challenging limitations, including a poor integration in the bioelectronic interfaces and low specificity of the outputs. In order to solve this, additive manufacturing and electrochemical approaches are explored in this work. Bioelectronic interfaces were produced *in situ*, growing silver microwires between CHO cells, offering an example of engineering of seamless functional interfaces controlled remotely. A model of wireless intracellular bioelectronic communication was also provided, where gold nanoparticles (AuNPs) conjugated with a redox-dependent fluorescent porphyrin were used as intracellular transducers, reducing the typical invasiveness of electronic systems and converting electronic inputs into a fluorescent output when an external electric field was applied. The last part of the investigation was to create conductive polymeric scaffolds fabricated by two-photon polymerisation (2PP) with nano- and micro-topographies to provide mechanical and electrical cues to human induced pluripotent stem cells-derived cardiomyocytes and advance their *in vitro* maturation state.

List of publications

Engineering the Spark into Bioelectronics Medicine. Sanjuan-Alberte P, Rawson FJ. ***Therapeutic delivery*** *(2019).*

Remotely Controlled in Situ Growth of Silver Microwires Forming Bioelectronic Interfaces. Sanjuan-Alberte P, Saleh E, Shaw AJ, Lacalendola N, Willmott G, Vaithilingam J, Alexander MR, Hague RJM, Rawson FJ. **ACS Applied Materials & Interfaces** (2019), 11 (9), 8928-8936.

Wireless Bioelectronic Nanosystems for Intracellular Communication. Sanjuán-Alberte P, Abayzeed SA, Fuentes-Domínguez R, Alea-Reyes ME, Clark M, Hague RJM, Alexander MR, Pérez-García L, Rawson FJ. **10.26434/chemrxiv.7106171.v2** (2018)

Isolation of adult rat cardiomyocytes using recombinant collagenases. Campora S, Sanjuan-Alberte P, Bruno C, Ghersi G. **Chemical Engineering Transactions** (2018) 64 25-30

Electrochemically Stimulating Developments in Bioelectronic Therapeutics. Sanjuan-Alberte P, Alexander MR, Hague RJM, Rawson FJ. **Bioelectronic Medicine** (2018) 4:1.

Acknowledgements

I would like to dedicate the first lines of this thesis to the memory of those who are not between us, but would be extremely proud of this achievement. To my grandparents Luisa, Amancio, Josefina and Jorge and my uncles Armando and Carlos for their infinite wisdom.

To my parents Beatriz and Juanra, for their understanding and unconditional support that made me the person I am today. To my brother Borja for always being present despite the distance and to all the increasing members of my family who fortunately are too many to be cited. Thank you for the warmest welcomes every time I come back home.

To Joao, for being the origin of this journey and my companion in many more to come.

To my family in Nottingham: Mariana, Duarte, Nora, Marta, Alejandro, Irene, Marina, Ioanna, JB and a very long etc.

To the technical staff and colleagues at Boots Science Building, Centre for Biomolecular Sciences and Advance Manufacturing Building for all the help, the laughs and the coffees that I very much needed during these years.

To Giulio, Stephanie and all the team involved in the Futform. Thank you for offering me this experience. (A thought for the brave Wistar rats that gave their life for science. May this sacrifice help to reduce animal work in the future.)

To two amazing researchers and two great friends: Simona and Jaya. Thank you for the late hours in the lab and the effort and dedication that you have shown during this time. Having worked with you is one of the most precious things I am taking from this PhD.

To my supervisors Richard, Morgan, Chris and my 'adoptive supervisor' Lluisa. I would have never come this far if it was not for their guidance, advice and motivation. Thank you for always being available for me.

Last but not least, to Frankie, for trusting me more than I did myself. Thank you for the passion, the energy and the love for science that you transmit to all of us.

To all, ¡gracias!

Paola

Table of contents

Abstract ..... **i**

List of publications ..... **ii**

Acknowledgements ..... **iii**

Table of contents ..... **v**

Table of figures ..... **x**

Table of tables ..... **xxi**

Abbreviations ..... **xxii**

Chapter 1. Literature Review **1**

1.1. Application of bioelectronic devices in medicine 4

1.1.1. Coupling of biological and electronic systems *5*

1.1.2. Current systems and their application in bioelectronic medicine *10*

1.1.3. Improving electronic targeting and specificity *15*

1.1.4. Limitations and opportunities in bioelectronic medicine *17*

1.2. Additive manufacturing to produce bioelectronic components ..21

1.2.1. Additive manufacturing of electronics *21*

1.2.2. Inkjet printing of conductive macro-structures *26*

1.2.3. Two-photon polymerisation of conductive microstructures *31*

1.3. Electrochemical reactions to target biological systems 35

1.3.1. General electrochemical reactions 35

1.3.2. Bipolar or wireless electrochemistry.....42

1.3.3. Basic principles of electronics 47

1.4. Aim and objectives 54

1.5. Summary.....56

Chapter 2. Materials and Methods 59

2.1. Materials and methods of Chapter 3.....61

2.1.1. Materials.....61

2.1.2. Inkjet printing process 61

2.1.3. Surface analysis 62

2.1.4. Resistance measurements 63

2.1.5. Microwire growth 63

2.1.6. Multi-component functional electronic device formation....64

2.1.7. Bioelectronic interface formation.....65

2.2. Materials and methods of Chapter 4.....69

2.2.1. Materials.....69

2.2.2. Inkjet printing of an electrochemical cell.....69

2.2.3. Electrodeposition of palladium onto unmodified gold nanoparticles (u-AuNPs).....70

2.2.4. Plasmonic-based detection of electrical charge modulation at u-AuNPs 71

2.2.5. Synthesis and characterisation of water soluble gold nanoparticles (ws-AuNPs)....73

2.2.6. Cell culture....73

2.2.7. Intracellular wireless actuation....75

2.3. Materials and methods of Chapter 5....77

2.3.1. Human induced pluripotent stem cell (hiPSC) differenciation into hiPSC-derived cardiomyocytes (hiPSC-CM)....77

2.3.2. Immunostaining of hiPSC-CM....77

2.3.3. Electrical stimulation of hiPSC-CM....78

2.3.4. Structure fabrication by two-photon polymerisation (2PP) .78

2.3.5. Viability studies....81

2.3.6. Morphological analysis of hiPSC-CM....81

Chapter 3. Development of a novel bionic manufacturing approach by inkjet printing and bipolar electrochemistry....82

3.1. Introduction....86

3.2. Results and Discussion....88

3.2.1. Inkjet printing of silver feeder electrodes....88

3.2.2. Electrochemical induction of silver microwire (AgMW) growth 98

3.2.3. Wireless electrochemical fabrication of functional 3D circuitry 105

3.2.4. Fabrication of in situ bioelectronic interfaces....109

3.3. Final considerations....116

Chapter 4. Wireless bioelectronic nanosystems for intracellular communication 117

4.1. Introduction 120

4.2. Results and Discussion 125

4.2.1. Inkjet printing of an electrochemical cell.....125

4.2.2. Wireless deposition of palladium on unmodified gold nanoparticles (u-AuNPs) 131

4.2.3. Study of plasmonic effects in u-AuNPs by dark field microscopy 140

4.2.4. Characterization and cell studies of chemically modified water-soluble gold nanoparticles (ws-AuNPs).....142

4.2.5. Intracellular wireless bioelectronic actuation.....150

4.3. Final considerations 155

Chapter 5. Two-photon polymerisation of conductive scaffolds to improve maturity of *in vitro* cardiomyocytes 157

5.1. Introduction 160

5.2. Results and discussion 164

5.2.1. Human induced pluripotent stem cell (hiPSC) differentiation 164

5.2.2. Viability studies on structures fabricated by two-photon polymerisation (2PP).....169

5.2.3. Preliminary maturation studies on 2D and 2.5D structures 175

5.2.4. Electrical stimulation of hiPSC-CM.....186

5.2.5. Maturation studies of hiPSC-CM on complex architectures 192

5.3. Final considerations.....198

Chapter 6. Conclusions and future directions 209

6.1. Conclusions.....209

6.2. Future work 212

References 214

Table of figures

Figure 1-1. Interaction between biological and electronic systems can be produced via (A) ionic currents inducing the polarisation of the cellular membrane, or (B) faradaic currents where the signal is transduced by redox mediators. 9

Figure 1-2. Ion vs faradaic conductance across the cell plasma membrane. Ionic currents are produced by the movement of charges across the membrane through the ion channels, whereas faradaic currents are produced by the movement of electrons between redox active species. 10

Figure 1-3. Schematic representation of a bioelectronic approach targeting the vagus nerve to control inflammation. Vagus nerve signalling interacts with the splenic nerve that reaches splenic T cells that produce acetylcholine, which reduces inflammation. 12

Figure 1-4. Different biological functions can be triggered by the application of electric fields. Currents can polarise (A) single cells and (B) tissues. Black arrows indicate the direction of the electrical currents whereas red arrows indicate the direction of the resulting polarised behaviour. 13

Figure 1-5. Transduction of signals on a bioelectrochemical system. An electronic input is mediated by redox active molecules and communicated to a cellular system triggering biological response 16

Figure 1-6. Examples of three dimensional (3D) conductive materials manufactured by (A) filament extrusion-based printing of silver on a non-flat surface, (B) inkjet printing of silver pillars and (C) two-photon polymerisation (2PP) of intricate microstructures containing gold particles. Images reproduced with permission from [103, 126, 134]. 25

Figure 1-7. Schematic representation of droplet deposition from a printer cartridge of a drop-on-demand (DOD) piezoelectric inkjet printer 28

Figure 1-8. Diagram of printing, curing and sintering processes of metallic inks 30

Figure 1-9. Schematic representation of 2PP to produce 3D structures ... 33

Figure 1-10. Transference of electrons between the energy levels of the electrodes and electroactive species in a solution.....37

Figure 1-11. Schematic representation of the interface between an electrode and a solution when a potential is applied and the double layer formation. It should be noted that ions should be solvated in an aqueous solution; however, this effect was not indicated in the diagram to avoid confusion. 40

Figure 1-12. Schematic representation of bipolar electrochemistry 43

Figure 1-13. (A) Diagram showing the proposed reactions to induce motion in objects (top) and microscope image of object in motion (bottom). (B) Schematic illustration of a bipolar sensor and the sensing principle for analyte detection (top) and microchip for simultaneous detection of lactate, choline chloride and glucose. Reproduced with permission from [191] and [198].....45

Figure 1-14. (A) Direction of electrons within a conductor material in direct current (DC) (top) and alternating current (AC) (bottom). (B) Magnitudes of potential and current in DC (blue) and AC (green) over time. 49

Figure 1-15. (A) Double layer formation in an electrochemical cell and (B) the representation of its equivalent electrical circuit. 50

Figure 1-16. Charges at both sides of a basic cellular membrane and its correspondent equivalent circuit 51

Figure 1-17. Modelled equivalent circuit of a neuron with sodium and potassium voltage-gated channels.....52

Figure 3-1. Schematic representation of bipolar electrochemistry system 89

Figure 3-2. Tripropylene glycol diacrylate (TPGDA) chemical structure. Simplified structure can be seen on the right. 90

Figure 3-3. (A) Jetting waveform and (B) droplet formation and ejection from nozzles of TPGDA ink 90

Figure 3-4. Mechanism of free radical formation after irradiating UV on TPGDA ink containing the photoinitiator DETX and co-initiator EDB.....91

Figure 3-5. Mechanism of polymerisation after photoinitiaton.....92

Figure 3-6. (A) Jetting waveform and (B) droplet formation and ejection from nozzles of silver nanoparticle ink (AgNP ink).....93

Figure 3-7. (A) Bi-dimensional and (B) three-dimensional images of and edge of an inkjet printed silver electrode obtained by AFM and (C) its height profile (N=3; n=3).....94

Figure 3-8. Atomic Force Microscopy (AFM) images of an inkjet printed silver film before (A) and after (B) thermal sintering (scale bar 200 nm). 95

Figure 3-9. Resistivity of (A) one layer of silver surfaces at different sintering temperatures, (B) one layer of silver surfaces sintered at 200°C at different times (C) different layers of silver surfaces sintered at 200°C (n=10, SD) 96

Figure 3-10. Optimisation of potentials applied (V) vs distance between feeder electrodes (mm) to induce microwire growth resulting in (I) thin microwires, (II) thick microwires and (III) deposition at the surface. Scale bar 100 um. 99

Figure 3-11. Figure 2.14. EDX analysis of (a) deposition on surface and (b) microwires consisting on (I) SEM image, (II) element composition, (III) carbon spectrum and (IV) silver spectrum. 100

Figure 3-12. Potential induced self-assembly of silver cations to form microwires at the positive electrode observed by (A) optical microscopy (scale bar 100 µm) and (B) scanning electron microscopy of self-assembled silver nanoparticles resulting in different diameters. Scale bar 1 µm. 101

Figure 3-13. Modelled electric field and electronic potential of 90 V applied using different geometries of feeder electrodes (contour: electric potential (V), arrow surface: electric field).....102

Figure 3-14. Optical microscopy images of AgMW connections between feeder electrodes in the shape of (A) square, (B) circle and (C) triangle. AgMWs were false coloured in red to highlight them. Scale bar 500 µm. 103

Figure 3-15. Diameter, number of connections and resistance of wires established between electrodes at different geometric shaped feeder electrodes. Error bars represent standard error mean (SE), further statistical

analysis was performed using one-way ANOVA with Tukey's HSD post hoc analysis (n = 9 ; p ≤ 0.0001). 104

Figure 3-16. Diagram of system to test functionality and three-dimensional growth of silver microwires. 1) Two pairs of silver feeder electrodes are printed on top of a TPGDA layer on glass and a LED is placed upside down between them. 2) A drop of MilliQ water is added covering a pair of feeder electrodes and one gold electrode from the LED and a potential difference is applied. 3) Microwire formation is completed and the systems is tested using a multimeter 106

Figure 3-17. (A) Top and frontal view of printed electrodes and placement of a light-emitting diode, (B) optical microscope image of magnified area within the red circle in I showing AgMWs forming a 3D connection with one of the gold electrodes of the LED, AgMWs were coloured in red and pointed with an arrow (scale bar 500 µm); and (C) test of functionality indicating green diode light (arrow). 107

Figure 3-18. Optical microscope image of AgMWs (red) growing between CHO cells (green). AgMWs form a conductive mesh surrounding cells (arrows). Circles of silver with a diameter of 67 ± 6.2 µm were printed between the feeder electrodes to guide silver wires acting as bipolar electrodes (BPEs). Scale bar 50 µm.....110

Figure 3-19. Optical microscope images of CHO cells and feeder electrodes (A) before and (B) after AgMW growth. Scale bar 200 µm. 111

Figure 3-20. Typical cyclic voltammograms (CV) obtained with solutions of phosphate buffered saline (A) prior MW growth without cells, (B) after MW growth and without cells, (C) prior MW growth in the presence cells and (D) after MW growth in the presence of cells. Scan rate 100 mV s-1. Mean values of three different samples were calculated and represented within the CVs. 112

Figure 3-21. (A) Percentage of viable cells after wire growth using direct current relative to percentage of viable cells prior potential application (N=3,

n=3 ; SD). (B) Optical microscopy image of CHO cells after Trypan blue viability assay after DC application of 90 V. 115

Figure 4-1. Schematic representation of gold nanoparticles used as bipolar electrodes 121

Figure 4-2. Jetting waveform of gold nanoparticle ink (AuNP ink) 126

Figure 4-3. Droplets of AuNP ink ejected from a nozzle 126

Figure 4-4. Atomic force microscopy (AFM) (A) bi-dimensional and (B) three-dimensional images of and edge of an inkjet printed gold electrode obtained by AFM and (C) its height profile (N=3; n=3) 127

Figure 4-5. Resistance of (A) one layer of silver surfaces sintered at 220°C at different times (B) different layers of silver surfaces sintered at 220°C (n=5, SD) 128

Figure 4-6. AFM images of printed gold electrodes (A) before and (B) after thermal sintering (scale bar 200 nm). 129

Figure 4-7. (A) Design and dimensions of an electrochemical cell consisting in two gold feeder electrodes and one silver pseudoreference electrode. (B) Image of the inkjet printed system and (C) optical microscopy image of the gap between feeder electrodes. 130

Figure 4-8. Cyclic voltammogram obtained using an inkjet printed electrochemical cell at a scan rate of 100 mV s^{-1} for 1 mM potassium hexacyanoferrate (III) in phosphate buffer saline solution. Blue dots represent the points measured and red line the average values. 131

Figure 4-9. Schematic representation of the theoretical redox reactions taking place to electrodeposit palladium on gold nanoparticles. 133

Figure 4-10. Size distribution of unmodified gold nanoparticles (u-AuNPs) with and without palladium when 10 V of direct current (DC) were applied for 1, 5 and 15 min (n=3: SD). 134

Figure 4-11. Solutions containing (A) gold nanoparticles and (B) gold nanoparticles + palladium after the application of potential for 1, 5 and 15min 135

Figure 4-12. SEM images of u-AuNPs+Pd a (top) and EDX images where the Au M series can be seen in orange and the Pd L series in blue (bottom) of AuNP+Pd after the application of 10 V for 5 minutes. 136

Figure 4-13. Effect of applying 10 V between 0 and 15 minutes to the pH of the solution.....138

Figure 4-14. DLS study of u-AuNPs in the presence and absence of 1 mM PdCl2 on buffer solutions for 1 and 15 minutes at pH 7, 4 and 2 (n=3 ; SD)..139

Figure 4-15. Microscopy images of voltage-modulated intensity sensing of by plasmonic nanoparticles. (A) A darkfield microscopy images of Au nanoparticles; (B) a map of the amplitude of the voltage-modulated scattering intensity (|S|) of 125nm Au nanoparticles, presented to support that low-voltage can be detected by Au nanoparticles and therefore can be used as electronic sensorsfor the voltage effect is presented in (B) mapping the amplitude of the voltage-modulated scattering intensity (|S|) of 125nm Au nanoparticles shown in the darkfield image in B. (C) is aA magnified view of the darkfield image where the intensity modulation spectrum (D) is obtained..141

Figure 4-16. Diagrammatic representations of functionalisation strategy for producing a gemini pyridinium based amphiphile incorporating Zn(II)meso-tetrakis(4-carboxylicphenyl)porphyrin sodium salt (Na-ZnTCPP) onto water-soluble gold nanoparticles (ws-AuNPs). 143

Figure 4-17. (A) DLS results showing size distribution of ws-AuNPs before and after chemical modification with Na-ZnTCPP (n=3 ; SD). (B) Transmitted electron microscopy (TEM) image of a pair of Na-ZnTCPP modified ws-AuNPs. Scale bar 100 µm. 144

Figure 4-18. (A) UV-VIS absorbance spectrum and (B) emission spectrum of ws-AuNPs (orange), free Na-ZnTCPP (black) and Na-ZnTCPP modified ws-AuNPs (green). 145

Figure 4-19. (A) Opticam microscopy image of Chinese hamster ovary (CHO) cells. Scale bar 200 µm. (B) Percentage of viable cells calculated using a Trypan blue assay. (C) Inductively coupled plasma mass spectrometry (ICP-MS) analysis

of concentration of fold internalised in the cells and in supernatant solution (left) and calculation of gold nanoparticles per cell (right). 147

Figure 4-20. WST-8 metabolic activity assay of CHO cells incubated with Na-ZnTCPP modified ws-AuNP at different concentrations of Na-ZnTCPP (C1: 11.8 µM, C2: 2.36 µM and C3: 1.18 µM) for 24, 48, 72 h. Cells incubated in complete media were used as negative control and cells incubated in TritonX 3% were used as positive control. Negative control was assumed as 100% viability and rest of values were presented relative to this (n=3; SD). 150

Figure 4-21. A) Diagram showing the result of the application of potentials. B) Fluorescence microscope images of CHO cells containing Na-ZnTCPP modified ws-AuNPs (i) before application of potentials and (ii) its correspondent coloured image and (iii) after applying the potential and (iv) coloured image. Scale bar 100 µm. 151

Figure 4-22. C) Corrected total cell fluorescence quantified in the area of the cells before and after applying the potential. Statistical significance was calculated using an unpaired two-tailed test (n=10; SD; *p=0.0117). 152

Figure 4-23. A) Diagram showing the ws-AuNPs incubated with CHO cells used as negative controls. Fluorescence microscope images of CHO cells containing ws-AuNPs (B) before application of potentials and (C) coloured image, and (D) after applying the potential and (E) coloured image. 153

Figure 5-1. Diagram showing the morphological differences and the different compontents that can be found in early, late and adult human pluripotent stem cell-derived cardiomyocytes. Reproduced with permission from [285]. 161

Figure 5-2. Schematic of *in vitro* strategies used to improve the developmental state of hiPSC-CM. Adapted with permission from [288]. 162

Figure 5-3. Images obtained by optical microscopy showing the differentiation process from human induced pluripotent stem cells (hiPSC) to immature cardiomyocytes induced by growth factors at different cell concentrations. Differentiation process is carried out at day 2 in the cycle of

hiPSCs, followed by a preconditioning step. hiPSC-cardiomyocytes (hiPSC-CM) start to spontaneously beat on day 8 of differentiation process. 166

Figure 5-4. Immunostaining of three batches of hiPSC-CM after dissociation. Cells were immunolabelled for cardiac troponin TNNI3 (green). Nuclei were counterstained with Hoechst. hiPSC-CM are positive for the green markers, whereas other cellular types are stained only with Hoechst. Immunostaining without antibody against TNNI3 represents the negative control (N=3, n=2; scale bar 200 µm). 168

Figure 5-5. Percentage of hiPSC-CM after differentiation calculated after immunostaining of three different batches of cells after dissociation (N=3, n=2; error bars represent standard deviation (±SD)). 169

Figure 5-6. Chemical structure of pentaerythritol triacrylate (PETrA) 170

Figure 5-7. Optimisation of spot energy absorption (J) during 2PP process, degree of conversion (%) and viability of hiPSC-CM as a function of PI concentration (N=2, n=3; SD on viability samples).....171

Figure 5-8. Fluorescence microscope images of hiPSC-CM on PETrA surfaces at different concentrations of photoinitiator (PI): (A) 0.5% PI, (B) 1% PI and (C) 3% PI and (D) glass surfaces stained with 1 µM acetoxymethyl calcein (C-AM) in PBS (green) and 5 µM ethidium homodimer I (EthD-1) in PBS (red). Scale bar 200 µm. 172

Figure 5-9. Percentage of viable hiPSC-CM on control, PETrA0.5%PI, PETrA1%PI and PETrA modified with multi-walled carbon nanotubes (PETrA+CNTs) at concentrations of 0.1 w/w% and 0.2 w/w% on day 6 after seeding. (N=3, n=2; SD) 174

Figure 5-10. PETrA structures produced by 2PP. (A) Optical microscopy of 100x100 µm (left) and 200x200 µm (right) flat surfaces. Scale bar 100 µm. (B) 500 nm wide nano-grooves with 750nm depth/pitch. Scale bar 1 µm.....176

Figure 5-11. Typical fluorescence images of hiPSC-CM on a PETrA1%PI structure where half of the surface is flat and the other half contains vertical grooves (virtually separated by dotted line). Nucleus were stained with Hoechst (blue) and actin with phalloidin (red). Scale bar 400 µm. 177

Figure 5-12. Fluorescence microscopy images of hiPSC-CM seeded on (A) glass, (B) 1x1 mm flat PETrA0.5%PI (fPETrA0.5%PI) and (C) 1x1 mm PETrA0.5%PI surfaces with grooves (gPETrA0.5%PI), (D) 1x1 mm flat PETrA1%PI (fPETrA1%PI), (E) 1x1 mm PETrA1%PI surfaces with grooves (gPETrA1%PI) and (F) 1x1 mm flat PETrA modified with MWCNTs 0.1 w/w % (PETrA+CNTs) printed by 2PP. Cells were immunolabelled for cardiac alpha-actinin (green), nuclei were stained with Hoechst (blue) and actin was stained with phalloidin (red). Direction of grooves is indicated by the arrow. Scale bar 200 µm 180

Figure 5-13. (A) Aspect ratio and (B) angle of alignment of hiPSC-CM on control surfaces, fPETrA0.5%PI, gPETrA0.5%PI, fPETrA1%PI, gPETrA1%PI and PETrA+CNTs surfaces on day 6 after seeding. Statistical significance was calculated using an ordinary one-way ANOVA statistical test (N=3, n=10; error bars represent the standard error of the mean (SEM)). 181

Figure 5-14. Methodology followed to measure sarcomere length of hiPSC-CM: (i) structural analysis of a cardiomyocyte on a PETrA surface with grooves immunolabelled for cardiac alpha-actinin, (ii) intensity graph of red line extracted with Image J line profile tool.....183

Figure 5-15. Fluorescence image of sarcomeres of hiPSC-CM immunolabelled for cardiac alpha-actinin on (A) control surfaces, (B) fPETrA0.5%PI, (C) gPETrA0.5%PI, (D) fPETrA1%PI, (E) gPETrA1%PI and (F) PETrA+CNTs. Direction of grooves is indicated by an arrow. Scale bar 20 µm. 184

Figure 5-16. Sarcomere length of hiPSC-CM on control surfaces, PETrA0.5%PI, PETrA1%PI, and PETrA+CNTs on flat and surfaces with grooves. Statistical significance was calculated using an ordinary one-way ANOVA statistical test. 10 measurements were taken in 10 cells per sample (N=3, n=10; SEM).....185

Figure 5-17. (A) Image of device used to perform the electrical stimulation of hiPSC-CM. Determination of excitation threshold by application of external electrical stimulation (e-stim.) with alternating current (AC) of hiPSC-CM. (B)

Number of contractions per minute at 1.5 Hz and varying potential and (C) Number of contractions per minute at 2 V and varying frequency. 187

Figure 5-18. (A) Fluorescence microscope images of hiPSC-CM one week after application of external electric fields with magnitudes of (i) 0 V (ii) 4 V, (iii) 6 V and (iv) 10 V. Viable cells were stained with 1 µM C-AM in PBS (green) and nonviable cells were stained with 5 µM EthD-1 in PBS (red). Scale bar 200 µm. (B) Percentage of viable cells (n=3; SD). 189

Figure 5-19. Fluorescence microscopy image of sarcomeres hiPSC-CM immunolabelled for cardiac alpha-actinin on (A) control, (B) PETrA1%PI and (C) PETrA+CNTs surfaces after electrical stimulation at 2 V and 3 Hz for 24 h. Scale bar 20 µm.....190

Figure 5-20. Sarcomere length of hiPSC-CM on control surfaces, PETrA1%PI, and PETrA+CNTs with and without e-stim. for 24 h. Statistical significance was calculated using an ordinary one-way ANOVA statistical test. 10 measurements were taken in 10 cells per sample (N=3, n=10; SEM) except on those samples marked with red asterisks 191

Figure 5-21. Effects of channel nanotopography on hiPSC-CM. (A) hiPSC-CM seeded on flat channels, channels with vertical grooves and channels with radial grooves. (B) Percentage of cardiomyocytes found in, partially in and out of the different channels. 192

Figure 5-22. (A) CAD design of a myofibril-like structure. Optical microscopy images of myofibril-like structures fabricated with (B) PETrA1%PI and (C) PETrA+CNTs. 193

Figure 5-23. SEM image of myofibril-like structure fabricated by 2PP with PETrA1%PI with dimensions: 1000 x 1000 x 15 µm with micro and nano-grooves. Scale bar 10 µm.....194

Figure 5-24. hiPSC-CM seeded on (A) PETrA1%PI and (B) PETrA+CNTs myofibril-like structure. Nucleus were stained with Hoechst (blue) and actin with phalloidin (red). Direction of channels is indicated by yellow arrow. Scale bar 400 µm.....195

Figure 5-25. Fluorescence microscopy image of sarcomeres of hiPSC-CM on myofibril-like structures immunolabelled for cardiac alpha-actinin on (A) PETrA1%PI, (B) PETrA1%PI after 24h e-stim., (C) PETrA+CNTs and (D) PETrA+CNTs after 24h e-stim 196

Figure 5-26. Sarcomere length of hiPSC-CM on myofibril-like structures of PETrA1%PI, and PETrA+CNTs with and without e-stim. for 24 h. Statistical significance was calculated using an ordinary one-way ANOVA statistical test. 10 measurements were taken in 10 cells per sample (N=3, n=10; SEM) except on those samples marked with red asterisks 197

Table of tables

Table 1-1. Categories of AM according to ASTM Standard F2792[117] and their use and application in the manufacturing of electronics.....24

Table 1-2. Bipolar electrochemistry systems with biological applications 46

Table 3-1. Resistivity values of silver electrodes obtained by thermal deposition, inkjet printing of five layers after sintering process and bulk silver at 295K (μΩcm)[240] (n=10). 97

Abbreviations

0D	Zero-dimensional
1PP	Single-photon polymerisation
2PP	Two-photon polymerisation
3D	Three-dimensional
A	Cross-sectional area of a conductive material (cm^2)
AFM	Atomic force microscopy
AgMW	Silver microwire
AgNP ink	Silver nanoparticle ink
AM	Additive manufacturing
ATP	Adenosine triphosphate
AuNP ink	Gold nanoparticle ink
BMP4	Bone morphogenetic protein 4
BPE	Bipolar electrode
C	Capacitance (F)
C	Concentration (mol)
CAD	Computer-aided design
C-AM	Acetoxymethyl calcein
C_{DL}	Double layer capacitance (F)
CHO	Chinese hamster ovary cells
C_{me}	Capacitance of cellular membrane (F)
CNTs	Carbon nanotubes
C_O	Concentration of oxidised electroactive species at the surface of the electrode (mol)
C_R	Concentration of reduced electroactive species at the surface of the electrode (mol)
CV	Cyclic voltammogram
D	Diffusion coefficient ($cm^2\ s^{-1}$)
DETX	Diethylthioxanthone
DLS	Dynamic light scattering
DOD	Drop-on-demand
E	Potential (V)
E_a	Potential at the anodic feeder electrode (V)
E_c	Potential at the cathodic feeder electrode (V)
ECM	Extracellular matrix
EDB	Ethyl-4-(dimethylamino)benzoate
EDX	Energy dispersive x-ray
E_f	Value of electric field ($V\ cm^{-1}$)

E_L	Electrochemical gradient of leak channels (V)
E^o	Standard potential (V)
e-stim	Electrical stimulation
EthD-1	Ethidium homodimer 1
E_x	Potential at a given point *x* on the surface of a particle (V)
F	Faradaic constant (F)
FFT	Fast Fourier transform
fPETrA0.5%PI	Flat PETrA structures with 0.5% PI
fPETrA1%PI	Flat PETrA structures with 1% PI
g_K	Conductance of potassium channels (S)
g_L	Conductance of leak channels (S)
g_{Na}	Conductance of sodium channels (S)
gPETrA0.5%PI	PETrA structures with grooves and 0.5%PI
gPETrA1%PI	PETrA structures with grooves and 1%PI
HBSS	Hank's Balanced Salt solution
hiPSC	Human induced pluripotent stem cell
hiPSC-CM	Human induced pluripotent stem cell-derived cardiomyocyte
HOMO	Highest occupied molecular orbital
i	Current (A)
ICP-MS	Inductively coupled plasma mass spectrometry
I_{me}	Total membrane current (A)
I_p	Current sources associated to ion pumps (A)
ITO	Indium-tin oxide
J	Flux of molecules (mol s^{-1} cm^{-2})
l	Length of a conductive material (cm)
L	Length of the bipolar electrode (cm)
LED	Light-emitting diode
LUMO	Lowest unoccupied molecular orbital
MWCNTs	Multi-walled carbon nanotubes
n	Number of moles of electrons
Na-ZnTCPP	Zn(II)meso-tetrakis(4-carboxylateyphenyl)porphyrin sodium salt
NIR	Near infrared
NP	Nanoparticles
ϕ	Electric potential in Nernst-Planck equation
PBS	Phosphate buffer saline
PETrA	Pentaerythritol triacrylate
PETrA+CNTs	PETrA modified with multi-walled carbon nanotubes
PETrA0.5%	PETrA formulation with 0.5% photoinitiator
PETrA1%	PETrA formulation with 1% photoinitiator
PI	Photoinitiator

Q	Flow of charge (C)
R	Electrical resistance (Ω)
r	Radius of particles (cm)
R	Gas constant (J mol^{-1} K^{-1})
R_{ET}	Electron transfer resistance (Ω)
R_i	Ionic resistance (Ω)
R_{me}	Resistance of cellular membrane (Ω)
SD	Standard deviation
SEM	Standard error of the mean
SEM	Scanning electron microscopy
T	Temperature (K)
TEM	Transmitted electron microscopy
TGF-beta	Transforming growth factor-beta
TPGDA	Triproplylen glycol diacrylate
u-AuNPs	Unmodified gold nanoparticles
V	Potential difference (V)
V_K	Potential of potassium channels (V)
V_L	Potential of leak channels (V)
V_{me}	Membrane potential (V)
V_{Na}	Potential of sodium channels (V)
ws-AuNPs	Water-soluble gold nanoparticles
WST-8	Water-soluble tetrazolium salt
z	Valence of ionic species
ΔE	Potential difference between the two extremities of the bipolar electrode (V)
Θ	Angle relative to the direction of the electric field
ρ	Resistivity (Ω cm)

Chapter 1. Literature Review

Bioelectronic medicine consists on the merging of biological and electronic components for therapeutic applications. Biological systems possess electrical activity in the form of ionic currents, endogenous electric fields and faradaic currents that induce a biological effect, such as signalling, growth, development and metabolism; that can be externally controlled and influenced. Current efforts in bioelectronic medicine are mainly directed to cells that can be easily excited, such as neuronal and cardiac cells by, for example, using direct vagus nerve or atrial stimulation, respectively. Non-excitable cells can also be targeted by electronic inputs, by applying external electric fields and faradaic currents, broadening the spectrum of cells that can be electrically influenced.

However, seamless integration between electronic and biological systems has not been achieved and is one of the main limitations in bioelectronic medicine. This is due to the structural and molecular differences of the properties that form electronic and biological systems. Additive manufacturing techniques could offer a solution to this, by producing conductive macro- and microstructures, which in some cases can achieve submicron resolution. This is

the case of inkjet printing and two-photon polymerisation, which have been able to create biocompatible structures and conductive patterns. Other limitations in bioelectronic medicine include the invasiveness of the techniques used and the lack of specificity of the electrical inputs applied. Highly specific electrochemical reactions could solve the lack of specificity and in particular, bipolar electrochemistry could reduce the invasiveness of traditional bioelectronics due to its ability to target electrochemical reactions wirelessly.

Additive manufacturing and electrochemical approaches can individually solve many of the current limitations in bioelectronic medicine, however in this work, the creation of novel bioelectronic tools was investigated using a combination of both that can be applied as therapeutic tools.

Keywords: Bioelectronics, bioelectronic medicine, additive manufacturing, electrochemistry

Part of the content of this chapter (1.1. Application of bioelectronic devices in medicine) is an extended version of *Electrochemically Stimulating Developments in Bioelectronic Therapeutics*. Sanjuan-Alberte P, Alexander MR, Hague RJM, Rawson FJ. **Bioelectronic Medicine** (2018) 4:1.

Chapter 1. Literature Review.....1

1.1. Application of bioelectronic devices in medicine.....4

1.1.1. Coupling of biological and electronic systems.....5

1.1.2. Current systems and their application in bioelectronic medicine 10

1.1.3. Improving electronic targeting and specificity.....15

1.1.4. Limitations and opportunities in bioelectronic medicine.....17

1.2. Additive manufacturing to produce bioelectronic components..21

1.2.1. Additive manufacturing of electronics.....21

1.2.2. Inkjet printing of conductive macro-structures.....26

1.2.3. Two-photon polymerisation of conductive microstructures.31

1.3. Electrochemical reactions to target biological systems.....35

1.3.1. General electrochemical reactions.....35

1.3.2. Bipolar or wireless electrochemistry.....42

1.3.3. Basic principles of electronics.....47

1.4. Aim and objectives.....54

1.5. Summary.....56

1.1. Application of bioelectronic devices in medicine

The term *bioelectronics* has been continuously evolving since it was first proposed in 1968. The initial definition referred to intermolecular electron transfer and its role in modulating cell behaviour[1]. However, development of technology, materials and manufacturing methods have accelerated the progress achieved within the area, where a synergistic combination of biological and electronic materials is now sought[2].

Coupling of biology and electronics is important in many areas and has been proven key to develop multiple subfields. This includes microbial fuel cells, where electrons are harvested from metabolic processes and organic electron donors present in microorganisms, generating a current of electrons[3-4]. Biological fuel cells can be used for efficient and sustainable generation of electricity[5], removal of organic molecules and pollutants from wastewater[6] or water desalination[7].

Other closely linked areas of interest include: bionics, to externally replicate or enhance cellular biology, tissues and organs[8-9]; biosensing for the detection of molecular reactions[10] and; more importantly in the context of this thesis, bioelectronic medicine, where integration of cellular and electronic elements has the potential to induce a therapeutic effect.

1.1.1. Coupling of biological and electronic systems

In order to accomplish an efficient electron exchange between biological and electronic systems, a good transduction of signals at the cellular-electronic interface must be achieved[11]. This has become a key challenge in developing bioelectronics as the building blocks of the extremely complex cellular structures differ from the typical conductive materials that can be found in electronics (proteins and lipids vs metals, with different chemistries and material properties). In addition, the minimum distance required to induce the electron-tunnelling between both elements is in the order of few nm[12-13], meaning that the seamless integration of electronics with biology is not yet possible[14].

Cells and tissues possess an electrical activity that can be taken advantage of when developing bioelectronic devices. This natural electrical activity or bioelectricity is present in the form of endogenous electric fields, ionic currents and/or faradaic currents[9], and it is vital for the cell development as it takes part in many processes including cellular communication[15-16], growth[17], proliferation[18] and metabolism[19]. Therefore, external electronic signals have the potential to replicate or influence the biological electrical activity which underpins, alongside other biological cues, the cellular behaviour.

Electrical communication that is mediated by neurons is the body's universal fast electrical communication system that orchestrates organ

function at a macro level. The underlying principles of the body's electrical communication system, from a traditional point of view, originates from the controlled bulk movement of ions across the plasma membrane of cells. Sodium-potassium pumps perform active transport of ions through the membrane by moving Na^+ and K^+ against concentration gradients by consuming adenosine triphosphate (ATP), and stabilise the resting membrane potentials[20]. Action potentials are then generated in voltage-gated ion channels that modulate membrane potentials[21] which fluctuate between negative and positive values and in doing so, produce an electrochemical potential gradient that can drive bulk charge movement to transmit information[22].

This type of communication is not exclusively found in neurons. Muscle cells can generate electrical signals by polarisation and depolarisation of the plasma membrane leading to action potentials that propagate quickly through the tissue[23]. This induces changes in the conformation of myofibril elements such as troponing and myosin, therefore inducing the contraction of the muscle[24]. It has also been established that changes in potentials of the cell membrane of endocrine cells can induce the release of hormones[25].

Importantly, all cell types have membrane potentials whose main function is not the production of action potentials in communication and signalling processes, but the maintenance of electromotive gradients. These membrane potentials are involved in the transport of molecules across the cell membrane

induced by the translocation of charges, or electrogenic transport. This includes the absorption of glucose from intestinal cells[26], movement of ADP/ATP in the mitochondria[27] and the transport of small molecules such as nicotine and peptides involved in a plethora of physiological roles[28-31].

This natural electrical behaviour present in all cell types can be organised and stimulated by applying electric currents that control the polarisation of the membrane potential. Due to the high resistance of the cellular membrane, ionic currents induced by artificial external electric fields are forced to surround the cells, imposing a potential gradient across the membrane surface. This transmembrane potential induces changes in function and/or orientation of membrane proteins and opening of ionic channels, leading to stimulation of intracellular signalling pathways[32]. The signalling cascade alters expression of genes which code for proteins involved in several biological functions including cell division, migration, proliferation and embryogenesis[32].

Faradaic currents can also be used in cell communication amongst other communication routes[33] and are vital for maintaining homeostasis. Some biochemical processes result in the production of faradaic current, which is defined as the movement of electrons generated in redox reactions[34]. In order for redox reactions to happen, an exchange of electrons between two biochemical entities, an electron donor and an electron acceptor, needs to be produced[35]. Faradaic currents are reliant on naturally occurring biological

electrochemical mediators, which are defined as molecules that readily accept or donate electrons. Some of the most well known and most abundant are NADH, NADPH, GSH, Ascorbic acid or ubiquinone[36].

Additionally, bio-macromolecules such as enzymes (i.e. oxido-reductases) can also act as electron shuttles[37]. Examples of faradaic signalling include the generation of oxidant sources within the mitochondrial respiratory chain in response to bacterial infection or inflammation[38]. Additionally, all cells use membrane electron transport systems to shuttle electrons across membranes for a wide range of purposes[39]. The electron transport via membrane bound systems have been implicated in cell signalling, nutrient metabolism, cell redox maintenance and can play an important role in diseases such as cancer[40-41].

Opportunities in bioelectronics arise when electrical components can be used to electrically stimulate cells or substitute a biological electrochemical mediator involved in generating an electrical faradaic current. This constitutes the two main pathways of electrical cellular intervention and will be described in detail in the following paragraphs. Electronic inputs can be transmitted in the form of ionic currents, inducing the polarisation of the cellular membrane, or faradaic currents, where the stimulation is mediated by a redox biomolecule[42] (Figure 1-1).

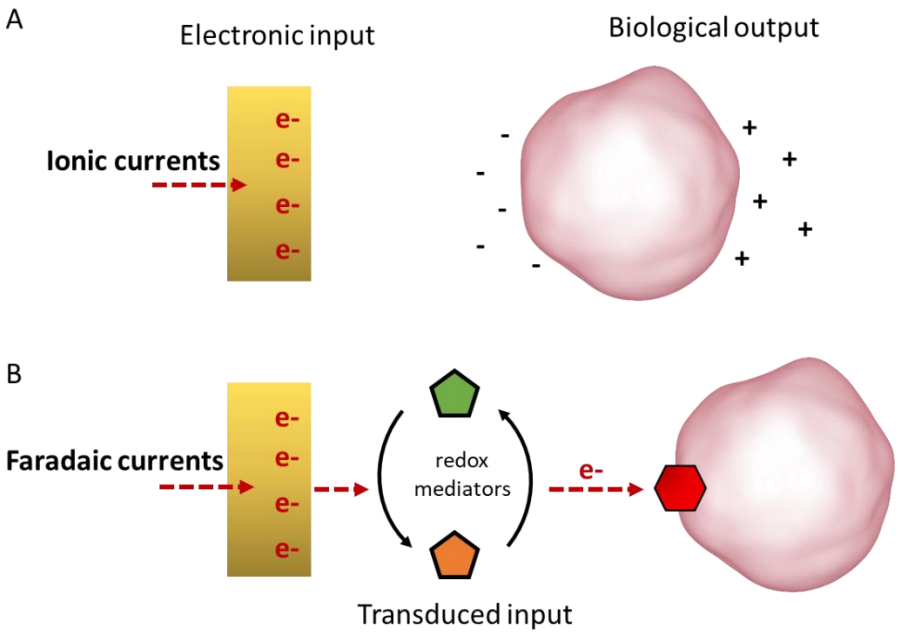

Figure 1-1. Interaction between biological and electronic systems can be produced via (A) ionic currents inducing the polarisation of the cellular membrane, or (B) faradaic currents where the signal is transduced by redox mediators.

Ionic currents are caused by the efflux of electrons from an electrode. This produce a gradient of potential or an electric field that surrounds the cell[43-44]. This effect can be used to control opening and closing of cellular ion channels in the membrane causing a polarisation that can ultimately trigger an action potential. This route is the most obvious and common pathway of intervention in bioelectronics designed for neural and cardiac stimulation, as these cells can easily respond to changes in polarisation.

On the other hand, faradaic currents are mediated by highly specific redox biomolecules. This yields the ability to control redox events when interfacing cells with electronics by modulating the electron flow in a specific biochemical

event by applying an electrical potential stimulus, leading to modulation of the underlying biochemistry as a result (Figure 1-2).

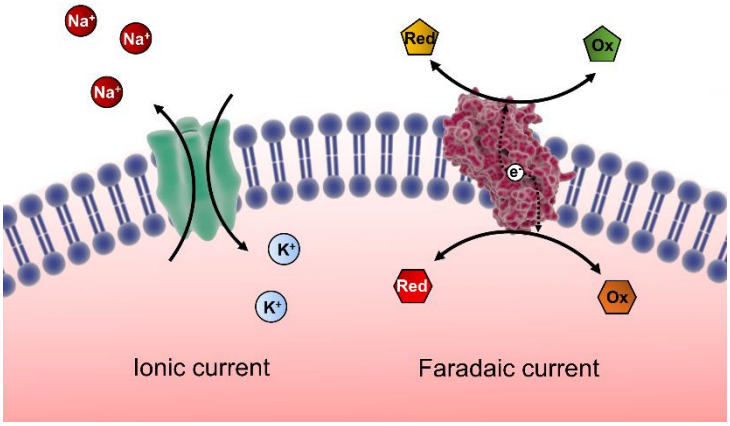

Figure 1-2. Ion vs faradaic conductance across the cell plasma membrane. Ionic currents are produced by the movement of charges across the membrane through the ion channels, whereas faradaic currents are produced by the movement of electrons between redox active species.

1.1.2. Current systems and their application in bioelectronic medicine

Bioelectronic medicine has been classically conceptualised as electronic technology that merges with neurons for therapeutic applications. However, as all cell types can be subjected to electronic stimulation as shown previously, this concept should be extended to include the merging of biological systems with electronic devices, allowing for the modulation of the underlying cells, tissue and ultimately organ function by regulating electrical communication.

Due to the ease of neural excitability, most of the efforts have been directed to nerve stimulation. Significant progress has been made with several

electronic devices successfully introduced as therapeutics aimed at palliating disabilities, and consequently become good examples of an effective transduction of signals. Examples include cochlear and retinal implants where sound and light, respectively, are converted into electrical signals that can be transmitted to the nervous system and interpreted by the patient's brain[45-46].

Stimulation of nerve fibres, based on direct vagus nerve stimulation, is gaining interest as a treatment of rheumatoid arthritis and metabolic syndrome[47-49]. In this case, the excitation of the vagus nerve is transmitted to the splenic nerve, where macrophages are deactivated and thus, the release of pro-inflammatory cytokines is inhibited, reducing the inflammation in diverse areas of the body (Figure 1-3)[50]. This therapeutic strategy demonstrates the influence of the nervous system over the different biological functions and disease state. Further investigation in this regard can possibly decode the neural circuits and how nerve stimulation correlates to the homeostatic state of an organism, leading to new means of treating and diagnosing disease. Similar devices based on the depolarisation of the sinus node to induce action potentials can be found for excitation of cardiac cells in the therapy of heart failure and atrial fibrillation[51].

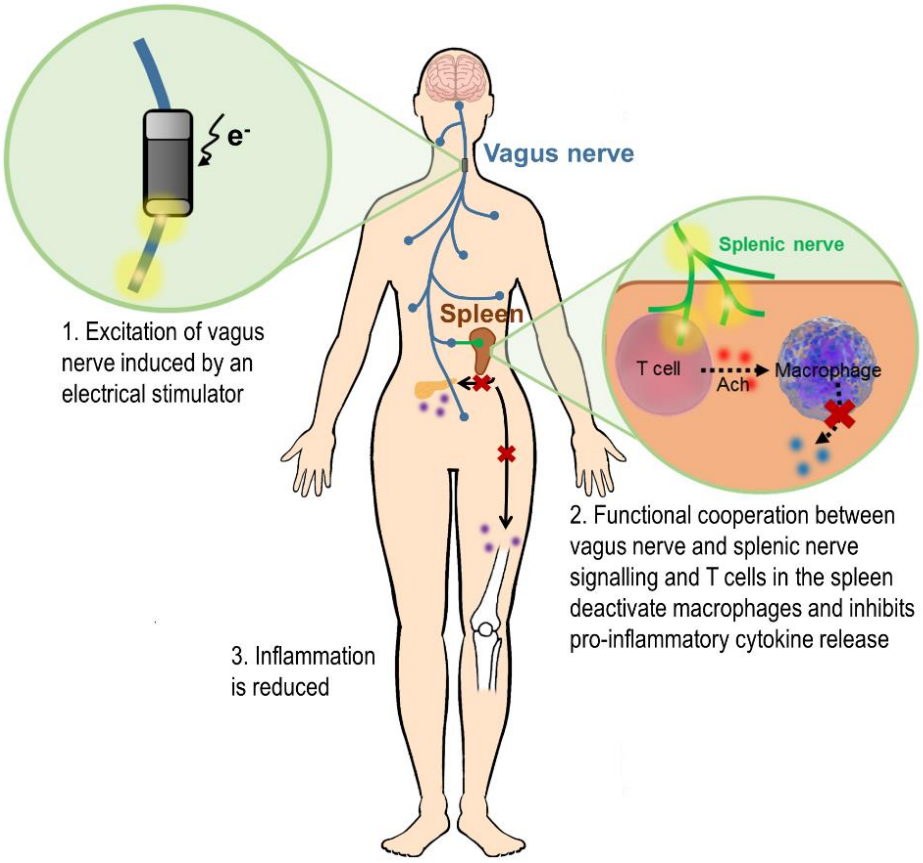

Figure 1-3. Schematic representation of a bioelectronic approach targeting the vagus nerve to control inflammation. Vagus nerve signalling interacts with the splenic nerve that reaches splenic T cells that produce acetylcholine, which reduces inflammation.

One of the main challenges of nerve and cardiac stimulation is that currently, electrical stimulation with these devices, is unable to target cells individually, rather inducing the excitation of the whole tissue. Due to the highly compact state of the nervous and cardiac systems, indiscriminate stimulation can lead to undesirable effects or mire the clinical outcomes[52]. Application of inputs on specific cells would be beneficial to achieve a fine degree of regulation.

As it was previously mentioned, cells that are unable to propagate action potentials, known as non-excitable cells, also possess electrical properties and endogenous electric fields to direct growth or healing[32], which in some cases affect the anatomical outcomes of the individuals[53]. Interfacing these cells with electronic devices gives rise to new opportunities that should allow for the control of cellular function[54].

Application of exogenous electric fields has been demonstrated to be effective in both single cells and tissues, triggering a wide range of biological actions (Figure 1-4)[55-56].

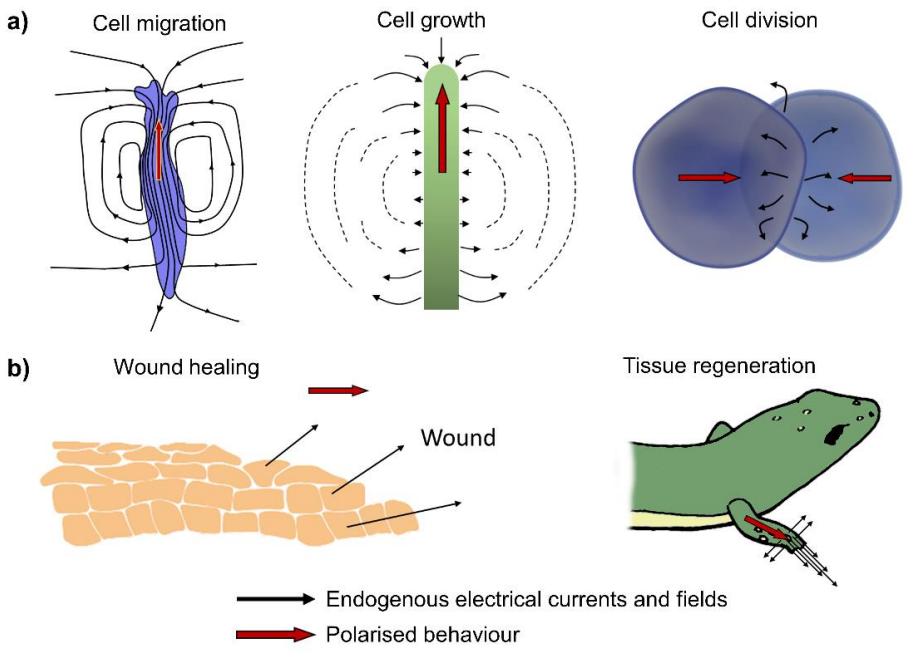

Figure 1-4. Different biological functions can be triggered by the application of electric fields. Currents can polarise (A) single cells and (B) tissues. Black arrows indicate the direction of the electrical currents whereas red arrows indicate the direction of the resulting polarised behaviour.

Defective ion and molecular transport have implications on diverse diseases such as cancer or pulmonary oedema[57-58]. There have been many studies reporting the differences in resting membrane potentials between tumour and non-tumour cells. Generally it can be established that cells with a high proliferative activity such as embryonic, stem and metastatic cells possess a depolarised membrane[59]. Metastatic phenotypes can be induced in healthy cells by depolarisation of their membrane and conversely, the activity in a metastatic cell induced by oncogenes can be supressed by preventing its depolarisation[32]. Voltage-gated sodium channels have also been identified to have a role in organ regeneration in amphibians and could present a new approach to organ repair[60]. Therefore, achieving a good degree of control of transport of molecules across the cellular membrane could have great repercussions in the treatment of these diseases.

Gap junctions between cells, which are channels connecting cellular cytoplasms[61], also have an important role when applying electric fields in order to generate a response at a tissue level. This slow communication route can amplify the intracellular signalling cascade produced in response to the changes in the potential[32]. Signals propagate through the tissue, triggering a coordinated cellular response, for example to wound healing or tissue regeneration. This approach has been introduced in the therapy of bone fracture healing and osteoarthritis, stimulating the chondrocyte and osteoblast

regeneration. As a result, osteogenesis and increases on bone mineral density can be observed[62].

Additional research in this area will allow a deeper understanding of the precise mechanisms involved, which may make it possible to program cellular activity via use of electric fields. Importantly this broadens the prospective applications of bioelectronic medicine beyond neural control.

1.1.3. Improving electronic targeting and specificity

In order to further develop bioelectronic tools with capabilities in cell programming, further specificity on the cellular outputs is desirable. Biomolecular entities, including redox biomolecules, are known to be highly specific as they represent a transfer system of biological information. Therefore, controlling faradaic currents involved in cellular redox reactions offers opportunities for the electrochemical mediated induced control of cells, tissues and organ function.

The faradaic processes can be hijacked by modulation of polarity or by using electrochemically active molecules. Electronic inputs are transduced into redox active mediators that ultimately activate a biological mechanism (Figure 1-5). Biological responses often correlate with the magnitude, frequency, and/or type of electronic input applied[63], indicating that a fine degree of control can be achieved.

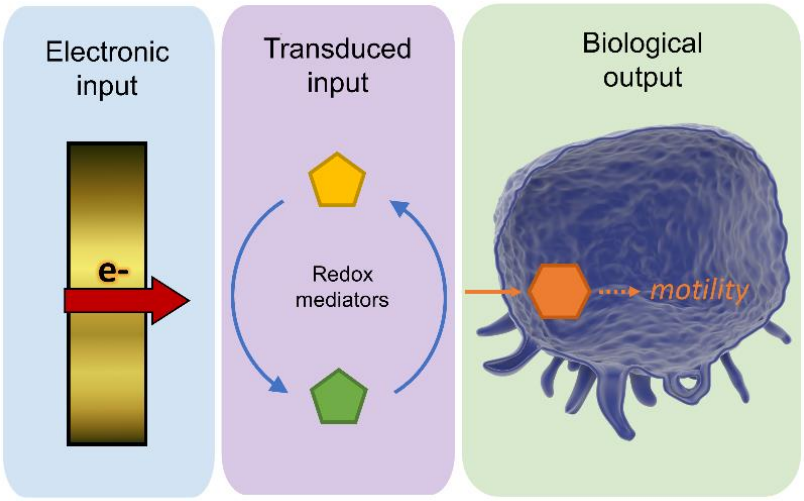

Figure 1-5. Transduction of signals on a bioelectrochemical system. An electronic input is mediated by redox active molecules and communicated to a cellular system triggering biological response

Engineering the electrode at the nanoscale also gives rise to potential for sensing and controlling faradic processes and has been reviewed recently[64-65]. In general, approaches to electrically 'wire' cell redox components rely on electrode modification with conducting polymers[66-67], nanowires based on carbon nanofibers[68], carbon nanotubes[69-70] and electrocatalysts[71]. This wiring can also be achieved via modification of electrode surfaces with chemical entities that bond to the saccharide groups of the eukaryotic cells that facilitate electron transfer[72]. In addition, structures integrated with biological components such as enzymes, lipid bilayers or antibodies are used to transduce ions into electrical currents and *vice-versa* for recording and stimulation of biological reactions in both intracellular and extracellular environments[73]. For instance, electrodes can be conjugated with neurotransmitters to induce

neural excitability[74] or regulate pH using protonic devices to control enzymatic function, and acid sensitive ion channels[73].

Reactive oxygen species (ROS) may be used to direct cell function. ROS are involved in signalling pathways that take part in several biological events associated to bacterial infection and cancer. The production of ROS can be controlled by electrochemical generation[71]. Gene transcription can be induced in response to oxidative stress, inducing cell motility or cell-to-cell communication[75]. Therefore electrochemical control of ROS generation may prove fruitful for directing cell behaviour. Further development of bioelectrochemical devices may have great implications in future cancer therapy by individually controlling plasma membrane electron transport systems (tPMETs). The system of tPMET ferri-reductase is upregulated and it is thought to enable faster rates of metabolism in cancer cells[76]. Therefore, electrochemical tools with capacity to control such systems may regulate metabolism and cellular development.

1.1.4. Limitations and opportunities in bioelectronic medicine

Despite the great advances achieved in this field, a seamless integration has not yet been achieved and current methods tend to be highly invasive. Additionally, the plasticity of young nervous systems and tissues present a key obstacle as implantable electronics cannot adapt or lose their activity due to biofouling[77], therefore needing regularly servicing. In order to reduce the

invasiveness, electronic elements should ideally have nano-scale features and be biocompatible and softer than biological components[78]. While considerable advances in materials and elements are being accomplished[79-82], manufacturing strategies represent a key step to achieve fully integrated devices.

Development of nanotechnology, using nano-field effect transistors[83-84] or nanowires capable of stimulating and recording signals from individual cells[11, 85-86], yield significant improvements in sensitivity and biocompatibility[14]; and production of injectable semiconducting systems[80, 87], flexible[88] and wearable[89] electronics avoid minimally invasive operation. It is therefore envisaged that future advancements in these areas will aid in the development of bioelectronic therapeutics aimed at increasing the selectivity and specificity of cellular control.

Furthermore, in order to produce bioelectronic systems with the ability to adapt to the topographical requirements of the tissues, technological methods fusing electronic and biological components are urgently required. This approach has been recently denominated as *bionic manufacturing*[90], where cells have been successfully coated with a wide range of materials in order to enhance functions for their potential use in bioelectronics or whole cell sensors[91]. Some examples of bionic manufacturing include coating with conducting polymers on yeast cells[92], deposition of nanoparticles on bacteria[93]

or functionalisation of bacteria with electropolymerised microtubes[94]. In all these examples, cells remained viable after the modification with the synthetic materials.

Despite the recent advances in bionic manufacturing, there is a lack of techniques capable to construct such complex systems fusing biological and electronic components. This deficiency arises as standard manufacturing techniques currently used to facilitate assembly of complex electronic systems do not have sufficient spatial-resolution on the nano- and micro-scale, or the ability to combine more than one material in a controlled manner. As cells, tissues and organs are continuously evolving, rational control when fabricating conducting functional devices for bioelectronics purposes is needed[95].

One of the most promising strategies that allow a fusion of biological and electronic components during the manufacturing process is digital approaches used for both two dimensional (2D) and three-dimensional (3D) printing / additive manufacturing (AM). Such approaches allow for the hierarchical integration of multi-functional materials in three dimensions combined with biology[96], and will be summarised in the section 1.2 Additive manufacturing to produce bioelectronic components. This integration could be used to enhance or restore original functions of organs or tissues. This has been successfully achieved by printing a combination of living chondrocytes and an inductive coil antenna to produce a bionic ear with enhanced auditory sensing[97].

Wireless approaches are also appealing to direct *in situ* and real-time actuation of electronically active species to produce non-invasive bioelectronic systems[98]. Wireless optoelectronic systems were successfully developed using soft and neural interfaces connected to an antenna to allow wireless modulation. These devices were implanted in a murine spinal cord and brain, reducing the traditional invasiveness of this technique[99-100]. To the best of the author's knowledge, there are no known examples in the literature of intracellular wireless systems that could be externally controlled electronically and thus, research in this area represents a good opportunity to advance the field of bioelectronic medicine.

1.2. Additive manufacturing to produce bioelectronic components

1.2.1. Additive manufacturing of electronics

Use of printing techniques is not new in the manufacturing of electronic devices. Screen printing and offset lithography have attracted considerable scientific interest for the production of large-scale and low-cost bioelectronic devices[82]. These approaches result in the reduction of fabrication costs and in-process complexity due to their ability to fabricate multi-material systems relatively straightforwardly in a single process and to create flexible structures[101-103].

Despite the notable improvement in printed electronic manufacturing techniques, there is still a challenge and necessity to miniaturise and control the general architecture of the final product in the context of biology and bioelectronic medicine. Moreover, this can only be achieved by developing new technology capable of downsizing the systems whilst maintaining their performance[104].

Additive manufacturing (AM) is an approach where a material of interest is deposited in a sequential layer-by-layer fashion from a computer-aided design (CAD) model[105-107]. The main difference between AM techniques and general

printing techniques is that they can be used to build nonstandard electronics with complex and intricate assemblies. Additionally, a wider range of materials can be processed, including thermoplastics[108], metals[109] or ceramics[110], though there can be challenges in combining highly dissimilar materials[111].

AM techniques have several advantages over conventional methods in the production of electronic systems. These technologies have the ability to produce electronic devices on irregular surfaces, which reduces the dependence on flat circuit boards, broadening the designing capabilities with an optimised functionality. This allows for complete customisation of devices. For instance, flexible 3D printed batteries were fully-printed for autonomous microdevices[112] or wearable electronics[113]. 3D printed batteries can outperform conventional batteries, in part because their shapes and dimensions can be adjusted to fit a particular application, crucially optimising design for functionality, not manufacturability.

Moreover, there are many examples showing the compatibility of additive manufacturing of electronics with biological structures[114]. This includes the production of functional printed electronic devices that can be fully printed directly on a moving hand[115].

Conventional manufacturing methods of electronic devices normally use a subtractive approach where material is removed where not required by harsh

chemical etching approaches. Digitally controlled additive processes can accurately control the amount of materials used, and thus, just the required materials are deposited. This has several advantages: final costs of the manufacturing process can be reduced as less material is going to waste and the final weight of the products manufactured is also reduced[116].

AM processes can be typically grouped in seven categories according to the ASTM Standard F2792[117] as shown in Table 1-1. Material extrusion and material jetting are the most common AM techniques used in the development of electronic systems and some examples are cited in Table 1-1. However, as highlighted in Table 1-1, it is also possible to develop metallic parts and conductive structures using other AM techniques and therefore can be used to partially manufacture electrical components. This demonstrates the versatility of taking an AM approach, though it should be noted that the various AM-methodologies have specific advantages and disadvantages. The choice and rationale of which system to use is of critical importance to success.

Table 1-1. Categories of AM according to ASTM Standard F2792[117] and their use and application in the manufacturing of electronics

Category	Description of the technique	Suitable for manufacturing electronics	Examples
Binder jetting (3D Printing)	A liquid binding agent is selectively deposited to join powder materials[118]	Partially	Manufacturing of complex copper parts[118] and piezoelectric materials[119]
Directed energy deposition (Direct Metal Deposition, Direct Laser Deposition)	Focused thermal energy is used to fuse materials by melting as they are being deposited[120]	Partially	Manufacturing of Stainless Steel 316L and Inconel 718 parts[121] and titanium matrix composites[122]
Material extrusion (Fused Filament Fabrication, Pressure-based Extrusion)	Material is dispensed through a nozzle or syringe in a selective manner[120]	Yes	3D interdigitated Li-ion microbatteries[112], stretchable sensors[123], organ models with sensing capabilities[124] and graphene electronic tattoo sensors[125]
Material jetting (Aerosol Jet, Inkjet Printing, Polyjet)	Droplets of material of interest are deposited from a nozzle	Yes	3D silver cantilevers and pillars[126], organic solar cells[127], wearable electronic devices[128] and paper-based sensors[129]
Powder bed fusion (Selective Laser Melting, Selective Laser Sintering)	Thermal energy selectively fuses regions of a powder bed[120]	Partially	Fabrication of smart parts with integrated sensors[130] and pneumatically controlled titanium prosthetics[131]
Sheet lamination (Laminated Object Manufacturing)	Sheets of material are bonded to form an object	Partially	Manufacturing of graphene foams[132]
Photopolymerisation (Stereolithography, Two-Photon polymerisation)	Photopolymer is selectively cured by a laser	Partially	Conductive microstructures containing gold[133-134] and carbon nanotubes[135]

The diversity of AM techniques is also translated into the variety of minimum feature size of the conductive structures that can be fabricated by the different techniques, and not all of them are suitable and can be integrated with biology. Filament extrusion-based printing has been one of the most exploited techniques for simultaneously printing conductive materials and cells[97], however, the minimum resolution that can be printed is 100 µm[136] (Figure 1-6A), limiting the targeting of intracellular components.

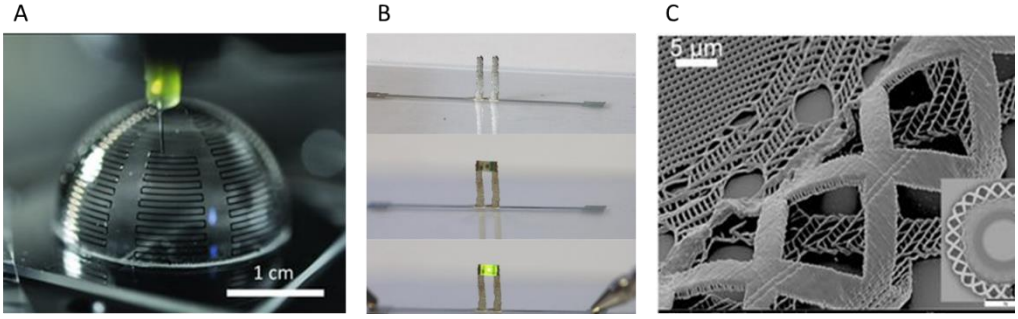

Figure 1-6. Examples of three dimensional (3D) conductive materials manufactured by (A) filament extrusion-based printing of silver on a non-flat surface, (B) inkjet printing of silver pillars and (C) two-photon polymerisation (2PP) of intricate microstructures containing gold particles. Images reproduced with permission from [103, 126, 134].

Inkjet printing is a versatile printing method, where conductive materials[137] and mammalian cells[138] can be printed offering a high degree of control over patterns and their thicknesses[139]. The resolution achieved by this technique is in the order of 20-50 µm in the X-Y axis, determined by ink wettability and surface energy of substrates[140-141]. This is not applicable to the z-plane, where

printing accuracy is limited and mainly dependant on the number of layers printed (Figure 1-6B).

Further downsizing of features of conductive materials is still challenging by additive manufacturing techniques intend for making macro-scale parts[142]. As the minimum feature size of conductive materials that can be fabricated is rather limited, other additive manufacturing approaches based on two-photon polymerisation of materials with integrated conductive nanostructures such as carbon nanotubes[135] and metallic nanoparticles[134] (Figure1-6C) can be appealing for the development of conductive structures with enough resolution (up to 100 nm) to target cellular components electrochemically.

Due to the versatility of the printing process, the minimum feature resolution and the compatibility with bioelectrochemical integration, inkjet printing and two-photon polymerisation techniques were selected for the manufacturing of the electrochemical systems in this project. An overview of both techniques will be given in the following sections.

1.2.2. Inkjet printing of conductive macro-structures

Inkjet printing is a photomask-free method of deposition of liquid-phase materials (inks) suitable for most substrates and printing patterns[143]. Inkjet printing can be divided into two categories: continuous inkjet and drop-on-

demand (DOD). While the first one is mainly used for industrial applications, DOD printers are more extended and used in many areas.

In DOD printing, fixed quantities of ink stored in a chamber are only ejected from a nozzle when required, and the spatial control is achieved by the movement of the print head[137]. DOD can also be subdivided depending on the mechanism by which droplets are ejected. In thermal DOD, bubbles of the ink's solvent are formed using a heater inside the print head. Expansion of those bubbles imparts the energy required to form a droplet[144]. In piezoelectric DOD, the deformation of a piezoelectric material in response to the application of external voltage produces a sudden increase in the volume of the chamber, generating an acoustic wave that ejects the drops (Figure 1-7)[145]. In both cases the drops formed fall under the action of gravity until they are deposited onto the substrate[146]. Advantages of piezoelectric DOD over thermal DOD include the potential to process higher viscosity material and its compatibility with many solvents, and thus, it is appropriate for a wide variety of ink formulations.

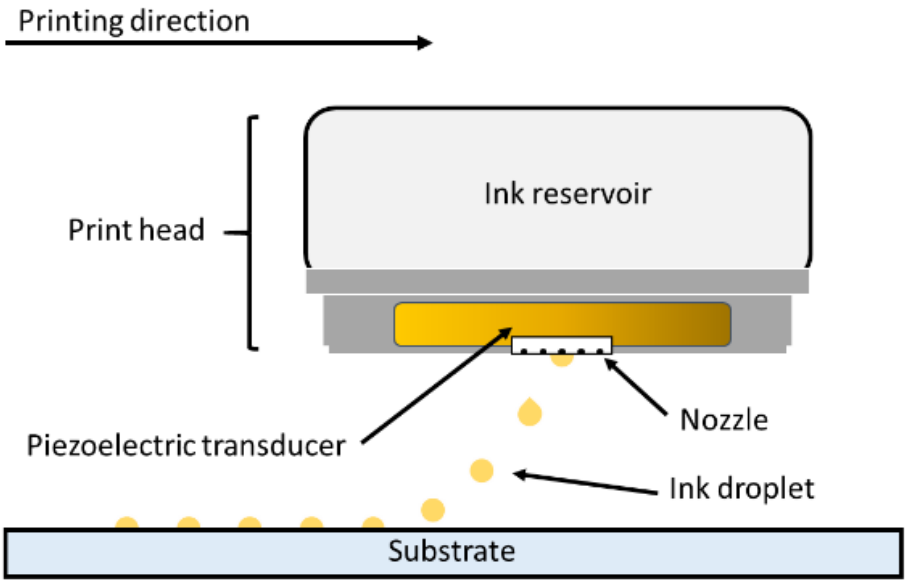

Figure 1-7. Schematic representation of droplet deposition from a printer cartridge of a drop-on-demand (DOD) piezoelectric inkjet printer

The inkjet printer used in this project was Dimatix printer, a commercial piezoelectric DOD with a print head containing 16 nozzles with 21 µm diameter each. This printing system is only capable of depositing one ink at the time, though it should be noted that there are more complex printers with higher number of nozzles that can work with several inks to create multi-material structures on a single process. Our choice was based on the ease of use of this printer and thus, more attention is given to piezoelectric DOD printers in this introduction.

Piezoelectric DOD printers are compatible with a wide range of inks, however, not all the materials in a liquid phase can be used as inks and printed. The main parameters that define the 'printability' of inks are: (i) *Viscosity*, inks

need to have a low viscosity in order to allow the flow of ink from the reservoir to the nozzles in a short period of time[147]. Good values of viscosity are between 1-30 cPs, being optimal at 10 cP; (ii) *Surface tension*, it has to be enough to hold the droplets at the nozzle (2.8-3.3 Nm^{-2}); (iii) *Particle distribution,* ≤ 0.2 µm[148] as nozzles typically have diameters of 20-30 µm. (iv) *Low-volatility solvents* to prevent nozzle drying and clogging[149].

Once the droplets are formed and ejected, the degree of spreading of inks to the substrate is what governs the final resolution of the printed patterns, which is typically up to 20-40 µm[150].

Currently, several types of inks can be used to print conductive structures. These include metallic nanoparticles[151], organic polymers[152], carbon nanotubes (CNTs)[153] and graphene oxide[154] inks.

Metallic nanoparticles (NP) are usually dispersed in water or organic solvents that rapidly evaporate after droplet formation, usually achieving good levels of conductivity after post-deposition sintering. The higher surface ratio of the particles compared to bulk materials have the advantage that lower temperatures are needed to produce the sintering of the materials[148]. However, these inks are susceptible to agglomeration, and in order to stabilise the dispersions, nanoparticles are surrounded by a capping agent (usually a polymer) that avoids aggregation and formation of clogs when printing and

can be removed during the curing and sintering processes[155]. Curing and sintering are performed in a post-process by the application of direct heat, IR light or UV light after the ejection of the droplets to remove the solvent and burn off the protective agent. Evaporation of the solvent takes place at curing temperatures (Figure 1-8), where there is a reduction in the volume of ink in the printed patterns. The sintering process occurs at higher temperatures, when the polymer degrades and direct contact between particles is created via percolating pathways[101]. The most commonly used metallic nanoparticles are gold and silver[156] due to their chemical stability, however other metals have been introduced such as copper or nickel though they do have a tendency to oxidise over time[148].

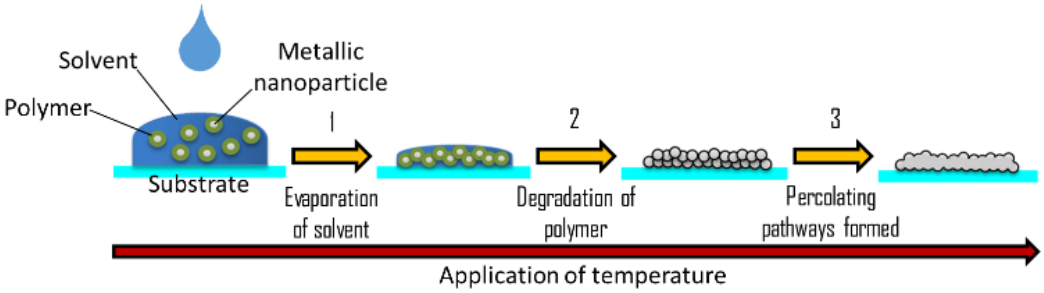

Figure 1-8. Diagram of printing, curing and sintering processes of metallic inks

Conductive polymers usually achieve significantly lower conductivities than metallic NP inks and in some cases need to be printed in a controlled atmosphere due to reactivity with oxygen and humidity[148]. These materials include polyaniline, polypyrrole and PEDOT, which have a conjugated π-electron that gives them conductive properties[157]. An advantage of using

conductive polymers is that these materials are usually more compatible with cellular systems than metallic inks[158].

Flakes of graphene oxide can be dispersed in water and printed to form conductive films, however very high temperatures (> 550 ^{o}C) are needed to reduce the graphene oxide and restore its conductive properties[148]. Sheets of graphene in the shape of hollow cylinders form carbon nanotubes (CNTs), and can also be printed by inkjet printing, creating conductive and transparent films[159]. In this case, the deposition and direction of the CNTs affect the electrical properties of the patterns printed, but inkjet printing of CNTs is still challenging as CNTs tend to also aggregate easily.

As it can be seen, there are multiple conductive inks with different properties that are compatible with inkjet printing in order to produce electrodes. This versatility in the materials that can be manufactured and a precise control over the patterns deposited, make inkjet printing an attractive technique in the production of bioelectronics.

1.2.3. Two-photon polymerisation of conductive microstructures

Localised polymerisation occurs when photoresists are excited by a well-defined waveform, creating 3D intricate structures with resolution in the order of nanometers[160]. Depending on the number of photons exciting the

photoresists, single-photon polymerisation (1PP) or two-photon polymerisation (2PP) can be found[161].

In 1PP the mechanism of polymerisation takes place after the initiators absorb one UV photon with a short wavelength as seen in Equation 1-1. However, in 1PP the polymerisation is planar and restricted to the surface of the photoresist[161].

$$^{h\vartheta}UV + initiator \rightarrow R^{\cdot}\ or\ R^{+}$$

$$R^{\cdot}\ or\ R^{+} + monomers \rightarrow free\ radical\ or\ cationic\ polymerisation \quad \textbf{Eq. 1-1}$$

In 2PP the initial step of radical formation on the initiator is slightly different. In this case, the initiator absorbs two near infrared (NIR) photons with long wavelength (Equation 1-2). In 2PP the polymerisation takes place within the volume of the photoresist and it is exclusive to the area of excitation[162] (Figure 1-9), producing truly 3D objects instead of fabricating them layer-by-layer as 1PP. The excitation spot is also smaller, creating structures with submicron resolution[160-161].

$$^{2h\vartheta}NIR + initiator \rightarrow R^{\cdot}\ or\ R^{+} \quad \textbf{Eq. 1-2}$$

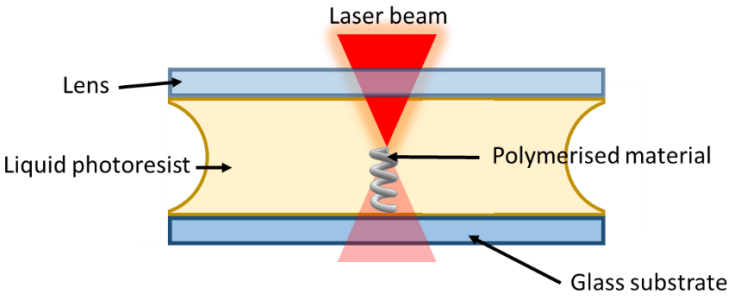

Figure 1-9. Schematic representation of 2PP to produce 3D structures

Photoresists consist on a dispersion of multi-functional monomers and photoinitiators. When the free radical or the cathodic radical of the initiator interacts with the monomer, it triggers the cross-linking of molecules inducing the polymerisation within the focus of the laser beam that cannot be dissolved[161]. The remaining non-polymerised materials can be dissolved and washed off during the post-processing. Fast curing speed and transparency of the materials are necessary in order to ensure the penetration of the laser through the photoresist and a quick polymerisation[161].

Conductivity of the photoresists can be increased by dispersing[163] or covalently binding[164] CNTs into UV curable monomers. This has proven to be a good method to create 3D structures incorporating CNTs, as conventional techniques require solvent removal and/or high temperatures[162]. Other strategies that increase the conductivity of the structures manufactured by 2PP include the addition of metallic salts to monomers that form metallic-polymeric hybrids after a process of photopolymerisation and photoreduction[134, 165].

Biomimetic environments can be manufactured using both hydrogels and polymers to control phenotypes and cell functions[166]. Scaffolds manufactured by 2PP have been successfully developed to induce maturation of human mesenchymal stem cells[167] and pluripotent stem cell-derived retinal cell grafts[168].

The biocompatibility of the structures produced by this technique and the development of conductive photoresists have the potential to produce systems for bioelectronic medicine.

1.3. Electrochemical reactions to target biological systems

One of the key points of this PhD is the use of electrochemical systems for two main purposes: i) to increase the specificity of the electric inputs applied and ii) to reduce the invasiveness of conventional systems. In this section an overview of general electrochemical reactions will be given as well as a description of the proposed methods to achieve the two aforementioned objectives.

1.3.1. General electrochemical reactions

Electrochemistry is a branch of physical chemistry that studies the chemical reactions involving a transference of electrons. This transference of electrons is produced between two species – electron donors and electron acceptors – involving the loss of electrons (oxidation) and gain of electrons (reduction), thus can also be named redox reactions (Equation 1-3). Redox reactions can be spontaneous, as for example occurs in voltaic cells, or can be externally controlled by the application of potentials from electrodes to solutions, where there is at least one electrolyte dissolved.

When a potential difference is applied, an electric field is created at the interface between the electrode and the solution, where the direction of the flow of electrons depends on the magnitude of the potentials applied.

Therefore, one key aspect of electrochemistry is the control and measurement of cell potentials and currents[34].

$$oxidation: A \rightarrow A^{+} + e^{-}$$
$$reduction: B + e^{-} \rightarrow B^{-} \qquad \textbf{Eq. 1-3}$$
$$overall\ reaction: A + B \rightarrow A^{+} + B^{-}$$

Typically, electrochemical systems or electrochemical cells have a three-electrode configuration. Redox reactions take place at the working electrode and, in order to accurately control and measure the potentials applied to the system, potentials are applied against an optional reference electrode with a well-known and stable potential based on a standard reaction. A counter or auxiliary electrode closes the circuit, where the current flows from the working to the counter electrode[169].

The transference of electrons between the electrodes and the electrochemically active species depends on the atomic levels of energy of both elements. The energy levels at the electrode can be externally modulated, and when the level of energy in the electrode is higher than the lowest unoccupied molecular orbital (LUMO) at the electrolyte, the electrons are transferred, resulting in a flow of current that reduces the electrochemical species (Figure 1-10). This situation can be reversed when a positive potential is imposed, lowering the level of energy in the electrode. At this point, it is more

energetically favourable for the electrons to jump from the highest occupied molecular orbital (HOMO) to the electrode. As a result, an oxidising current is formed (Figure 1-10)[170-171]. The critical potential at which these processes take place is unique for each system, which makes these reactions very specific as they only occur after a threshold potential is applied which is related to the standard potential (E^o) of the constituents involved[34].

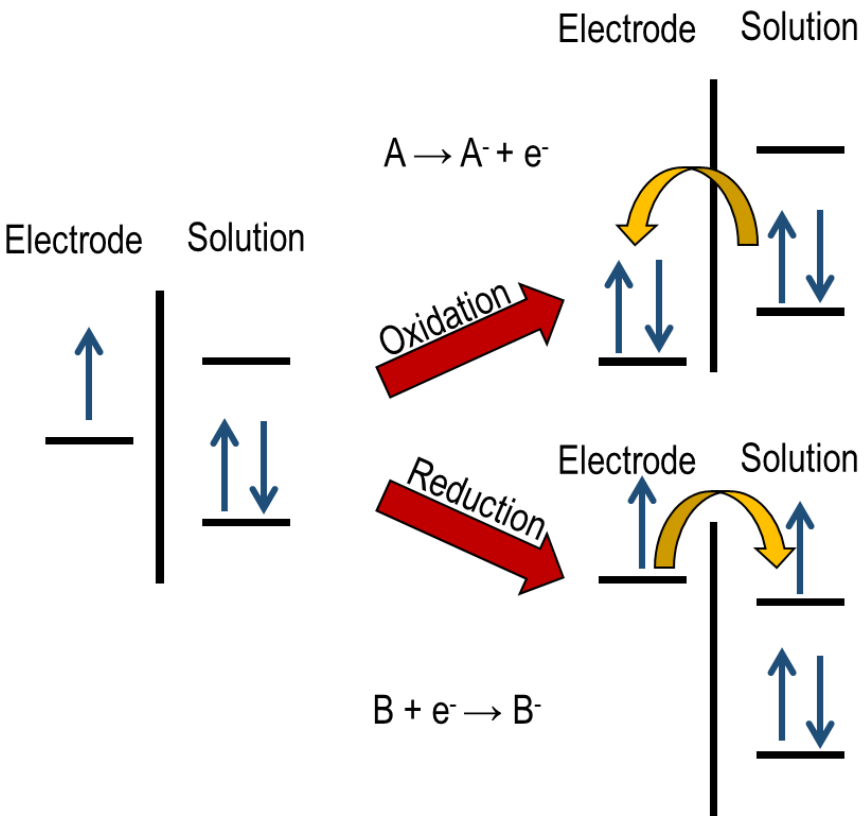

Figure 1-10. Transference of electrons between the energy levels of the electrodes and electroactive species in a solution

Electrical charge (Q) is measured in Coulombs, where 1 Coulomb equals 6.24×10^{18} electrons. The amount of charge that flows per second throughout a given point is defined as electrochemical current (i) which is measured in Amperes (Equation 1-4).

$$i = \frac{Q}{t}$$ **Eq. 1-4**

Electrochemical systems transform electrical energy into chemical energy. This relationship is established through the Nernst Equation (Equation 1-5), which is one of the most important postulates in electrochemistry. Nernst equation can be used to determine the theoretical value of the potentials in the system of interest and predict the direction of the reactions depending on the potential applied, given by the ratio of concentrations of the redox species at the surface of the electrode[172].

$$E = E^o - \frac{RT}{nF} ln \frac{C_R}{C_O}$$ **Eq. 1-5**

Where *E* represents potential, E^o the standard potential, *R* is the gas constant, *T* temperature, *n* number of moles of electrons involved in the redox exchange, *F* is the Faradaic constant and C_R and C_O are the concentrations of the reduced and oxidised species at the surface of the electrode.

This demonstrates the dependence of redox molecules to the potentials applied to the system and more importantly, it demonstrates the ability to externally control and influence the redox state of electroactive molecules which are highly specific to the potentials applied.

Some physicochemical factors can affect the kinetics and magnitude of the electrochemical reactions. This includes the formation of double layers and limitations due to mass transport and will be reviewed in the following paragraphs.

When an electrode is immersed in an electrolyte solution and potentials are applied, a double layer is formed[173]. At the electrode, a layer of charges of a certain polarity is produced due to the potential difference, and at the interface between electrode and solution, chemically adsorbed molecules of solvent form the inner layer (Figure 1-11). After this, free ions with opposing polarity to the electrode are electrochemically attracted forming the outer layer. Free ions of both polarities can be found in the diffusion layer (Figure 1-11)[174].

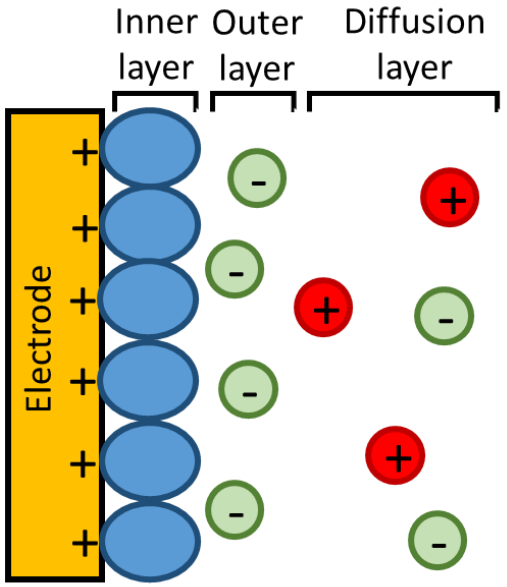

Figure 1-11. Schematic representation of the interface between an electrode and a solution when a potential is applied and the double layer formation. It should be noted that ions should be solvated in an aqueous solution; however, this effect was not indicated in the diagram to avoid confusion.

Both layers of ions with opposing polarity separated by solvent molecules form the electrical double layer that can store charge electrochemically, acting as an electronic capacitor. The amount of charge that can be stored is linearly proportional to the potentials applied[175].

The other factor affecting electrochemical reactions is the mass transfer. Movement of particles from different locations in a solution are produced by electrical or chemical potentials between two points[176]. Particles can move by diffusion, under the influence of a concentration gradient; migration, under the influence of an electric field; and convection, due to the influence of the

movement of the whole medium produced by mechanical and thermal gradients[34].

Mass transfer to the electrode is governed by the Nernst-Planck equation, which is an extension of Fick's Law and describes the movement of charged chemical species in a solution, depending on the flux of ions and the gradient concentration[177]. In one-dimensional mass transfer along the x-axis, the contribution of each mass transport phenomenon to the final flux of ions is represented in Equation 1-6[178].

$$J(x) = -D\frac{\partial C(x)}{\partial x} - \frac{zF}{RT}DC\frac{\partial \phi(x)}{\partial x} + Cv(x) \qquad \textbf{Eq. 1-6}$$

Where *J* represents the flux of molecules, *D* the diffusion coefficient, *C* concentration, *x* distance, *z* valence of ionic species, *F* Faradaic constant, *R* Boltzmann's constant, *T* temperature, ϕ electric potential and *υ* hydrodynamic velocity. The three terms on the right part of the equation represent the contributions from the diffusion, migration and convection to the flux respectively, in units of $mol\ s^{-1}\ cm^{-2}$.

Double layer formation and mass transfer have to be taken into consideration in each system as concentrations of electroactive species at the surface of the electrodes may change, limiting the kinetics of the redox reactions. This can create some discrepancies between theoretical values

obtained from Nernst equation and real values observed in practise. Despite these discrepancies, they can be easily corrected and explained using electroanalytical tools such as cyclic voltammetry[170, 179-180] or impedance spectroscopy[181-182] measurements, where mass transfer phenomena and capacitive behaviour of the systems can be studied. Furthermore, they do not affect the specificity of the electrochemical reactions.

1.3.2. Bipolar or wireless electrochemistry

Based on the same theoretical concepts of energy barriers and direction of electron flow, *bipolar or wireless electrochemistry* is a technique that consists on the polarisation of a conducting material immersed in an electrolyte solution when an external electric field is applied by two feeder electrodes[183]. This polarisation is proportional to the electric field applied, and when it is strong enough, it can generate a difference of potential between the two extremities of the bipolar electrode (BPE)[184] (Figure 1-12).

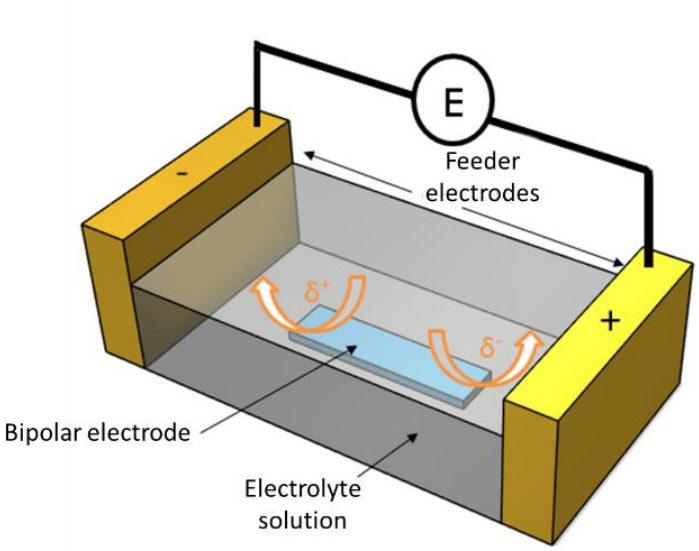

Figure 1-12. Schematic representation of bipolar electrochemistry

The term *bipolar electrode* is referred to those materials that exhibit a polarised electrochemical behaviour at their surface, where reduction and oxidation reactions are simultaneously taking place. Importantly, these reactions are induced in the absence of direct contact with an external power supply, and it can be exploited as a method to generate wireless redox reactions[183-186].

In bipolar electrochemistry the redox reactions are taking place at the BPE. In this case, the key factor is to control the potential at the BPE, which depends on the magnitude of the electric field and the characteristics of the BPE (Equation 1-7).

$$E_f = \frac{E_a - E_c}{d} \qquad \textbf{Eq. 1-7}$$

$$\Delta E = E_f \cdot L$$

Where E_f represents the value of electric field, E_a and E_c the potential at the feeder electrodes, d the distance between feeder electrodes, ΔE the potential difference between the two extremities of the BPE and L the length of the BPE.

The concept of bipolar electrochemistry has been known for a long time and it is widely used in industry under the name of fluidised bed electrodes, for different applications such as water splitting, electrodeposition or optimisation of fuel cell performances[187]. However, it has recently attracted attention for surface modification of nano- and micro-sized objects since this effect was first described in 1985 by Fleischmann[188-190].

One of the biological applications that is currently being investigated in bipolar electrochemistry, include the generation of micro swimmers, where a platinum pole catalyses a hydrogen peroxide reduction. During this process, the micro swimmers form bubbles that induce motion into the object[191-193]. These self-powered structures represent a novel approach in drug and protein delivery, cell manipulation and non-invasive medicine[194-197] (Figure 1-13A).

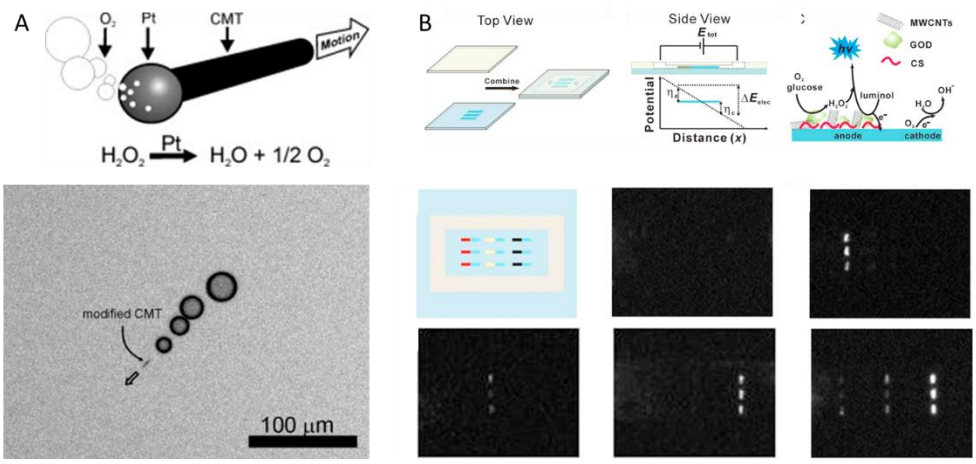

Figure 1-13. (A) Diagram showing the proposed reactions to induce motion in objects (top) and microscope image of object in motion (bottom). (B) Schematic illustration of a bipolar sensor and the sensing principle for analyte detection (top) and microchip for simultaneous detection of lactate, choline chloride and glucose. Reproduced with permission from [191] and [198].

Another point of interest is the development of sensing methods based in bipolar electrochemistry. These platforms are capable of sensing biological molecules, for example in the detection of specific sequences of DNA or RNA that bind to the cathodic pole of the BPE, triggering oxidation reactions at the anodic section resulting in electrogenerated chemiluminiscence (Figure 1-13B) or dissolution of silver that can easily be detected[186, 199-203]. The main advantage of these sensors is that multiple analyses can be performed at the same time without complex machinery, which potentially makes bipolar electrochemistry a high-throughput and low-cost method[200]. These and other examples of bipolar electrochemistry with biological applications are summarised in Table 1-2.

Table 1-2. Bipolar electrochemistry systems with biological applications

Example of bipolar electrochemistry system	Description	Electrochemical reactions involved	Application
Micro-swimmers	Carbon microtubes (5-20 µm) with a platinum pole that can induce motion into the object[191]	Oxidation of H_2O_2 to O_2, forming bubbles that generate motion, and reduction of H_2O_2 to H_2O[192]	Drug delivery[196], transport of cells[204], non-invasive endoscopes[205]
Biosensors (by generation of electrogenerated chemiluminescence)	ITO microbeds that respond with chemiluminiscence to certain analytes[202]	Oxidation of a rutherdium or iridium compound and reduction of the analyte	High throughput DNA sensors[203] and detection of H_2O_2[202] and pathogenic bacteria[206]
Biosensors (by electrodissolution of silver electrodes)	Silver electrodes that dissolve in response to analyte detection[200]	Oxidation of silver from the electrode and reduction of the analyte	High throughput DNA sensors[200]
Water treatment methods	Stainless steel electrodes with ability to disinfect drinking water	Generation of OH^- radicals from H_2O that interfere with bacterial development[207]	Removal of spores of *Bacillus subtilis* from drinking water[208]
Single-cell traps	Dielectrophoresis technique to capture single cells in microfluidic devices in areas with high ion enrichment[209]	Increase and decrease of ionic strength by oxidation and reduction, respectively, of H_2O molecules[209]	Cell manipulation, sorting and filtering

Despite these efforts, very little exploration of applications of this technique to biological systems has been undertaken, and there are no known reports of its use in the formation of cellular bioelectronic systems. However, bipolar electrochemistry can induce wireless electrochemical reactions and has the potential to reduce invasiveness of bioelectronics while maintaining the specificity of electrochemical reactions.

1.3.3. Basic principles of electronics

In this thesis, biological systems are combined with electronic components that can ultimately be modelled as a network of passive electrical circuit elements. It is therefore important to understand some basic concepts of electronics in addition to electrochemical reactions.

The electrical attraction or repulsion created between two charged species is denominated potential difference, and it represents the ability of charged particles to produce work and energy[210].

It has been previously stated that electric currents consist of the flow of electric charges. In biological systems, these currents are produced by the movement of ions. However, in electronic circuits this movement is produced by the flow of electrons in a wire[211]. Wires are typically metals, where electrons from each atom are loosely bound and can move freely within the metal[212].

Materials that allow the flow of electrons are called conductors and those where electrons cannot move freely are called insulators. Between these two categories, we can find the semiconducting materials. The capacity by which materials allow the movement of electrons is determined by the conductivity of the material, or its inverse, the resistance, and it depends on the chemical composition and the dimensions of the material[212].

The resistance of any material with an uniform cross-sectional area and length can be calculated from Equation 1-8.

$$R = \rho \frac{l}{A} \qquad \textbf{Eq. 1-8}$$

Where *R* represents electrical resistance, *ρ* resistivity (constant for each type of material), *l* the length of the material, and *A* its cross section.

The relationship between potential, current and resistance is given by the Ohm's Law (Equation 1-9) that states that a current through two points of a conductor is directly proportional to the potential difference between those points[213].

$$i = \frac{V}{R} \qquad \textbf{Eq. 1-9}$$

In direct currents (DC), electrons flow in a constant direction and the polarity is maintained. In alternating currents, both flow of electrons and polarity are continuously switched (Figure 1-14)[213].

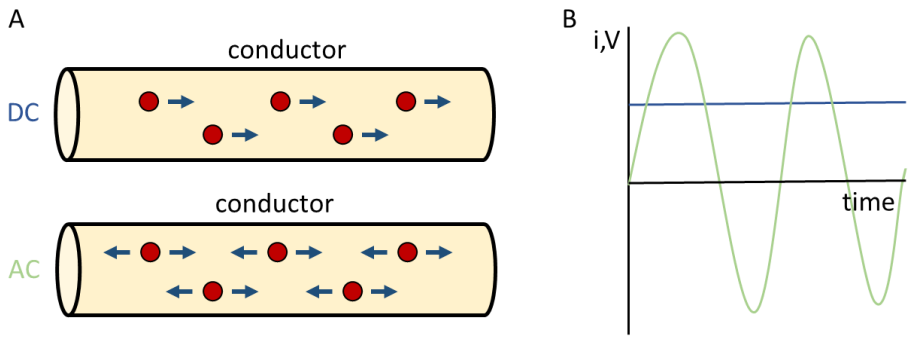

Figure 1-14. (A) Direction of electrons within a conductor material in direct current (DC) (top) and alternating current (AC) (bottom). (B) Magnitudes of potential and current in DC (blue) and AC (green) over time.

Another electrical component of interest that was mentioned in 1.3.1 General electrochemical reactions, due to its contribution in the double layer formation, is the capacitor. Capacitors are generally two conductive materials separated by an insulation layer that can store energy in the form of potential difference[214]. The voltage across the capacitor builds up at different rates depending on the capacitance value of the system. Once the system has stored its maximum amount of charge, the voltage across the capacitor equals the source voltage. The capacitance (C) of a system is given by the following equation (Equation 1-10)[215].

$$C = \frac{Q}{V} \qquad \textbf{Eq. 1-10}$$

A basic electrochemical circuit with a double layer (Randles cell) can be represented as a circuit. In this case we can find the aforementioned double layer capacitance (C_{DL}) at the interface between the electrode and the

electrolytes in solution, the resistance produced due to the electron transfer (R_{ET}) and an ionic resistance (R_i) from the electrolyte solution (Figure 1-15).

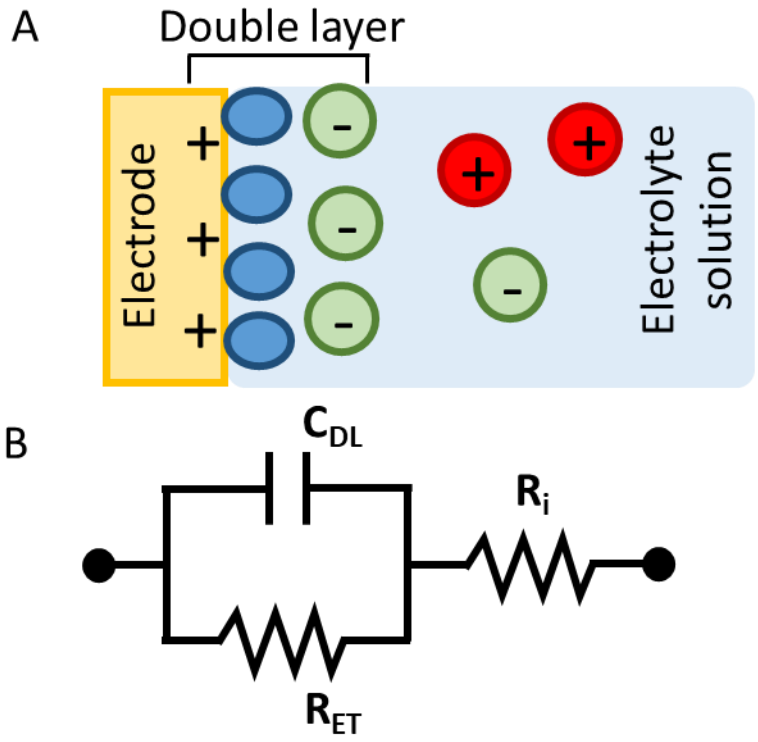

Figure 1-15. (A) Double layer formation in an electrochemical cell and (B) the representation of its equivalent electrical circuit.

Cellular membranes can also be modelled to develop their equivalent circuit[216]. In a basic cellular membrane composed by lipids and proteins there is a resistance created by the lipids due to their insulating properties[217] and certain resistance from the proteins (R_{me}). This insulating layer separates ions at both the inner and the outer faces of the membrane, acting as a capacitor[218] (C_{me}). The equivalent circuit of a basic cellular membrane can be seen in Figure 1-16[219].

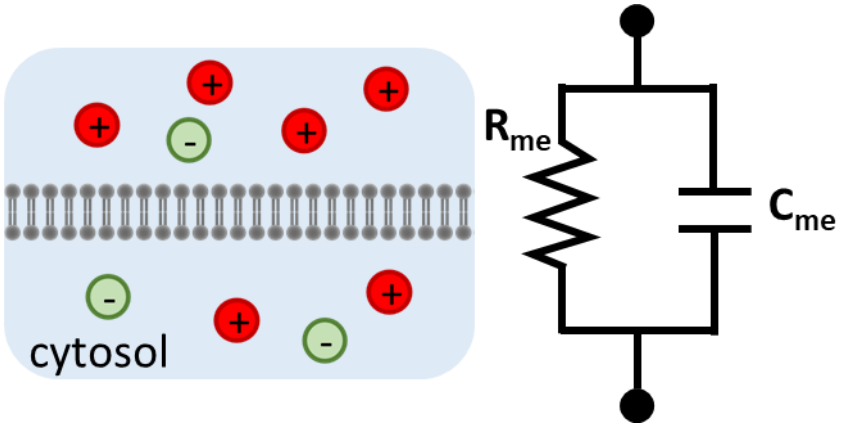

Figure 1-16. Charges at both sides of a basic cellular membrane and its correspondent equivalent circuit

Excitable cells possess ion channels that are sensitive to changes in membrane potentials[220], adding complexity to the modelling of their equivalent electrical circuits. They can be represented by the well-studied Hodgkin-Huxley approach on a squid neuron[221], where C_{me} represents the capacitance of the membrane, I_p the current sources associated to ion pumps, and each voltage-gated channel possesses an electrical resistance (or conductance, in this case) represented by g and an electrochemical gradient driven from the ions (E). Natural permeability of the membrane to ions is referred to as 'leak channel' and has a constant conductance (g_L). The modelled circuit of the membrane of a neuron with Na/K voltage-gated channels can be seen in Figure 1-17. The arrow over the resistance symbols in the circuit means that the conductance is not constant in the channels and varies with the potentials of the membrane.

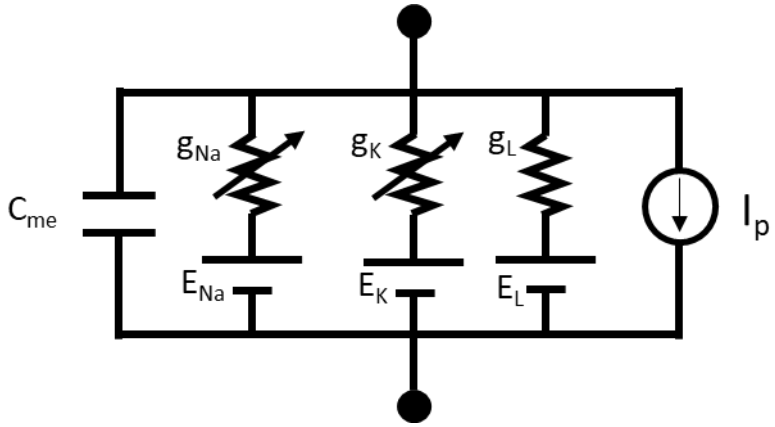

Figure 1-17. Modelled equivalent circuit of a neuron with sodium and potassium voltage-gated channels

This modelled circuit can be then used to calculate the total current that goes through the cellular membrane using the following equation (Equation 1-11)[222].

$$I_{me} = C_{me}\frac{dV_m}{dt} + g_K(V_{me} - V_K) + g_{Na}(V_{me} - V_{Na}) + g_L(V_{me} - V_L) \quad \textbf{Eq. 1-11}$$

Where I_{me} represents the total membrane current; C_{me} the capacitance of the membrane, V_{me} the membrane potential; g_K, g_{Na} and g_L the conductance of potassium, sodium and leak channels respectively; and V_K, V_{Na} and V_L the potential at potassium, sodium and leak channels.

It can be therefore concluded from this section that all electrochemical and biological systems can be modelled as electrical circuits and valuable

information such as potential and currents can be measured from their corresponding mathematical equations. However, this is beyond the scope of this thesis and this area will not be studied in depth in the following chapters.

1.4. Aim and objectives

The aim of this project is to create novel bioelectronic tools that could be applied as future therapeutics. Towards this, a combination of additive manufacturing and electrochemical approaches is sought due to their versatility and ability to be integrated with biology. This combination of methods has not been explored in bioelectronic medicine up to date, and while the fusion of both fields might have infinite outcomes, three areas are explored herein:

i) Production of bionic manufactured interfaces between conductive structures and mammalian cells with enhanced biosensing capabilities (Chapter 3. Development of a novel bionic manufacturing by inkjet printing and bipolar electrochemistry).

ii) Development of wireless intracellular bioelectronic actuators, reducing the invasiveness of typical bioelectronic systems and translating specific redox outputs in a wireless manner (Chapter 4. Wireless bioelectronic nanosystems for intracellular communication).

iii) Additive manufactured conductive cellular scaffolds that can be controlled via external application of potentials with the ability to

trigger further maturation of *in vitro* cultured cardiomyocytes (Chapter 5. Two-photon polymerisation of conductive scaffolds to improve maturity of *in vitro* cardiomyocytes).

1.5. Summary

Bioelectronic medicine is a growing field where major advancements in treatment and diagnoses of diseases are being achieved. Therapies based on neural stimulation and application of electric fields are currently used to improve patient's quality of life, but additional control of the effects is still required.

The main challenges include the creation of effective biological-electrical interfaces and the transduction of signals. In order to modulate the electron transfer events, an intimate contact of the electronic component with the active sites is required. Therefore, technological advancements in the interfacing of electronics with such active sites are necessary to fully integrate biological systems and electronic devices.

Additive manufacturing techniques such as inkjet printing and two-photon polymerisation have the potential to produce conductive macro and microstructures that can be integrated with cells. This integration is hypothesised to help the achievement of good integration between biological and electronic systems.

A higher specificity of the electronic inputs applied can be achieved by controlling highly specific redox biomolecules and the biological output with

great precision, adding new proportions to the bioelectronic medicine field. However, bioelectrochemical therapies still require a multidisciplinary approach to produce less invasive techniques, e.g. using wireless systems. In order to achieve this, the development of nanotechnology, materials and new methodologies will greatly contribute to this field offering new therapeutic tools. In particular, bipolar electrochemistry has the potential to target specific electrochemical reactions wirelessly and its use can be explored in bioelectronic medicine.

Chapter 2. Materials and Methods

Chapter 2. Materials and Methods 59

2.1. Materials and methods of Chapter 3 61

2.1.1. Materials 61

2.1.2. Inkjet printing process 61

2.1.3. Surface analysis 62

2.1.4. Resistance measurements 63

2.1.5. Microwire growth 63

2.1.6. Multi-component functional electronic device formation 64

2.1.7. Bioelectronic interface formation 65

2.1.8. Alternative systems and further indications 67

2.2. Materials and methods of Chapter 4 69

2.2.1. Materials 69

2.2.2. Inkjet printing of an electrochemical cell 69

2.2.3. Electrodeposition of palladium onto unmodified gold nanoparticles (u-AuNPs) 70

2.2.4. Plasmonic-based detection of electrical charge modulation at u-AuNPs 71

2.2.5. Synthesis and characterisation of water soluble gold nanoparticles (ws-AuNPs) 73

2.2.6. Cell culture 73

2.2.7. Intracellular wireless actuation 75

2.3. Materials and methods of Chapter 5.....77

2.3.1. Human induced pluripotent stem cell (hiPSC) differenciation into hiPSC-derived cardiomyocytes (hiPSC-CM).....77

2.3.2. Immunostaining of hiPSC-CM 77

2.3.3. Electrical stimulation of hiPSC-CM.....78

2.3.4. Structure fabrication by two-photon polymerisation (2PP) .78

2.3.5. Viability studies.....81

2.3.6. Morphological analysis of hiPSC-CM 81

2.1. Materials and methods of Chapter 3

2.1.1. Materials

76 x 26 mm glass slides (Cole-Parmer) were used as substrates and washed with acetone and isopropanol prior to use. Inks consisted of a silver nanoparticle ink (AgNP ink) with an approximate 30% of solid content purchased from ANP Ltd and a synthesised tripropylen glycol diacrylate (TPGDA) ink. Surface mount Osram Opto LG R971, CHIPLED 0805 Series Green 570 nm light-emitting diodes (LEDs) and silver paste were purchased from RS Components. Ethanol HPLC gradient, 3-(trimethoxysilyl) propyl methacrylate (TMSPMA) 98%, toluene anhydrous 99.8%, Dulbecco's Modified Eagles high glucose Medium, HEPES solution 1 M, pH 7.0-7.6; Fetal Bovine Serum (FBS), trypsin solution, penicillin/streptomycin solution, Trypan blue and phosphate buffered saline (PBS) in tablets were acquired from Sigma-Aldrich.

2.1.2. Inkjet printing process

The instrument used was a piezo electric drop-on-demand Dimatix Materials Printer (Model DMP-2800, FUJIFILM, Dimatix, Inc. Santa Clara, CA). Inks were filtrated (HPLC Nylon 5.0 µm syringe filters, Cole-Parmer) and injected into the propylene print cartridge (DMC-11610, 10 pl), which was fixed to a printhead consisting of 16 nozzles (21 µm in diameter). Bit-maps of patterns were developed by GNU Image Manipulation Program (version 2.8.16) and adapted using the Dimatix materials printer software. Patterns were

printed by jetting 846.67 drops per inch (DPI), corresponding to a drop spacing of 30 um, and using custom print waveforms. The firing voltage varied over a range of 24-30 V. Droplet ejection was monitored using a camera incorporated in the printer.

To avoid any curing inside the cartridge when printing TPGDA due to ambient light, the cartridge was wrapped with duct tape. Five layers of TPGDA were printed and cured with a UV light (365 nm and 6000 mJ cm^{-2}) mounted directly on to the printing unit allowing it to move with the print head and induce real-time UV illumination and curing (Printed Electronics Ltd.).

Three layers of AgNP ink were printed on top of the five layers of TPGDA, to improve the adhesion of the silver to the substrate, achieving a good level of conductivity. Single nozzles were used to improve the resolution of the silver patterns and avoid the formation of clogs. The glass substrates were heated and held at 200 °C during the printing process to enable solvent evaporation and thermal sintering.

2.1.3. Surface analysis

Roughness of 1 x 1 µm areas and thickness of one layer of printed patterns in areas of 20 x 20 µm were established by Atomic Force Microscopy (AFM) using a Dimension FastScan AFM system (Bruker Corporation) in peak force mode mapping in air at room temperature. Probes consisted of a RTESPA MPP-

11120-10 model with a cantilever size of 3.5 – 4.5 µm and a frequency of 347 – 393 kHz. Data analysis of the AFM images was performed using WSxM 5.0 and Gwyddion 2.43 software.

2.1.4. Resistance measurements

Resistance of inkjet printed silver surfaces was measured using a 25 kHz LCR Meter HM8018 (Rhode & Schwartz) in 2 x 2 mm squares varying the temperature and time of sintering and number of layers printed and sintering time (n=10). Small droplets of silver paste were deposited over the printed silver layers to prevent scratches from the contact with the probes of the LCR Meter, allowing them to dry at room temperature during approximately 10 minutes. Thermally deposited silver films (Georg-Albert PVD) were used as a comparison. Data was processed in GraphPad PRISM version 7.01.

2.1.5. Microwire growth

Micorwires were grown by applying a potential difference of 90 V in an aqueous electrolyte was applied using an in-house-made high-voltage pulsed power supply in pulses of 300 ms with a gap between pulses of 200 ms for a duration of 10 s. Different geometries of electrodes were tested. The separation between the electrodes was 1 mm.

Values of resistance were measured (n = 9) using a digital multimeter (Eurisem Technics, model EP719). Number and diameter of connections were obtained after the application of potential differences (n = 9). Wires were only counted if they formed a continuous connection between the feeder electrodes. Diameter was measured in wires connected to the negative feeder electrode (effective interconnections) (n = 10 per sample). Data was analysed using GraphPad PRISM. A D'Agostino & Pearson normality test was carried out to check Gaussian distribution and One-way ANOVA with Tukey's post analysis was carried out to compare data between groups.

Digital Imaging Microcopy was performed using a Nikon ECLIPSE TE300 fluorescent microscope equipped with a QImaging optiMOS, Scientific CMOS camera. 20 frames per second were acquired. Electron Dispersive X-ray (EDX) of uncoated wires were performed in a Hitachi TM 3000 Tabletop Scanning Electron Microscope. Scanning Electron Microscopy (SEM) images were obtained in a JEOL 6060LV at 20 kV. Wires were deposited on SEM pin stubs and coated with gold.

2.1.6. Multi-component functional electronic device formation

Two pairs of silver electrodes with an area of 10.29 mm^2 each were printed. Each pair of electrodes had a separation of 1.8 mm and the separation between each pair was 2.6 mm. A surface mount light-emitting diode (LED) was placed upside down between the two pairs of printed electrodes at a distance of 0.4

mm. LED was attached to the surface with a drop of TPGDA and cured under UV light for 10 s. 10 µl of deionized water were deposited partially covering the two extremes of one pair of the printed silver electrodes and one Au electrode of the LED. A continuous potential difference of 150 V was applied over the pair of printed silver electrodes during 15 s, inducing the micro-wire formation. This was repeated on the other pair of electrodes. The functionality of the system was tested using a multimeter in diode test mode.

2.1.7. Bioelectronic interface formation

Glass slides were chemically modified before the printing process to increase the adhesion of TPGDA to glass substrate over longer periods of time. Glass was cleaned in ethanol during 10 minutes prior O_2 plasma-etching. Glass slides were then placed into the plasma chamber between two copper band electrodes connected to a power source (Coaxial Power Ltd.). The chamber was evacuated and needle valves (BOC Edwards) were used to control the oxygen pressure. Pressure was monitored with a Pirani gauge (Kurt J. Lesker Ltd.) and a glow-discharged plasma was initiated when the pressure was stabilised to $9x10^{-2}$ Mbar (50 W for 3 minutes). Cleaned glass slides were then silanised in 1% 3-(Trimethoxysilyl)propyl methacrylate (TMSPMA) (Sigma-Aldrich) in toluene for an hour and washed in MilliQ water.

CHO cells were cultured in corning T-75 cm^2 flasks in 15 ml of media (supplemented with 10% FBS, 5% HEPES solution and 1%

penicillin/streptomycin) for 2-3 days in an incubator at 37ºC in 5% CO_2 atmosphere and passaged when 70-80% confluent. A sticky-Slide well (Ibidi, Martinsried, Germany) with a growth area per well of 1 cm^2 was attached to a glass slide where silver electrodes were previously printed. Electrodes had 1 mm separation between them and 67 ± 6.2 µm diameter circles were randomly printed between them to facilitate microwire growth. 300 µl of media containing approximately 5 × 10^5 cells was added and cultured for 3 hours at 37ºC in 5% CO_2 atmosphere. Once the cells were attached to the surface, media was washed with PBS and substituted with milliQ water during microwire growth. A potential difference of 90 V was applied during 10 s.

Electrochemical measurements were carried out at room temperature using a VersaSTAT 4 potentiostat interfaced with a personal computer and integrated with VersaStudio Software (Princeton Applied Research). The supporting electrolyte was PBS dissolved in MilliQ water. Potentials are reported vs. an Ag/AgCl reference electrode. Printed silver feeder electrodes were used as working electrodes and a platinum wire was used as auxiliary electrode. Cyclic voltammogram (CV) was acquired when a potential was applied from 0.5 V to -0.2 V at a scan rate of 100 mV s^{-1}. Current was measured in three different samples prior and after AgMW growth in the presence and absence of the cells.

2.1.8. Alternative systems and further indications

Different electrode materials, solutions and types of electronic input were explored in this chapter with more or less success. This section aims at providing advice to future researchers on systems and parameters that were taken into consideration and failed.

Solutions: PBS and Hank's Balanced Salt Solution (HBSS) were initially used as aqueous solutions to grow wires as these solutions induce fewer perturbations to cells. However, the high content of ions present in the solutions drastically increases the movement of charges, which increases the temperature and water hydrolysis resulting in cell death. Ionic liquids were also explored, and some growth was seen in the absence of cells (this was not observed in the presence of cells).

Electronic input: alternating currents (AC) could offer a solution to application a direct currents (DC), reducing the potentials applied and ultimately increasing the cell viability. However, the continuous change of polarity creates perturbations in the solutions that affect the self-assembly of microwires. Some thin wires were grown in the absence of cells, but this was not done in the presence of cells.

Electrode material: alternative electrode materials were also explored, such as gold, graphene and PEDOT:PSS. There are still some limitations in

current the inks that can be printed with these materials that lead to very low conductivities or poor attachment to substrates. Therefore, electrodes need very high potentials to be applied or were destroyed when they were in contact with the aqueous solutions. As these materials are not electrochemically instable, it is necessary to add to the aqueous solutions metallic salts such as $AuCl_3$. Concentrations of metallic salts need to be carefully optimised, as high salt contents can lead to high currents as seen with PBS or HBSS.

2.2. Materials and methods of Chapter 4

2.2.1. Materials

Unless otherwise stated, materials were purchased from Sigma-Aldrich, UK

2.2.2. Inkjet printing of an electrochemical cell

An electrochemical cell consisting of two gold feeder electrodes and one silver/silver chloride pseudo reference electrode was inkjet printed. Kapton tape (RS Components, UK) composed of polyimide was attached to 76 x 26 mm glass slides (Cole-Palmer) and used as substrates. Glass slides were washed with acetone prior to use. Inks consisted of a silver nanoparticle ink (AgNP ink) with an approximate 30% of solid content purchased from ANP Ltd, and a gold nanoparticle ink (AuNP ink) with 40% of solid content (UTDots, Inc.).

Inks were filtrated and injected into print cartridges (DMC-11610, 10 pl and DMCLCP-11610), prior to printing, on a piezo electric drop-on-demand Dimatix Materials Printer (Model DMP-2800, FUJIFILM Dimatix, Inc. Santa Clara, CA). Bit-maps of patterns were developed using parameters presented in the point 2.1.2 Inkjet printing process. Single nozzles were used. When printing, the temperature was set and held to 100°C using a custom-built heater inside the printer. Sintering of nanoparticles was carried out in an oven at 150°C and

250°C for an hour for the AgNP ink and the AuNP ink respectively. Three layers of AgNP ink and five layers of AuNP ink were printed.

Roughness, thickness and resistance measurements of gold patterns were performed following the procedure presented in 2.1.3. Surface analysis and 2.1.4. Resistance measurements

Testing of printed electrochemical cell was carried out at room temperature using a VersaSTAT 4 potentiostat interfaced with a personal computer and integrated with VersaStudio Software (Princeton Applied Research). The supporting electrolyte was phosphate buffer saline (PBS) dissolved in deionised water (0.01 M phosphate buffer, 0.0027 M potassium chloride and 0.137 M sodium chloride), 1 mM potassium hexacyanoferrate (III) in PBS was used as the electroactive species. Potentials are reported vs. an inkjet Ag pseudoreference electrode. Printed gold feeder electrodes were used as working and auxiliary electrodes. Cyclic voltammograms (CVs) were acquired when a potential was applied from 0.8 V to -0.3 V at a scan rate of 5 mV s^{-1}.

2.2.3. Electrodeposition of palladium onto unmodified gold nanoparticles (u-AuNPs)

50 nm unmodified gold nanoparticles, OD 1, stabilised in 0.1 mM PBS and reactant free (u-AuNPs) were used as bipolar electrodes within the printed cell,

where the gap between gold feeder electrodes was 210 µm. A solution of 1 mM palladium chloride in PBS was added to the dispersion of u-AuNPs. 20 µl of this suspension were placed in contact with all the elements of the system. Chronoamperometry was performed in the aforementioned instrument. 10 V were applied for varying times of 1, 5 and 15 minutes.

Size characterisation of the u-AuNPs dispersion was carried out by Dynamic Light Scattering (DLS) using a Malvern zetasizer Nano ZS (Malvern Instruments, UK) after the electrodeposition. Scanning Electron Microscopy (SEM) was used to examine the morphology of the deposits. The sample preparation required the deposition of the suspensions into a holey carbon Transmission Electron Microscopy (TEM) grid. Visualisation of the nanoparticles was carried out in FEI Quanta 650 SEM. Elemental mapping results were performed with an energy-dispersive X-ray spectrometer (EDX) incorporated in the SEM.

In order to discard pH-induced aggregation, solutions were incubated in PBS (pH 7.4 at 25°C), a commercial buffer solution at pH 4 ± 0.01 at 20°C (SLS Select) and a commercial buffer solution at pH 2 ± 0.02 at 25°C (Reagecon). Size of particles was measured by DLS in aqueous after 1 and 15 minutes. pH of the system was also monitored for 15 minutes when the potentials were applied and measured on a pH meter (Metler Toledo).

2.2.4. Plasmonic-based detection of electrical charge modulation at u-AuNPs

A darkfield microscopy setup was used to image the voltage effect on the u-AuNPs. In this setup, the sample was illuminated with a 633 nm collimated light. The sample plane was imaged on CMOS camera (SV643M, Epix) to collect the forward-scattered light by nanoparticles. To study the low voltage effect on u-AuNPs, an electrostatic layer-by-layer self-assembly process was used to bond the particles to a conducting substrate to avoid being washed out while serving as a working electrode. Firstly, a layer of potassium hydroxide (KOH) solution was deposited for 1 hour on a glass cover-slip coated with 10 nm of Indium-Tin-Oxide (ITO). Then, two synthetic polymers, poly(allylamine hydrochloride) (PAH) and poly(sodium 4-styrenesulfonate) (PSS), were deposited for 30 minutes each. Between all these steps, the substrate was washed with deionised water and dried with nitrogen. Once the polymer layers were completed, a solution of u-AuNPs (125 nm diameter) was drop-coated and dried overnight. For sensitive detection of the voltage effect, the wavelength and the particle size and shape have to be carefully selected. Here, the wavelength of 633 nm is located at the highest gradient of the scattering spectrum of the 125 nm u-AuNPs, in aqueous solution, where maximum change in scattering due to the applied voltage is obtained. A sinusoidal voltage modulation with 0.8 Vpp at 4 Hz was applied to the substrate-integrated nanoparticles, against a platinum reference electrode, while recording modulation of light scattering simultaneously using CMOS camera (SV643M, Epix, Buffalo Grove, IL, USA) with 100 Hz sampling frequency. To map the voltage effect on the Au nanoparticles, a fast Fourier transform (FFT) of the

dynamic scattering intensity was computed for each pixel. The map was produced by selecting the amplitude of the voltage-modulated intensity at the frequency of the applied signal.

2.2.5. Synthesis and characterisation of water soluble gold nanoparticles (ws-AuNPs)

Details about synthesis and characterisation were described elsewhere[223]. Measurements of absorbance and emission spectra were performed on a Tecan microplate reader. Absorbance was scanned form 200 nm to 1000 nm at room temperature with a wavelength step size of 2 nm of solutions of 1.17 mM of a Zn(II)meso-tetrakis(4-carboxylatephenyl)porphyrin sodium salt (Na-ZnTCPP), and 2.77 µM ws-AuNPs with and without Na-ZnTCPP in PBS. Emission spectra of the previous solutions was measured from 550 nm to 750 nm at an excitation wavelength of 420 nm at room temperature. A 10 µl drop of suspension of Na-ZnTCPP modified ws-AuNPs was deposited on a TEM carbon-coated copper grid (Agar Scientific) and dried at room temperature before measurements. TEM measurements were performed on a Jeol 2100 Plus TEM at an accelerating voltage of 80 kV.

2.2.6. Cell culture

Chinese Hamster Ovary (CHO) cells were cultured in corning T-75 cm^2 flasks in 15 ml of media supplemented with 10% foetal bovine serum (FBS), 2.4%

HEPES buffer solution and 1% penicillin/streptomycin for 2-3 days in an incubator at 37ºC in 5% CO_2 atmosphere and passaged with trypsin when 70 – 80 % confluent.

Uptake of Na-ZnTCPP modified ws-AuNPs was analysed by inductively coupled plasma mass spectrometry (ICP-MS). Approximately 1.50×10^{-3} cells were reseeded on 6 well-plates 24 hours before experiments. Na-ZnTCPP modified ws-AuNPs were added at a final concentration of 2.54 µM in Hank's Balanced Salt solution (HBSS) and incubated for 0.5, 1 and 4 hours. After each time point, solution was collected, centrifuged at 4000 rpm for 5 minutes and pellet saved for ICP-MS analysis. Cells were rinsed three times with PBS and trypsinised and collected in a Falcon tube. 10 µl of cell suspension were mixed with Trypan blue in a ration 1:1 and counted on a haemocytometer after each time point. Well plates were washed with 10% FBS in HBSS solution and collected with the cells prior centrifugation at 1200 rpm for 5 minutes. Pellets containing the cells were saved for ICP-MS analysis. Solutions were digested in 5% aqua regia (trace metal grade HCl and HNO_3 in a proportion of 3:1) and left overnight. After digestion, solutions were diluted to reach a final concentration of acid of 2%, filtered and collected for analysis on an iCAPQ Thermo Fischer inductively coupled plasma mass spectrometer. Standard solutions were used to develop a calibration curve. The number of nanoparticles per cell was calculated by firstly gaging the number of Au atoms present in the 50 nm nanoparticles assuming a crystalline structure. This allows us to know the mass

of Au per nanoparticle and compare it to ICP-MS results to obtain the total number of particles in each sample. The cells were counted as described earlier, we can then calculate the number of particles per cell at the different time points.

Biocompatibility studies for longer incubation times were performed using a water-soluble tetrazolium salt (WST-8) assay. 7500 cells were incubated on 96 well plates 24 hours prior experiment. Na-ZnTCPP modified ws-AuNPs at different concentrations were added (C1: 11.8 µM, C2: 2.36 µM and C3: 1.18 µM) and incubated with cells for 24, 48 and 72 hours. After each incubation time, media was replaced with 10% WST-8 in complete DMEM and incubated for an hour before reading absorbance at 450 nm in a Tecan microplate reader. Controls (culture media as negative control and TritonX-100 3% as positive control) and blanks were used. Values are presented relative to negative controls.

2.2.7. Intracellular wireless actuation

CHO cells were incubated in a 6 well plate with 2.54 µM of Na-ZnTCPP modified ws-AuNPs, incubated for 4 hours and suspended. 20 µl of suspension containing cells was placed between gold feeder electrodes and 150 V were applied using an in-house-made voltage power supply. 550 nm laser was used as excitation source. Changes in fluorescence of modified particles were monitored using a Nikon ECLIPSE TE300 fluorescent microscope equipped with

a QImaging optiMOS, Scientific CMOS camera. ImageJ 1.52a open source software was used to perform image analysis and quantification of the corrected total cell fluorescence. Statistical significance was calculated using an unpaired t-test on Graphpad Prism 7.01.

2.3. Materials and methods of Chapter 5

2.3.1. Human induced pluripotent stem cell (hiPSC) differenciation into hiPSC-derived cardiomyocytes (hiPSC-CM)

A REBL-PAT hiPSC line was derived from a skin punch biopsy from a male subject. Procedures of isolation, culture, differentiation and dissociation are described elsewhere[224].

2.3.2. Immunostaining of hiPSC-CM

hiPSC-CM were fixed in 2% formaldehyde (VWR) and permeabilised with 0.1% Triton-X 100 (Sigma-Aldrich). Non-specific binding was blocked with 4% foetal bovine serum (FBS) (Sigma-Aldrich) in PBS for 1 h. Samples used to calculate the percentage of hiPSC-CM after differentiation were immunostained with a monoclonal primary antibody against TNNI3 produced in mouse (Sigma Aldrich # WH0007137M4) at a concentration of 1:1000 in PBS. Samples aimed at analysing the morphology and maturity of hiPSC-CM were immunostained with a monoclonal primary antibody against sarcomeric alpha-actinin produced in mouse (Abcam #ab9465) at a concentration of 1:400 in PBS. In both cases, samples were incubated at 4°C overnight. A solution of 0.05% of Tween-20 was used to wash the samples and a solution of goat anti-Mouse secondary antibody IgG was added (1:1000; Abcam # ab6785) and incubated

for 2 h. Samples were washed with washing solution and exposed to Hoechst 33258 (5 $\mu g ml^{-1}$; Sigma Aldrich) and phalloidin (1:150, ThermoFischer Scientific). Fluorescence images were taken on an inverted EVOS FL Fluorescence microscope.

2.3.3. Electrical stimulation of hiPSC-CM

Electrical stimulation was performed in an in-house made electro-bioreactor with platinum positive and negative electrodes similar to electro-bioreactors previously described[54] and adapted to fit in a 6-Well plate. Potentials were applied in AC mode from 0 to 2 V and 1 to 5 Hz and cell responses analysed in a Nikon ECLIPSE TE300 fluorescent microscope equipped with a QImaging optiMOS, Scientific CMOS camera.

2.3.4. Structure fabrication by two-photon polymerisation (2PP)

Glass coverslips were precleaned in Ethanol and cleaned on an O_2 plasma-etching chamber for 5 minutes as described in 2.1.7. Bioelectronic interface formation. Glass was then modified with 1% TMSPMA in Ethanol for 1 hour and washed with water prior printing in order to increase the adhesion of polymers during 2PP process.

3 mL of pentaerythritol diacrylate (PETrA) were weighed in an amber coloured bottle and various photoinitiator (Irgacure 369) concentrations

including 0.5 w/w%; 1 w/w%; 2 w/w% and 3 w/w% were added to the monomer and stirred using a magnetic follower for 24 hours at 200 rpm. To make the composite resin, a calculated amount of carboxylic acid functionalised multi-walled carbon nanotubes (MWCNTs) were added to the monomer and continuously stirred for 24 hours using a magnetic stirrer. Later, the composite mixture was subjected to probe sonication for 30 minutes to fully disperse the MWCNTs. This dispersion was then centrifuged at 6000 rpm for 30 minutes using mini-spin Eppendorf to remove large aggregates of the MWCNTs. The resulting mixture was weighed and 1% w/w photoinitiator was added to the mixture and stirred for 24 hours and used for the fabrication.

Two photon polymerisation was performed using the commercial Nanoscribe Photonic Professional GT, equipped with a fibre laser (780 nm). A silanised cover slip was secured on the build platform and a droplet of oil was placed on one side of the coverslip which is exposed to the lens. A 50 µL droplet of the ink was placed on the other side of the silanised coverslip. The stray is inserted onto the machine. A 63x oil immersion objective lens with a working distance of 190 µm was used to focus the laser beam. The patterns were fabricated by moving the laser beam in X and Y directions with the aid of galvo scanner and the piezo-stage was moved in Z direction. The laser power used ranged from 15 to 60 mW and the scanning speed was varied from 10 mm s^{-1} to 60 mm s^{-1}.

On fabrication, the coverslip containing the sample was removed from the tray, soaked in propylene glycol monomethyl etheracetate (PGMEA) for 1 hour, and later soaked in the iso-propyl alcohol for 1 hour to remove residual monomers. The sample was then air dried and stored in a Petri dish until further use.

Structures were sterilised in ethanol for 30 minutes, thoroughly washed in complete PBS and washed in antibiotic (penicillin/streptomycin solution 10.000 units penicillin 10 mg streptomycin ml^{-1}; Sigma Aldrich) for 1 hour. Dissociation of cells took place 6-8 weeks after differentiation process and cells were seeded on structures fabricated by 2PP at an approximate concentration of 2 million cells/ml in basal RPMI medium (Life Technologies #11875093) supplemented with 1xB27 (Life Technologies #17504044), Y-27632 ROCK inhibitor (1:1000; Tocris #1254) and 10 % foetal bovine serum. Media was changed after 24 hours to RPMI/B27 media and cells were incubated for 6 days before performing further experiments.

Surface morphology of the 2PP printed sample was obtained using a scanning electron microscope fitted with a field-emission gun (FEG-SEMl JOEL 7100F) using a secondary electron mode at an acceleration voltage of 5KV and a working distance of 10 mm. to avoid charging of the samples, the printed polymeric structure was sputter coated with iridium (10 nm thick).

2.3.5. Viability studies

hiPSC-CM were washed in complete PBS (Sigma Aldrich) and incubated for 30 min in 1 µM acetoxymethyl (AM) calcein solution (Sigma Aldrich #C1359) in PBS to stain viable cells and dead cells were stained with 5 µM ethidium homodimer I (Sigma Aldrich #E1903) in PBS. Fluorescence images were taken on an inverted EVOS FL Fluorescence microscope.

2.3.6. Morphological analysis of hiPSC-CM

hiPSC-CMs were immunostained following previous protocol and samples mounted in VectaShield hardening mounting medium (Vector Labs, UK) and imaged using an automated fluorescence microscope (Zeiss 200M fluorescence microscope). Aspect ratio and alignment were measured on 10 individual cells per sample in triplicate. Lenghts of sarcomeres within myofibrils were measured using Image J line profile tool downloaded from http://imagej.nih.gov/ij/. 10 sarcomeres were measured per cell, on 10 cells per sample in triplicate. Statistical significance was calculated using an ordinary one-way ANOVA statistical test (N=3, n=10; SEM).

Chapter 3. Development of a novel bionic manufacturing approach by inkjet printing and bipolar electrochemistry

As discussed in Chapter 1, it is necessary to advance our ability to construct three-dimensional multimaterial functional bioelectronics with seamless integration of biological and electronic components. Additionally, to ease the transition of building cellular electronic systems, a remote approach to merge electrical components with biology is desirable. A new method is described herein, that combines 3D digital inkjet printing with electrochemistry to remotely control and fabricate conductive silver wires.

Wires were formed by self-assembly of silver nanoparticles induced by applying a potential difference to inkjet printed electrodes. Wires fabricated displayed outstanding omnidirectional electrical properties and alignment. It is demonstrated that by tailoring the electrode geometry, the electric field and thus, diameter, number of connections and resistance of wires could be controlled.

Conductive wires were grown via bipolar electrochemistry in a 3D coordinated manner to connect electrical components with a significant reduction in the size of electrical interconnects and importantly, forming connections between elements in different z-planes. Moreover, it is demonstrated that this technology could be used to grow and interface conductive conduits *in situ* with mammalian cells to sense cell redox events. This approach provides a generic platform to construct 3D bioelectronic devices.

Keywords: Bionic manufacturing, bioelectronic interfaces, electrical interconnects, three-dimensional circuits

Part of the content of this chapter appears in *Remotely Controlled in Situ Growth of Silver Microwires Forming Bioelectronic Interfaces.* Sanjuan-Alberte P, Saleh E, Shaw AJ, Lacalendola N, Willmott G, Vaithilingam J, Alexander MR, Hague RJM, Rawson FJ. **ACS Applied Materials & Interfaces** (2019), 11 (9), 8928-8936.

Ehab Saleh is acknowledged for developing the in-house built power supply used in the experiments of this chapter and providing advice in experimental set up. Marta Alvarez-Paino and Jacqueline M Hicks are thanked for providing help with SEM imaging and setting up the optical microscope, respectively.

Geoff Willmott and Nicola Lavacalendola from the Department of Physics of the University of Auckland are acknowledged for carrying out the simulation of electric fields and electric potentials of feeder electrodes with different geometries shown in 3.2.2. Electrochemical induction of silver (AgMW) growth.

Chapter 3. Development of a novel bionic manufacturing approach by inkjet printing and bipolar electrochemistry 82

3.1. Introduction 86

3.2. Results and Discussion 88

3.2.1. Inkjet printing of silver feeder electrodes 88

3.2.2. Electrochemical induction of silver microwire (AgMW) growth 98

3.2.3. Wireless electrochemical fabrication of functional 3D circuitry 105

3.2.4. Fabrication of in situ bioelectronic interfaces 109

3.3. Final considerations 116

Note for readers: Materials and methods corresponding to this chapter can be found in 2.1. Materials and methods of Chapter 3

3.1. Introduction

Electronic devices and systems are almost entirely pre-assembled prior to integration with biology during the manufacturing of current state-of-the-art bioelectronics[225]. This possess issues in the development of bioelectronic systems as to work optimally they require seamless integration between electronic and biological structures[226]. Merging of electronic and biotic elements is essential to develop tools with ability to regulate[227] and monitor[228] biological activity. In this chapter, a novel method to direct electronic systems *in situ* in a wirelessly manner is reported. This presents a step change in thought of how to build electronics and seamlessly integrate these with biology by growing devices or electronic components *in situ*.

The aim of the work presented in this chapter was to develop new bionic manufacturing approaches to fabricate cellular-electrical bioelectronic interfaces for future applications in non-invasive surgery of bioelectronic devices in a wireless controlled manner. A key objective to achieving this was to overcome these limitations by combining the design freedom of digital inkjet printing[149, 229] with bipolar electrochemistry[230] by investigating how the geometry of feeder electrodes modulate nano/micro wire synthesis.

This new approach is then utilised to fabricate functional hybrid bioelectronic systems by self-assembling silver nanoparticles that align with the geometry of the electronic field. Functionality and z-plane control of the *in situ* grown wires was tested via the powering of a light emitting diode. Once this was demonstrated, wires were grown without any direct electrical contact and interfaced with eukaryotic Chinese hamster ovary (CHO) cells.

Thereby, in a first demonstration of its kind, a new contactless method of creating bioelectronic functional systems *in situ* is presented[231]; this represents a step change in the production of complex circuitry and considerably increases the manufacturing capabilities of merging cells with electronics remotely. The improvements offered by this new approach, as indicated by the 3D functional conduits produced, increase prospects of interfacing such devices with biological materials, for a wide range of applications such as real-time monitoring of cellular, biochemical and physiological components, remote sensing and optical communications.

3.2. Results and Discussion

3.2.1.Inkjet printing of silver feeder electrodes

The initial approach to the controlled fabrication of 3D electronic systems was to develop a printed electrochemical cell that enabled the growth of conducting conduits using bipolar electrochemistry in a controlled 3D manner. Towards this goal, a pair of silver electrodes that were subsequently used to apply the potentials (feeder electrodes) were printed using a drop-on-demand (DOD) inkjet printer. Silver nanoparticle infused ink (AgNP ink) was used to print feeder and bipolar electrodes (Figure 3-1) as its electrochemical behaviour can be taken advantage of to wirelessly grow conductive conduits in a single step without the need for addition of metallic salts. Furthermore, it is suitably conductive and has ideal printing properties that result in it being one of the most used metals in inkjet printing for electronic applications[136, 156, 232]. It is important to note that the material used is not a key point of this work, but the ability to combine conductive and biological structures remotely.

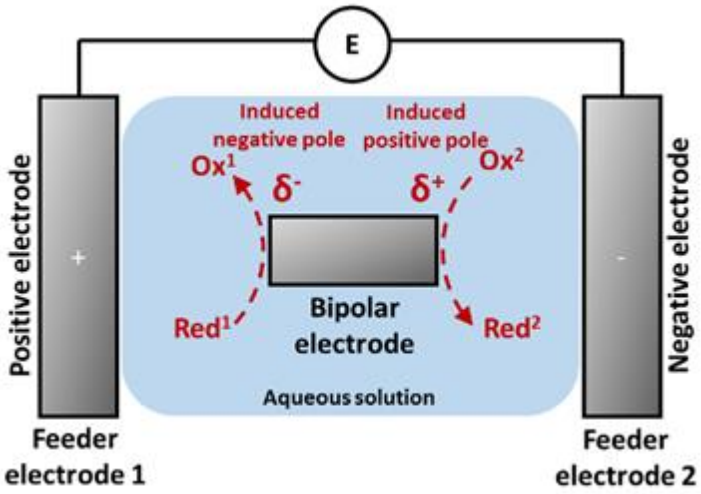

Figure 3-1. Schematic representation of bipolar electrochemistry system

A pair of printed silver electrodes were used to generate an electric field when a potential difference was applied inducing changes in polarity of the elements within the range of the electric field. Poor adhesion strength between metal-glass interfaces is often an issue when printing metallic inks[233-234]. To avoid this and increase the adhesion of silver electrodes to the substrate, an underlying polymeric film with an approximate thickness of 22 µm of tripropylene glycol diacrylate (TPGDA) was inkjet printed following the methodology of a previous study[235]. This polymeric layer could increase the surface energy of the substrate, increasing the adhesion of the subsequently printed silver layers. The structure of TPGDA can be seen in Figure 3-2.

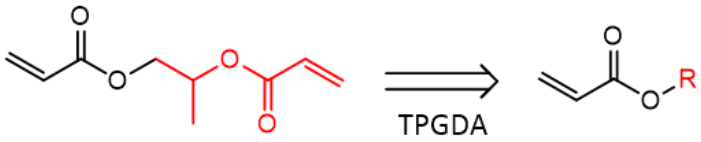

Figure 3-2. Tripropylene glycol diacrylate (TPGDA) chemical structure. Simplified structure can be seen on the right.

The jetting waveform used to impart the force required to generate and eject the droplets from the nozzles can be seen in Figure 3-3A. Droplets formed from the nozzles were stable with long tails, and the printing parameters were optimised to ensure an optimal speed of droplet ejection between 6-12 m s^{-1} (Figure 3-3B).

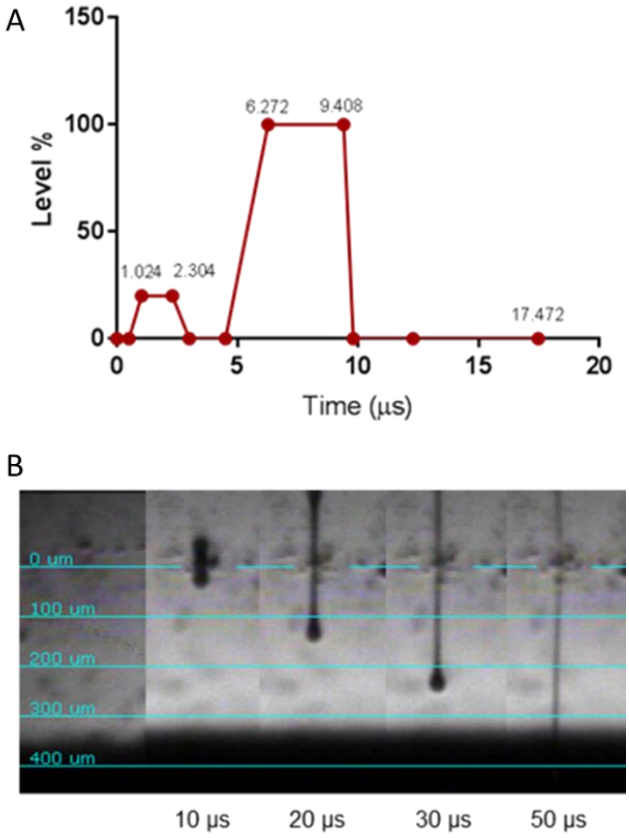

Figure 3-3. (A) Jetting waveform and (B) droplet formation and ejection from nozzles of TPGDA ink

TPGDA ink formulations contain the type II photoinitiator diethylthioxanthone (DETX) and the co-initiator ethyl-4-(dimethylamino)benzoate (EDB). When UV light is irradiated on the printed patterns of TPGDA, DETX is excited to the triplet state (Figure 3-4) and an electron transfer from EDB produces a DETX anion radical and EDB cation radical[236].

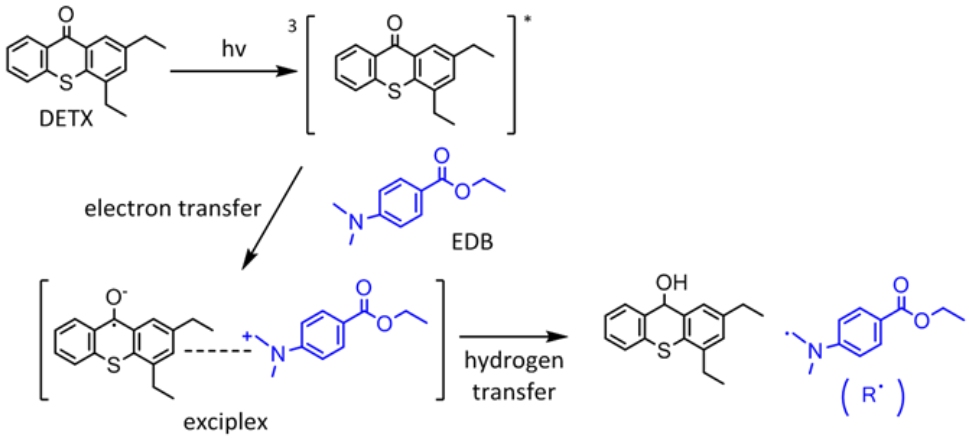

Figure 3-4. Mechanism of free radical formation after irradiating UV on TPGDA ink containing the photoinitiator DETX and co-initiator EDB

This is followed by a rapid proton loss from the EDB, resulting in a neutral α-amino radical which triggers the polymerisation by attacking the double bond of TPGDA (Figure 3-5). This results in a new free radical with the ability to attack a new double bond of TPGDA until the polymerisation is completed[237].

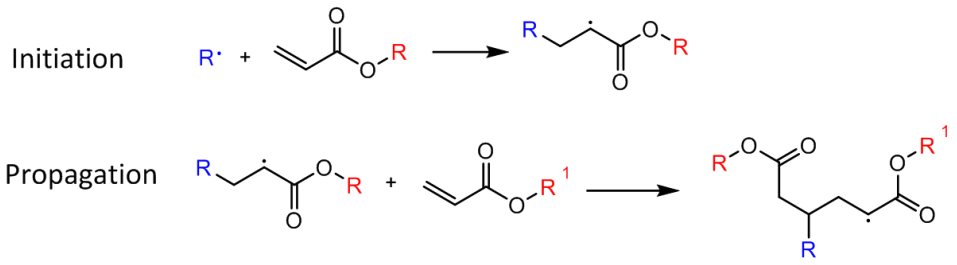

Figure 3-5. Mechanism of polymerisation after photoinitiaton

Once three layers of TPGDA film were photopolymerised, electrodes were printed using the AgNP ink. The jetting waveform used can be seen in Figure 3-6A. Settings were optmised during the process to produce stable 10 µl droplets, allowing for an optimal speed of ink droplet ejection from the nozzles (Figure 3-6B).

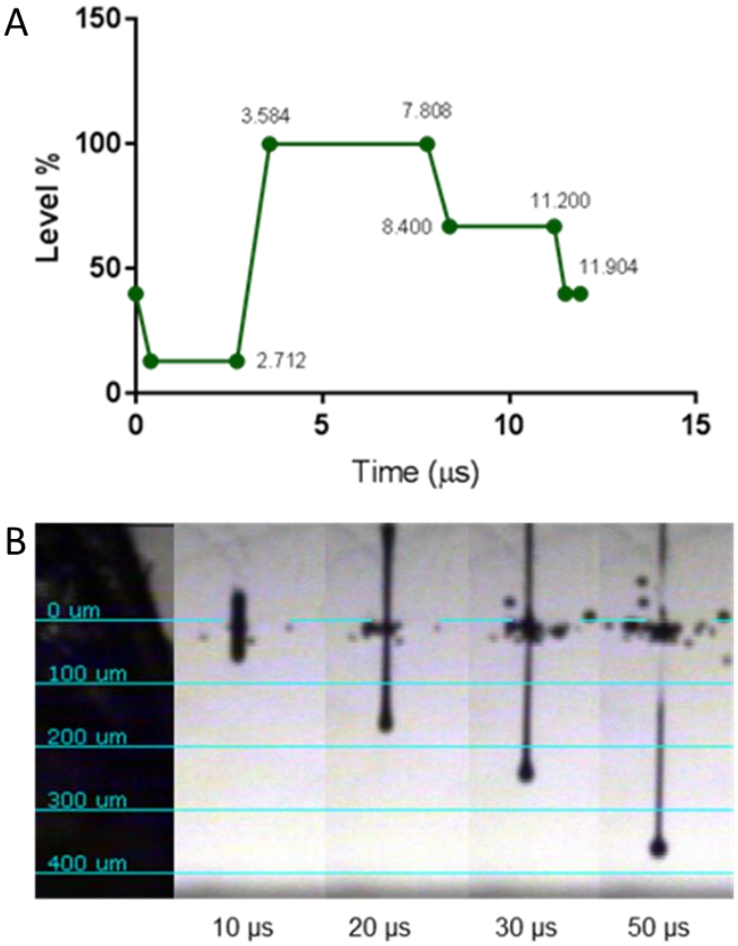

Figure 3-6. (A) Jetting waveform and (B) droplet formation and ejection from nozzles of silver nanoparticle ink (AgNP ink)

The thickness of the silver film was calculated from the surface profiles of one layer of printed silver electrodes by atomic force microscopy (AFM) (Figure 3-7), providing a thickness of 259.33 ± 82.10 nm per layer.

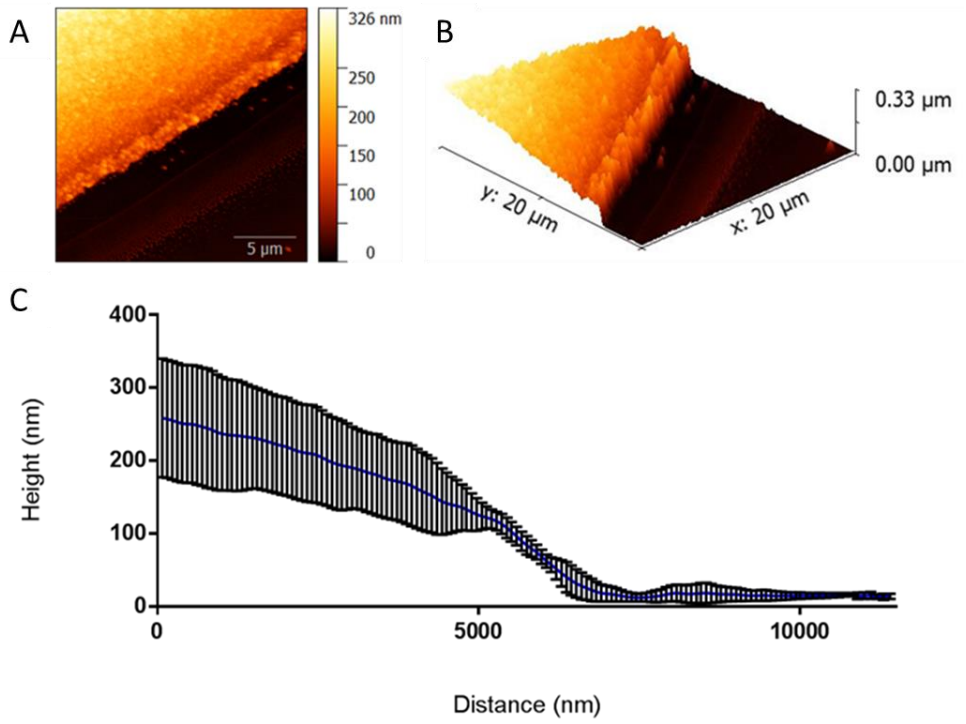

Figure 3-7. (A) Bi-dimensional and (B) three-dimensional images of and edge of an inkjet printed silver electrode obtained by AFM and (C) its height profile (N=3; n=3)

Subsequent thermal sintering formed percolating pathways between particles[238], improving the electrical properties and altering the topography of the printed electrodes. This effect can be seen in Figure 3-8, where AFM images of silver films before and after thermal sintering were taken.

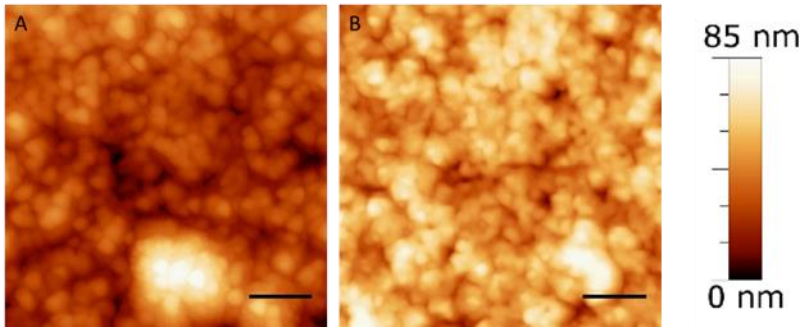

Figure 3-8. Atomic Force Microscopy (AFM) images of an inkjet printed silver film before (A) and after (B) thermal sintering (scale bar 200 nm).

The presence of the percolating pathways decreased the resistivity of the silver film from 145 µΩcm of single layers before starting the sintering process, to 56 µΩcm after application of 200°C (Figure 3-9A). After 15 minutes of sintering at 200°C, resistivity values reached a plateau phase where no significant reductions are seen (Figure 3-9B). This agrees with what has been described in the literature[239].

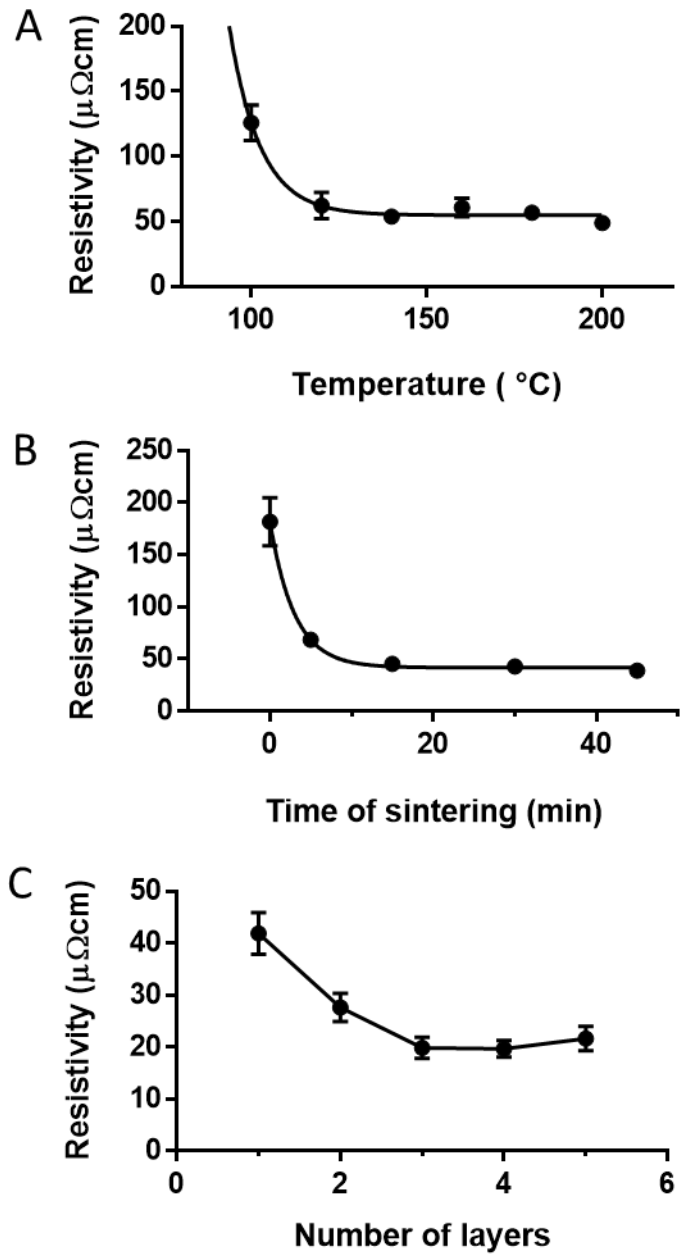

Figure 3-9. Resistivity of (A) one layer of silver surfaces at different sintering temperatures, (B) one layer of silver surfaces sintered at 200ºC at different times (C) different layers of silver surfaces sintered at 200ºC (n=10, SD)

In addition to the sintering process, the number of printed layers of silver has an influence over the values of resistivity. Single layers presented values of

41.9 µΩcm in contrast to 19.87 µΩcm for five layers and 20 minutes of thermal sintering. This reduction of resistivity is potentially due to the increase in thickness with the additional layers of silver. After printing more than three layers, no substantial reduction in the value of resistivity occurred (Figure 3-9C).

These values were compared to resistivity of thermally deposited silver films and bulk silver, showing that despite there is a clear difference between inkjet printed films and bulk and thermally deposited silver, printed films are conductive (Table 3-1).

Table 3-1. Resistivity values of silver electrodes obtained by thermal deposition, inkjet printing of five layers after sintering process and bulk silver at 295K (µΩcm)[240] (n=10).

Material	Sheet resistance (Ω sq^{-1})	Thickness (nm)	Resistivity (µΩ cm)
Thermally deposited silver	0.063 ± 0.01	300	1.875 ± 0.306
Inkjet printed silver	0.137 ± 0.02	260 per layer	19.867 ± 0.774
Bulk silver	-	-	1.610

From this section, it can be concluded that silver films were successfully printed, and parameters needed during the printing and post-processing of the silver films were optimised. Conductivity values of printed silver were sufficient and comparable to literature values, making them suitable for subsequent manufacturing of feeder electrodes.

3.2.2.Electrochemical induction of silver microwire (AgMW) growth

The next part of the investigation was to optimise the mechanism of silver microwire (AgMW) induced metal deposition, which would be used later in electrochemical wireless studies to produce functional bioelectronic systems. When a potential difference is applied to silver feeder electrodes separated by an aqueous phase, the negative electrode oxidises silver atoms on its surface, making them available in the solution as silver cations (Equation 3-1). The positive electrode subsequently reduces these cations depositing them onto its surface as it follows:

$$Negative\ electrode: Ag(s) - e^- \rightarrow Ag^+(aq)$$
$$Positive\ electrode: Ag^+(aq) + e^- \rightarrow Ag(s) \quad \textbf{Eq. 3-1}$$

The magnitude and kinetics of the redox reactions depend on the potentials applied and the electric field intensity[241]. Optimised conditions allowed for the selection of the optimal parameters for electrodeposition of silver. This was achieved by studying the deposits formed as a function of potential applied and distance between feeder electrodes. At distances < 1 mm between feeder electrodes and potentials above 50 V, the reactions were too violent due to too much current being passed, resulting in burnt feeder electrodes (Figure 3-10). Lower potentials induced an unorganised deposition that formed a thin film on the surface of the TPGDA. Distances > 1 mm between feeder electrodes at 30-60 V applied induced an organised reduction of silver in the shape of silver

microwires (AgMWs). Magnitudes of potentials above 70 V made thinner wires compared to those where relatively lower potentials were applied (Figure 3-10). These differences responded to the magnitude of energy required to induce the redox reactions and the kinetics of the reactions. Therefore higher values of potentials supply enough energy to the system to form organised structures in contrast to lower potential.

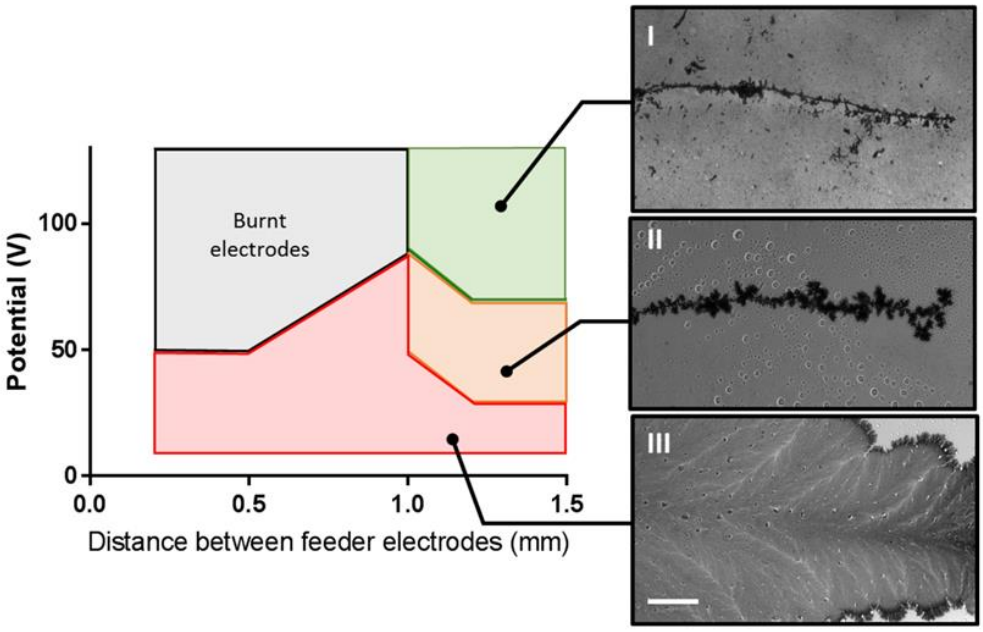

Figure 3-10. Optimisation of potentials applied (V) vs distance between feeder electrodes (mm) to induce microwire growth resulting in (I) thin microwires, (II) thick microwires and (III) deposition at the surface. Scale bar 100 um.

Once the potentials and distances between feeder electrodes were optimised, a potential difference of 90 V was applied in pulses of 300 µs over a period of 10 s through feeder electrodes with a separation of 1 mm. This induced the reduction of silver cations and self-assembly of AgMWs at the

positive electrode. The morphology of the AgMWs was characterised by light microscopy and Scanning Electron Microscopy (SEM). Energy dispersive X-ray (EDX) spectroscopic images confirmed that silver was the predominant element in the wires (Figure 3-11A), and the expected electrochemical reactions were taking place within the printed system. Regarding the unorganised film, a random distribution of silver can be observed in the EDX images (Figure 3-11B).

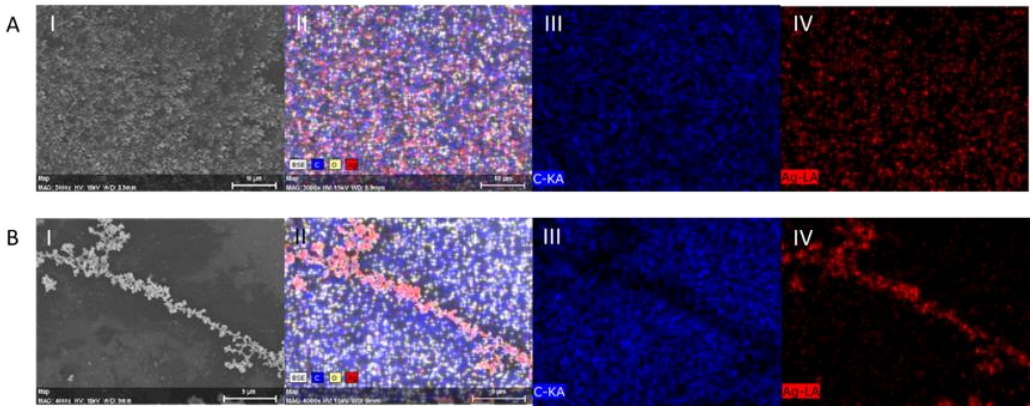

Figure 3-11. Figure 2.14. EDX analysis of (a) deposition on surface and (b) microwires consisting on (I) SEM image, (II) element composition, (III) carbon spectrum and (IV) silver spectrum.

Further examination of the microwires using SEM revealed that AgMWs were formed by clusters of deposited silver nanoparticles (NPs), rather than having the shape of a continuous wire (Figure 3-12). According to SEM images of wires formed, silver electrodeposited NPs had an average size of 212.07 ± 47.50 nm (n = 25). The assembly between these particles is affected by the magnitude of the potential, which influences the diameter of the AgMWs, with a minimum diameter equivalent to the size of single NPs (Figure 3-12).

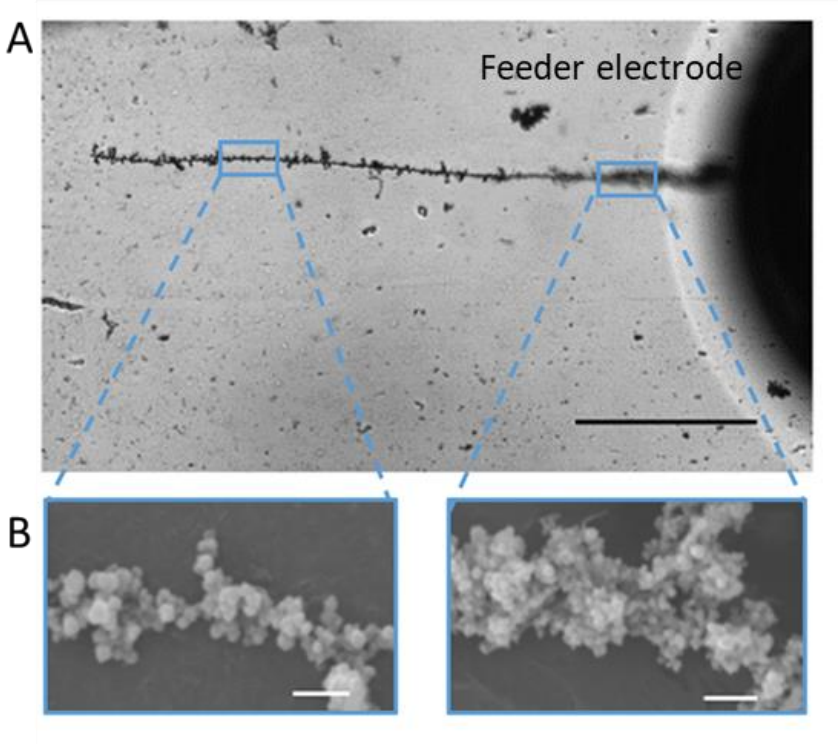

Figure 3-12. Potential induced self-assembly of silver cations to form microwires at the positive electrode observed by (A) optical microscopy (scale bar 100 µm) and (B) scanning electron microscopy of self-assembled silver nanoparticles resulting in different diameters. Scale bar 1 µm.

In order to induce the electrolytic nucleation that leads to silver electrodeposition and AgMW growth, a potential difference was applied. The potential difference is in turn, a property of the electric field strength and dimensions. Increases in the strength of the applied electric field affect the migration of ions within the solution and thus, the rate of assembly of silver particles. Therefore, the ability to control the electrical field characteristics is of significant importance in terms of influencing AgMW growth[241-242]. To note, these studies are the first detailed mechanistic study for controllable growth of

wires via bipolar electrochemistry for bioelectronic applications; in particular, the geometry of feeder electrodes and the effect this has on the electric field – and thus self-assembly of silver nanoparticles into conductive micro-wires – has not been studied previously.

Images of the simulation of electric fields and potentials of feeder electrodes with different geometries can be seen in Figure 3-13, showing the effect of geometry on resulting electric fields. Therefore, the ability to modulate wire growth via feeder electrode geometry was investigated as a tool to control AgMW electronic properties, as this is an important consideration when developing bioelectronic functional systems.

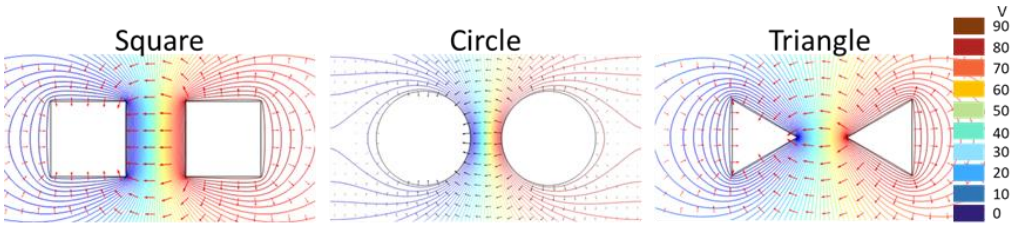

Figure 3-13. Modelled electric field and electronic potential of 90 V applied using different geometries of feeder electrodes (contour: electric potential (V), arrow surface: electric field)

In this work, three simple geometries (square, circle and triangle) of feeder electrodes were tested under the conditions mentioned above. AgMW assembly was observed *in situ* and in real time by optical microscopy (Figure 3-14). Wire growth matched the simulated electric field lines from Figure 3-13.

For all the geometries, a reduction in voltage and electric field was evident when a certain number of AgMWs bridged the pair of feeder electrodes, thus stopping the redox exchange and wire growth.

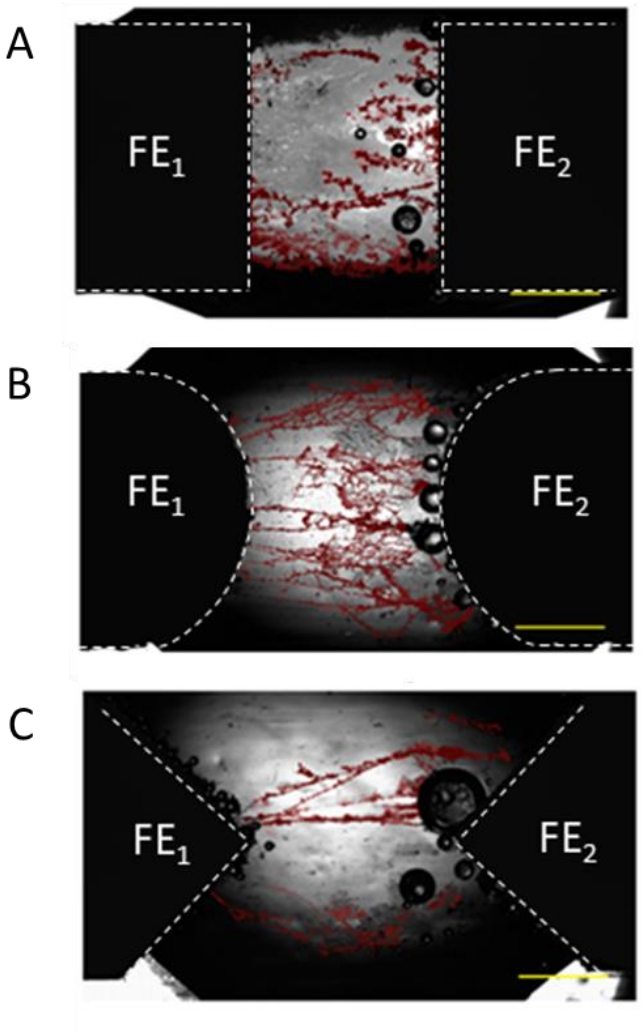

Figure 3-14. Optical microscopy images of AgMW connections between feeder electrodes in the shape of (A) square, (B) circle and (C) triangle. AgMWs were false coloured in red to highlight them. Scale bar 500 µm.

AgMWs are more polarisable than the surrounding dielectric medium, being subjected to the dielectrophoretic force that induces growth in the

direction of increasing electric field strength. The geometry of the feeder electrodes will thus affect the electric field; this explains the differences found in wire growth between the different geometries. In the square electrodes, dendritic wires with a mean diameter of 8.402 ± 1.483 µm are formed (Figure 3-15). This is likely due to Joule heating and thermal fluctuations produced, interfering with the field alignment and producing the dendrites. Circular electrodes distribute the field more evenly, producing a larger number of thinner wires (7.78 ± 0.55 wires with a diameter of 2.216 ± 0.158 µm on average). Whereas triangular electrodes produced sharp and thin AgMWs with mean diameter of 2.692 ± 0.231 µm (Figure 3-15).

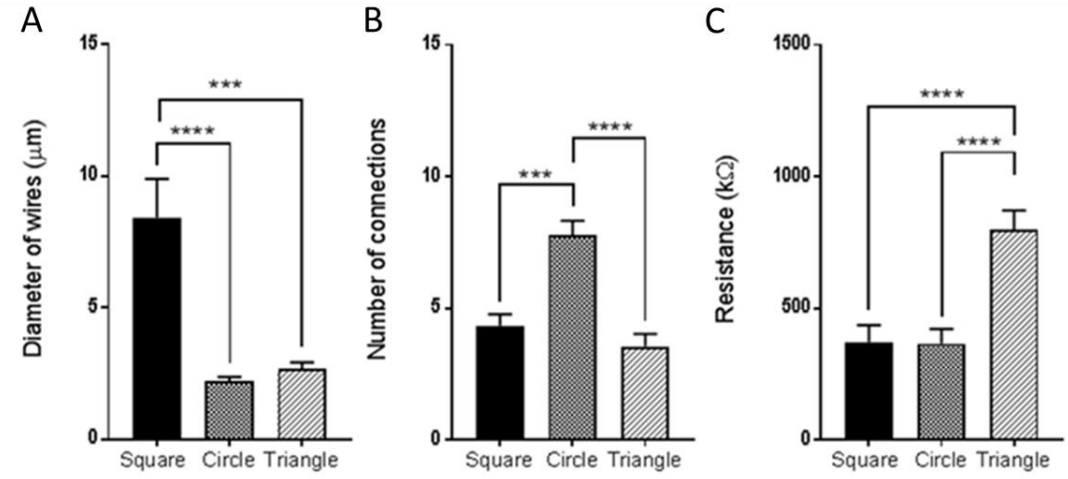

Figure 3-15. Diameter, number of connections and resistance of wires established between electrodes at different geometric shaped feeder electrodes. Error bars represent standard error mean (SE), further statistical analysis was performed using one-way ANOVA with Tukey's HSD post hoc analysis (n = 9 ; p ≤ 0.0001).

The number and diameter of wires also influence the resistance measured. Higher values 880.7 ± 66.89 kΩ are found on the triangular electrodes, in contrast to 371.7 ± 64.68 kΩ and 366 ± 56.15 kΩ in the square and circular electrodes, respectively (Figure 3-15). The growth and electrical properties of AgMWs can thus be easily modified through changes in the geometry of the feeder electrodes, which can be adjusted depending on the applications pursued.

However, the values of resistance obtained are different from theoretical values calculated using the very well-known formula of electrical resistance (Equation 1-8), assuming a minimum diameter of the cross-section of single wires of 200 nm which provides the maximum value of resistance theoretically expected (5.0525 Ω). 200 nm was selected, as it is the minimum thickness that can be seen in the SEM images (Figure 3-12) and according to the equation, it should give us the maximum value of resistance it should be observed within the system in optimal conditions.

3.2.3. Wireless electrochemical fabrication of functional 3D circuitry

Subsequent experiments were aimed at demonstrating that controlled growth of AgMWs connecting conduits in a functional electronic 3D-circuit could be achieved. The principle of this was to use wireless electrochemistry to control and direct growth of wires from a light emitting diode to the 3D inkjet

printed electronic system, thereby completing the circuit (Figure 3-16). Dimensions and construction details can be found in the experimental details.

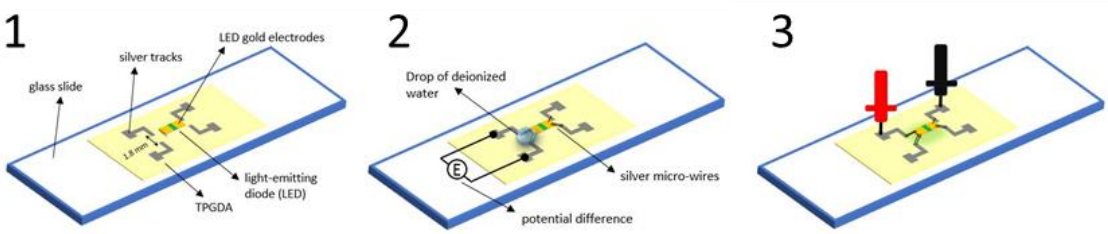

Figure 3-16. Diagram of system to test functionality and three-dimensional growth of silver microwires. 1) Two pairs of silver feeder electrodes are printed on top of a TPGDA layer on glass and a LED is placed upside down between them. 2) A drop of MilliQ water is added covering a pair of feeder electrodes and one gold electrode from the LED and a potential difference is applied. 3) Microwire formation is completed and the systems is tested using a multimeter

Two pairs of square feeder electrodes were inkjet printed (Figure 3-17A). This geometry was chosen due to the low resistance values and improved stability of AgMWs, as compared to wires grown at other feeder electrode geometries due to increased wire thickness (Figure 3-15). A light-emitting diode (LED) was placed upside-down between the two pairs, leaving a gap in the z-plane of 500 µm between the gold electrodes of the LED and the substrate and thus, the silver feeder electrodes (Figure 3-17A).

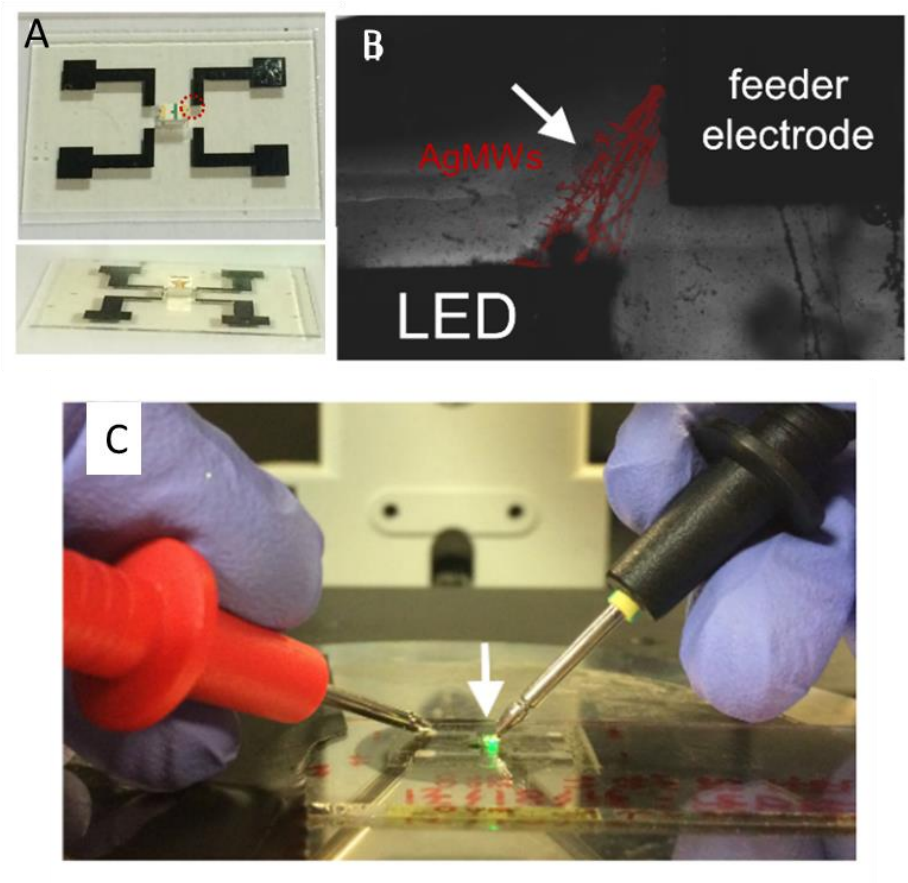

Figure 3-17. (A) Top and frontal view of printed electrodes and placement of a light-emitting diode, (B) optical microscope image of magnified area within the red circle in I showing AgMWs forming a 3D connection with one of the gold electrodes of the LED, AgMWs were coloured in red and pointed with an arrow (scale bar 500 µm); and (C) test of functionality indicating green diode light (arrow).

A potential difference of 150 V was applied in an aqueous environment without any gold or silver cations present in solution prior to applying a potential. Polarisation of the gold electrode occurs when electrodes are in different z-planes when a threshold potential is applied. The gold electrodes are renowned for being inert so no redox associated with gold would, however, at high potentials they can participate in the electron transfer reactions of

other chemical species. The polarisation of the feeder electrodes causes silver redox leading to AgMW formation between feeder electrodes. Wires grew to the surface of the LED. This yielded wires that run from the feeder electrode to the bipolar electrode at an angle of approximately 25^0 relative to the glass surface based on the geometry, configuring three-dimensional interconnects between the elements of the system (Figure 3-17B).

The underlying principle of this lies in the fact that when a conductive material such as the gold electrode of the LED is located between the feeder electrodes, polarisation can lead to formation of new positively and negatively charged centres. In the right conditions, these will also produce reactions of oxidation and reduction and form interconnects by wireless electrodeposition of silver.

The wireless electrochemical augmented growth of 3D orientated wires were shown to act as binding conductive conduits. When the system was tested with a multimeter, the LED illuminated, demonstrating the wire growth completing the circuit (Figure 3-17C). The contact with the probes of the multimeter can be made between silver electrodes at both positive and negative poles of the LED or between one electrode on the surface and opposite gold electrode of the LED. The difference is the number of interconnects through which current circulates.

3.2.4.Fabrication of in situ bioelectronic interfaces

Whilst the ability to couple wireless electrochemistry with inkjet printing to fabricate 3D electronic functional systems has been demonstrated, it was apparent that such an approach could also be important in future bioelectronic applications. Consequently, the ability to use the combined wireless electrochemistry enabled by inkjet printing to form 3D conductive cellular conduits *in situ* without any physical electrical connection was investigated, with the aim to explore the potential to use this to sense cell behaviour.

In order to demonstrate this, Chinese hamster ovary (CHO) cells were cultured and placed between feeder electrodes. When a potential of 90 V was applied, a mesh of conductive conduit-cellular constructs was formed (Figure 3-18). These wires passed around the cells because of the high resistance of the plasma membrane compared to the surrounding media, which resulted in wire growth adapting to the shape of the cells not aligning with the electric field.

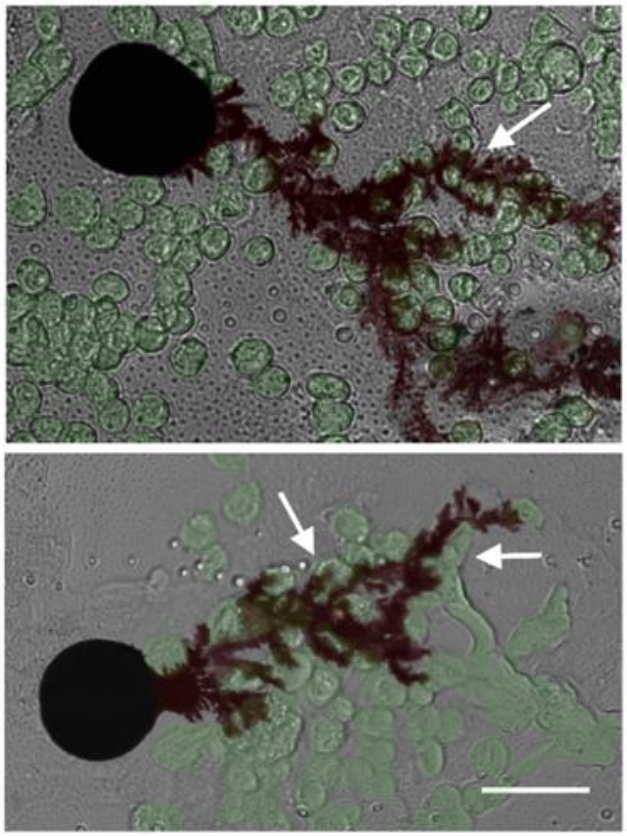

Figure 3-18. Optical microscope image of AgMWs (red) growing between CHO cells (green). AgMWs form a conductive mesh surrounding cells (arrows). Circles of silver with a diameter of 67 ± 6.2 µm were printed between the feeder electrodes to guide silver wires acting as bipolar electrodes (BPEs). Scale bar 50 µm

Circles of silver with dimensions of 67 ± 6.2 µm were printed between the feeder electrodes to act as BPEs and facilitate guidance of AgMW growth, reducing the circuit resistance created by the cells. The wires that are grown in the presence of the cells are formed in an asymmetric way and are not continuous between the feeder electrodes (Figure 3-19). This happens because the diffusion of the cation from the negative electrode comes in to contact with the bipolar electrodes before reaching the positive electrode. The bipolar

electrodes are then sufficiently polarised to provide the thermodynamic driving force to reduce Ag^+ to Ag(s).

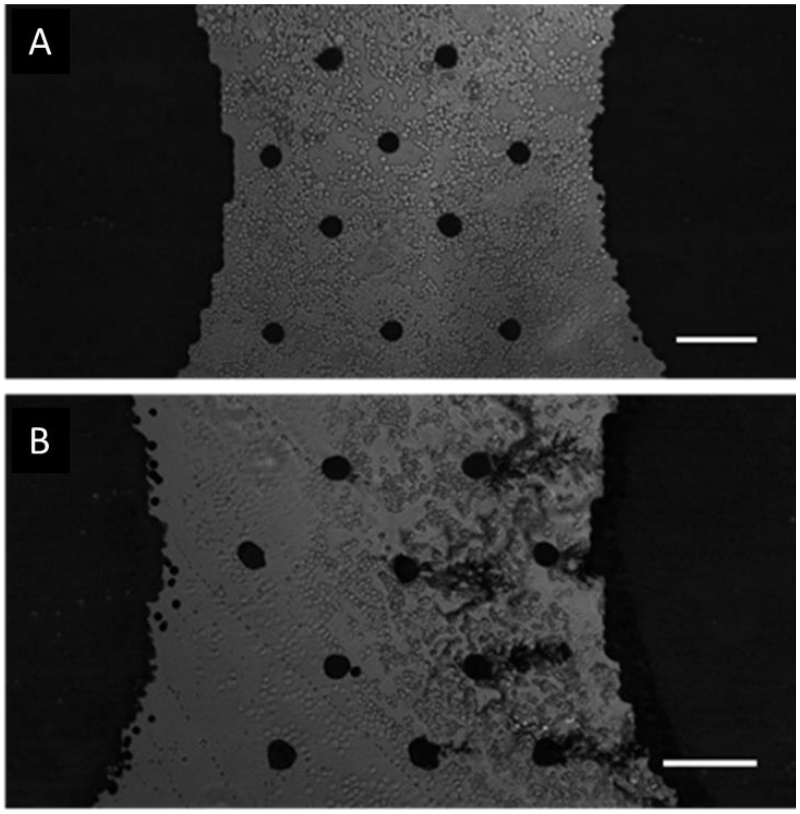

Figure 3-19. Optical microscope images of CHO cells and feeder electrodes (A) before and (B) after AgMW growth. Scale bar 200 µm.

Cyclic voltammetry was performed to elucidate the ability of the wirelessly formed bioelectronic system, via cellular-conduit connects to sense biological redox events electrochemically. Cyclic voltammograms (CVs) were performed with printed electrodes using a starting potential of 0.5 V, a switching potential of -0.2 V and an end potential of 0.5 V at a scan rate of 100 mV s^{-1} with phosphate buffer saline (PBS) as electrolyte.

These CVs were performed prior to and after wireless growth of AgMWs in the absence and presence of cells (Figure 3-20). Redox peaks were observed in the CVs in the presence of the AgMWs and the cells, with a mean potential peak observed at -0.130 ± 0.022 V (± 1 SD n=3) and at 0.279 ± 0.047 V (± 1 SD n=3), for the reduction and oxidation event respectively (Figure 3-20D). I can be concluded that this observed redox behaviour is of biological origin as no resulting redox peaks were observed in CVs without the cells.

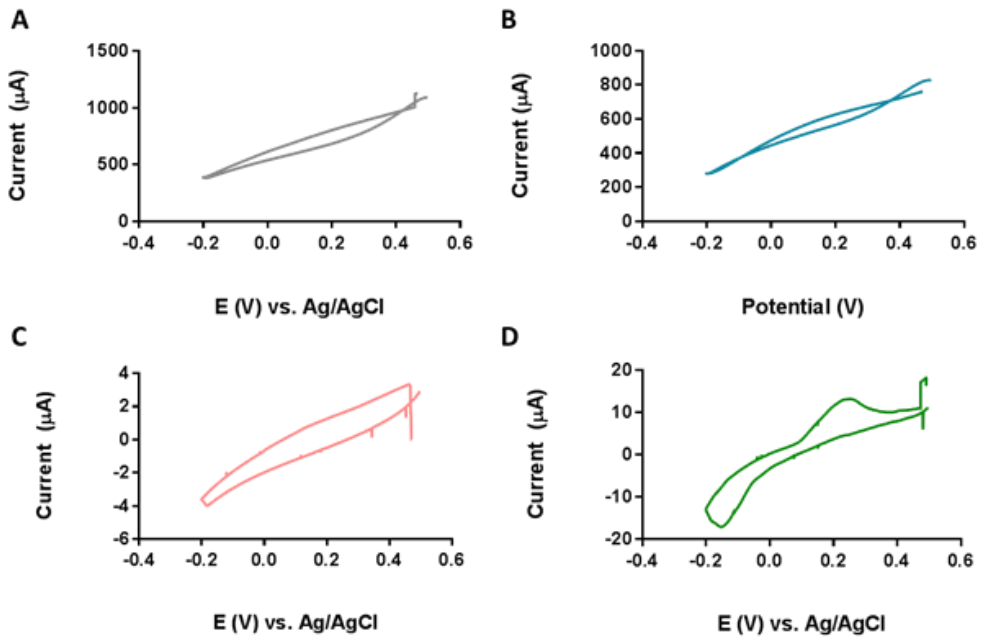

Figure 3-20. Typical cyclic voltammograms (CV) obtained with solutions of phosphate buffered saline (A) prior MW growth without cells, (B) after MW growth and without cells, (C) prior MW growth in the presence cells and (D) after MW growth in the presence of cells. Scan rate 100 mV s-1. Mean values of three different samples were calculated and represented within the CVs.

It is interesting to observe that when the CVs in the absence and in the presence of cells are compared, the magnitude of the current in the presence of the cells is around three orders of magnitude smaller (Figure 3-20C and figure 3-20D). This occurs as the cells increase the circuit resistance and hinder electron transfer.

Redox events occurring due to silver redox as the electrochemical behaviour – if it was silver – could be discounted, as it would be expected to have been observed in wires grown in the absence of cells (Figure 2-30A and figure 2-30B). From this, it can be concluded that the conductive mesh of conduits is capable of sensing electrochemical signals of biological origin. However, it should be noted that the specific biochemistry resulting from this signal is not known. The key aspect to note here is that this demonstrates that *in situ* grown bioelectronic tools can be used to observe cell redox.

As previously explained in 1.1.1. Coupling of biological and electronic systems, cell redox reactions are crucial in biology and they are involved in metabolism and signalling pathways. It is tentatively infered from these results that intermit contact with the AgMWs is facilitating the exchange of electrons between them and the cells which could be used as a communication route via external electrical stimulation or interpretation of cell electrical activity[11]. It can be possible to discard that the redox species associated with the observed signal in CVs were of solution origin. This is because this electrochemical

behaviour would also be seen prior to wire growth in the presence of cells; however, this is not the case.

A Trypan blue viability assay was performed to elucidate the percentage of viable cells prior and after microwire growth. Prior to application of potentials, 98.9% of viable cells were found at all points between feeder electrodes. In order to identify the effect of potential application and discard effects on viability due to material and solvents, this value was assumed as 100% in the next calculations.

After the application of 90 V using direct current, it is possible to observe a pronounced decay on the values of viability in areas next to the negative electrode (Figure 3-21A). Cells are attracted to the negative electrode due to the effects of ionic current and in areas near this electrode, the cell mortality is higher (Figure 3-21B). In areas near the positive electrode the viability is higher (44.9%), however, the cell number is more reduced.

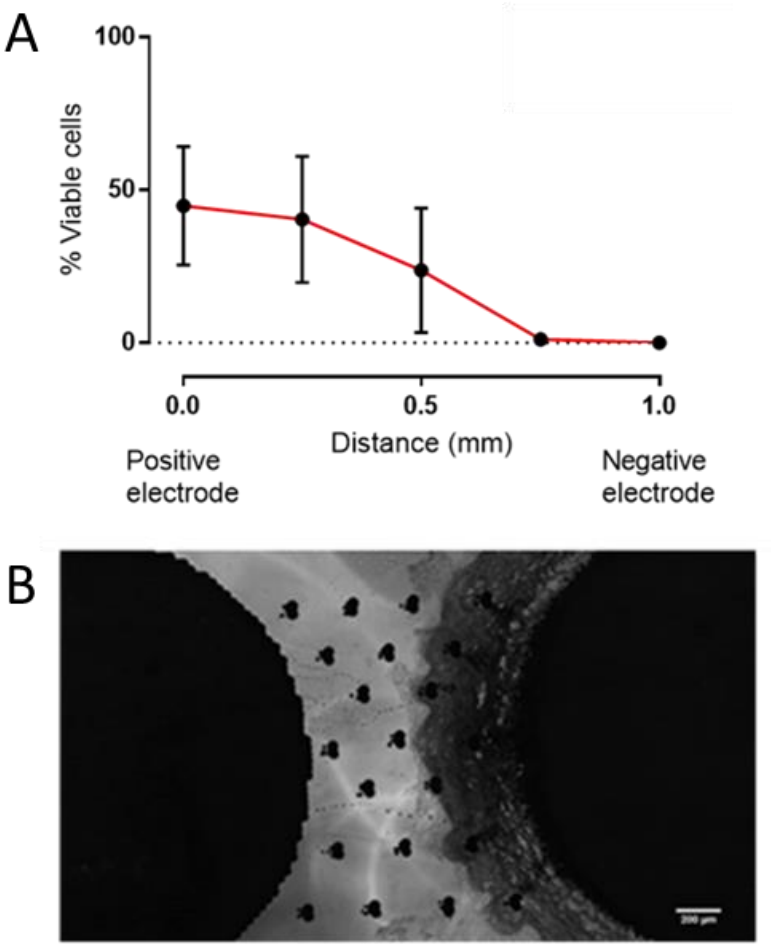

Figure 3-21. (A) Percentage of viable cells after wire growth using direct current relative to percentage of viable cells prior potential application (N=3, n=3 ; SD). (B) Optical microscopy image of CHO cells after Trypan blue viability assay after DC application of 90 V.

3.3. Final considerations

The approach taken here was based on the combination of both inkjet printing and wireless electrochemistry resulted in the production of conductive conduits of silver which could be used to build novel 3D multi-material, multicomponent functional bioelectronic systems remotely.

Wires were formed by clusters of electrodeposited silver nanoparticles and showed the dependence on the electric field applied tuned via feeder electrode geometry. Thus, this technological advancement provides a promising fabrication platform to develop innovative 3D multifunctional multi-material bioelectronic systems with potential applications in biosensing, bioelectronic medicine and fabrication of 3D circuits.

Chapter 4. Wireless bioelectronic nanosystems for intracellular communication

In order for bioelectronics to make an impact on healthcare, there is a requirement for the development of wireless electronic systems to both sense and actuate cell behaviour. In this chapter, an example of an innovative intracellular wireless electronic communication system is reported for the first time. It is demonstrated that chemistry can be electrically modulated in a "wireless" manner on the nanoscale at the surface of conductive nanoparticles uptaken by cells at unreported low potentials. The system is made functional by modifying gold nanoparticles incorporating a Zn-porphyrin, which are taken up by cells and are shown to have a lack of cytotoxicity. It is also demonstrated that the redox state of Zn-porphyrin modified gold nanoparticles is modulated and reported on fluorescently when applying an external electrical potential. This provides an attractive new wireless approach to develop novel bioelectronic devices for modulating and sensing cellular behaviour using intracellular monitoring.

Keywords: Wireless bioelectronics, intracellular communication, nanotechnology, electrochemical sensors

The author would like to acknowledge Maria E Alea-Reyes and Lluisa Perez-Garcia for synthesising the Na-ZnTCPP modified water-soluble gold nanoparticles used in 4.2.4. Characterisation and cell studies of chemically modified water-soluble gold nanoparticles (ws-AuNPs) and 4.2.5 Intracellular wireless bioelectronic actuation.

Sidahmed A Abayzeed, Rafael Fuentes-Dominguez and Matthew Clark are acknowledged for developing the protocol, carry out the experiments and data analysis from 4.2.3 Study of plasmonic effects in u-AuNPs by dark field microscopy.

Dr. Scott Young and Dr. Saul Vazquez-Reina are thanked for their assistance with ICP-MS analysis. Dr. Marion Limo is thanked for help provided for TEM analysis and and Dr. Michael Fey for assistance on SEM analysis. The authors thank the Nanoscale and Microscale Research Centre (nmRC) for providing access to instrumentation.

The content of this chapter has been partially published in Sanjuán-Alberte, P.; Abayzeed, S. A.; Fuentes-Domínguez, R.; Alea-Reyes, M. E.; Clark, M.; Hague, R.; Alexander, M.; Pérez-García, L.; Rawson, F. J., Wireless Bioelectronic Nanosystems for Intracellular Communication. **10.26434/chemrxiv.7106171.v2** 2018.

Chapter 4. Wireless bioelectronic nanosystems for intracellular communication 117

4.1. Introduction 120

4.2. Results and Discussion 125

4.2.1. Inkjet printing of an electrochemical cell 125

4.2.2. Wireless deposition of palladium on unmodified gold nanoparticles (u-AuNPs) 131

4.2.3. Study of plasmonic effects in u-AuNPs by dark field microscopy 140

4.2.4. Characterization and cell studies of chemically modified water-soluble gold nanoparticles (ws-AuNPs).....142

4.2.5. Intracellular wireless bioelectronic actuation.....150

4.3. Final considerations 155

Note for readers: Materials and methods corresponding to this chapter can be found in 2.2. Materials and methods of Chapter 4

4.1. Introduction

The field of bioelectronic medicine offers a new paradigm in therapeutic intervention as it was described in Chapter 1[49, 243]. The limitations were evident as technology is in its infancy and one of the key challenges is to develop new non-invasive methods to both electrically sense and actuate cell behaviour[244].

There are many examples in literature of electrochemical communication with the internal environment of a cell via use of nanowire electrodes[14, 68, 71, 245-246]. However, these methods tend to be invasive in nature as they necessarily have to pierce the plasma membrane which can lead to cell perturbations[247-248]. In addition, these electrodes require physical electrical connectivity from inside of the cells to the outside, thus hindering their use in more complex biological environments.

Therefore, an approach to address these issues is to develop novel wireless electronic systems for the development of intracellular sensors and actuators. The development of novel bioelectronics using such a wireless-electronic approach may subsequently enable significant advancements in the ability to use intracellular electronics to facilitate cell communication and actuation. The aim of this chapter is to develop a new bioelectronic approach for sensing electrical changes in response to the application of an externally applied

voltage inside biological cells, thereby offering the first example of a wireless electronic tool to modulate redox inside of cells[13-14].

This work was inspired by the fields of bipolar electrochemistry and drug delivery. The principle of bipolar electrochemistry was explained in detail in 1.3.2. Bipolar or wireless electrochemistry and relies on placing a conductive particle between feeder electrodes which have potential difference placed across them (Figure 4-1). This causes the conductive particle to polarise which causes a potential difference between the electrolyte and poles of the particle. This potential difference provides the thermodyamic driving force required to modulate redox reactions[230, 249-250]. If we consider the nanoparticles as perfect spheres, it is possible to calculate the potential at a point *x* at their surface from Equation 4-1.

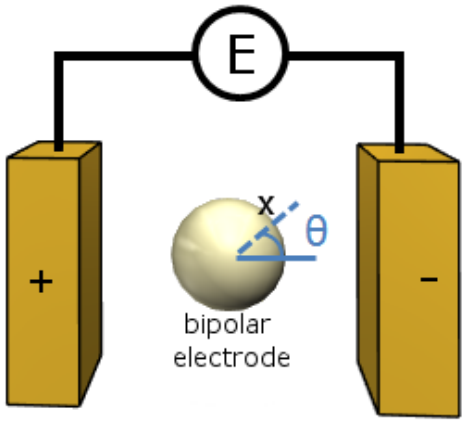

Figure 4-1. Schematic representation of gold nanoparticles used as bipolar electrodes

$$E_x = 2r \cdot E_f \cdot \cos\theta \qquad \textbf{Eq. 4-1}$$

In this equation E_x represents the potential at a given point *x* on the surface of the particles (V), *r* radius of particles, E_f value of electric field and θ angle relative to the direction of the electric field[251]. The potential is constant at all the points that belong to the same virtual plane.

For an electrochemical reaction to happen, a potential at point *x* must overcome a threshold potential that is equal to the difference of the standard potentials of anodic and cathodic reactions. In spherical electrodes there is a vertical plane where polarity is equal to zero. Moving to the poles, a potential gradient is established along their surface, having its maximum value at the poles perpendicular to the vertical middle plane[252]. In this approach however, according to the equation above, the magnitude of the potentials required at nanoscale particles is in the kV range[253] which could limit its use in biology.

Nanoparticles have been used as drug delivery vectors for a number of years. In particular, one of the mechanisms that has been used are conductive gold nanoparticles[254]. These have been shown to be up taken by cells in a non-invasive manner, are biocompatible[255-256] and have been extensively reviewed[257-259].

Their use in drug delivery research is widespread because the surface of gold is readily adaptable to surface chemistry modifications, facilitating functionalisation of the nanoparticle with drugs.

It is hypothesised that by using conductive gold nanoparticles, which could be functionalised with a redox reporter, it could be then possible to polarise these nano-particles, through application of an external electric field, to report on voltage induced changes by wireless modulation of the redox moiety attached to the gold nanoparticles. Thereby demonstrating a new wireless bioelectronic communication nanosystem.

The strategy for developing a wireless bioelectronic tool includes three key steps:

(1) Firstly, to provide evidence that biocompatible lower potentials are capable of inducing wireless redox effects at gold nanoparticles. This is achieved by modulating the electrochemical deposition of palladium in a wireless manner.

(2) Development of a dark field microscopy tool in order to provide direct evidence that gold nanoparticles could be used as electronic sensors at low voltages. This is achieved by imaging the electrical surface charge via plasmonic effects on the gold nanoparticles.

(3) Wireless intracellular redox reactions are induced by modifying gold nanoparticles modified with a fluorescent Zn(II)meso-tetrakis(4-carboxylateyphenyl)porphyrin sodium salt (Na-ZnTCPP). It can be seen that the modified gold nanoparticles could act as electrical reporters, by modulating the redox state of the Na-ZnTCPP, which could be optically followed by fluorescence microscopy.

4.2. Results and Discussion

4.2.1. Inkjet printing of an electrochemical cell

The goal of this work is to develop a new wireless nano-electronic communication system inside of cells however, prior to that, it is necessary to produce the macroelectrodes that will be providing the external electric field needed to induce redox reactions at the nanosystem.

An electrochemical cell was produced by inkjet printing following the procedure presented in 3.2.1. Inkjet printing of silver feeder electrodes. In this case, an alternative to silver is needed due to its electrochemical instability. Therefore, a commercial ink consisting on gold nanoparticles (AuNP ink) with 40% solid content was used and its printing parameters optimised. Droplets of AuNP ink were ejected from the nozzles using the jetting waveform from Figure 4-2.

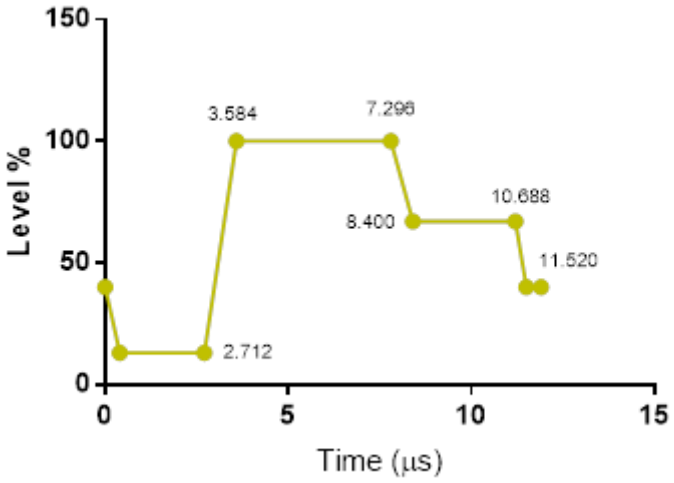

Figure 4-2. Jetting waveform of gold nanoparticle ink (AuNP ink)

This jetting waveform allowed for the ejection of stable 10 µl droplets of AuNP ink from the nozzles of the cartridge (Figure 4-3). The firing voltage was modified between 20-25 V to allow an optimal speed of droplet ejection of 10 m s^{-1} and single nozzles were used.

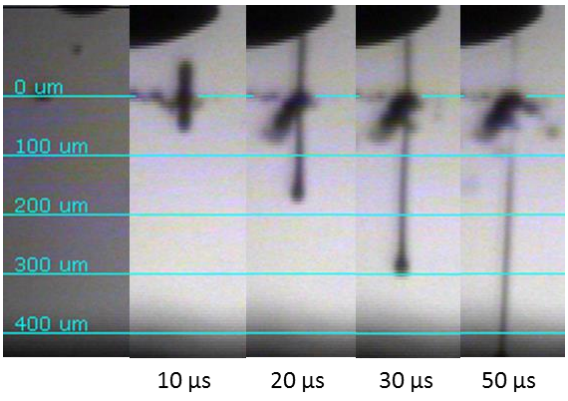

Figure 4-3. Droplets of AuNP ink ejected from a nozzle

Thickness of 5 x 5 mm patterns printed with AuNP ink of single layers was measured by atomic force microscopy (AFM). Bi-dimensional (Figure 4-4A) and three-dimensional (Figure 4-4B) images of the edge of the printed patterns

were obtained and their height profile plotted. The profile was slightly more irregular than the profile of the patterns printed with the AgNP ink (Figure 4-7). This might be due to the higher sintering temperature needed in the case of AuNP ink, leading to incomplete sintering and increased of roughness. Nevertheless, each layer of patterns printed with AuNP ink have an approximate thickness of 300 nm each (Figure 4-4C).

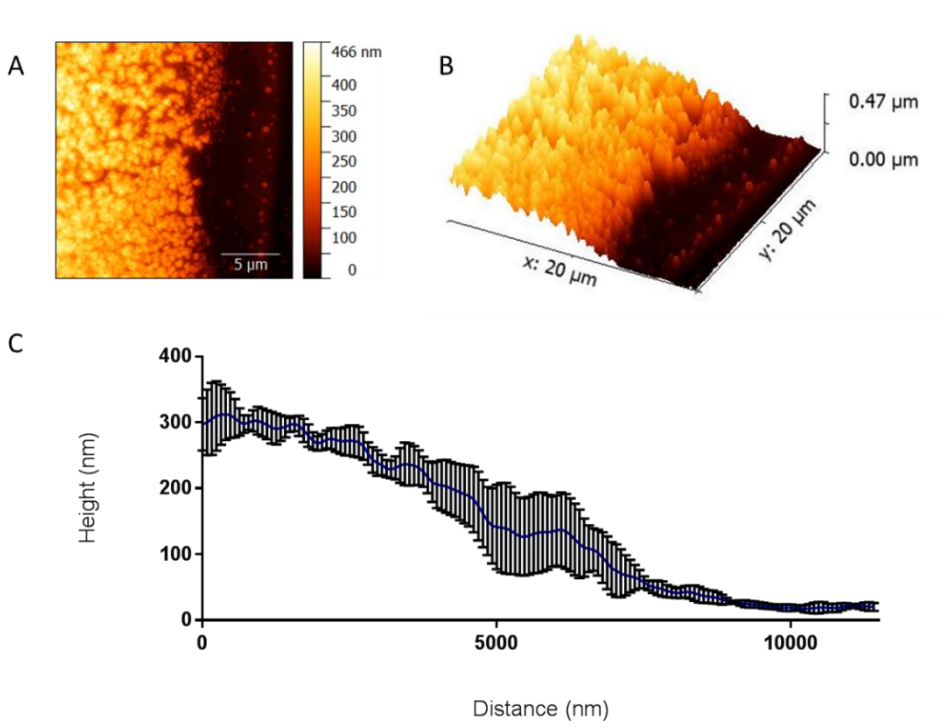

Figure 4-4. Atomic force microscopy (AFM) (A) bi-dimensional and (B) three-dimensional images of and edge of an inkjet printed gold electrode obtained by AFM and (C) its height profile (N=3; n=3)

The optimal sintering temperature of 220ºC suggested by the manufacturer of the AuNP ink was used. In order to guarantee high conductivity of printed patterns, time of duration of sintering process was optimised and resistance of printed 2 x 2 mm areas was measured at different sintering times. Resistance

was transformed to resistivity using thickness values from Figure 4-4C. After 15 minutes applying temperature to printed patterns, a plateau was reached were no decrease in values of resistivity were seen (Figure 4-5A). Therefore, optimal sintering time was established at 15 minutes.

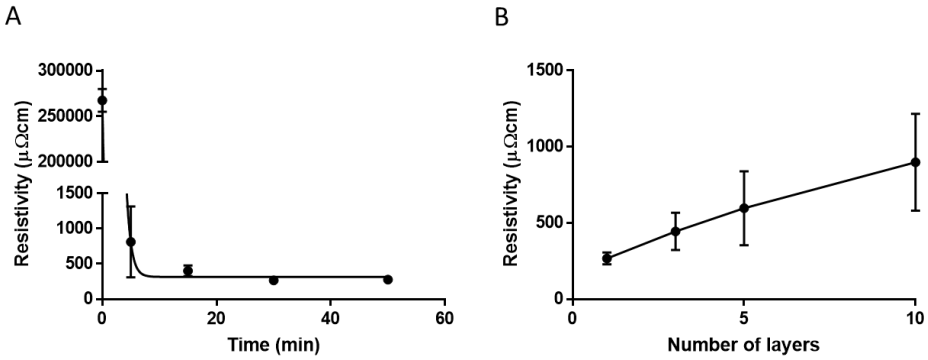

Figure 4-5. Resistance of (A) one layer of silver surfaces sintered at 220°C at different times (B) different layers of silver surfaces sintered at 220°C (n=5, SD)

Resistivity was also measured at for a various numbers of printed layers. While resistance decreases when more layers are printed, resistivity values can slightly increase (Figure 4-5B). This could be due to the higher roughness that is introduced when more layers are printed. This effect could be confirmed by AFM of surfaces prior and after thermal sintering. Less particles are visible after sintering, however, the surface of the samples are still irregular (Figure 4-6).

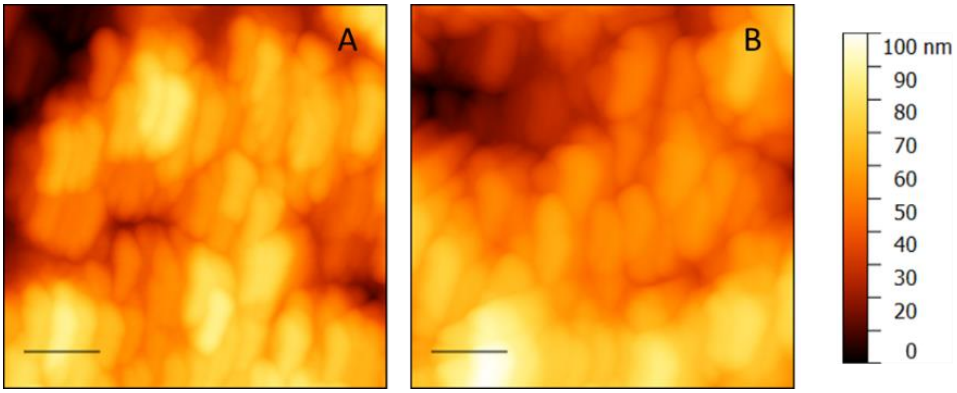

Figure 4-6. AFM images of printed gold electrodes (A) before and (B) after thermal sintering (scale bar 200 nm).

Once the printing parameters were optimised for both the AuNP and AgNP inks (Chapter 3), an electrochemical cell consisting on two gold feeder electrodes with a separation of 210 µm and a silver pseudo-reference electrode was printed (Figure 4-7).

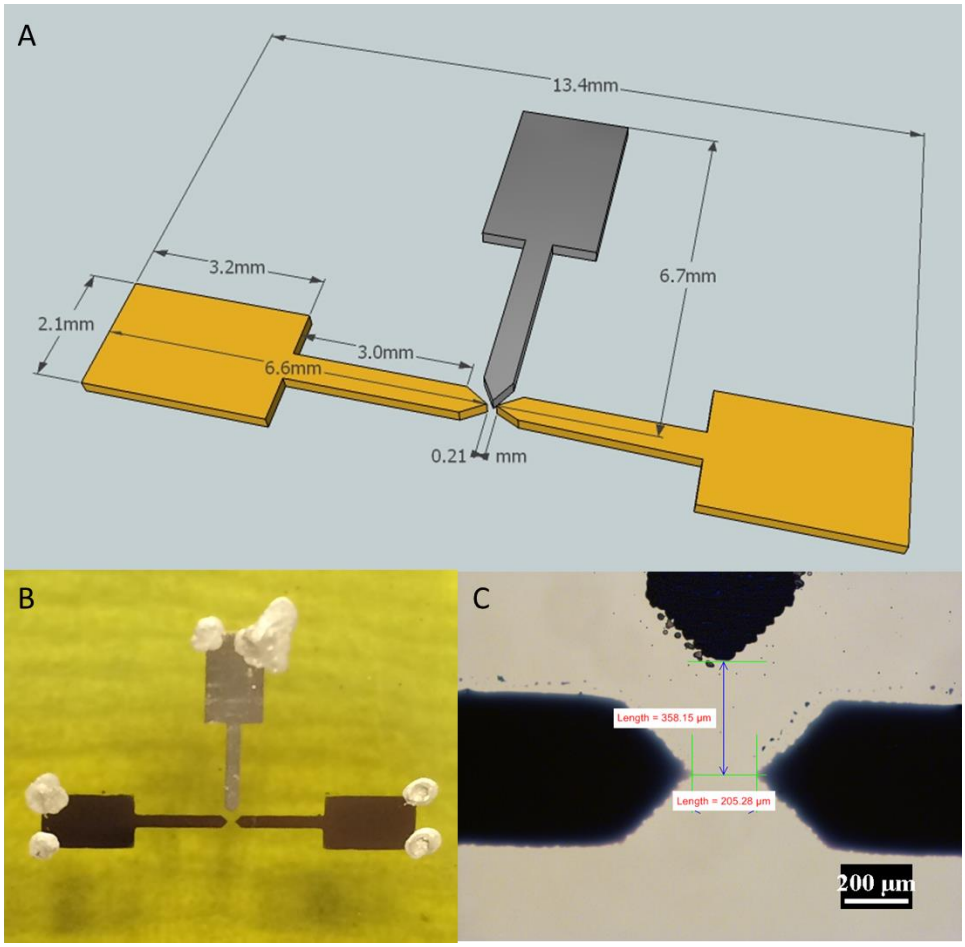

Figure 4-7. (A) Design and dimensions of an electrochemical cell consisting in two gold feeder electrodes and one silver pseudoreference electrode. (B) Image of the inkjet printed system and (C) optical microscopy image of the gap between feeder electrodes.

The functionality of the electrochemical cell and its ability to apply a potential difference was established by elucidating the redox behaviour of one of the most widely used and redox-active molecules, potassium hexacyanoferrate (III). Cyclic voltammetry was performed on a solution of 1 mM potassium hexacyanoferrate (III) in phosphate buffer saline (PBS) at a scan rate of 5 mV s^{-1}. Reduction and oxidation peaks were observed at 0.02 V and

0.19 V, respectively (Figure 4-8). The characteristic peak of gold reduction was also identified at 0.37 V.

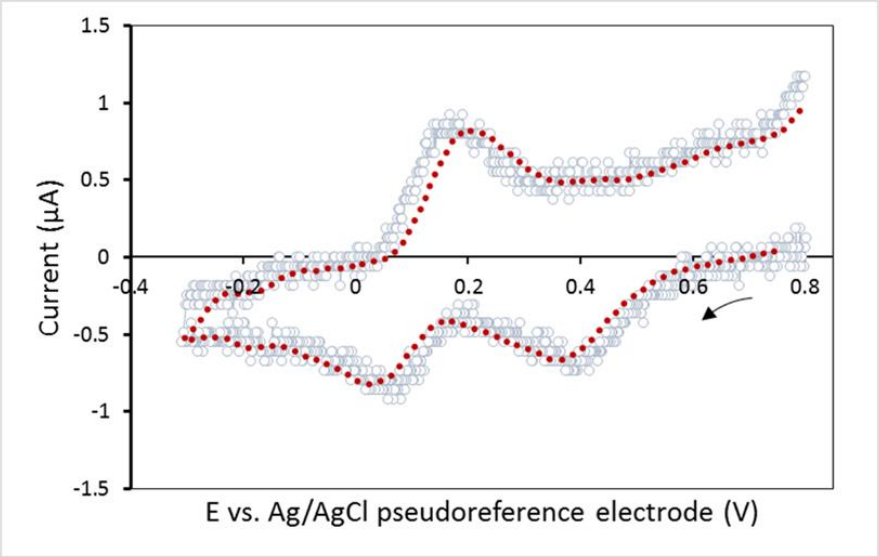

Figure 4-8. Cyclic voltammogram obtained using an inkjet printed electrochemical cell at a scan rate of 100 mV s^{-1} for 1 mM potassium hexacyanoferrate (III) in phosphate buffer saline solution. Blue dots represent the points measured and red line the average values.

An electrochemical cell consisting on two gold feeder electrodes and one pseudoreference silver electrode was fabricated by inkjet printing and it can be concluded that changes in the potential were able to induce electrochemical reactions in a redox active molecule.

4.2.2. Wireless deposition of palladium on unmodified gold nanoparticles (u-AuNPs)

As previously mentioned, this part of the project was in part motivated by bipolar electrochemistry. However, most of the efforts in the field have been directed to induce reactions in macro- and microsized structures[260-261].

According to the theoretical equations presented in 1.4.2 Bipolar or wireless electrochemistry, in order to induce bipolar electrochemistry reactions at nanosized objects, values of E_f in the order of kV would be needed.

Therefore initially, the investigation of the effect of placing 50 nm sized unmodified gold nanoparticles (u-AuNPs) between printed feeder electrodes after application of a potential difference was undertaken. The u-AuNPs were commercially purchased and were stabilised with citrate. These particles were suspended in an aqueous solution in the presence and absence of 1 mM palladium chloride ($PdCl_2$) and a potential difference of 10 V was applied between the feeder electrodes.

It was envisaged that the u-AuNPs would be aligned and polarised under the effect of the electric field, thereby causing a potential difference between the poles. This potential difference could then provide sufficient energy to reduce $Pd^{+2}_{(aq),}$ thus depositing $Pd^{0}_{(s)}$ on the surface of the u-AuNPs as depicted in (Figure 4-9).



Figure 4-9. Schematic representation of the theoretical redox reactions taking place to electrodeposit palladium on gold nanoparticles.

After applying the electrical input of 10 V at the varying times of 0, 1, 5 and 15 minutes, the suspension of u-AuNPs containing $PdCl_2$ was collected and the size of the particles was characterised by Dynamic Light Scattering (DLS).

The u-AuNPs in the suspension that were not exposed to the potential difference of 10 V were estimated to have a size of 50 nm. In the presence of the palladium chloride the size increased to 108.3 ± 1.3 nm. After one minute of applying 10 V there was no difference in the size of the nanoparticles when compared to those which were not exposed to a potential difference of 10 V (Figure 4-10). After exposure to the potential difference for 5 and 15 minutes there was a significant difference in size of the u-AuNPs in the presence and absence of the $PdCl_2$ with an increase in size to approximately 745.5 ± 51.8 nm and 718.0 ± 38.4 nm, respectively.

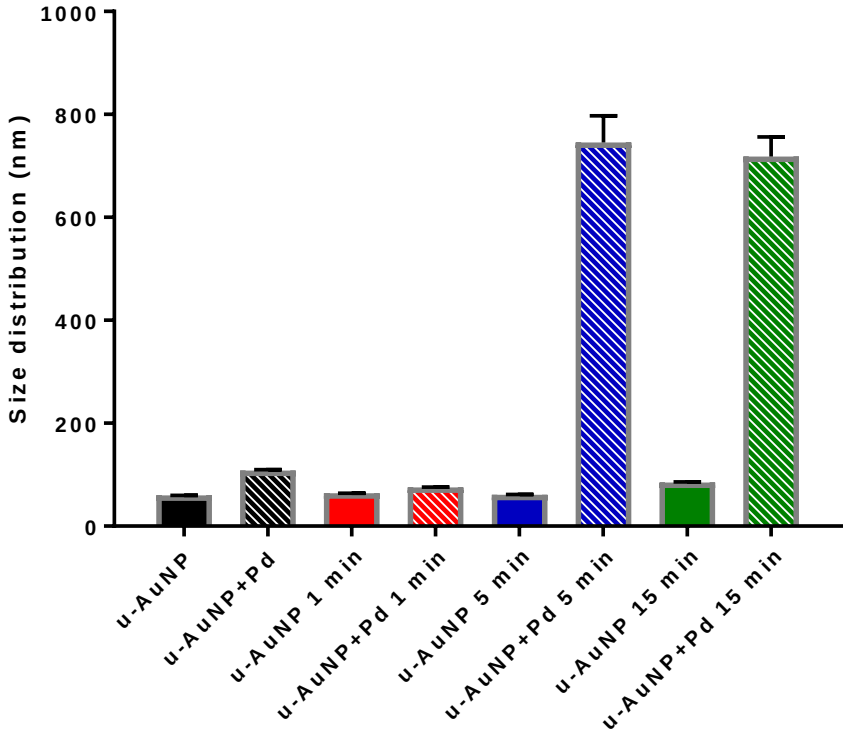

Figure 4-10. Size distribution of unmodified gold nanoparticles (u-AuNPs) with and without palladium when 10 V of direct current (DC) were applied for 1, 5 and 15 min (n=3: SD).

This change in particle size was also reflected in the colour of the collected solutions, going from red to blue (Figure 4-11), which is a well-known phenomenon that, depending on the size of the gold nanoparticle, the SPR peak in absorption spectrum shifts resulting in different coloured solutions depending on the size of the gold particles.

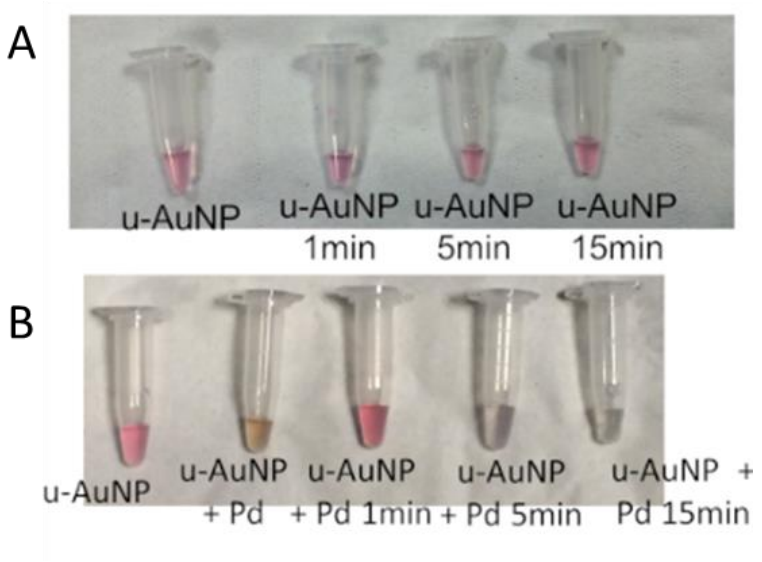

Figure 4-11. Solutions containing (A) gold nanoparticles and (B) gold nanoparticles + palladium after the application of potential for 1, 5 and 15min

It can be speculated that this difference in size occurs because the reduction of the palladium and oxidation of the chloride ions occurs at the surface of u-AuNPs, leading to deposition of $Pd^0_{(s)}$ resulting in larger particles.

The size of particles was further investigated to provide additional evidence of the mechanism resulting in their increase in size. Consequently the different samples were placed into a holey carbon grid and scanning electron microscopy (SEM) investigations were performed, coupled with Energy Dispersive X-ray (EDX) on the $Pd^0_{(s)}$ u-AuNPs. Large micron sized clumps (Figure 4-12) were observed, and elemental mapping with EDX indicated that there was a distribution of Pd and Au suggesting the application of an electric field resulted in the wireless electrodeposition of $Pd^0_{(s)}$ on the gold.

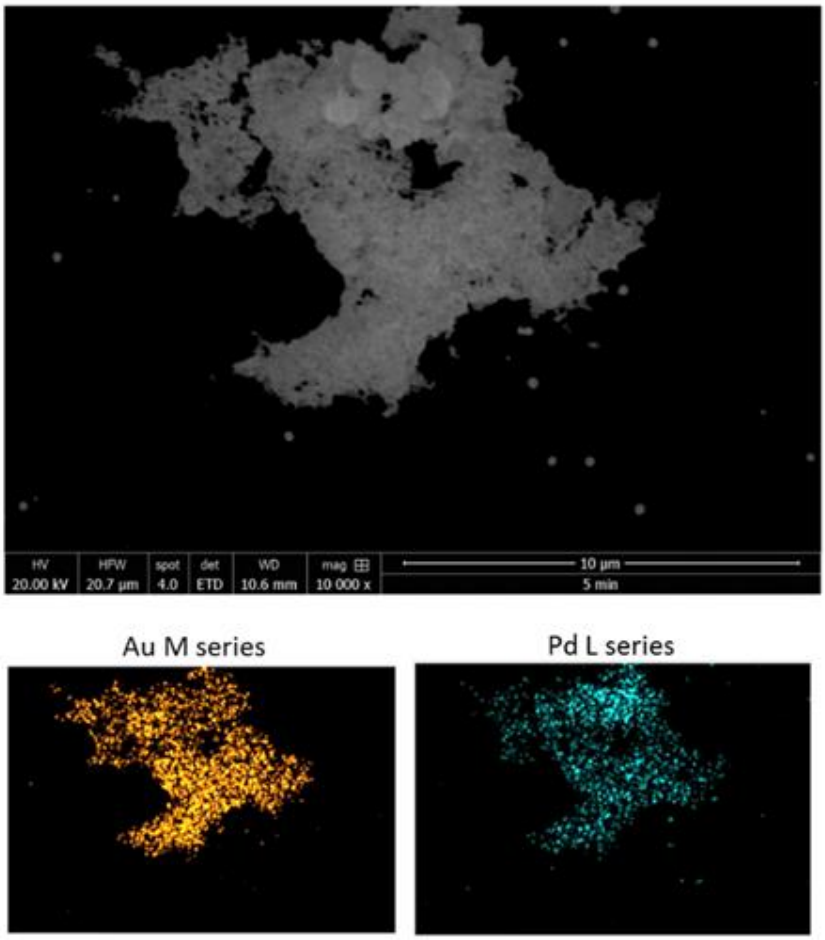

Figure 4-12. SEM images of u-AuNPs+Pd a (top) and EDX images where the Au M series can be seen in orange and the Pd L series in blue (bottom) of AuNP+Pd after the application of 10 V for 5 minutes.

This significant finding demonstrates the feasibility to "wirelessly" mediate redox reactions at the surface of the gold nanoparticles, without the need for any physical wiring to the gold nanoparticles. The discrepancy in particle size between the different techniques may be due to differences in sample preparation. An important aspect to note though is that the increase in size of the gold nanoparticles only occurred when applying an electric field *and* a potential difference between the feeder electrodes, indicating that applying

the potential difference between the feeder electrodes induces the wireless modulation of redox effects at the gold nanoparticle solution interface.

This redox mediated deposition at gold nanoparticles displayed some unique properties since the deposition was occurring at relatively low potentials compared to the other electrical induced redox effect investigated at the nanoscale, which required application of kV[253]. At this stage the reason for this is not clear. However, it is tentatively suggested it could be due to plasmon effects which lower the energetics associated with electronically modulating the redox reactions[262-263].

At the magnitude of the potential applied, water electrolysis would occur at the feeder electrodes and therefore protons would be generated; it was therefore sought to establish the effect of the production of proton on Pd deposition on the Au to ensure the electronic effect was not an indirect one mediated by electrolysis of water. The pH of solutions containing u-AuNPs and $PdCl_2$ was measured at 0, 1, 5 and 15 minutes after applying a potential difference of 10 V between the feeder electrodes.

It was demonstrated that there was a linear correlation between the pH of the solution and the time that potentials were applied (R^2 = 0.995), i.e. with a change in pH from 7.36 ± 0.13 to 5.72 ± 0.87 after 15 minutes of application of 10 V (Figure 4-13).

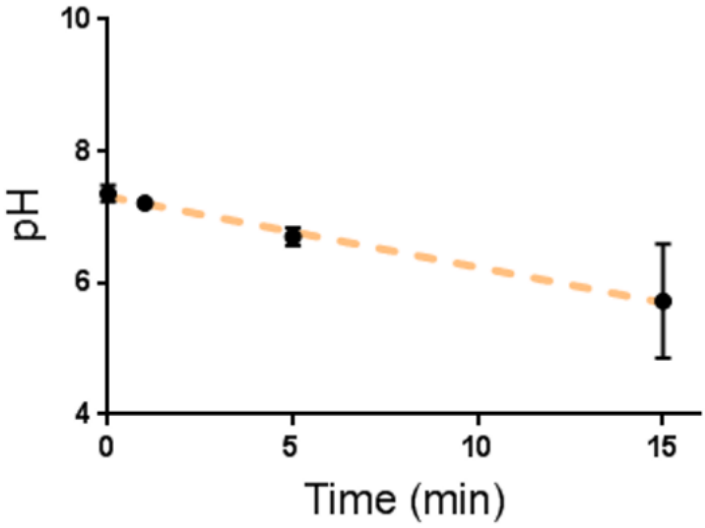

Figure 4-13. Effect of applying 10 V between 0 and 15 minutes to the pH of the solution

This was further investigated to rule out the possibility that aggregation was being mediated by changes in the pH via this proton generation. u-AuNPs were incubated in the presence and absence of 1 mM $PdCl_2$ in buffer solutions at pH 2, 4 and 7 for 1 and 15 minutes. The nanoparticle size was analysed by DLS showing that at pH 7 and 4 there was no change in size for any of the solutions (Figure 4-14). However, at pH 2 there was a significant increase in the size of nanoparticles confirming such acidic pH could induce aggregation of the nanoparticles due to instabilities on the surface produced by protonation of the citrate molecule[264].

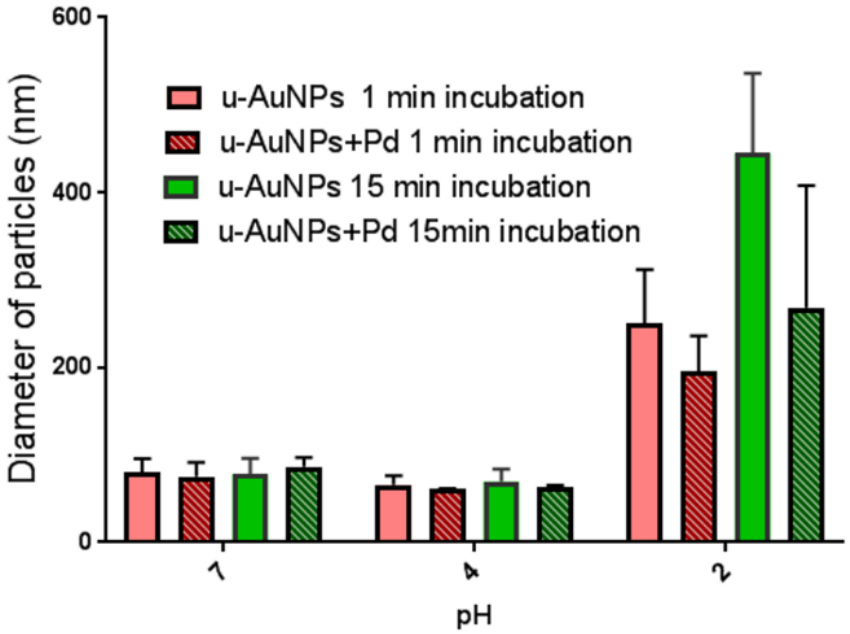

Figure 4-14. DLS study of u-AuNPs in the presence and absence of 1 mM PdCl2 on buffer solutions for 1 and 15 minutes at pH 7, 4 and 2 (n=3 ; SD)

Nevertheless, as the pH recorded with an application of potential for 15 minutes only resulted in a reduction of the pH to 5.72, the premise that protons play any significant part in particle aggregation upon Pd^{2+} reduction and the increases in size of the nanoparticles can be rejected.

Therefore, this provides further evidence that the change in size of the nanoparticle on application of an electrical input occurs due to u-AuNPs being directly affected by the electrical input, resulting in wireless redox induced communication with the nanoparticles via Pd^{2+} reduction.

4.2.3. Study of plasmonic effects in u-AuNPs by dark field microscopy

The observations suggested that it is possible to wirelessly drive redox chemistry via the application of an electrical field at a low potential difference that was orders of magnitude lower to that reported at other nanostructures, such as carbon nanotubes (CNTs)[253]. To further prove this hypothesis that redox reactions could be triggered at relatively low voltage, an alternative label-free approach based on the voltage sensitivity of plasmonic nanostructures[265-270] was explored.

To test the effect of low voltage on u-AuNP, a darkfield microscopy approach to monitor the dynamics of the voltage-modulated intensity of light scattered by the nanoparticles was used. 125 nm u-AuNPs were immobilised on a glass slide coated with Indium-Tin-Oxide (ITO) to be used as a working electrode in a two-electrode electrochemical cell.

A darkfield microscopy image of these gold nanoparticles is presented in Figure 4-15. On application of the electrical potential there is a shift in the plasmon resonance which is proportional to the charge density. To detect the charge density modulation with high spatial resolution, a relatively low alternating voltage (0.8 Vpp, 4 Hz) was applied. The voltage effect was mapped by computing a fast Fourier transform (FFT) of the time-varying intensity at each pixel.

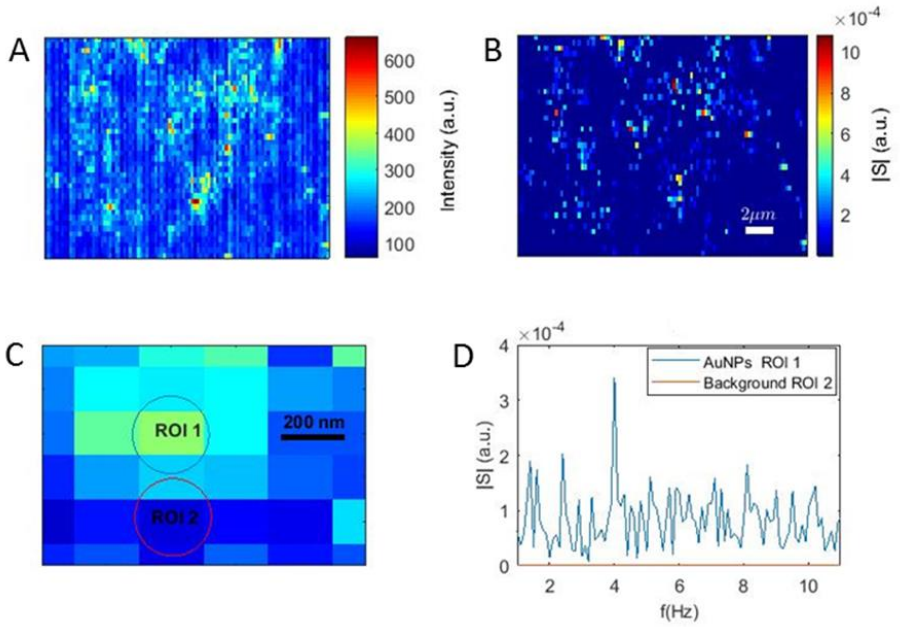

Figure 4-15. Microscopy images of voltage-modulated intensity sensing of by plasmonic nanoparticles. (A) A darkfield microscopy images of Au nanoparticles; (B) a map of the amplitude of the voltage-modulated scattering intensity (|S|) of 125nm Au nanoparticles, presented to support that low-voltage can be detected by Au nanoparticles and therefore can be used as electronic sensorsfor the voltage effect is presented in (B) mapping the amplitude of the voltage-modulated scattering intensity (|S|) of 125nm Au nanoparticles shown in the darkfield image in B. (C) is aA magnified view of the darkfield image where the intensity modulation spectrum (D) is obtained.

By selecting the amplitude of the intensity modulation at the frequency of the applied signal (i.e. 4 Hz), a map of the charge density effect is produced as shown in Figure 4-15B. It is worth commenting that these signals are acquired at a scale of 200 nm (i.e. the pixel size). A signal at the single nanoparticle scale (Figure 4-15C) is shown in Figure 4-15D which confirmed that it is possible to observe intensity modulation at 4 Hz that corresponds to the frequency of the applied voltage signal. Therefore, it is experimentally confirmed that voltage

modulated resonance position is proportional to charge density[267] and this can be used for quantitative imaging of the electric field in a subsequent work.

These results bring out the conclusion that observing localised resonance position modulation on applying a potential difference confirms the accumulation of electrical change around the gold nanoparticle at low potentials. Thus this supports the earlier assertion that u-AuNPs are acting as electrical actuators at relatively low voltages.

4.2.4. Characterization and cell studies of chemically modified water-soluble gold nanoparticles (ws-AuNPs)

To develop the wireless electrical approach further in order to facilitate an intracellular communication system, chemically modified gold nanoparticles were used. This consisted on a gemini pyridinium based amphipile which mediated the incorporation of Na-ZnTCPP onto water-soluble gold nanoparticles (ws-AuNPs)[223] (Figure 4-16) with the electrical input.

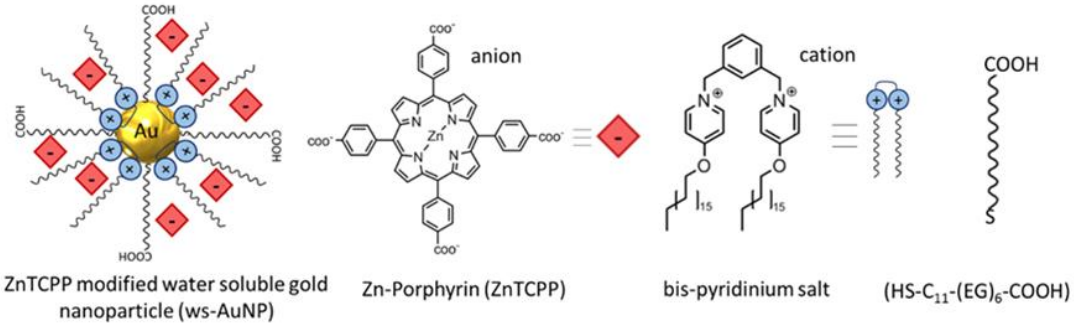

Figure 4-16. Diagrammatic representations of functionalisation strategy for producing a gemini pyridinium based amphiphile incorporating Zn(II)meso-tetrakis(4-carboxylicphenyl)porphyrin sodium salt (Na-ZnTCPP) onto water-soluble gold nanoparticles (ws-AuNPs).

It was predicted that the Na-ZnTCPP would act as a redox reporter by analysing the changes in its fluorescence. The premise for this was built on the fact that the oxidation state of the Na-ZnTCPP affects the fluorescent intensity[271]. It was envisaged that by converting the electrical input into an optical output that it would be possible to electronically communicate with the internal environment of a cell. Others have noted that, on application of voltages at Zn-porphyrin modified electrodes, the redox state of the porphyrin could be modulated[272]; however, this had never been previously achieved in a wireless manner in a cell.

To do this, initially the size of the ws-AuNPs prior and after the incorporation of the Na-ZnTCPP (Figure 4-17A) were characterised with DLS. The mean size of the particle was approximately 40 nm before and 60 nm after adding the Na-ZnTCPP. This was an indication that the Na-ZnTCPP had been incorporated, thereby increasing particle size. This resulted from the

electrostatic interactions between the positive charge of the bis-pyridinium salt conforming the shell of the ws-AuNPs and the negative charge of the Na-ZnTCPP after the modification. Particles were also characterised by Transmitted electron microscopy (TEM) (Figure 4-17B) which resulted in a mean size of 70 nm. Interestingly, a halo can be seen in the TEM images which represent the surface modification of the Na-ZnTCPP modified ws-AuNPs.

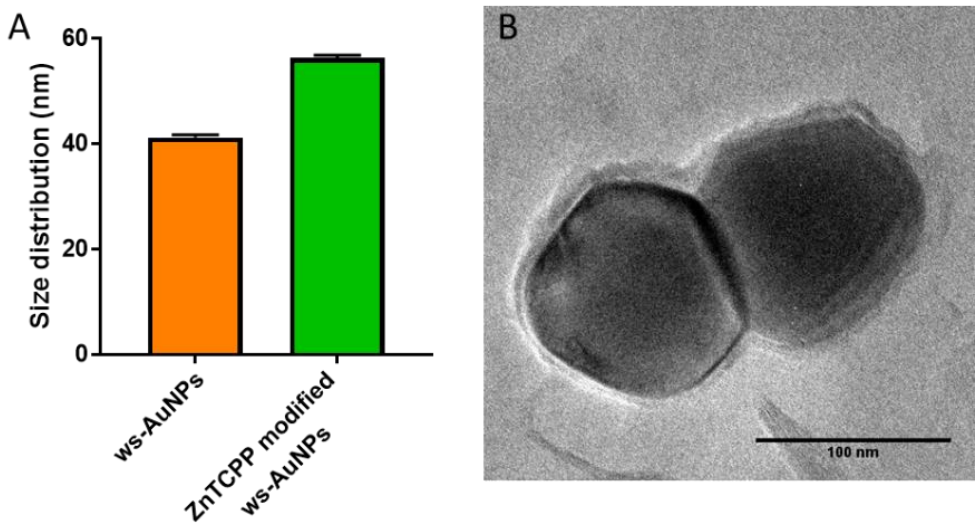

Figure 4-17. (A) DLS results showing size distribution of ws-AuNPs before and after chemical modification with Na-ZnTCPP (n=3 ; SD). (B) Transmitted electron microscopy (TEM) image of a pair of Na-ZnTCPP modified ws-AuNPs. Scale bar 100 µm.

The steady state absorbance and emission spectra obtained for solutions of free Na-ZnTCPP, ws-AuNPs and Na-ZnTCPP modified ws-AuNPs are shown in Figure 4-18. An absorbance spectrum of a solution of 1.17 mM Na-ZnTCPP in PBS showed an intense and defined Soret band at 422 nm and two Q bands characteristic of zinc porphyrins[223, 273] (Figure 4-18A). A less intense Soret band

is also present in the Na-ZnTCPP modified ws-AuNPs. Solutions containing Na-ZnTCPP modified ws-AuNPs present smaller concentrations of porphyrin than those of free ZnTCPP, corresponding to 1.26 µM Na-ZnTCPP and thus there is a reduction in the intensity of the peak at 422 nm.

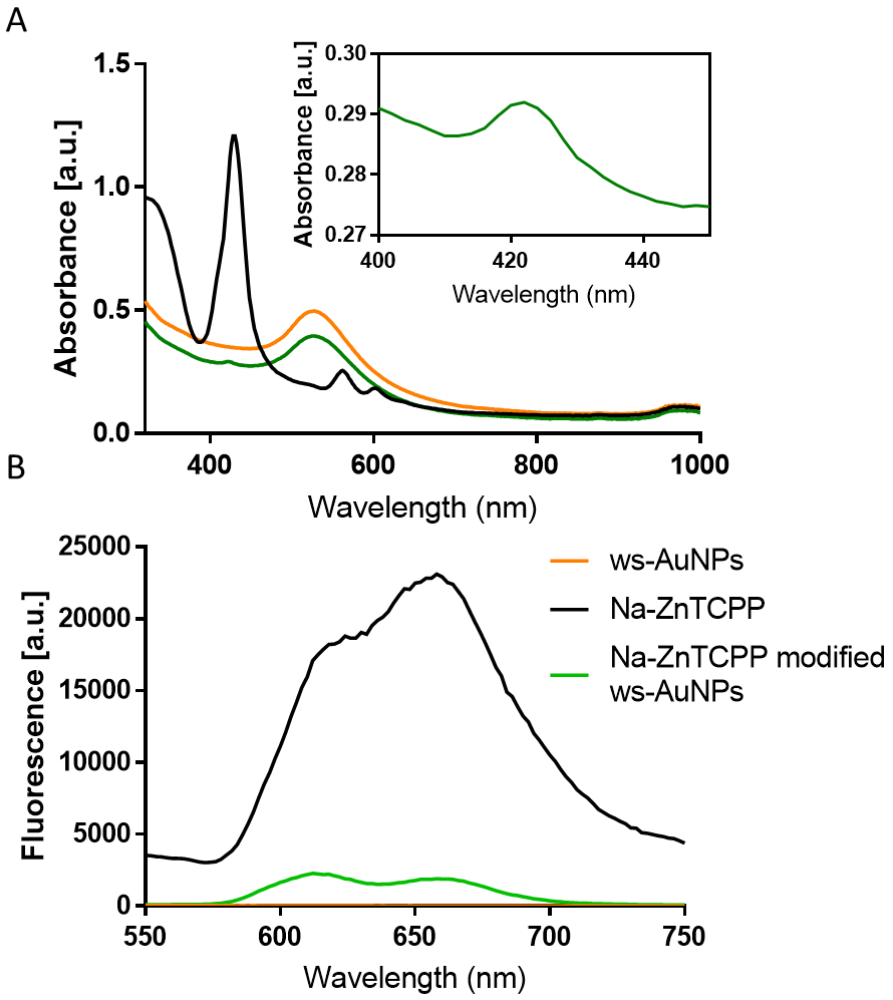

Figure 4-18. (A) UV-VIS absorbance spectrum and (B) emission spectrum of ws-AuNPs (orange), free Na-ZnTCPP (black) and Na-ZnTCPP modified ws-AuNPs (green).

Regarding the emission spectrum, no observable fluorescent signal was obtained for ws-AuNPs over the wavelength range applied between 550 and 750 nm at λ_{exc} of 420 nm (Figure 4-18B). Whereas peaks in the free Na-ZnTCPP

spectrum at approximately 625 nm and 655 nm were observed, respectively. These peaks result from the fluorescence associated with the porphyrin[223, 274], which can also be seen in the emission spectrum of Na-ZnTCPP modified ws-AuNPs as peaks at the equivalent position can be seen.

No observable fluorescence was noted at the ws-AuNPs, but after performing the surface modification procedure it was observed there were peaks at the same position as the free Na-ZnTCPP, suggesting the particles were modified with the Na-ZnTCPP. Moreover, it was noted that the emission peak ratios were inverted when compared to the free molecule, which may be attributed to the differing configurations of the electrons when the molecule is bound to the surface[273]. This data combined confirm that the particles have been successfully modified as indicated.

Prior to performing experiments on wireless intracellular communication, cell uptake was studied. In order to test this, the Na-ZnTCPP modified ws-AuNPs with a model Chinese Hamster Ovary (CHO) cell line (Figure 4-19A) were incubated. Additionally, the time required for the cells to uptake the nanoparticles to maximise the concentration inside the cells was also determined, and therefore increase the signal to noise ratio of the electronic reporter in the next experiments.

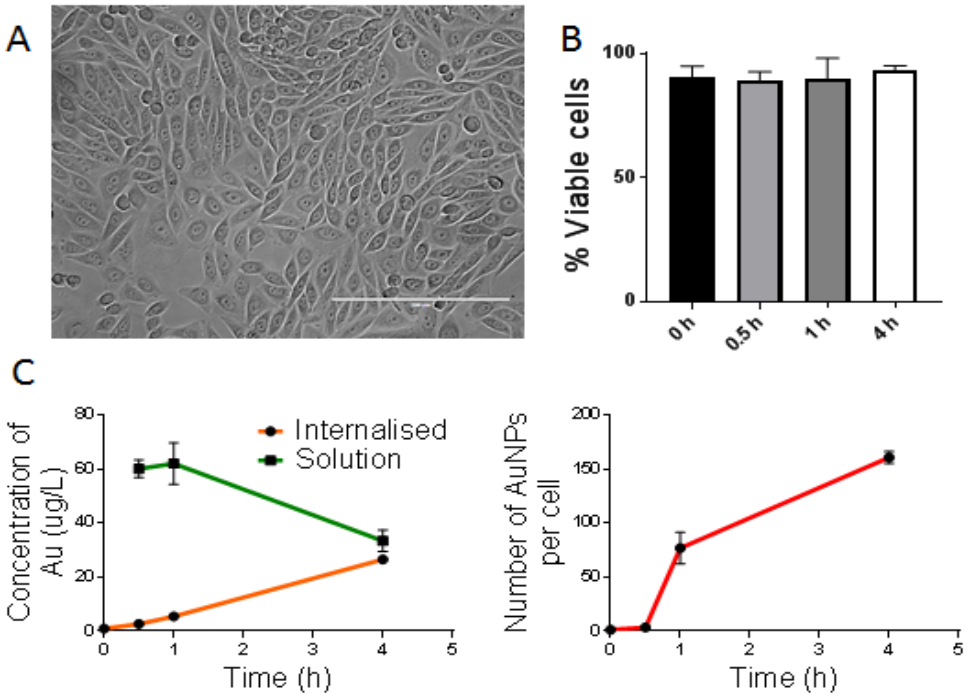

Figure 4-19. (A) Opticam microscopy image of Chinese hamster ovary (CHO) cells. Scale bar 200 µm. (B) Percentage of viable cells calculated using a Trypan blue assay. (C) Inductively coupled plasma mass spectrometry (ICP-MS) analysis of concentration of fold internalised in the cells and in supernatant solution (left) and calculation of gold nanoparticles per cell (right).

Na-ZnTCPP modified ws-AuNPs were incubated with CHO cells at time intervals up to 4 hours and inductively coupled plasma mass spectrometry (ICP-MS) analysis was performed to detect ws-AuNPs. This was performed on samples containing supernatant and samples containing the cell pellet in order to quantify the amount of gold present outside and inside the cells.

Incubation with an initial concentration of 100 µg L^{-1} of Na-ZnTCPP modified ws-AuNPs in Hank's Balanced Salt solution (HBSS) was studied for 4 hours. During this period of time, the percentage of viable cells was monitored by Trypan blue analysis. The results obtained for ICP-MS analysis can be seen in

Figure 4-19C. On incubations with the cells, the concentration of gold in the supernatant was reduced by 27.6 µg L^{-1} over the 4 hours, whilst the concentration of the gold associated with the cell pellet rose to approximately 26.4 µg L^{-1}-.

This provides evidence that the cells were up-taking the Na-ZnTCPP modified ws-AuNPs. Moreover, the number of Na-ZnTCPP modified ws-AuNPs per cell from the ICP-MS data were quantified and it was found that at 30 minutes there were 4, at 1 hours there were 76 and by 4 hours there were approximately 160 nanoparticles per cell (Figure 4-19D). Details of this calculation are given in the point 2.2.6 Cell culture of the methods section.

For following experiments it can be concluded that an incubation of 4 hours was suitable for obtaining a high number of Na-ZnTCPP modified ws-AuNPs per cell, thereby maximising the signal to noise ratio. It was also important to show that over 4 hours that the cells were viable and there was no detrimental loss in membrane integrity, which could have affected the results of the ICP-MS due to gold nanoparticles leaking from the cells in to the supernatant. Consequently, a dye membrane exclusions study in which Trypan blue was incubated with cell exposed to the Na-ZnTCPP modified ws-AuNPs nanoparticles was performed for up to 4 hours (Figure 4-19B). No difference in membrane viability, and therefore cell death, was observed over the 4 hours suggesting the nanoparticles caused no membrane degradation.

The Trypan blue exclusion study determined that over 4 hours the nanoparticles caused no cell death; however, the practicality of using such a system long term meant that from this data it is not possible to infer if they were biocompatible on longer time scales. Additionally, the Trypan blue cell viability assay does not report on sub-lethal toxic effects. As a result, it was important to assess the effect that the modified gold nanoparticles had on the cells for longer periods and to use an assay that could report sub-lethal effects such as a metabolic reporter assay.

Subsequently the well-known WST-8 metabolic reporter assay[274] was chosen. If cellular metabolism was being perturbed by the nanoparticles, it would be expected to see a drop in the percentage of viable cells as indicated by the positive control, TritonX-100, which is a widely used toxicant and completely stops metabolism (Figure 4-20). At all the doses investigated, there was no decrease in the absorbance relative to the negative control (culture media only and cells). This indicated that the Na-ZnTCPP modified ws-AuNPs were not inducing detrimental metabolic effects on a longer time scale.

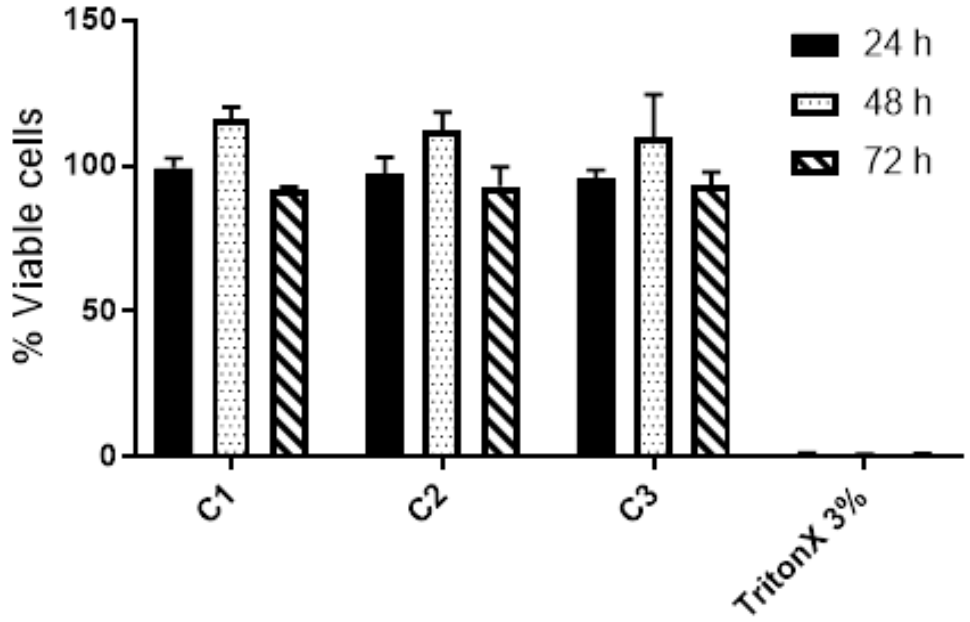

Figure 4-20. WST-8 metabolic activity assay of CHO cells incubated with Na-ZnTCPP modified ws-AuNP at different concentrations of Na-ZnTCPP (C1: 11.8 µM, C2: 2.36 µM and C3: 1.18 µM) for 24, 48, 72 h. Cells incubated in complete media were used as negative control and cells incubated in TritonX 3% were used as positive control. Negative control was assumed as 100% viability and rest of values were presented relative to this (n=3; SD).

4.2.5. Intracellular wireless bioelectronic actuation

The hypothesis that electrically-mediated communication with the inside of the cells was then tested. It was expected that the redox state of the Na-ZnTCPP could be modulated via external application of potentials, hence shifting the energy levels of the molecule and ultimately reducing the magnitude of the fluorescence. This relationship between the redox state of Zn porphyrins and their emission fluorescence has been previously studied, and due to the electrochemical reversibility of Zn porphyrins, it should be possible

to switch the fluorescence on and off by controlling the excited-state electron transfer[275-276].

Na-ZnTCPP modified ws-AuNPs (Figure 4-21A) were incubated with CHO cells for 4 hours to ensure optimal uptake which made them inherently fluorescent, and a sample of cell suspension was placed on the printed electrochemical cell. Due to the electrical properties of cell membranes, acting as resistors and capacitors[277], higher potentials were applied.

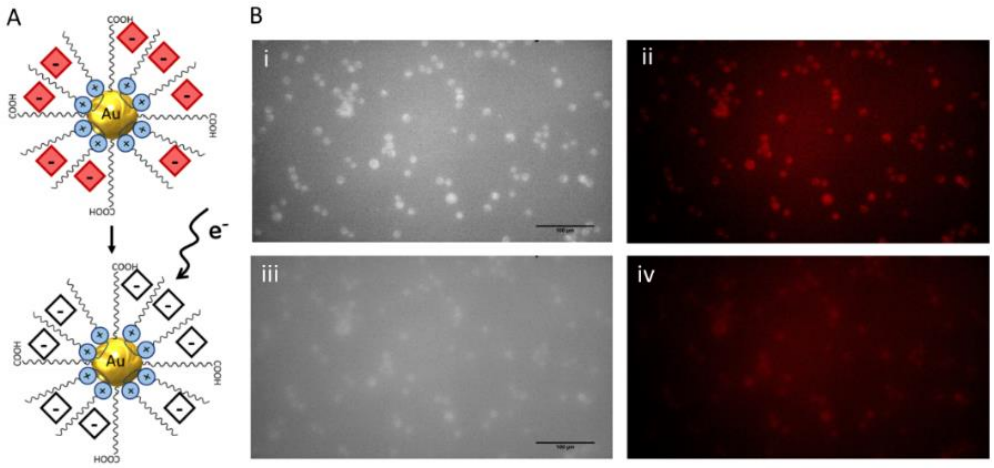

Figure 4-21. A) Diagram showing the result of the application of potentials. B) Fluorescence microscope images of CHO cells containing Na-ZnTCPP modified ws-AuNPs (i) before application of potentials and (ii) its correspondent coloured image and (iii) after applying the potential and (iv) coloured image. Scale bar 100 µm.

A potential difference of 150 V was applied between the feeder electrodes while the fluorescence exposed to a 550 nm laser excitation source was simultaneously monitored and collected. After the application of the potential

difference, it was observed that there was a reduction in the fluorescence inside the cells (Figure 4-21B).

This was confirmed by quantitative measurement of fluorescence intensity of the cells before and after the application of potential. Corrected total cell fluorescence in the area of the cells, calculated by applying the formula below (Equation 4-2)[278], determined a significant ($P<0.05$) reduction in the fluorescence (Figure 4-22).

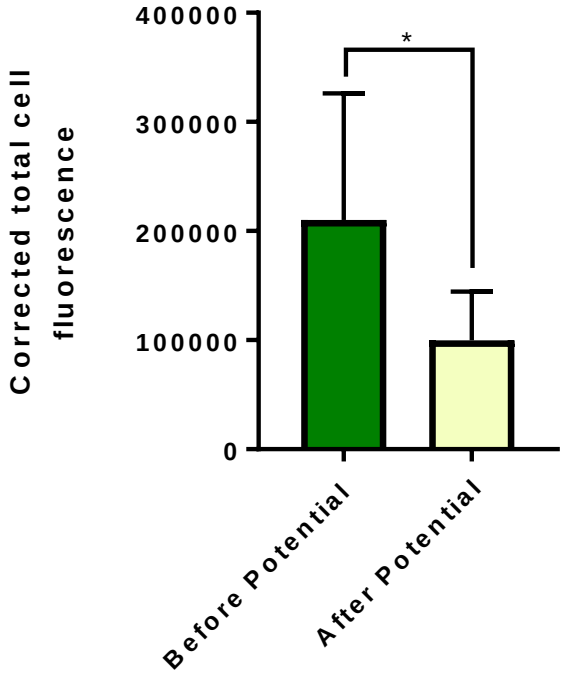

Figure 4-22. C) Corrected total cell fluorescence quantified in the area of the cells before and after applying the potential. Statistical significance was calculated using an unpaired two-tailed test (n=10; SD; *p=0.0117).

$$Corrected\ total\ cell\ fluorescence\ (CTCF) = Integrated\ density - (Area\ of\ selected\ cell\ X\ Mean\ fluorescence\ of\ background\ readings) \quad \textbf{Eq. 4-2}$$

This occurs as the Zn is oxidised, causing a reduction in the fluorescence that was not observed in the controls when incubating the CHO cells with ws-AuNPs, as they do not have the porphyrin (Figure 4-23). In this case there was no fluorescence at all. It is also worth noting that on the application of the potential the background noise increases, which is an artefact of the electrochemistry and therefore results in a lower signal noise. Nevertheless a significant difference was still observable and therefore the results are still valid.

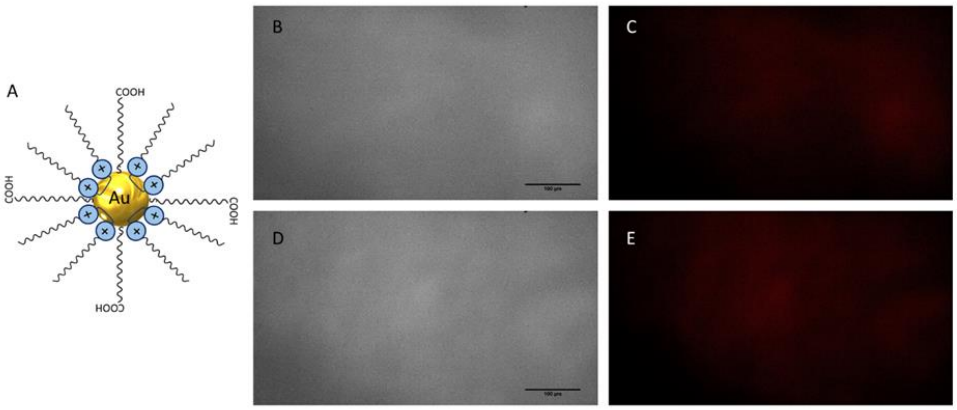

Figure 4-23. A) Diagram showing the ws-AuNPs incubated with CHO cells used as negative controls. Fluorescence microscope images of CHO cells containing ws-AuNPs (B) before application of potentials and (C) coloured image, and (D) after applying the potential and (E) coloured image.

This result indicates that changes in fluorescence are mediated by wireless induced intracellular cell redox changes, as they only occur after the application of external potentials. It is important to note that the integrity of the cell membrane seems to be intact, as cells conserve their round shape after potential application (Figure 4-21B). Thus, this represents a new wireless

electronic system then can intracellularly communicate with the internal environment of the cells.

4.3. Final considerations

It has been shown in this chapter that inkjet printing of AuNP ink and AgNP ink can manufacture functional electrochemical cells with capabilities in detection of redox active molecules. This printed electrochemical cell was used to wirelessly modify gold nanoparticle surface chemistry by electrical input at relatively low applied electrical potentials.

This dependence of low potentials was then confirmed by dark field microscopy, suggesting that plasmonic effects can reduce energy barriers and induce electrochemical reactions at lower potentials than the ones that should be expected from the bipolar electrochemistry theory.

Gold naonparticles were then designed to be water soluble with a gemini pyridinium-based amphiphile incorporating a fluorescence Zn(II)meso-tetrakis(4-carboxylatephenyl)porphyrin sodium salt (Na-ZnTCPP). These were shown to be biocompatible and could penetrate the membrane of cells.

Once the nanoparticles were incubated inside of the cells, an external electrical stimulus was applied and the nanosensors that could convert the electrical input into chemical to a fluorescence output. Despite the mechanism by which this is produced is not fully understood yet, it is hypothesised that could be mediated by electrochemical reduction of Zn molecule.

This demonstrates the establishment of a generic wireless method to communicate electronically with the inside of cells. This will have important implications for future non-invasive sensing and actuating platform that may be used to advance the field of bioelectronics and biosensing.

Chapter 5. Two-photon polymerisation of conductive scaffolds to improve maturity of *in vitro* cardiomyocytes

Cardiac tissue is unable to recover after damage due to the minimal regeneration capacity of cardiomyotes. Depending on the damaged area, the consequences could lead to catastrophic heart failure where the only current solution is heart transplantation. Cardiomyocytes cultured *in vitro* from stem cells have the potential to be used in regenerative medicine and other areas such as toxicology and physiology. However, our ability to replicate the *in vivo* conditions needed for the cardiomyocytes to achieve the typical mature state that they have in the ventricles, is very limited.

A combination of mechanical cues, such as material chemistry and topography, and electrical cues are studied herein. After development of materials, these were processed by two-photon polymerisation (2PP) in order to manufacture three-dimensional structures in a first example of its use with human cardiomyocytes derived from stem cells.

Cells were cultured on 2PP structures showing a better alignment and aspect ratio than those on control surfaces. This is also translated into a better maturation state indicated by the length of the sarcomeric units of the cells. This effect can be enhanced by the application of electrical stimulation to the cells where values of sarcomere length were similar to physiological values, which could have potential applications in bioelectronic medicine.

Keywords: regenerative medicine, cardiomyocytes, stem cells, conductive microstructures, nano-topographies, additive manufacturing

Jayasheelan Vaithilingam is deeply acknowledged for his contributions by developing and characterising the materials and printing the structures used in this chapter

Simona Campora is acknowledged for the development of the initial immunostaining protocols described in section 2.3.2. Immunostaining of hiPSC-CM

Chapter 5. Two-photon polymerisation of conductive scaffolds to improve maturity of *in vitro* cardiomyocytes

..... 157

5.1. Introduction 160

5.2. Results and discussion 164

5.2.1. Human induced pluripotent stem cell (hiPSC) differentiation 164

5.2.2. Viability studies on structures fabricated by two-photon polymerisation (2PP).....169

5.2.3. Preliminary maturation studies on 2D and 2.5D structures 175

5.2.4. Electrical stimulation of hiPSC-CM.....186

5.2.5. Maturation studies of hiPSC-CM on complex architectures 192

5.3. Final considerations 198

Note for readers: Materials and methods corresponding to this chapter can be found in 2.3. Materials and methods of Chapter 5

5.1. Introduction

The regeneration capacity of the cardiac tissue after an infarction or damage is rather limited, as human cardiomyocytes are post-mitotic cells and unable to regenerate[279]. Damaged areas of the heart end up being replaced by fibroblasts leading to a loss in organ function which can ultimately lead to catastrophic heart failure[280]. Currently, heart transplantation is the only solution available to this irreversible situation, extremely limited by availability of donors and the complexity of surgical processes[281].

A potential alternative source of *de novo* cardiomyocytes could result from the *in vitro* development of human induced pluripotent stem cell-derived cardiomyocytes (hiPSC-CM) with native-like properties. *In vitro* platforms of hiPSC-CMs could be used as disease models to study myocardial physiology or as a drug screening system[281-282], and to engineer cardiac patches for regenerative medicine purposes[283].

A main limitation to this is that hiPSC-CM grown *in vitro* express typical foetal cardiac genes and are at an immature state compared with adult cardiomyocytes. This is translated into immature electrophysiological properties; use of alternative sources of energy, glucose instead of fatty acids;

and several morphological differences such as a smaller size and disarrayed sarcomeres[284] (Figure 5-1).

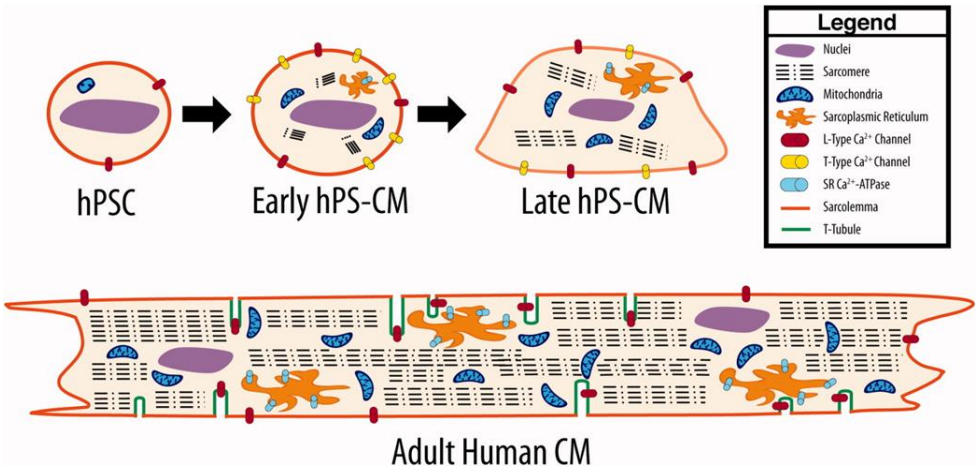

Figure 5-1. Diagram showing the morphological differences and the different compontents that can be found in early, late and adult human pluripotent stem cell-derived cardiomyocytes. Reproduced with permission from [285].

Some external cues can be applied in order to mimic *in vivo* conditions and developmental gestation. This includes the modification of substrate stiffness and chemistry, surface patterning and electrical and mechanical stimulation[286-288]. Also, the role of cell-substrate interactions that can trigger cardiomyocyte maturation is still unkown[289]. External cues that can be used to develop hiPSC-CM to an adult state are summarised in Figure 5-2.

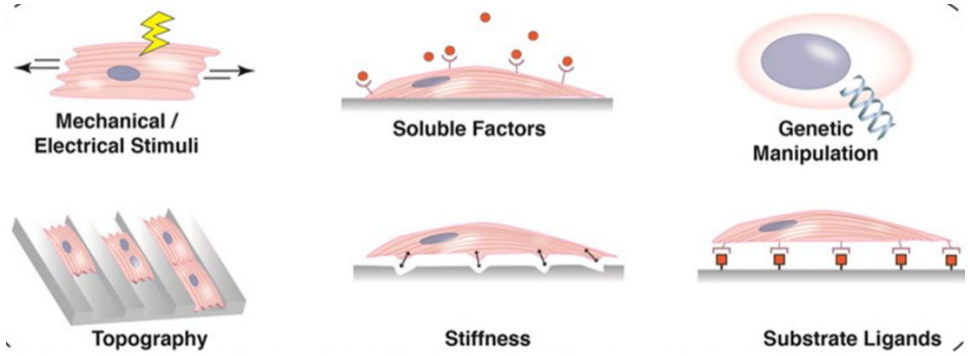

Figure 5-2. Schematic of *in vitro* strategies used to improve the developmental state of hiPSC-CM. Adapted with permission from [288].

Current techniques of microfabrication such as two-photon polymerisation (2PP) could aid the development of cardiac scaffolds, achieving high degrees of control of micro- and nano-architectures up to 100 nm during the manufacturing process[290]. Nano-architectures could be used to control and affect cell morphology and create biomimetic environments in high detail. The fundamentals of this technique can be found in 1.3.3. Two-photon polymerisation of conductive microstructures. Biomimetic structures have the ability to control phenotypes and cell functions[166]. Scaffolds manufactured by 2PP have been successfully developed to induce osteogenic maturation of human mesenchymal stem cells[167] and produce human induced pluripotent stem cell-derived retinal cell grafts[168]. Despite the use of this technique on different cell types, there are no known reports of 2PP structures used in the development of hiPSC-CM.

In this chapter, studies were performed to establish whether the influence of factors such as material chemistry, nano- and micro-topographies given by 2PP, and external electrical stimulation can trigger a further maturation state in hiPSC-CM.

These bioelectronic platforms combining mechanical and electrical stimulation could have the potential to be used in bioelectronics medicine to engineer cardiac patches for the treatment of cardiac failure or develop *in vitro* sensors of cardiotoxicity associated to drugs, reducing the dependence on animal tests.

5.2. Results and discussion

5.2.1. Human induced pluripotent stem cell (hiPSC) differentiation

Cardiomyocytes were differentiated from human induced pluripotent stem cells (hiPSC) following previously developed methods[224]. HiPSCs were passaged every three days and differentiation was initiated on Day 2 of this cycle by preconditioning the culture media with a bone morphogentic protein 4 (BMP4), which belongs to the transforming growth factor-beta (TGF-beta) ddsuperfamily[291]. After 12-16 hours, the culture presented a cheese-like structure (Figure 5-3), initiating the cycle of differentiation.

Further differentiation stages were carried out by changing the composition of the culture media (basal E8 medium, to Stem-Pro 34 to RPMI/B27) and more importantly, by adding different growth factors. On the initial stages of the differentiation process (from Day 0 to Day 2), culture media was supplemented with BMP4 and Activin A. These two molecules belong to the TGF-beta superfamily and are responsible for the regulation of the differentiation. This step was followed by the addition to the culture media of KY02111 and XAV939. KY02111 promotes cardiac differentiation[292], whereas XAV939 induces the cardiomyogenic development[293]. On Day 8, hiPSC-derived cardiomyocytes (hiPSC-CM) started to spontaneously beat and the differentiation process was completed. From this point, culture media was

routinely changed every two days and hiPSC-CM were dissociated after 6-8 weeks and re-seeded to perform subsequent experiments.

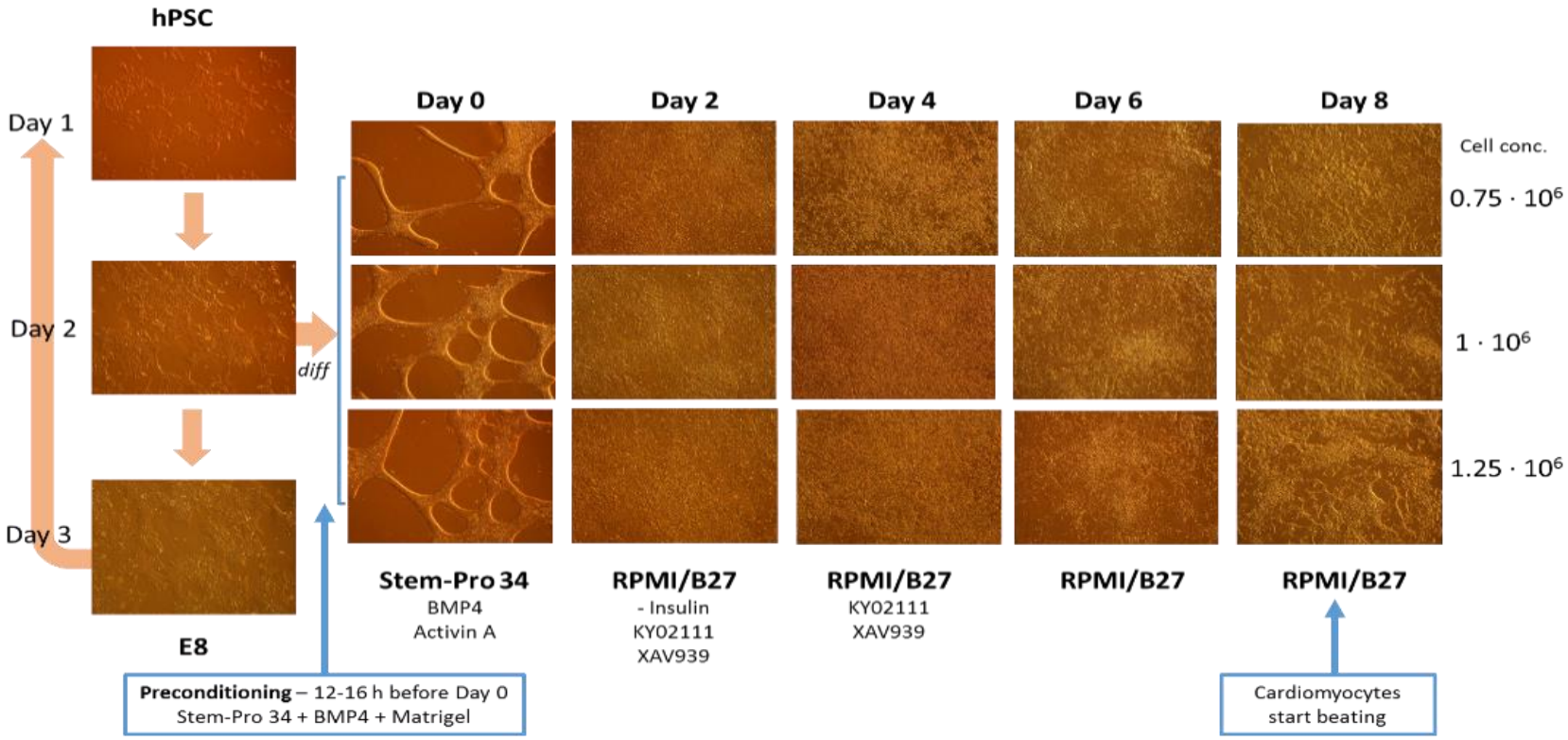

Figure 5-3. Images obtained by optical microscopy showing the differentiation process from human induced pluripotent stem cells (hiPSC) to immature cardiomyocytes induced by growth factors at different cell concentrations. Differentiation process is carried out at day 2 in the cycle of hiPSCs, followed by a preconditioning step. hiPSC-cardiomyocytes (hiPSC-CM) start to spontaneously beat on day 8 of differentiation process.

The success of the differentiation process depends in some measure on the initial cell densities used. An optimal seeding concentration varies depending on the seeding area, corresponding to 40.000 cells cm^{-2} or 1 million cells per Corning T25 flask.

In order to analyse the purity of the cardiomyocytes in the differentiated culture, it is important to calculate the percentage of resulting hiPSC-CM obtained after the process, as other cell types, such as fibroblasts and endothelial cells, can be generated during the differentiation development affecting the results of the studies. This was performed after the differentiation of each batch of cells as a 'quality control' measure. Cardiac troponin, specific of hiPSC-CM, was immunolabelled with a TNNI3 marker which can also provide information of the developmental state of the hiPSC-CM[294]. The nuclei of all cell types were counterstained with Hoechst (Figure 5-4) and by calculating the number of cells stained with both TNNI3 and nuclei markers and those only stained with the nuclei marker, the purity of the culture is measured (Equation 5-1).

$$\%\ hiPSC - CM = \frac{Blue + Green_{stained\ cells}}{Blue + Green_{stained\ cells} + Blue_{stained\ cells}} x100 \quad \textbf{Eq. 5-1}$$

The purity of three different batches of cells after differentiation was calculated. Each batch of cells was analysed in triplicate and two areas of the stained culture per replicate were analysed. In all the cases, the percentage of hiPSC-CM present in the culture was above 90% (Figure 5-5) and good values of purity can be found above 70%. Therefore, it can be concluded that the differentiation process from hiPSC to hiPSC-CM was successful, reproducible and final cultures had an acceptable proportion of hiPSC-CM.

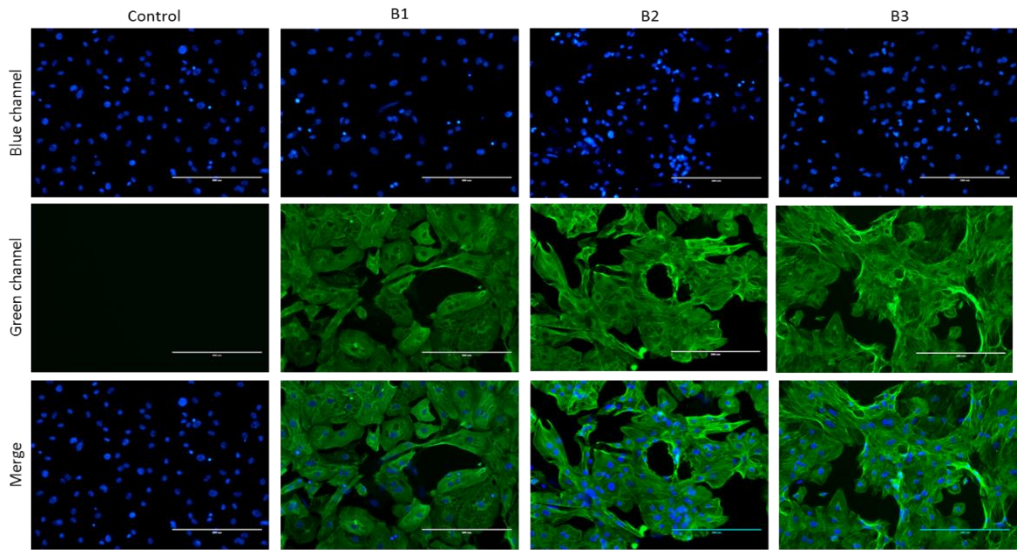

Figure 5-4. Immunostaining of three batches of hiPSC-CM after dissociation. Cells were immunolabelled for cardiac troponin TNNI3 (green). Nuclei were counterstained with Hoechst. hiPSC-CM are positive for the green markers, whereas other cellular types are stained only with Hoechst. Immunostaining without antibody against TNNI3 represents the negative control (N=3, n=2; scale bar 200 µm).

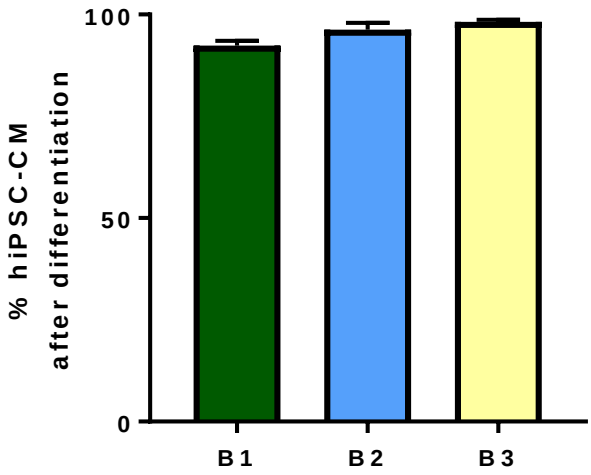

Figure 5-5. Percentage of hiPSC-CM after differentiation calculated after immunostaining of three different batches of cells after dissociation (N=3, n=2; error bars represent standard deviation (±SD)).

5.2.2. Viability studies on structures fabricated by two-photon polymerisation (2PP)

Pentaerythritol triacrylate (PETrA) was the monomer selected for the 2PP fabrication of structures due to its printability properties by 2PP provided by the presence of acrylate groups on its structure[295], its chemical adaptability and capability of being modified with multi-walled carbon nanotubes (MWCNTs), via the –OH group, and biocompatibility[296] (Figure 5-6). This polymer was selected from a high-throughput screened library of materials similar to the one presented in Patel's work[289].

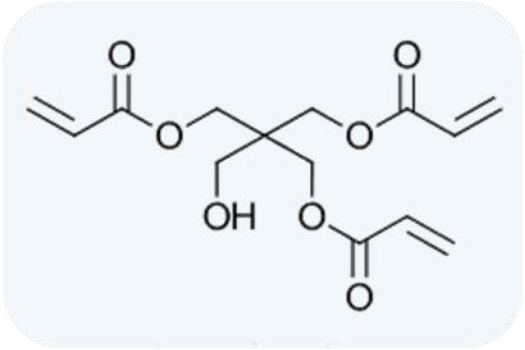

Pentaerythritol triacrylate (PETrA)

Figure 5-6. Chemical structure of pentaerythritol triacrylate (PETrA)

In order to develop the ink formulation, a photoinitiator (PI) Irgacure 369 needs to be added to trigger the photopolymerisation induced by laser photons. Various PI concentrations were studied, ranging from 0.5% to 3%. During the manufacturing process, the energy absorption decreased from 4 $x10^{-12}$ J to 2 x 10^{-12} J with increasing concentrations of PI (Figure 5-7), as the polymerisation is triggered more easily when the concentration of PI is higher. Regarding the degree of conversion, this slightly increased with the concentration of PI from 25% to 30% as the kinetics of the process is faster and more monomer is transformed into polymer.

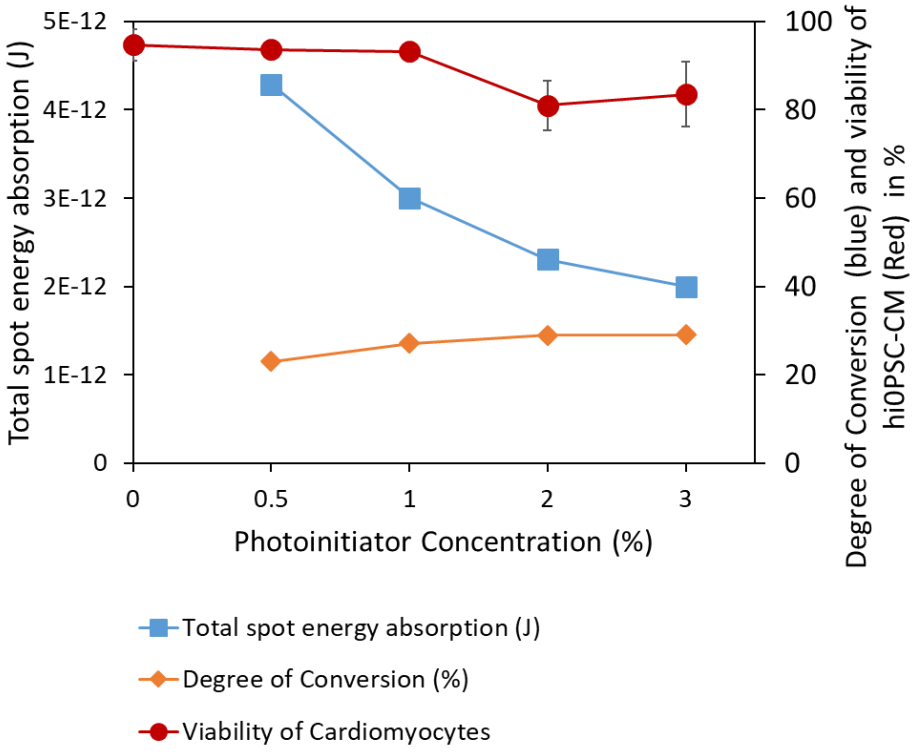

Figure 5-7. Optimisation of spot energy absorption (J) during 2PP process, degree of conversion (%) and viability of hiPSC-CM as a function of PI concentration (N=2, n=3; SD on viability samples).

It has been reported in the literature that some minor cytotoxic effects can be associated to the photoinitiator Irgacure 369 above concentrations of 2%[297]. For this reason, the viability of cells seeded on PETrA flat structures at different concentrations of PI were studied. After 6 days of culture into the polymeric structures, cells were incubated with acetoxymethyl calcein (C-AM) and ethidium homodimer 1 (EthD-1). C-AM is a fluorescence marker whose emission wavelength is in the green spectrum and can be up-taken through the cellular membrane of live cells. On the other side, EthD-1 has an emission wavelength in the red spectrum and penetrates the disrupted membranes of compromised cells and binds into DNA (Figure 5-8).

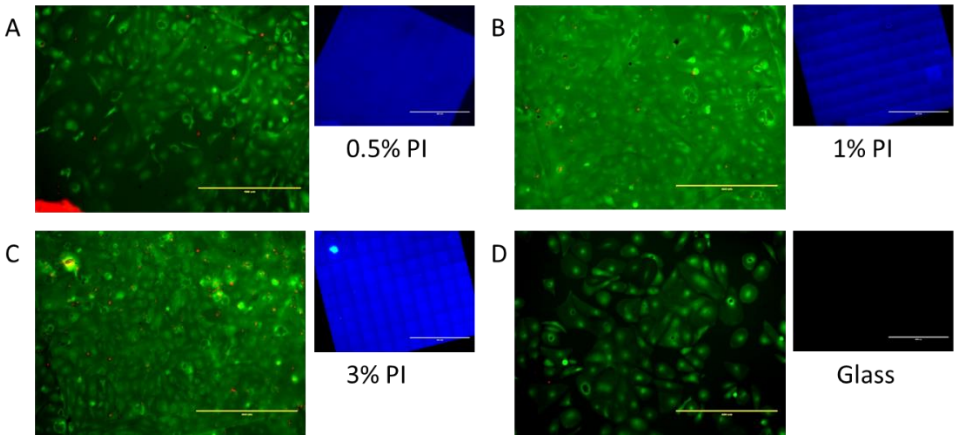

Figure 5-8. Fluorescence microscope images of hiPSC-CM on PETrA surfaces at different concentrations of photoinitiator (PI): (A) 0.5% PI, (B) 1% PI and (C) 3% PI and (D) glass surfaces stained with 1 µM acetoxymethyl calcein (C-AM) in PBS (green) and 5 µM ethidium homodimer I (EthD-1) in PBS (red). Scale bar 200 µm.

Up to concentrations of 1%, the cell viability is above 90% and the effect of the PI is minimum on the percentage of viable cells, compared to controls with no PI. Ink formulations of PETrA containing more than 2% PI reduced the cell viability to 80% (Figure 5-7). Considering the values of cell viability and degree of conversion of monomers, the PETrA formulations chosen for subsequent experiments are those containing 0.5% and 1% PI (PETrA0.5% and PETrA1%) to minimise the effect of the ink formulations on the cell development.

Viability studies were also performed on PETrA structures modified with multi-walled carbon nanotubes (MWCNTs) as the incorporation of MWCNTs in the formulation can increase the cytotoxic effects of the materials[298]. Two different concentrations of MWCNTs, 0.1 and 0.2 w/w% were studied at 1% PI.

These concentrations of MWCNTs have been previously used in the manufacturing of 2PP structures, generating conductive systems in the order of 10^{-9} Scm^{-1} [164].

Results revealed that in both cases, the cell viability is affected by the incorporation of MWCNTs and a slight increment in the concentration of MWCNTs can have very detrimental effects on the viability of hiPSC-CM. In 0.1 w/w% structures, 87% of the hiPSC-CM were viable, however, in 0.2% w/w the number of viable cells was reduced to 54% (Figure 5-9). In future experiments the highest concentration was discarded due to the high difference in cell viability and in future experiments, only the formulation of PETrA+CNTs 0.1w/w% (PETrA+CNTs) was used.

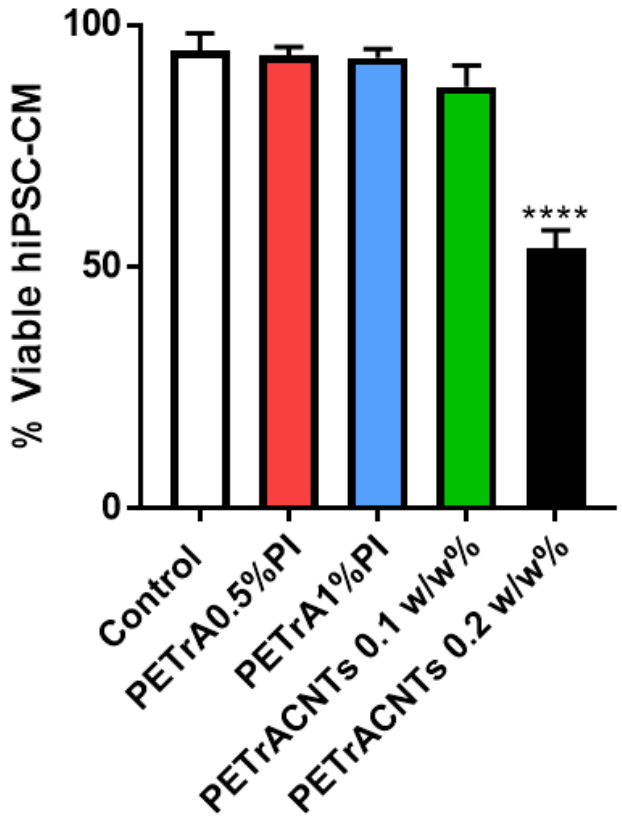

Figure 5-9. Percentage of viable hiPSC-CM on control, PETrA0.5%PI, PETrA1%PI and PETrA modified with multi-walled carbon nanotubes (PETrA+CNTs) at concentrations of 0.1 w/w% and 0.2 w/w% on day 6 after seeding. (N=3, n=2; SD)

It can be concluded from this section that all ink formulations applied in these studies can be used to successfully manufacture structures by 2PP. However, inks whose formulations contain more than 1% photoinitiator and more than 0.1 w/w% MWCNTs can compromise the hiPSC-CM viability.

5.2.3. Preliminary maturation studies on 2D and 2.5D structures

Disorganised myofibrils and round cell shapes are typical characteristics of immature hiPSC-CM. Having control over the substrate chemistry and topography, material and electrical properties is vital to ultimately control cell phenotypes and morphologies. Following this premise, nano-topographies were patterned on PETrA structures, designing these patterns on a CAD software in order to guide hiPSC-CM growth and control the alignment and cell aspect ratio to achieve physiological values (aspect ratio of 7:1)[286]. This high aspect ratio is translated into elongated cells, whose sarcomeres and myofibrils are organised and parallel to the elongated axis of the cells.

In order to induce such elongation and guidance in cells, 500 nm wide nano-grooves were designed on the PETrA structures. Printed surfaces were subdivided into stitched 100x100 µm areas (Figure 5-10A) due to manufacturing limitations of 2PP, due to the small area that can be focused by the laser beam of the instrument to trigger the polymerisation each time. However, this does not affect the overall shape of the structures and it is a common strategy in the manufacturing of large-sized constructs by 2PP. Structures had a solid fill and their thickness was 5 µm. The intricacy and level of detail of the patterned grooves can be seen in the SEM images from Figure 5-10B.

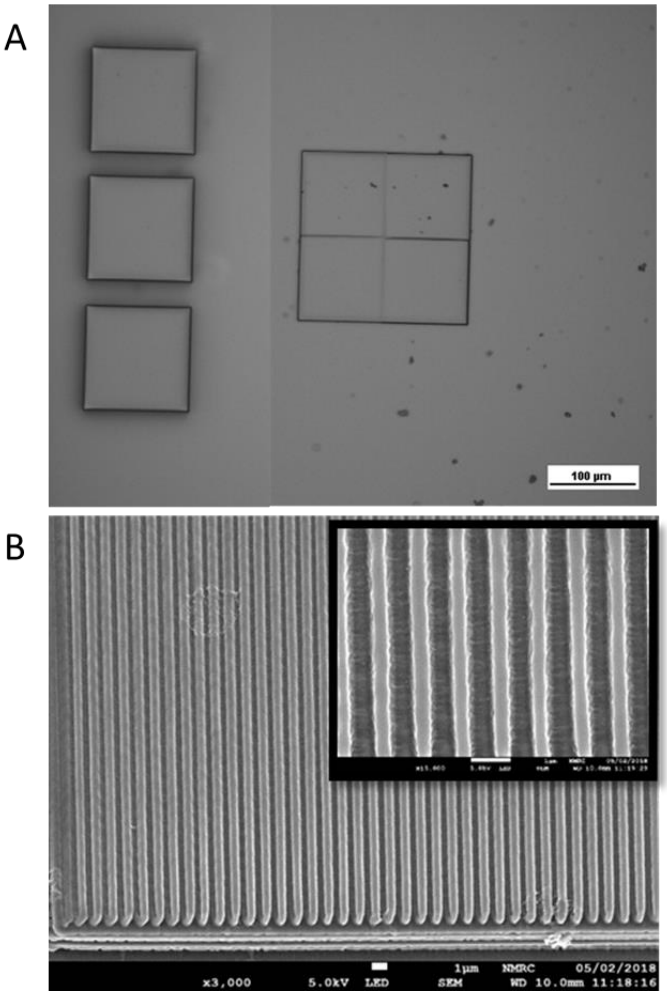

Figure 5-10. PETrA structures produced by 2PP. (A) Optical microscopy of 100x100 µm (left) and 200x200 µm (right) flat surfaces. Scale bar 100 µm. (B) 500 nm wide nano-grooves with 750nm depth/pitch. Scale bar 1 µm

After dissociation, hiPSC-CM were seeded on PETrA structures and incubated for 6 days . The morphology of hiPSC-CM cultured on the structures with nano-topographies (2.5D structures) was then compared to those on flat surface's (2D structures). For this, hiPSC-CM were fixed, permeabilised and their nuclei and actin stained with the fluorescence markers Hoechst and phalloidin, respectively.

Actin filaments are a major component of cellular cytoskeleton and contractile apparatus of muscle cells[299]. Therefore, knowing its location within the cells can provide information about the organisation of myofibrils. When stained hiPSC-CM on flat surfaces were observed under a fluorescence microscope, it can be seen that actin is distributed radially from the cell nucleus (Figure 5-11). This distribution is typical from immature hiPSC-CM[286]. However, hiPSC-CM seeded on structures with 500 nm wide grooves presented more organised actin filaments, parallel to the direction of the grooves.

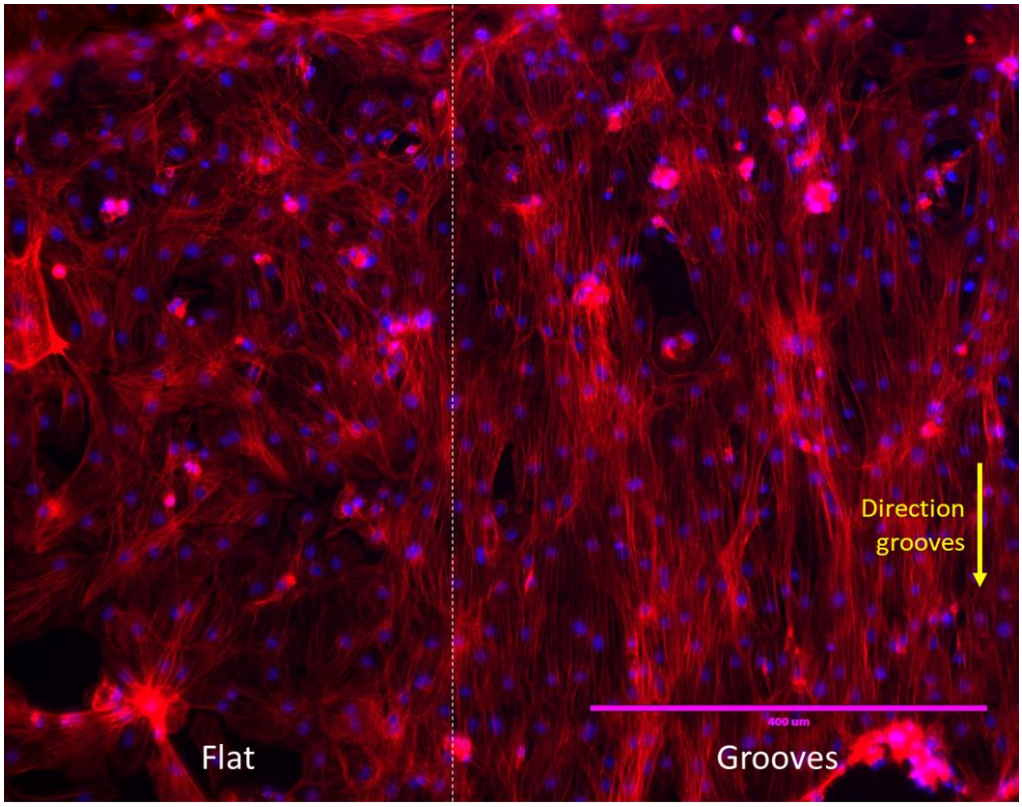

Figure 5-11. Typical fluorescence images of hiPSC-CM on a PETrA1%PI structure where half of the surface is flat and the other half contains vertical grooves (virtually separated by dotted line). Nucleus were stained with Hoechst (blue) and actin with phalloidin (red). Scale bar 400 µm.

Alpha-actinin markers are used for two purposes in this work: they can be used to tag and identify hiPSC-CM, and for the determination of sarcomere lengths as a sarcomeric unit will be delimited by two alpha-actinin lines (Z-lines). Sarcomeres were labelled with a specific marker of cardiac alpha-actinin. This molecule is a component of sarcomeric units in hiPSC-CM, specifically; it is a structural protein of the Z-discs[300].

hiPSC-CM were studied on the different materials and topographies printed. This includes glass slides as a negative control surface and structures manufactured by 2PP with different materials and topographies, including flat and grooved PETrA at different PI concentrations and PETrA modified with MWCNTs (fPETrA0.5%PI, gPETrA0.5%PI, fPETrA1%PI, gPETrA1%PI and PETrA+CNTs).

Fluorescence microscopy images of hiPSC-CM on glass substrates presented the typical shape of immature cardiomyocytes[301] with round or polygonal edges with a single nucleus in the centre of the cell (Figure 5-12A). The aspect ratio of 10 cells in triplicate were calculated by dividing the length of the long axis of hiPSC-CM by their short axis length (Equation 5-2), corresponding to 1.5:1 and far from the physiological values of 7:1 previously mentioned (Figure 5-13A).

$$Aspect\ ratio = \frac{Length\ of\ long\ axis\ of\ cells}{Length\ of\ short\ axis\ of\ cells} \quad \textbf{Eq. 5-2}$$

In order to study the alignment of the cells in the sample, the angle between the long axis of the cells and the x-axis of the images, used as reference, was measured. As glass surfaces were unpatterned, hiPSC-CM grew in all directions. This effect can be more clearly seen in Figure 5-13B where the angle of alignment is approximately 45° but the big deviation suggests that cells are aligned in all directions, as expected.

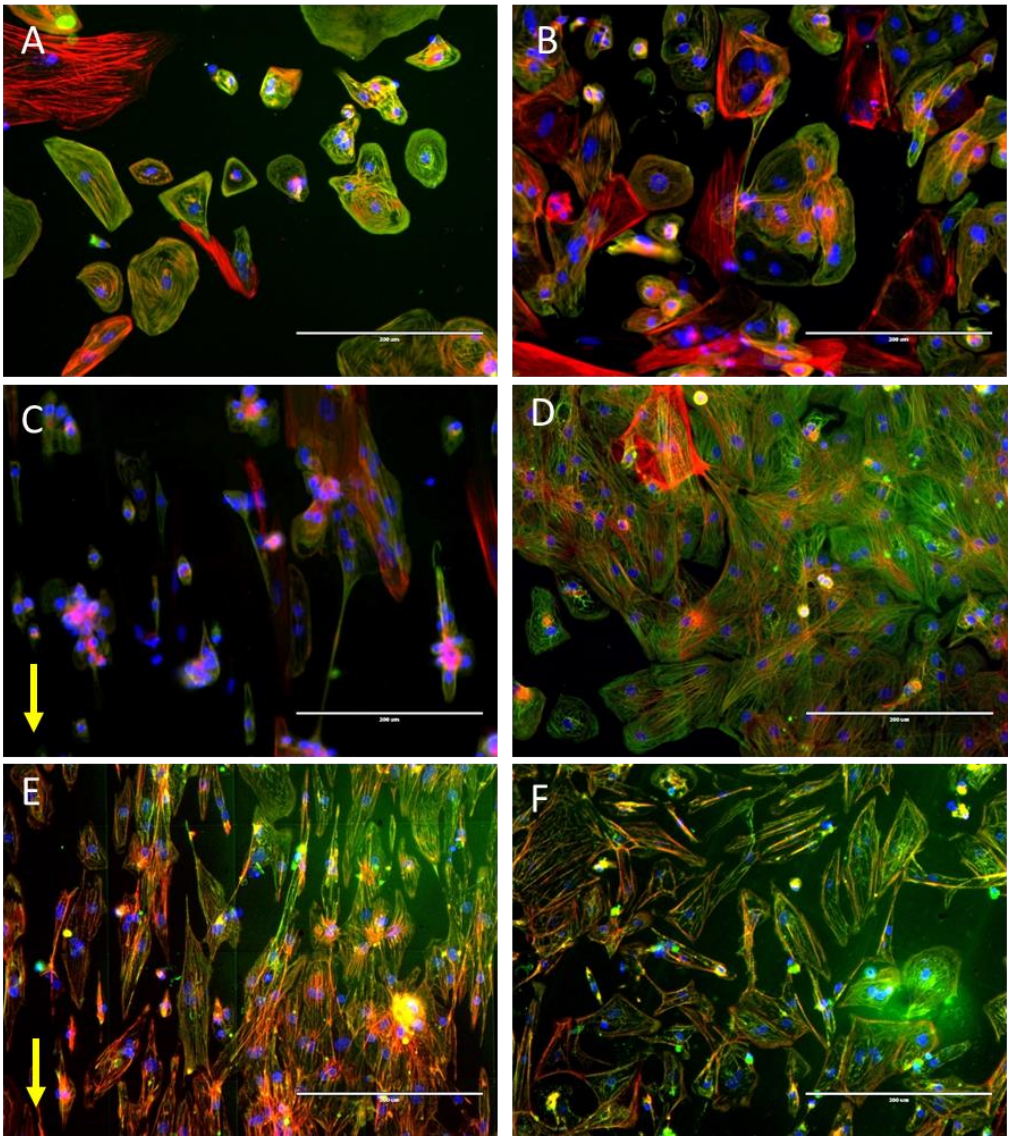

Figure 5-12. Fluorescence microscopy images of hiPSC-CM seeded on (A) glass, (B) 1x1 mm flat PETrA0.5%PI (fPETrA0.5%PI) and (C) 1x1 mm PETrA0.5%PI surfaces with grooves (gPETrA0.5%PI), (D) 1x1 mm flat PETrA1%PI (fPETrA1%PI), (E) 1x1 mm PETrA1%PI surfaces with grooves (gPETrA1%PI) and (F) 1x1 mm flat PETrA modified with MWCNTs 0.1 w/w % (PETrA+CNTs) printed by 2PP. Cells were immunolabelled for cardiac alpha-actinin (green), nuclei were stained with Hoechst (blue) and actin was stained with phalloidin (red). Direction of grooves is indicated by the arrow. Scale bar 200 µm

Similar results were found in fPETrA0.5%PI and fPETrA1%PI structures, where it can be seen the polygonal shape of the cells (Figure 5-12B and Figure

5-12D), which is also translated into low aspect ratios (2:1) (Figure 5-13A) despite the differences in stiffness of glass and polymers. Cells are misaligned with an approximate angle of 45° respect to the x-axis reference, since there are no nano-architectures in the design of flat structures (Figure 5-13B). No differences were seen in terms of the morphology that could be associated to the concentration of PI.

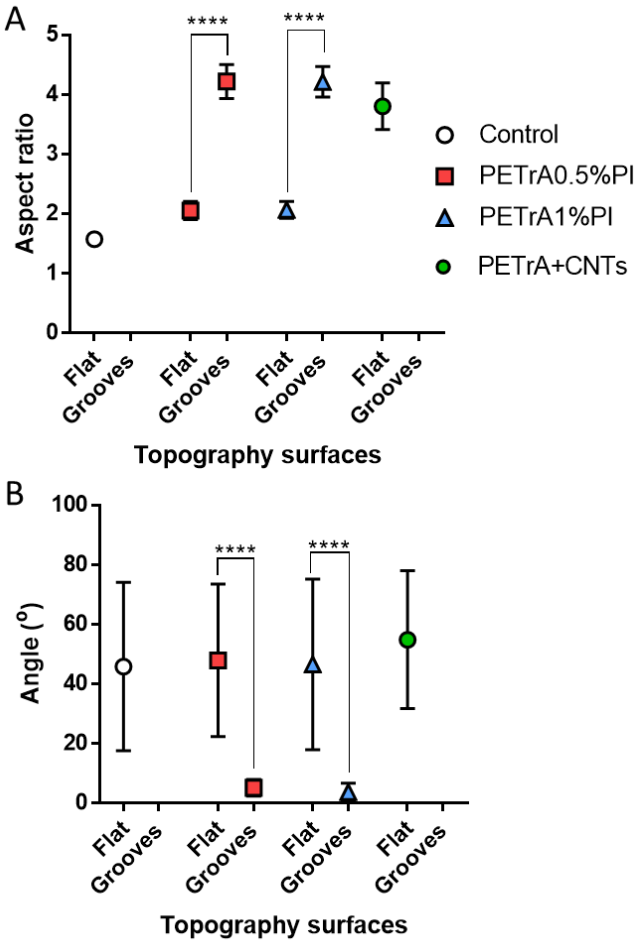

Figure 5-13. (A) Aspect ratio and (B) angle of alignment of hiPSC-CM on control surfaces, fPETrA0.5%PI, gPETrA0.5%PI, fPETrA1%PI, gPETrA1%PI and PETrA+CNTs surfaces on day 6 after seeding. Statistical significance was calculated using an ordinary one-way ANOVA statistical test (N=3, n=10; error bars represent the standard error of the mean (SEM)).

Patterned structures with grooves (gPETrA0.5% and gPETrA1%) presented very clear differences in the morphology of the cells. hiPSC-CM incubated on these structures were thin and elongated as grooves guided the cell growth, and some of them presented more than one nucleus (Figure 5-12C and Figure 5-12E). This meant that the aspect ratio of the cells significantly increased to 4:1 (Figure 5-13A). The alignment in this case was studied by measuring the angle between the long axis of the cells and the direction of the grooves. In both cases, a significant reduction in the magnitude of the angle and the statistical deviation was seen (Figure 5-13B) as cells were aligned with the grooves of the PETrA structures. Once more, there are no differences between concentrations of PI.

Interestingly, hiPSC-CM presented elongated shapes when incubated in PETrA+CNTs flat structures (Figure 5-12F) and higher aspect ratios (3.75:1) (Figure 5-13A) than cells on other flat surfaces. This effect could be induced by the presence of MWCNTs integrated within the structure, as similar effects were seen and described in the literature[302]. It is not possible to identify at this point whether this is due to areas with higher conductivity, higher stiffness, the fibrous structure of MWCNTs or a contribution of several of these factors. Regarding the alignment, the angle between the long axis of the cells and the x-axis of the samples was again around 45º (Figure 5-13B).

The aspect ratio and the alignment of the cells on the structures can only provide information about the morpohology of hiPSC-CM. In order to determine the maturity status, other parameters need to be analysed. Molecular biology techniques are very useful for the determination of maturity markers of hiPSC-CM, such as the number of mitochondria[303] and T-tubules[304] per cell and ratio of genes TNNI1 and TNNI3[285, 294]. However, molecular techniques are specially challenging in this case since the structures are rather small and cells are distributed on a bigger area of the plates. For this reason, it is not possible to differentiate the cells on the structures from the ones outside them, and molecular biology techniques cannot be applied to analyse the maturity.

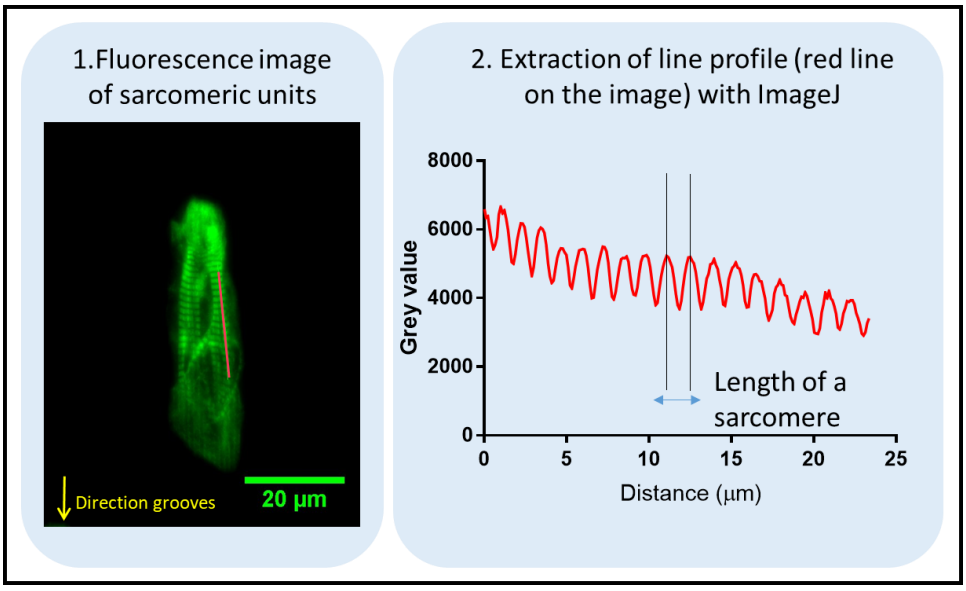

Figure 5-14. Methodology followed to measure sarcomere length of hiPSC-CM: (i) structural analysis of a cardiomyocyte on a PETrA surface with grooves immunolabelled for cardiac alpha-actinin, (ii) intensity graph of red line extracted with Image J line profile tool

Measurement of sarcomeric units could offer a solution to this issue. Structural maturity of the myofibrils can be determined by the length of the sarcomeres, which represent the basic motor units of the myofibrils and have physiological values up to 2.2 µm[289]. Alpha-actinin of hiPSC-CM was previously immunolabelled and cells were imaged using a fluorescence microscope. The profile of an intensity graph of a line drawn on the images can be extracted, where each peak represents the Z-discs and the distance between them the length of a sarcomeric unit (Figure 5-14). 10 sarcomeres were measured in 10 different cells in triplicate for this calculation.

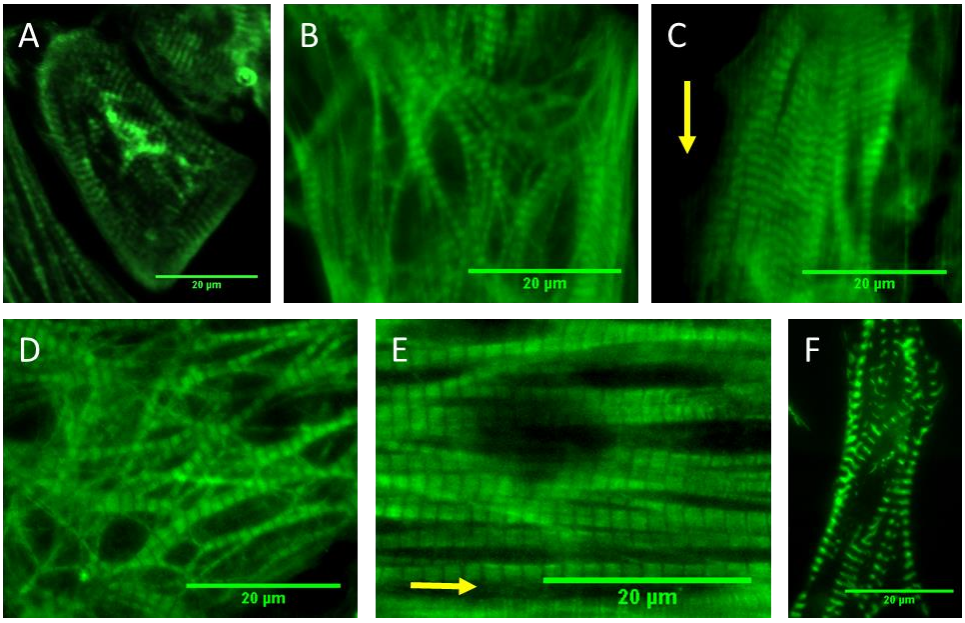

Figure 5-15. Fluorescence image of sarcomeres of hiPSC-CM immunolabelled for cardiac alpha-actinin on (A) control surfaces, (B) fPETrA0.5%PI, (C) gPETrA0.5%PI, (D) fPETrA1%PI, (E) gPETrA1%PI and (F) PETrA+CNTs. Direction of grooves is indicated by an arrow. Scale bar 20 µm.

Sarcomeres from hiPSC-CM incubated on the different structures were analysed and a more detailed image of the myofibrils was taken. Disorganised myofibril structures can be seen in the cardiomyocytes cultured on control, fPETrA0.5%PI and fPETrA1%PI structures (Figure 5-15A, Figure 5-15B and Figure 5-15D). This contrasted the images of myofibrils from hiPSC-CM on gPETrA0.5%PI, gPETrA1%PI and PETrA+CNTs, where organised structures and parallel myofibrils were seen (Figure 5-15C, Figure 5-15E and Figure 5-15F).

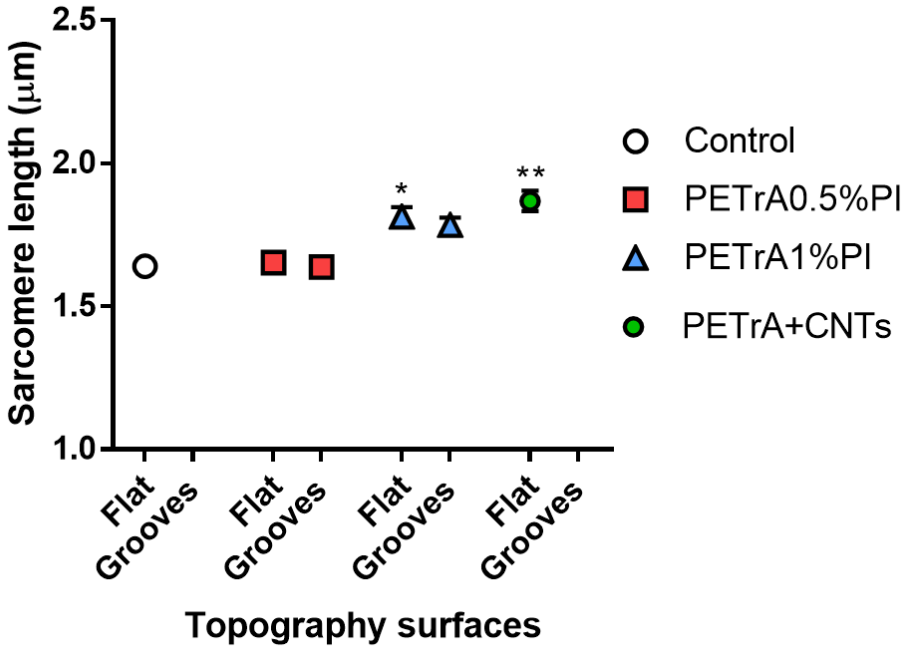

Figure 5-16. Sarcomere length of hiPSC-CM on control surfaces, PETrA0.5%PI, PETrA1%PI, and PETrA+CNTs on flat and surfaces with grooves. Statistical significance was calculated using an ordinary one-way ANOVA statistical test. 10 measurements were taken in 10 cells per sample (N=3, n=10; SEM)

Sarcomere lengths of control surfaces were 1.64 µm and similar values were seen in fPETrA0.5%PI and gPETrA0.5%PI (Figure 5-16). Significantly longer

lengths were measured on hiPSC-CM on fPETrA1%PI (1.81 µm) and PETrA+CNTs (1.86 µm). Differences found in PETrA at different PI concentrations could be related to degrees of monomer conversion from Figure 5-5, improving the structural properties of the material. This could also be the reason behind the longer lengths found in PETrA+CNTs or it could be due to the electrical properties of the material[164]. These values were similar to values of sarcomere length seen in previous works and performed better than gelatine controls (1.50 µm)[288].

It is important to note though, that at this stage values of sarcomere lengths are still far from values of adult cardiomyocytes. However, it seems that the nano-topographies manufactured by 2PP can influence the cell aspect ratio and the alignment, and the nature of the material of the substrate can also affect, in the absence of other external cues, the degree of maturation of the cells.

5.2.4. Electrical stimulation of hiPSC-CM

Exogenously applied electrical stimulation of hiPSC-CM has been proven to influence cell growth and behaviour by inducing alignment of myofibrils and expression of cardiac markers[279, 283, 305]. For these studies, a pulsatile electric field with a monophasic sine wave was applied from a power supply to an electro-bioreactor with platinum electrodes[54] (Figure 5-17A).

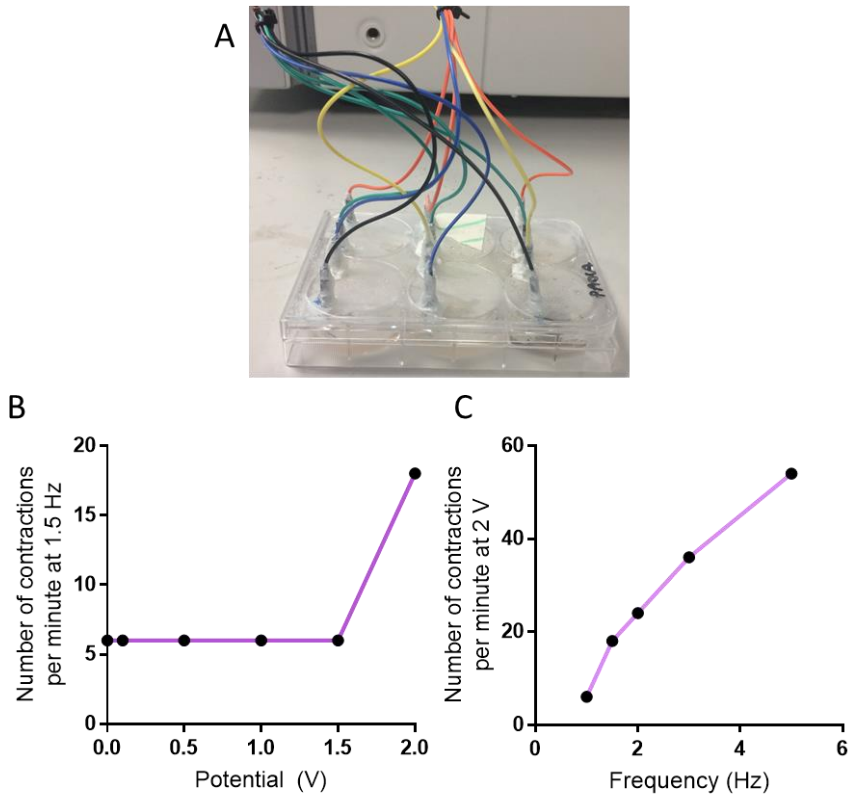

Figure 5-17. (A) Image of device used to perform the electrical stimulation of hiPSC-CM. Determination of excitation threshold by application of external electrical stimulation (e-stim.) with alternating current (AC) of hiPSC-CM. (B) Number of contractions per minute at 1.5 Hz and varying potential and (C) Number of contractions per minute at 2 V and varying frequency.

The electrical conditions needed to be applied to induce synchronous contractions of the cells can be defined as excitation threshold[306]. Parameters of the electrical stimulation applied were optimised in order to identify the excitation threshold and minimise the potentials used, as high potentials can induce hydrogen generation from the electrodes and changes in pH of the media that could perturb the cells.

Cells were closely monitored by optical microscopy while electrical stimulation was being applied and the number of contractions per minute was determined. At constant frequencies, there is no cell response bellow 2 V. However, when hiPSC-CM were stimulated at 2 V, the rate of contractions tripled and the excitation threshold was established at this potential (Figure 5-17B). The magnitude of the values of frequency can also affect the rate of contractions of hiPSC-CM when the potential input is maintained constant. It can be seen in Figure 5-17C that the number of contractions per minute increases with higher values of frequency. Following these findings and values used in literature[305], the parameters selected for the application of potentials were 2 V and 3 Hz.

Viability of hiPSC-CM following previous protocols was studied after the application of short electrical stimulation (e-stim) to determine the limits of potentials that can be applied without damaging the cells. Up to 6 V cells seem to be intact, however, when 10 V were applied, most of cells were detached from the surfaces of the plates and the remaining cells were dead (Figure 5-18A).

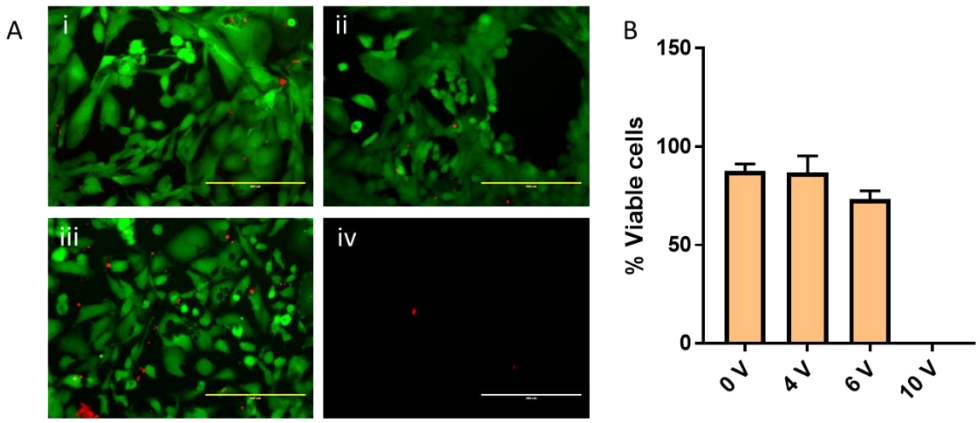

Figure 5-18. (A) Fluorescence microscope images of hiPSC-CM one week after application of external electric fields with magnitudes of (i) 0 V (ii) 4 V, (iii) 6 V and (iv) 10 V. Viable cells were stained with 1 µM C-AM in PBS (green) and nonviable cells were stained with 5 µM EthD-1 in PBS (red). Scale bar 200 µm. (B) Percentage of viable cells (n=3; SD).

The percentage of viable cells after application of 4 V is comparable to values of viability from previous electrical stimulation (Figure 5-18B). At 6 V the percentage of viable cells reduced to 73.4% and no viable cells can be seen when 10 V are applied. This means that the selected parameters are within the range at which cells remain viable.

A combination of electrical and topographical cues was then used to assess the maturity of hiPSC-CM. For this, hiPSC-CM were cultured on structures manufactured by 2PP for 5 days and then the electrical stimulation was applied for 24hr prior to fixation and immunolabelling of sarcomeres. Fluorescence microscope images of myofibrils of cells on control, PETrA1%PI and PETrA+CNTs surfaces can be seen in Figure 5-19.

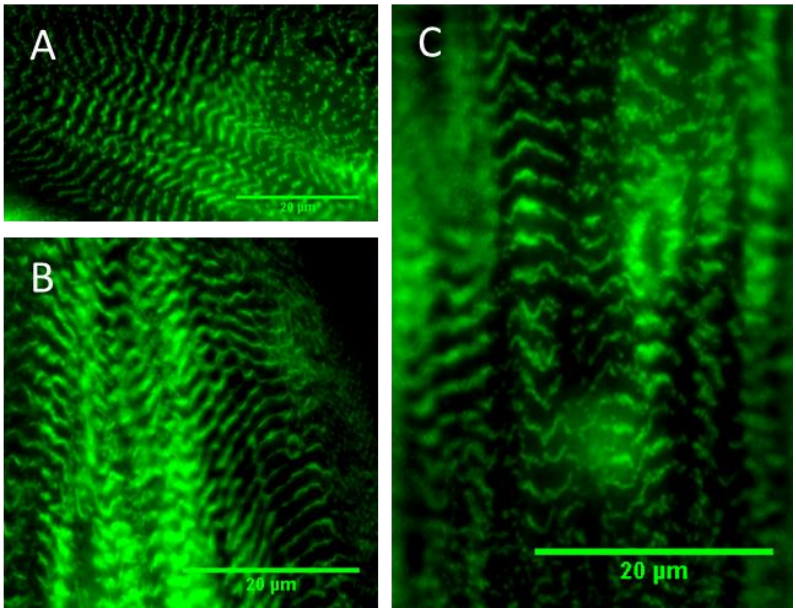

Figure 5-19. Fluorescence microscopy image of sarcomeres hiPSC-CM immunolabelled for cardiac alpha-actinin on (A) control, (B) PETrA1%PI and (C) PETrA+CNTs surfaces after electrical stimulation at 2 V and 3 Hz for 24 h. Scale bar 20 µm

The level of organisation of the myofibrils of electrically stimulated cells is higher than those from cells that were not electrically stimulated (Figure 5-15). This could be due to a greater contribution of the electrical stimulation (e-stim) at the early stages of maturation of hiPSC-CM than physical stimulation induced by the materials. After e-stim on control surfaces, the sarcomere lengths significantly increased from 1.64 µm to 2.05 µm (Figure 5-20).

The combination of PETrA1%PI surfaces and e-stim is particularly good in terms of sarcomere lengths as they reached the value of 2.28 µm. It is not possible to obtain any conclusions from PETrA+CNTs as the number of cells analysed was very low and this could lead to incorrect assumptions. However,

if the cells that have been analysed are considered, the length of sarcomeres after e-stim does not seem to be significant.

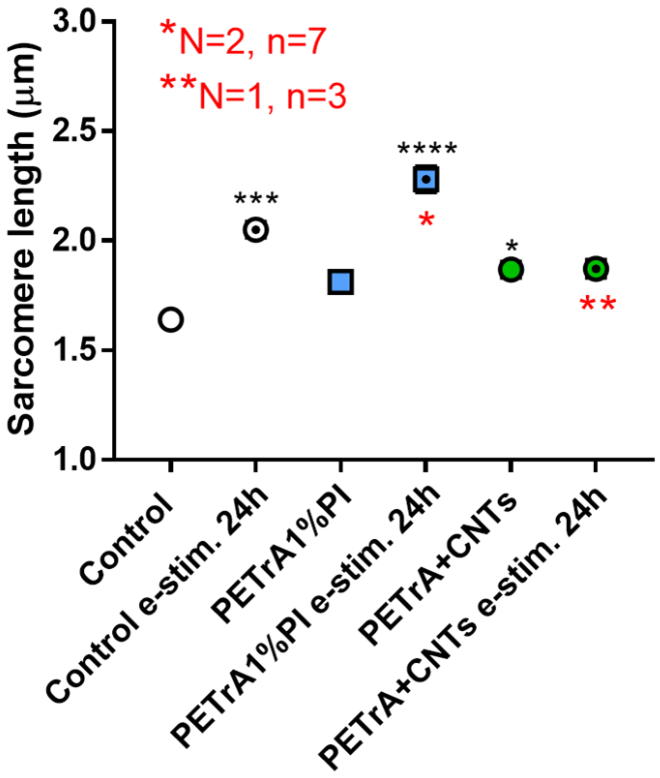

Figure 5-20. Sarcomere length of hiPSC-CM on control surfaces, PETrA1%PI, and PETrA+CNTs with and without e-stim. for 24 h. Statistical significance was calculated using an ordinary one-way ANOVA statistical test. 10 measurements were taken in 10 cells per sample (N=3, n=10; SEM) except on those samples marked with red asterisks

hiPSC-CM responded to the electrical stimulation applied from the electro-bioreactor and were viable using the parameters applied. Organised myofibrils were seen after 24hr of electrical stimulation and the combination of the electrical and the physical stimulation from PETrA structures are the most effective to increase sarcomere lengths up to physiological values.

5.2.5. Maturation studies of hiPSC-CM on complex architectures

Three-dimensional (3D) environments are fundamental in cell and tissue engineering as the architectural cues could represent better the *in vivo* conditions. Due to the design freedom that 2PP offer, it is possible to manufacture complex architectures for hiPSC-CM that could mimic physiological structures.

A combination of micro- and nano-topographies was produced by printing 3D channels with nano-grooves on PETrA1%PI. Grooves were distributed vertically and radially to study the effect of the direction of the nanotopographies on the cells. hiPSC-CM were incubated on the structures and stained with fluorescence markers after 6 days (Figure 5-21A).

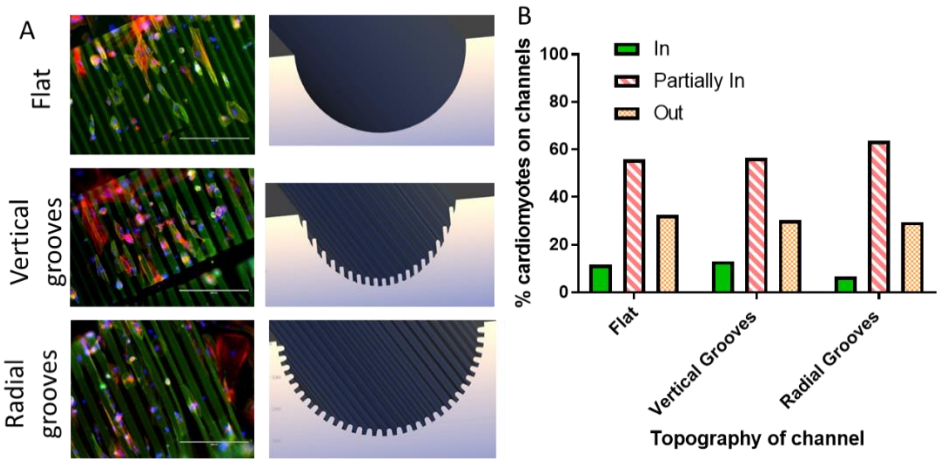

Figure 5-21. Effects of channel nanotopography on hiPSC-CM. (A) hiPSC-CM seeded on flat channels, channels with vertical grooves and channels with radial grooves. (B) Percentage of cardiomyocytes found in, partially in and out of the different channels.

Flat channels and channels with vertical grooves retained the higher number of cells inside them as cells settled faster on them due to the effect of gravity, driving the hiPSC-CM towards the centre of the channel (Figure 5-21B). Radial grooves retained the cells on the sides of the channels and thus, the percentage if cells that are partially inside the channel was increased. In all the cases, the walls between channels were too thick, and a very high percentage of cells were found in these locations.

From this preliminary study, the design of the structures was redefined to maximise the number of cells in contact with the 3D aspects of the structure and resemble the physiological architecture of a myofibril (Figure 5-22A). Structures were fabricated using both PETrA1%PI (Figure 5-22B) and PETrA+CNTs (Figure 5-22C) inks.

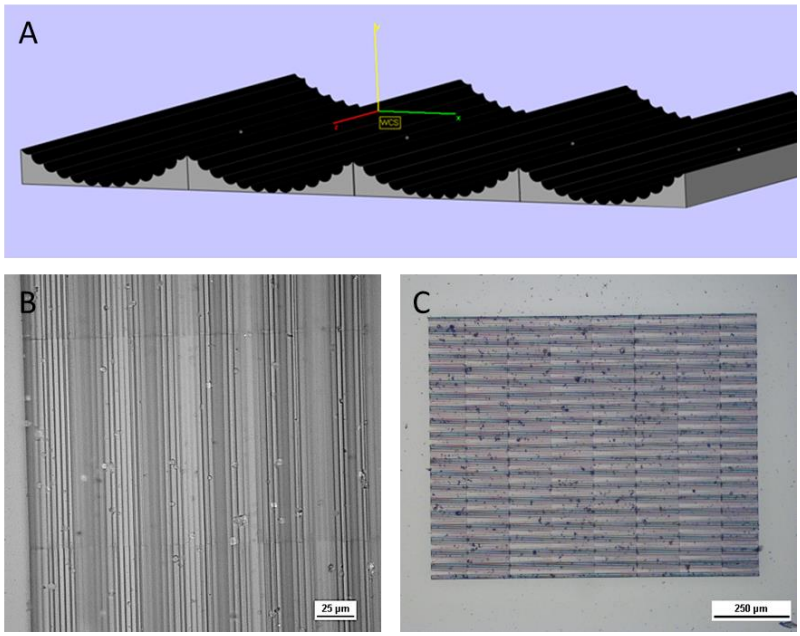

Figure 5-22. (A) CAD design of a myofibril-like structure. Optical microscopy images of myofibril-like structures fabricated with (B) PETrA1%PI and (C) PETrA+CNTs.

Topographical details of the myofibril-like structure were obtained by scanning electron microscopy (SEM), where micro-channels and nano-grooves can be seen (Figure 5-23).

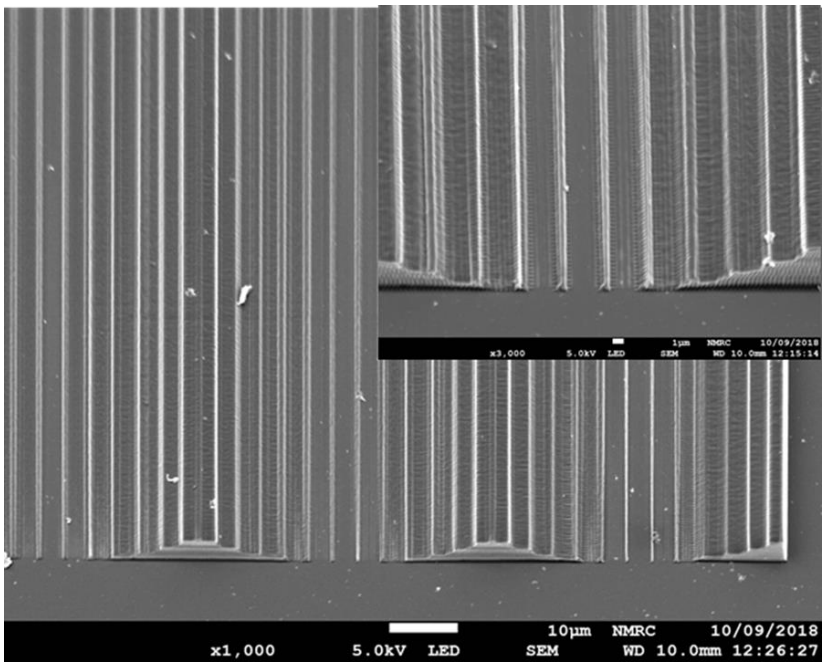

Figure 5-23. SEM image of myofibril-like structure fabricated by 2PP with PETrA1%PI with dimensions: 1000 x 1000 x 15 µm with micro and nano-grooves. Scale bar 10 µm

hiPSC-CM were incubated on the myofibril-like structures and they were aligning and growing on the direction of the channels and grooves (Figure 5-24). It is also possible to compare the morphology of the cells on the structures and the ones outside (limit of the structure is indicated by the dotted line) which present an unorganised growth.

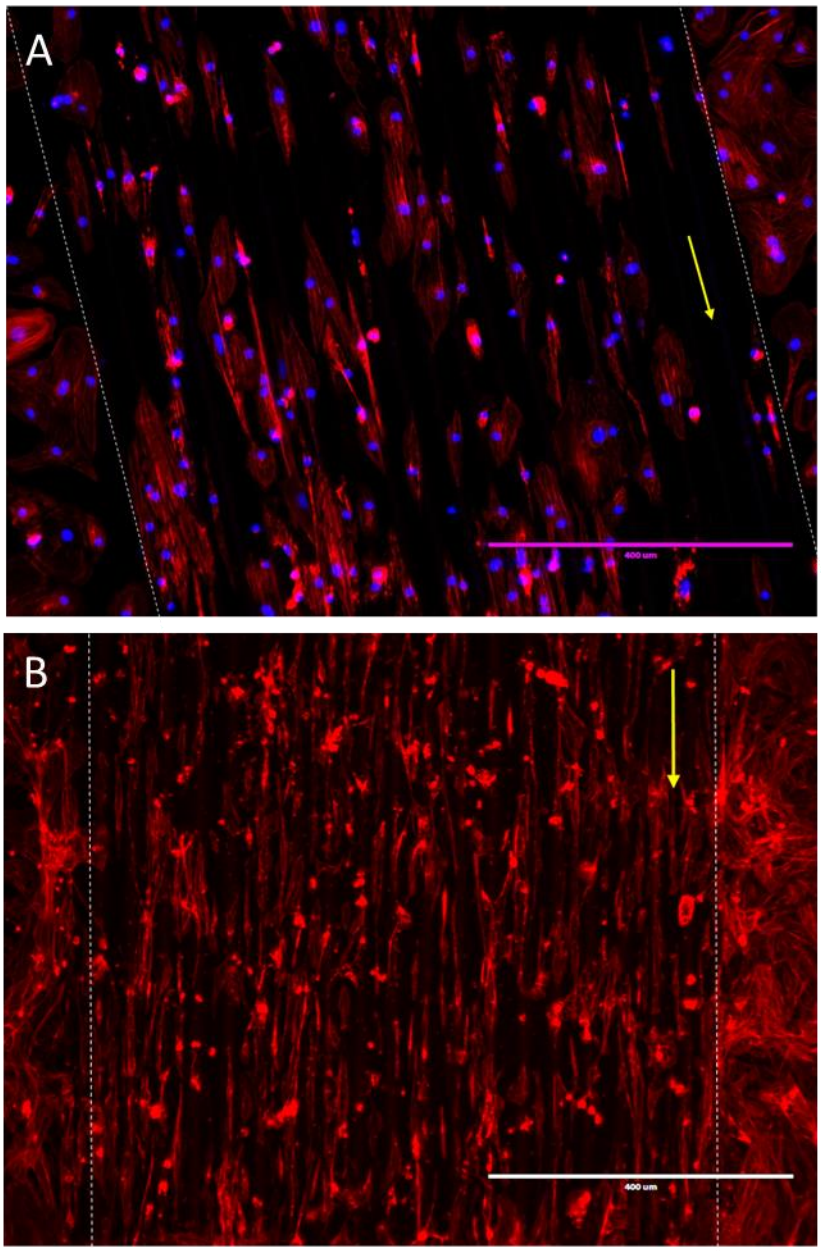

Figure 5-24. hiPSC-CM seeded on (A) PETrA1%PI and (B) PETrA+CNTs myofibril-like structure. Nucleus were stained with Hoechst (blue) and actin with phalloidin (red). Direction of channels is indicated by yellow arrow. Scale bar 400 µm.

Myofibrils of the cells on PETrA1%PI and PETrA+CNTs before and after 24h of electrical stimulation were organised in all the cases (Figure 5-25).

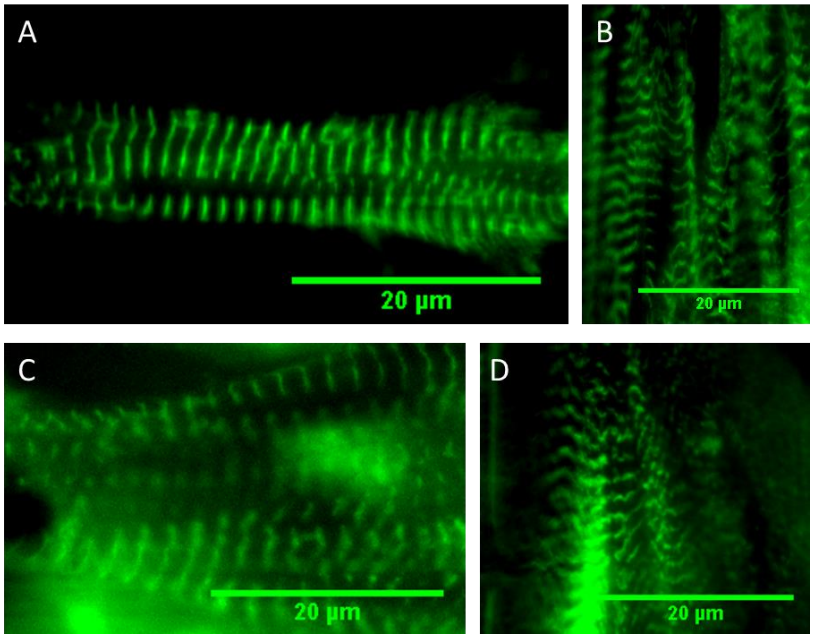

Figure 5-25. Fluorescence microscopy image of sarcomeres of hiPSC-CM on myofibril-like structures immunolabelled for cardiac alpha-actinin on (A) PETrA1%PI, (B) PETrA1%PI after 24h e-stim., (C) PETrA+CNTs and (D) PETrA+CNTs after 24h e-stim

Values of sarcomere length on PETrA1%PI are 1.65 µm prior e-stim and they are significantly higher after e-stim (2.21 µm) (Figure 5-26). In this case, the combination of architectural cues with PETrA+CNTs can increase the sarcomere length prior stimulation (1.94 µm) which could mean that the addition of CNTs is favourable for cardiac maturation in the absence of e-stim. After e-stim there is a slight increase in sarcomere length up to 2.12 µm.

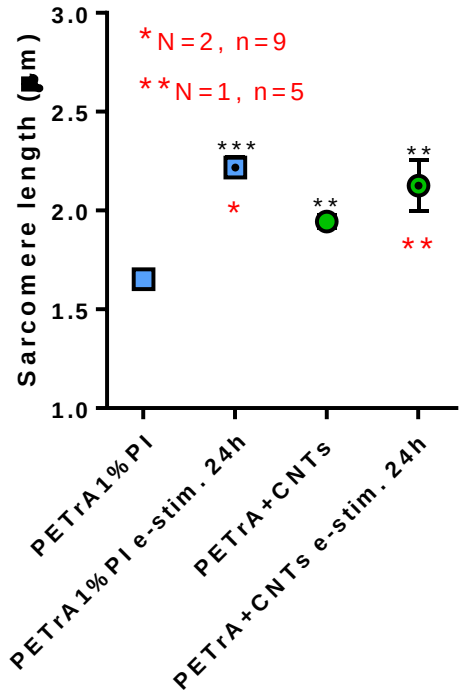

Figure 5-26. Sarcomere length of hiPSC-CM on myofibril-like structures of PETrA1%PI, and PETrA+CNTs with and without e-stim. for 24 h. Statistical significance was calculated using an ordinary one-way ANOVA statistical test. 10 measurements were taken in 10 cells per sample (N=3, n=10; SEM) except on those samples marked with red asterisks

From this section it can be concluded that e-stim is still the predominant stimulus in order to advance the maturation state of hiPSC-CM. In the absence of e-stim, the combination of MWCNTs and complex architectures can advance the maturity of hiPSC-CM.

5.3. Final considerations

In this chapter, hiPSC-CM were successfully differentiated from hiPSC. Cells expressed typical markers of cardiac cells and the percentage of hiPSC-CM respect to other cells was above 90% after performing the differentiation.

Inks of different polymeric materials with different concentrations of photoinitiators and incorporation of MWCNTs were used to manufacture structures by 2PP. Different photoinitiator concentrations and MWCNTs were studied, revealing that the limits for a good cell viability were 1% PI and 0.1 w/w% respectively.

Nano-topographies were included in the design of the structures achieving a better alignment and aspect ratio on the cells that were incubated in structures with grooves. Sarcomere lengths were used as an indicator of maturation state of hiPSC-CM. In the absence of electrical stimulation, cells cultured on PETrA1%PI and PETrA+CNTs presented longer sarcomeres.

Electrical stimulation was applied using an electro-bioreactor. Parameters were optimised to detect the excitation threshold without causing harm to the cells. Parameters selected were 2 V at 3 Hz and after 24 h of stimulation, the combination of PETrA1%PI and electrical stimulation gave the best values of sarcomere lengths, compatible with physiological values.

Due to the design freedom of 2PP, complex structures fabricated by PETrA1% and PETrA+CNTs were manufactured. These structures were formed by a combination of channels and grooves. hiPSC-CM were incubated in this structures, aligning to them and after electrical stimulation, the values of sarcomere length that combined PETrA1%PI and e-stim were similar to physiological values.

Electrical stimulation seems to be necessary to increase further the maturity of hiPSC-CM, however this needs to be associated to the physical cues provided by the structures manufactured by 2PP.

Chapter 6. General discussion

Part of the content of this chapter appears in *Engineering the Spark into Bioelectronics Medicine*. Sanjuan-Alberte P, Rawson FJ. **Therapeutic delivery** (2019).

Bioelectronic medicine is an exciting and relatively new field that seeks to treat diseases by modulating bioelectrical signals[307]. It has been stated in the previous chapters that current bioelectronic tools such as deep brain stimulators[308] tend to be highly invasive. This is in part due to the composition of materials used and the size of their components, as it is currently necessary to physically 'connect' biological systems with electronic devices in order to electrically induce/sense an effect. Strategies and approaches to improve this connectivity are required; however, this remains as one of the main challenges in the field.

Advancements in reducing the invasiveness are underway which include injectable electronics, as demonstrated by Prof Lieber's group at the University of Harvard, and flexible wearable electronics and tattoos with diagnostic capabilities that can be directly applied to the patient's skin[309-310]. Lithium batteries are traditionally used as power source in wearable devices, however, are difficult to miniaturise and have a limited lifetime. Consequently, efforts are underway to address this with longer lasting batteries and biologically

powered devices. For example, studies performed on enzymatic fuel cells have shown the potential to be a sustainable technology to power bioelectronic devices[311]. Organic electronic parts could also replace the traditional rigid metallic elements. These systems could locally release of GABA molecules that inhibit the activity of brain regions involved in epilepsy[312].

Connectivity issues could also be completely removed with the use of wireless systems, inducing a response remotely. In this sense, bipolar electrochemistry has deeply inspired and impacted the work of this thesis, as it has proven that direct contact with electrical sources are not needed to drive electrochemical reactions on conductive materials if magnitudes of externally applied electric fields are high enough (More information can be found in 1.3.2. Bipolar or wireless electrochemistry). This premise was followed throughout this thesis, where external potentials and electric fields were applied to systems to remotely control them.

The responses induced by the external electric fields varied in each chapter presented in this work, as different applications where pursued to display a range of effects and systems. This variety of responses was achieved by changing the nature of the potentials, the materials used and the dimensions of the electrodes/bipolar electrodes. These factors were changed as it follows:

- Chapter 3: direct currents on silver feeder and bipolar macroelectrodes.

- Chapter 4: direct currents on gold feeder macroelectrodes and chemically modified gold nanoparticles as bipolar electrodes.
- Chapter 5: alternating currents on platinum macroelectrodes and polymeric microstructures modified with carbon nanotubes as bipolar electrodes.

In all the cases however, conductive materials were developed by additive manufacturing methods (inkjet printing and two-photon polymerisation) to produce either the conductive feeder electrodes or bipolar electrodes or both.

The materials used in bipolar electrochemistry need to be carefully selected to tailor a specific application, as different materials will also have a different behaviour under the effect of a polarising electric field or when in contact with an aqueous solution. For instance, when silver macroelectrodes separated by aqueous solutions were used as feeder electrodes and bipolar electrodes, a controlled self-assembly of silver microwires was induced. The advantage of doing this, using theoretical concepts of bipolar electrochemistry, is that bioelectronic interfaces can be produced and controlled without a direct contact with biology. The electrochemical lability of silver means that silver electrodes will always be subjected to this redox behaviour in aqueous solutions as discussed in Chapter 3 and alternatives to silver are needed (such as the gold electrodes or platinum wires that were used in subsequent chapters) to suppress this effect.

The size of the bipolar electrode is also a key factor in bipolar electrochemistry, as the potentials applied should linearly decrease with the size of the bipolar electrode in order to be able to induce a redox reaction according to the theory[184]. Our findings however, differ from this theory, as electrochemically induced reactions were driven intracellularly in 50 nm gold nanoparticles at relatively low potentials[244] as shown in Chapter 4. This lead us to think that the theory might not be applied to nano-sized objects (< 100 nm), where the high surface area and zero-dimensional (0D) behaviour might affect the polarity and current density of bipolar nano-electrodes.

If this is the case, the potential needed to drive electrochemical reactions on these bipolar electrodes could be smaller than the theoretically expected. Some other groups have also reported electrochemical reactions induced at 15 nm platinum nanoparticles when < 30 V were applied, supporting our theory. These particles were used to produce hydrogen peroxide molecules that induce apoptosis of cancer cells locally, significantly reducing the size of tumours[313]. We can expect that further investigation in this regard could provide more evidence of electrochemical reactions taking place in nano-electrodes wirelessly.

This effect is especially important in the context of bioelectronics and bioelectronic medicine, as lower potentials are less disruptive to cells and the possibility of directing wireless reactions avoid the connectivity issues. The use

of wireless system has the potential to have an important impact in the therapy of a range of disorders that will be described in the following paragraphs.

For instance, wireless reactions could be used in cancer therapy to improve the targeting of tumour treating fields (low intensity electric fields at intermediate frequencies with a proven inhibitory effect in the growth rate of tumour cell lines[314]). This effect is thought to be produced by inhibition of voltage-gated T-type Ca^{2+} channels[315] and disruption of microtubule formation that induces nuclear aberrations during mitotic phases[316]. This is one of the current strategies in the treatment of glioblastoma, and despite being FDA approved, there are still some limitations including skin irritation or abrasions from the transducer pads or inconveniences associated to wearing the device that limit the quality of life of patients[317]. Nanoparticles delivered locally in areas close to the glioblastoma could reduce the magnitude of the potentials applied, which in turn could reduce the skin irritation and abrasions from the transducer pads. The use of nanoparticles in areas close to the tumour has also the potential to magnify the effects seen due to the proximity of these to the areas affected.

Similar systems that combine chemical and electrical approaches are based on pulsed electric fields (100 µs pulses at 1-1.5 kV cm^{-1}). These electric pulses can modify the permeability of the cellular membrane by adding water-filled pores that can be used as a drug delivery route[318]. Hydrophilic molecules such

as bleomycin can easily penetrate the cellular membrane through these electrically induced pores and target the active sites of intracellular components, with this approach being used in the treatment of melanoma[318]. As the previous example, local release of wireless bipolar electrodes and proximity to tumours could reduce the magnitude of the potentials applied.

The ability to wirelessly control redox biomolecular chemistry could also be used in cancer therapy. Plasma membrane and intracellular electron transport systems (tPMETs), are upregulated in cancer cell lines. We hypothesise that this enables the reprogramming of metabolism which, is a hallmark of cancer[41]. These electron transport systems have the potential to be hijacked and yield a potential new therapeutic approach based on a cellular electrical instructed "reverse prodrugs"[319]. In the future, these cellular electrical pathways will be targeted, causing a detoxification of locally applied potent therapeutics. Other redox biomolecules such as thioredoxin systems are involved in reducing oxidative stress of cells and inhibition of proapoptotic proteins. Understanding and controlling these mechanisms could aid in programming apoptosis processes in cancer cells[320].

Biological processes of regeneration and wound healing could also be induced by wireless systems to trigger opening and closing of membrane channels. This could be done by using systems similar to the one presented in Chapter 5 with hiPSC-CMs. Voltage-gated sodium channels have been

identified to have a role in organ regeneration in amphibians and therefore, manipulation of these channels can alter their anatomical organisation[321], which could present a new approach to organ repair. Low-frequency pulsed electric fields can also promote osteoblast proliferation and regeneration to enhance bone repair in the treatment of bone fracture healing and osteoarthritis. Electrical signals applied play an instructive role, guiding migration of bone cells and disposition of extracellular matrix (ECM) components[322], which ultimately repairs the damaged tissues.

Wireless bioelectronics could also have a high impact in neurodegenerative diseases. Activation of glial cells is a characteristic of complex neurodegenerative diseases such as sclerosis, Parkinson's disease or Alzheimer's disease, where reactive oxygen species (ROS) are generated and oxidative stress is produced, leading to neurodegeneration. In some cases, this can be accompanied by chronic viral infections, which can increase the progression of neurodegenerative diseases.

Autoimmune responses seem to play a crucial role in neurodegenerative diseases; however, the correlation between immune cells and nerves is yet to be fully understood. Recent stimulation with extremely low frequency electromagnetic fields at particular combinations of field intensity and frequency has been seen to affect calcium influx processes, which can induce neuroprotective effects from oxidative stress and counter attack the

production of proinflammatory molecules[323]. Techniques that allow early detection and modulation of ROS species by redox biomolecules are needed, such as use of wireless intracellular electrochemical actuators and sensors as the one presented in Chapter 4, and could aid the treatment and diagnosis of neurodegenerative diseases[71].

To conclude this discussion, bipolar electrochemistry has deeply inspired the work presented in this thesis. This is due to the lack of contact with the electrodes needed to drive electrochemical reactions, opposite to the devices currently used in bioelectronics. Different effects can be induced depending on the magnitude and type of potentials applied and the materials and size of bipolar and feeder electrodes.

The fact that bipolar electrochemical concepts can be transferred to the nanoscale could mean that redox reactions in the bipolar nanoelectrodes could be controlled wirelessly, which could then be used in bioelectronic medicine as intracellular transducers or as locally released injectable electrodes. Wireless intracellular redox transducers as the one shown in Chapter 4 could be a promising solution to reduce the invasiveness of typical bioelectronics, converting an external electronic input into a redox output that could trigger a specific biological response such as apoptosis in the treatment of cancer[244]. In addition there is now the potential to facilitate the remote *in situ* construction of the bioelectronic components as shown in Chapter 3[231]. This bionic

manufacturing approach now needs to be taken forward *in vivo* to aid the pathway to translation in, for example, the treatment of glioblastoma due to the intimate contact of the bioeletronic interfaces. Further work on bioelectronic scaffolds as the one presented in Chapter 5 to trigger opening and closing of ionic channels has the potential not only to aid the development and maturation of cardiomyocytes, but to also influence investigations on organ repair and tissue regeneration.

Chapter 7. Conclusions and future directions

7.1. Conclusions

Development of novel bioelectronic tools have the potential to offer new therapeutic strategies, increasing the prospects of controlling cellular behaviour using electronic devices. There are some challenges to achieve this, including a seamless integration between biological and electronic systems and inducing a specific cellular response to electronic inputs.

It was proposed in this work the combination of additive manufacturing and electrochemical methods could overcome the aforementioned challenges. This is due to the capacity of additive manufacturing techniques, such as inkjet printing and two-photon polymerisation, to produce conductive materials that can be integrated with cells and the possibility of programming cell behaviour via intracellular redox events. Towards this goal, several combinations of additive manufacturing and electrochemical methods were explored herein.

This includes the generation of functional bioelectronic interfaces showed in Chapter 3, consisting on merging silver microwires and mammalian cells *in situ* with the ability to detect cellular redox events. The application of this technology could offer new non-invasive strategies in the production of

bioelectronic devices, creating adaptable systems that could be controlled remotely.

Wireless nanoelectronic systems developed in Chapter 4 were also aimed at reducing the invasiveness of bioelectronic systems and to show that nanomaterials can be used to deliver and transmit electronic inputs intracellularly. These nanoelectronic systems are the first example of wireless intracellular communication using electronic inputs as source of stimulation.

The last part of the investigations was to develop bioelectronic platforms to increase the maturity on human induced pluripotent stem cell-derived cardiomyocytes produced *in vitro* (Chapter 5). The strategy followed consisted on applying mechanical and electronic cues to the cells to mimic *in vivo* conditions, achieving a higher sarcomeric organisation and improving the sarcomeric length to values similar to physiological conditions. Further investigation in this regard could lead to engineering of cardiac patches to replace damaged areas of the heart and to create cellular platforms to detect cardiotoxic effects of drugs.

The combination of additive manufacturing and electrochemical techniques are still under-explored in bioelectronics in general and bioelectronic medicine in particular. It is therefore envisaged that the work shown in this thesis could be used as the foundations of novel bioelectronic

tools with therapeutic interest, and an inspiration across disciplines to create new systems with applications in this area

7.2. Future work

As it was previously stated, the work presented represents foundational insights into the potential of what such an approach can offer, and further development is needed in order to produce systems for their use in bioelectronic medicine.

This could be achieved by, for example, further investigating alternative materials to those used in Chapter 3, as silver is not ideal due to its cytotoxic properties. Conductive polymers could represent a good alternative, as they can be easily printed, are flexible and biocompatible. Conductive structures that can adapt to the morphology of the cells and which growth is controlled remotely would be interesting in the treatment of spinal cord injuries, restoring conductive properties of damaged nerves, and implantable sensors and bionic parts.

Further research in intracellular wireless communication from Chapter 4, in terms of material chemistry of nanoelectronic systems, could direct the nanoparticles to a specific cellular type and trigger a specific redox mediated response when an electronic input is applied. However, mechanisms that mediate these responses need to be studied in detail. The most obvious application for this would be the treatment of cancer, targeting exclusively carcinogenic cells by modification of their surface with specific receptors and

inducing their apoptosis via redox mediated reactions, acting as ‘nanobombs’. These systems could also be used as a ‘biotransducer’, converting electronic inputs into biological outputs and vice versa.

High-resolution conductive cellular scaffolds like the ones presented in Chapter 5 can affect the phenotype of the cells. This could be used as a tool to understand cell biology and offer new disease models, not only in cardiomyocytes but also in many other cell types including neurons, endocrine cells or immune cells. Further study of the specific cues that trigger maturation of cardiomyocytes, by molecular biology methods by quantifying specific maturation markers such as number of mitochondria per cell and/or TNNI1/TNNI3 proteins ratio; would aid the engineering of cardiac patches to replace damaged areas of the heart after an infarction or other pathologies.

To conclude, the systems and tools proposed in this work show the potential for new alternatives to the treatment of diseases and manufacturing of bioelectronic devices, however, further research is still needed. These examples show the synergistic combination of different methods and ultimately different disciplines. In order to further advance the development of bioelectronic systems for their use in bioelectronic medicine, a multidisciplinary approach is required, increasing the prospects of the area and offering new exciting researching opportunities.

References

1. Szent-Györgyi, A., Bioelectronics. *Science* **1968,** *161* (3845), 988-990.
2. Carrara, S.; Iniewski, K., *Handbook of Bioelectronics: Directly Interfacing Electronics and Biological Systems*. Cambridge University Press: 2015.
3. MacVittie, K.; Halámek, J.; Halámková, L.; Southcott, M.; Jemison, W. D.; Lobel, R.; Katz, E., From "cyborg" lobsters to a pacemaker powered by implantable biofuel cells. *Energy Environ Sci* **2013,** *6* (1), 81-86.
4. Shukla, A.; Suresh, P.; Berchmans, S.; Rajendran, A., Biological fuel cells and their applications. *Curr. Sci* **2004,** *87* (4), 455-468.
5. Rabaey, K.; Verstraete, W., Microbial fuel cells: novel biotechnology for energy generation. *Trends Biotechnol* **2005,** *23* (6), 291-8.
6. Clauwaert, P.; Rabaey, K.; Aelterman, P.; de Schamphelaire, L.; Pham, T. H.; Boeckx, P.; Boon, N.; Verstraete, W., Biological denitrification in microbial fuel cells. *Environ Sci Technol* **2007,** *41* (9), 3354-60.
7. Cao, X.; Huang, X.; Liang, P.; Xiao, K.; Zhou, Y.; Zhang, X.; Logan, B. E., A new method for water desalination using microbial desalination cells. *Environ Sci Technol* **2009,** *43* (18), 7148-7152.
8. Tavakoli, M.; Rocha, R. P.; Lourenço, J.; Lu, T.; Majidi, C., Soft bionics hands with a sense of touch through an electronic skin. In *Soft Robotics: Trends, Applications and Challenges*, Springer: 2017; pp 5-10.
9. Thompson, B. C.; Murray, E.; Wallace, G. G., Graphite Oxide to Graphene. Biomaterials to Bionics. *Adv Mater* **2015,** *27* (46), 7563-82.
10. Baaske, M. D.; Foreman, M. R.; Vollmer, F., Single-molecule nucleic acid interactions monitored on a label-free microcavity biosensor platform. *Nat Nanotechnol* **2014,** *9* (11), 933-9.
11. Carrad, D. J.; Mostert, B.; Meredith, P.; Micolich, A. P., Hybrid Nanowire Ion-to-Electron Transducers for Integrated Bioelectronic Circuitry. *Org Sens Bioelectron* **2016,** *9944*.
12. Kumar, A.; Hsu, L. H. H.; Kavanagh, P.; Barrière, F.; Lens, P. N. L.; Lapinsonnière, L.; Schröder, U.; Jiang, X.; Leech, D., The ins and outs of microorganism–electrode electron transfer reactions. *Nat Rev Chem* **2017,** *1* (3), 0024.
13. Woo, D.; Choi, E.; Yoon, Y.; Kim, K.; Jeon, I.; Kang, H., Current–distance–voltage characteristics of electron tunneling through an electrochemical STM junction. *Surf Sci* **2007,** *601* (6), 1554-1559.
14. Zhang, A.; Lieber, C. M., Nano-Bioelectronics. *Chem Rev* **2016,** *116* (1), 215-257.
15. Hormuzdi, S. G.; Filippov, M. A.; Mitropoulou, G.; Monyer, H.; Bruzzone, R., Electrical synapses: a dynamic signaling system that shapes the activity of neuronal networks. *Biochim Biophys Acta* **2004,** *1662* (1-2), 113-137.
16. Torihashi, S.; Ward, S. M.; Nishikawa, S.; Nishi, K.; Kobayashi, S.; Sanders, K. M., c-kit-dependent development of interstitial cells and electrical activity in the murine gastrointestinal tract. *Cell Tissue Res* **1995,** *280* (1), 97-111.
17. Spitzer, N. C., Electrical activity in early neuronal development. *Nature* **2006,** *444* (7120), 707.
18. Gibson, E. M.; Purger, D.; Mount, C. W.; Goldstein, A. K.; Lin, G. L.; Wood, L. S.; Inema, I.; Miller, S. E.; Bieri, G.; Zuchero, J. B., Neuronal activity promotes oligodendrogenesis and adaptive myelination in the mammalian brain. *Science* **2014,** *344* (6183), 1252304.
19. Dean, P. M.; Matthews, E. K., Glucose-induced electrical activity in pancreatic islet cells. *J Physiol* **1970,** *210* (2), 255-64.
20. Skou, J. C., Sodium-potassium pump. In *Membr Transp*, Springer: 1989; pp 155-185.

21. Kandel, E. R.; Schwartz, J. H.; Jessell, T. M.; Biochemistry, D. o.; Jessell, M. B. T.; Siegelbaum, S.; Hudspeth, A., *Principles of neural science*. McGraw-hill New York: 2000; Vol. 4.
22. Cohen, L. B., Changes in neuron structure during action potential propagation and synaptic transmission. *Physiol Rev* **1973,** *53* (2), 373-418.
23. Loewenstein, W. R., Junctional intercellular communication: the cell-to-cell membrane channel. *Physiol Rev* **1981,** *61* (4), 829-913.
24. Guccione, J.; Waldman, L.; McCulloch, A., Mechanics of active contraction in cardiac muscle: Part II—Cylindrical models of the systolic left ventricle. *J Biomech Eng* **1993,** *115* (1), 82-90.
25. Schlegel, W.; Winiger, B. P.; Mollard, P.; Vacher, P.; Wuarin, F.; Zahnd, G. R.; Wollheim, C. B.; Dufy, B., Oscillations of cytosolic Ca2+ in pituitary cells due to action potentials. *Nature* **1987,** *329* (6141), 719.
26. Murer, H.; Hopfer, U., Demonstration of electrogenic Na+-dependent D-glucose transport in intestinal brush border membranes. *Proc Natl Acad Sci U S A* **1974,** *71* (2), 484-8.
27. Gropp, T.; Brustovetsky, N.; Klingenberg, M.; Muller, V.; Fendler, K.; Bamberg, E., Kinetics of electrogenic transport by the ADP/ATP carrier. *Biophys J* **1999,** *77* (2), 714-26.
28. Sundelacruz, S.; Levin, M.; Kaplan, D. L., Role of Membrane Potential in the Regulation of Cell Proliferation and Differentiation. *Stem Cell Rev Rep* **2009,** *5* (3), 231-246.
29. Rothbard, J. B.; Jessop, T. C.; Lewis, R. S.; Murray, B. A.; Wender, P. A., Role of membrane potential and hydrogen bonding in the mechanism of translocation of guanidinium-rich peptides into cells. *J Am Chem Soc* **2004,** *126* (31), 9506-9507.
30. van Horssen, J.; Bo, L.; Vos, C. M.; Virtanen, I.; de Vries, H. E., Basement membrane proteins in multiple sclerosis-associated inflammatory cuffs: potential role in influx and transport of leukocytes. *J Neuropathol Exp Neurol* **2005,** *64* (8), 722-9.
31. Franco, R.; Bortner, C. D.; Cidlowski, J. A., Potential roles of electrogenic ion transport and plasma membrane depolarization in apoptosis. *J Membr Biol* **2006,** *209* (1), 43-58.
32. Levin, M., Molecular bioelectricity: how endogenous voltage potentials control cell behavior and instruct pattern regulation in vivo. *Mol Biol Cell* **2014,** *25* (24), 3835-3850.
33. Boyd, A. W.; Bartlett, P. F.; Lackmann, M., Therapeutic targeting of EPH receptors and their ligands. *Nat Rev Drug Discov* **2014,** *13* (1), 39-62.
34. Bard, A. J.; Faulkner, L. R., *Electrochemical methods: fundamentals and applications*. 2nd ed.; John Wiley & Sons, Inc.: US, 2001.
35. Morokuma, K., Why do molecules interact? The origin of electron donor-acceptor complexes, hydrogen bonding and proton affinity. *Acc Chem Res* **1977,** *10* (8), 294-300.
36. Fultz, M. L.; Durst, R. A., Mediator compounds for the electrochemical study of biological redox systems: a compilation. *Anal Chim Acta* **1982,** *140* (1), 1-18.
37. Gon, S.; Giudici-Orticoni, M. T.; Mejean, V.; Iobbi-Nivol, C., Electron transfer and binding of the c-type cytochrome TorC to the trimethylamine N-oxide reductase in Escherichia coli. *J Biol Chem* **2001,** *276* (15), 11545-51.
38. Holmstrom, K. M.; Finkel, T., Cellular mechanisms and physiological consequences of redox-dependent signalling. *Nat Rev Mol Cell Biol* **2014,** *15* (6), 411-21.
39. Merker, M. P.; Bongard, R. D.; Kettenhofen, N. J.; Okamoto, Y.; Dawson, C. A., Intracellular redox status affects transplasma membrane electron transport in pulmonary arterial endothelial cells. *Am J Physiol Lung Cell Mol Physiol* **2002,** *282* (1), L36-43.
40. Herst, P. M.; Tan, A. S.; Scarlett, D. J.; Berridge, M. V., Cell surface oxygen consumption by mitochondrial gene knockout cells. *Biochim Biophys Acta* **2004,** *1656* (2-3), 79-87.
41. Sherman, H. G.; Jovanovic, C.; Stolnik, S.; Rawson, F. J., Electrochemical System for the Study of Trans-Plasma Membrane Electron Transport in Whole Eukaryotic Cells. *Anal Chem* **2018,** *90* (4), 2780-2786.
42. Sanjuan-Alberte, P.; Alexander, M. R.; Hague, R. J. M.; Rawson, F. J., Electrochemically stimulating developments in bioelectronic medicine. *Bioelectron Med* **2018,** *4* (1), 1.
43. Giaever, I.; Keese, C. R., Micromotion of mammalian cells measured electrically. *Proc Natl Acad Sci U S A* **1991,** *88* (17), 7896-900.
44. Robinson, K. R., The responses of cells to electrical fields: a review. *J Cell Biol* **1985,** *101* (6), 2023-2027.

45. Heiduschka, P.; Thanos, S., Implantable bioelectronic interfaces for lost nerve functions. *Prog Neurobiol* **1998,** *55* (5), 433-461.
46. Humayun, M. S.; de Juan, E., Jr.; Dagnelie, G., The Bionic Eye: A Quarter Century of Retinal Prosthesis Research and Development. *Ophthalmology* **2016,** *123* (10S), S89-S97.
47. Pavlov, V. A.; Tracey, K. J., The vagus nerve and the inflammatory reflex--linking immunity and metabolism. *Nat Rev Endocrinol* **2012,** *8* (12), 743-54.
48. Koopman, F. A.; Chavan, S. S.; Miljko, S.; Grazio, S.; Sokolovic, S.; Schuurman, P. R.; Mehta, A. D.; Levine, Y. A.; Faltys, M.; Zitnik, R. J., Vagus nerve stimulation inhibits cytokine production and attenuates disease severity in rheumatoid arthritis. *Proc Natl Acad Sci* **2016,** *113* (29), 8284-8289.
49. Famm, K.; Litt, B.; Tracey, K. J.; Boyden, E. S.; Slaoui, M., Drug discovery: a jump-start for electroceuticals. *Nature* **2013,** *496* (7444), 159-61.
50. Tracey, K. J., Inhibition of inflammatory cytokine production by cholinergic agonists and vagus nerve stimulation. Google Patents: 2003.
51. Dobrzynski, H.; Boyett, M. R.; Anderson, R. H., New insights into pacemaker activity. *Circulation* **2007,** *115* (14), 1921-1932.
52. Hosobuchi, Y.; Adams, J. E.; Linchitz, R., Pain relief by electrical stimulation of the central gray matter in humans and its reversal by naloxone. *Science* **1977,** *197* (4299), 183-6.
53. Pai, V. P.; Pietak, A.; Willocq, V.; Ye, B.; Shi, N. Q.; Levin, M., HCN2 Rescues brain defects by enforcing endogenous voltage pre-patterns. *Nat Commun* **2018,** *9* (1), 998.
54. Mobini, S.; Talts, Ü.-L.; Xue, R.; Cassidy, N. J.; Cartmell, S. H., Electrical Stimulation Changes Human Mesenchymal Stem Cells Orientation and Cytoskeleton Organization. *J Biomater Tissue Eng* **2017,** *7* (9), 829-833.
55. Chang, F.; Minc, N., Electrochemical control of cell and tissue polarity. *Annu Rev Cell Dev Biol* **2014,** *30*, 317-36.
56. Balint, R.; Cassidy, N. J.; Cartmell, S. H., Electrical stimulation: a novel tool for tissue engineering. *Tissue Eng Part B Rev* **2012,** *19* (1), 48-57.
57. Prevarskaya, N.; Skryma, R.; Shuba, Y., Ion channels and the hallmarks of cancer. *Trends Mol Med* **2010,** *16* (3), 107-121.
58. Hollenhorst, M. I.; Richter, K.; Fronius, M., Ion transport by pulmonary epithelia. *J Biomed Biotechnol* **2011,** *2011*, 174306.
59. Binggeli, R.; Weinstein, R. C., Membrane potentials and sodium channels: hypotheses for growth regulation and cancer formation based on changes in sodium channels and gap junctions. *J Theor Biol* **1986,** *123* (4), 377-401.
60. Tseng, A. S.; Beane, W. S.; Lemire, J. M.; Masi, A.; Levin, M., Induction of vertebrate regeneration by a transient sodium current. *J Neurosci* **2010,** *30* (39), 13192-200.
61. Söhl, G.; Willecke, K., Gap junctions and the connexin protein family. *Cardiovasc Res* **2004,** *62* (2), 228-232.
62. Maziarz, A.; Kocan, B.; Bester, M.; Budzik, S.; Cholewa, M.; Ochiya, T.; Banas, A., How electromagnetic fields can influence adult stem cells: positive and negative impacts. *Stem Cell Res Ther* **2016,** *7* (1), 54.
63. Gordonov, T.; Kim, E.; Cheng, Y.; Ben-Yoav, H.; Ghodssi, R.; Rubloff, G.; Yin, J. J.; Payne, G. F.; Bentley, W. E., Electronic modulation of biochemical signal generation. *Nat Nanotechnol* **2014,** *9* (8), 605-10.
64. Du, J.; Catania, C.; Bazan, G. C., Modification of abiotic–biotic interfaces with small molecules and nanomaterials for improved bioelectronics. *Chem Mater* **2013,** *26* (1), 686-697.
65. Ajo-Franklin, C. M.; Noy, A., Crossing over: nanostructures that move electrons and ions across cellular membranes. *Adv Mater* **2015,** *27* (38), 5797-5804.
66. Saboe, P. O.; Conte, E.; Chan, S.; Feroz, H.; Ferlez, B.; Farell, M.; Poyton, M. F.; Sines, I. T.; Yan, H.; Bazan, G. C., Biomimetic wiring and stabilization of photosynthetic membrane proteins with block copolymer interfaces. *J Mater Chem A* **2016,** *4* (40), 15457-15463.
67. Khodagholy, D.; Doublet, T.; Gurfinkel, M.; Quilichini, P.; Ismailova, E.; Leleux, P.; Herve, T.; Sanaur, S.; Bernard, C.; Malliaras, G. G., Highly conformable conducting polymer electrodes for in vivo recordings. *Adv Mater* **2011,** *23* (36), H268-72.

68. Rawson, F. J.; Cole, M. T.; Hicks, J. M.; Aylott, J. W.; Milne, W. I.; Collins, C. M.; Jackson, S. K.; Silman, N. J.; Mendes, P. M., Electrochemical communication with the inside of cells using micro-patterned vertical carbon nanofibre electrodes. *Sci Rep* **2016,** *6*, 37672.
69. Rawson, F. J.; Yeung, C. L.; Jackson, S. K.; Mendes, P. M., Tailoring 3D single-walled carbon nanotubes anchored to indium tin oxide for natural cellular uptake and intracellular sensing. *Nano Lett.* **2012,** *13* (1), 1-8.
70. Gooding, J. J.; Wibowo, R.; Liu, J.; Yang, W.; Losic, D.; Orbons, S.; Mearns, F. J.; Shapter, J. G.; Hibbert, D. B., Protein electrochemistry using aligned carbon nanotube arrays. *J. Am. Chem. Soc.* **2003,** *125* (30), 9006-9007.
71. Rawson, F. J.; Hicks, J.; Dodd, N.; Abate, W.; Garrett, D. J.; Yip, N.; Fejer, G.; Downard, A. J.; Baronian, K. H. R.; Jackson, S. K., Fast, ultrasensitive detection of reactive oxygen species using a carbon nanotube based-electrocatalytic intracellular sensor. *ACS Appl Mater Inter* **2015,** *7* (42), 23527-23537.
72. Stephenson-Brown, A.; Yong, S.; Mansor, M. H.; Hussein, Z.; Yip, N. C.; Mendes, P. M.; Fossey, J. S.; Rawson, F. J., Electronic communication of cells with a surface mediated by boronic acid saccharide interactions. *Chem Commun* **2015,** *51* (97), 17213-6.
73. Strakosas, X.; Selberg, J.; Hemmatian, Z.; Rolandi, M., Taking Electrons out of Bioelectronics: From Bioprotonic Transistors to Ion Channels. *Adv Sci* **2017**.
74. Simon, D. T.; Kurup, S.; Larsson, K. C.; Hori, R.; Tybrandt, K.; Goiny, M.; Jager, E. W.; Berggren, M.; Canlon, B.; Richter-Dahlfors, A., Organic electronics for precise delivery of neurotransmitters to modulate mammalian sensory function. *Nat Mater* **2009,** *8* (9), 742-6.
75. Tschirhart, T.; Kim, E.; McKay, R.; Ueda, H.; Wu, H.; Pottash, A. E.; Zargar, A.; Negrete, A.; Shiloach, J.; Payne, G. F., Electronic control of gene expression and cell behaviour in Escherichia coli through redox signalling. *Nat Comm* **2017,** *8*, 14030.
76. Rawson, F. J., New dimensions in controlling cellular function with electroceutics. *Ther Deliv* **2015,** *6* (1), 5-8.
77. Ward, W. K., A review of the foreign-body response to subcutaneously-implanted devices: the role of macrophages and cytokines in biofouling and fibrosis. SAGE Publications: 2008.
78. Liu, J.; Xie, C.; Dai, X.; Jin, L.; Zhou, W.; Lieber, C. M., Multifunctional Three-Dimensional Macroporous Nanoelectronic Networks for Smart Materials. *Proc Natl Acad Sci U S A* **2013,** *110* (17), 6694-6699.
79. Malliaras, G.; Abidian, M. R., Organic Bioelectronic Materials and Devices. *Adv Mater* **2015,** *27* (46), 7492.
80. Liu, J.; Fu, T.-M.; Cheng, Z.; Hong, G.; Zhou, T.; Jin, L.; Duvvuri, M.; Jiang, Z.; Kruskal, P.; Xie, C.; Suo, Z.; Fang, Y.; Lieber, C. M., Syringe-injectable electronics. *Nat Nano* **2015,** *10* (7), 629-636.
81. Akinwande, D.; Petrone, N.; Hone, J., Two-Dimensional Flexible Nanoelectronics. *Nat Commun* **2014,** *5*, 5678.
82. Zeng, W.; Shu, L.; Li, Q.; Chen, S.; Wang, F.; Tao, X. M., Fiber-based wearable electronics: a review of materials, fabrication, devices, and applications. *Adv Mater* **2014,** *26* (31), 5310-36.
83. Qing, Q.; Jiang, Z.; Xu, L.; Gao, R.; Mai, L.; Lieber, C. M., Free-Standing Kinked Nanowire Transistor Probes for Targeted Intracellular Recording in Three Dimensions. *Nat Nanotechnol* **2014,** *9* (2), 142-147.
84. Gao, R.; Strehle, S.; Tian, B.; Cohen-Karni, T.; Xie, P.; Duan, X.; Qing, Q.; Lieber, C. M., Outside looking in: Nanotube transistor intracellular sensors. *Nano Lett.* **2012,** *12* (6), 3329-3333.
85. García-Carmona, L.; Moreno-Guzmán, M.; Martín, A.; Martínez, S. B.; Fernández-Martínez, A. B.; González, M. C.; Lucio-Cazaña, J.; Escarpa, A., Aligned copper nanowires as a cut-and-paste exclusive electrochemical transducer for free-enzyme highly selective quantification of intracellular hydrogen peroxide in cisplatin-treated cells. *Biosens Bioelectron* **2017,** *96*, 146-151.

86. Xie, C.; Liu, J.; Fu, T.-M.; Dai, X.; Zhou, W.; Lieber, C. M., Three-dimensional macroporous nanoelectronic networks as minimally invasive brain probes. *Nat mater* **2015,** *14* (12), 1286-1292.
87. Kim, T. I.; McCall, J. G.; Jung, Y. H.; Huang, X.; Siuda, E. R.; Li, Y.; Song, J.; Song, Y. M.; Pao, H. A.; Kim, R. H.; Lu, C.; Lee, S. D.; Song, I. S.; Shin, G.; Al-Hasani, R.; Kim, S.; Tan, M. P.; Huang, Y.; Omenetto, F. G.; Rogers, J. A.; Bruchas, M. R., Injectable, Cellular-Scale Optoelectronics with Applications for Wireless Optogenetics. *Science* **2013,** *340* (6129), 211-216.
88. Someya, T.; Bao, Z.; Malliaras, G. G., The rise of plastic bioelectronics. *Nature* **2016,** *540* (7633), 379.
89. Kim, J.; de Araujo, W. R.; Samek, I. A.; Bandodkar, A. J.; Jia, W.; Brunetti, B.; Paixão, T. R. L. C.; Wang, J., Wearable temporary tattoo sensor for real-time trace metal monitoring in human sweat. *Electrochem Commun* **2015,** *51*, 41-45.
90. Srivastava, S. K.; Yadav, V. G., Bionic Manufacturing: Towards Cyborg Cells and Sentient Microbots. *Trends Biotechnol* **2018,** *36* (5), 483-487.
91. Fakhrullin, R. F.; Zamaleeva, A. I.; Minullina, R. T.; Konnova, S. A.; Paunov, V. N., Cyborg cells: functionalisation of living cells with polymers and nanomaterials. *Chem Soc Rev* **2012,** *41* (11), 4189-206.
92. Niu, J.; Lunn, D. J.; Pusuluri, A.; Yoo, J. I.; O'Malley, M. A.; Mitragotri, S.; Soh, H. T.; Hawker, C. J., Engineering live cell surfaces with functional polymers via cytocompatible controlled radical polymerization. *Nat Chem* **2017,** *9* (6), 537-545.
93. Konnova, S. A.; Lvov, Y. M.; Fakhrullin, R. F., Nanoshell Assembly for Magnet-Responsive Oil-Degrading Bacteria. *Langmuir* **2016,** *32* (47), 12552-12558.
94. Stanton, M. M.; Park, B. W.; Miguel-Lopez, A.; Ma, X.; Sitti, M.; Sanchez, S., Biohybrid Microtube Swimmers Driven by Single Captured Bacteria. *Small* **2017,** *13* (19).
95. Rogers, J. A., Electronics for the human body. *Jama* **2015,** *313* (6), 561-562.
96. Kong, Y. L.; Gupta, M. K.; Johnson, B. N.; McAlpine, M. C., 3D Printed Bionic Nanodevices. *Nano Today* **2016,** *11* (3), 330-350.
97. Mannoor, M. S.; Jiang, Z.; James, T.; Kong, Y. L.; Malatesta, K. A.; Soboyejo, W. O.; Verma, N.; Gracias, D. H.; McAlpine, M. C., 3D Printed Bionic Ears. *Nano Lett* **2013,** *13* (6), 2634-2639.
98. Crespi, F., Wireless in vivo voltammetric measurements of neurotransmitters in freely behaving rats. *Biosens Bioelectron* **2010,** *25* (11), 2425-30.
99. Park, S. I.; Brenner, D. S.; Shin, G.; Morgan, C. D.; Copits, B. A.; Chung, H. U.; Pullen, M. Y.; Noh, K. N.; Davidson, S.; Oh, S. J.; Yoon, J.; Jang, K. I.; Samineni, V. K.; Norman, M.; Grajales-Reyes, J. G.; Vogt, S. K.; Sundaram, S. S.; Wilson, K. M.; Ha, J. S.; Xu, R.; Pan, T.; Kim, T. I.; Huang, Y.; Montana, M. C.; Golden, J. P.; Bruchas, M. R.; Gereau, R. W. t.; Rogers, J. A., Soft, stretchable, fully implantable miniaturized optoelectronic systems for wireless optogenetics. *Nat Biotechnol* **2015,** *33* (12), 1280-1286.
100. Kim, T.-i.; McCall, J. G.; Jung, Y. H.; Huang, X.; Siuda, E. R.; Li, Y.; Song, J.; Song, Y. M.; Pao, H. A.; Kim, R.-H., Injectable, cellular-scale optoelectronics with applications for wireless optogenetics. *Science* **2013,** *340* (6129), 211-216.
101. Perelaer, J.; Smith, P. J.; Mager, D.; Soltman, D.; Volkman, S. K.; Subramanian, V.; Korvink, J. G.; Schubert, U. S., Printed electronics: the challenges involved in printing devices, interconnects, and contacts based on inorganic materials. *J. Mater. Chem.* **2010,** *20* (39), 8446-8453.
102. Subramanian, V.; Chang, J. B.; de la Fuente Vornbrock, A.; Huang, D. C.; Jagannathan, L.; Liao, F.; Mattis, B.; Molesa, S.; Redinger, D. R.; Soltman, D. In *Printed electronics for low-cost electronic systems: Technology status and application development*, Solid-State Circuits Conference, 2008. ESSCIRC 2008. 34th European, IEEE: 2008; pp 17-24.
103. Kong, Y. L.; Tamargo, I. A.; Kim, H.; Johnson, B. N.; Gupta, M. K.; Koh, T. W.; Chin, H. A.; Steingart, D. A.; Rand, B. P.; McAlpine, M. C., 3D printed quantum dot light-emitting diodes. *Nano Lett* **2014,** *14* (12), 7017-23.

104. Banerjee, K.; Souri, S. J.; Kapur, P.; Saraswat, K. C., 3-D ICs: A novel chip design for improving deep-submicrometer interconnect performance and systems-on-chip integration. *Proc IEEE* **2001,** *89* (5), 602-633.
105. Lewis, J. A.; Ahn, B. Y., Device fabrication: Three-dimensional printed electronics. *Nature* **2015,** *518* (7537), 42-3.
106. Secor, E. B.; Hersam, M. C., Emerging Carbon and Post-Carbon Nanomaterial Inks for Printed Electronics. *J Phys Chem Lett* **2015,** *6* (4), 620-6.
107. Compton, B. G.; Lewis, J. A., 3D-printing of lightweight cellular composites. *Adv Mater* **2014,** *26* (34), 5930-5.
108. Ning, F.; Cong, W.; Qiu, J.; Wei, J.; Wang, S., Additive manufacturing of carbon fiber reinforced thermoplastic composites using fused deposition modeling. *Comp Part B* **2015,** *80*, 369-378.
109. Herzog, D.; Seyda, V.; Wycisk, E.; Emmelmann, C., Additive manufacturing of metals. *Acta Biomater* **2016,** *117*, 371-392.
110. Eckel, Z. C.; Zhou, C.; Martin, J. H.; Jacobsen, A. J.; Carter, W. B.; Schaedler, T. A., Additive manufacturing of polymer-derived ceramics. *Science* **2016,** *351* (6268), 58-62.
111. EP/P031684/1: Enabling Next Generation Additive Manufacturing https://gow.epsrc.ukri.org/NGBOViewGrant.aspx?GrantRef=EP/P031684/1.
112. Sun, K.; Wei, T. S.; Ahn, B. Y.; Seo, J. Y.; Dillon, S. J.; Lewis, J. A., 3D printing of interdigitated Li-ion microbattery architectures. *Adv Mater* **2013,** *25* (33), 4539-43.
113. Wang, Y.; Chen, C.; Xie, H.; Gao, T.; Yao, Y.; Pastel, G.; Han, X.; Li, Y.; Zhao, J.; Fu, K. K., 3D-Printed All-Fiber Li-Ion Battery toward Wearable Energy Storage. *Adv Funct Mater* **2017,** *27* (43).
114. Bihar, E.; Roberts, T.; Zhang, Y.; Ismailova, E.; Herve, T.; Malliaras, G.; De Graaf, J. B.; Inal, S.; Saadaoui, M., Fully printed all-polymer tattoo/textile electronics for electromyography. *Flex Print Electron* **2018**.
115. Zhu, Z.; Guo, S. Z.; Hirdler, T.; Eide, C.; Fan, X.; Tolar, J.; McAlpine, M. C., 3D Printed Functional and Biological Materials on Moving Freeform Surfaces. *Adv Mater* **2018,** *30* (23), e1707495.
116. Forrest, S. R., The path to ubiquitous and low-cost organic electronic appliances on plastic. *Nature* **2004,** *428* (6986), 911-8.
117. ASTM F2792-12a, Standard Terminology for Additive Manufacturing Technologies, (Withdrawn 2015), ASTM International, West Conshohocken, PA, 2012, www.astm.org.
118. Bai, Y.; Williams, C. B., An exploration of binder jetting of copper. *Rapid Prototyp J* **2015,** *21* (2), 177-185.
119. Gaytan, S.; Cadena, M.; Karim, H.; Delfin, D.; Lin, Y.; Espalin, D.; MacDonald, E.; Wicker, R., Fabrication of barium titanate by binder jetting additive manufacturing technology. *Ceramics Inter* **2015,** *41* (5), 6610-6619.
120. Pinkerton, A. J., Lasers in additive manufacturing. *Optics Laser Technol* **2016,** *78*, 25-32.
121. Shah, K.; ul Haq, I.; Khan, A.; Shah, S. A.; Khan, M.; Pinkerton, A. J., Parametric study of development of Inconel-steel functionally graded materials by laser direct metal deposition. *Mater Design* **2014,** *54*, 531-538.
122. Pouzet, S.; Peyre, P.; Gorny, C.; Castelnau, O.; Baudin, T.; Brisset, F.; Colin, C.; Gadaud, P., Additive layer manufacturing of titanium matrix composites using the direct metal deposition laser process. *Mater Sci Eng A* **2016,** *677*, 171-181.
123. Muth, J. T.; Vogt, D. M.; Truby, R. L.; Mengüç, Y.; Kolesky, D. B.; Wood, R. J.; Lewis, J. A., Embedded 3D printing of strain sensors within highly stretchable elastomers. *Adv Mater* **2014,** *26* (36), 6307-6312.
124. Qiu, K.; Haghiashtiani, G.; McAlpine, M. C., 3D Printed Organ Models for Surgical Applications. *Annu Rev Anal Chem* **2018,** *11* (1), 287-306.
125. Kabiri Ameri, S.; Ho, R.; Jang, H.; Tao, L.; Wang, Y.; Wang, L.; Schnyer, D. M.; Akinwande, D.; Lu, N., Graphene Electronic Tattoo Sensors. *ACS Nano* **2017,** *11* (8), 7634-7641.

126. Vaithilingam, J.; Saleh, E.; Körner, L.; Wildman, R. D.; Hague, R. J.; Leach, R. K.; Tuck, C. J., 3-Dimensional inkjet printing of macro structures from silver nanoparticles. *Mater Design* **2018,** *139*, 81-88.
127. Eggenhuisen, T.; Galagan, Y.; Biezemans, A.; Slaats, T.; Voorthuijzen, W.; Kommeren, S.; Shanmugam, S.; Teunissen, J.; Hadipour, A.; Verhees, W., High efficiency, fully inkjet printed organic solar cells with freedom of design. *J Mater Chem A* **2015,** *3* (14), 7255-7262.
128. Gao, M.; Li, L.; Song, Y., Inkjet printing wearable electronic devices. *J Mater Chem C* **2017,** *5* (12), 2971-2993.
129. Ruecha, N.; Chailapakul, O.; Suzuki, K.; Citterio, D., Fully Inkjet-Printed Paper-Based Potentiometric Ion-Sensing Devices. *Anal Chem* **2017,** *89* (19), 10608-10616.
130. Hossain, M. S.; Gonzalez, J. A.; Hernandez, R. M.; Shuvo, M. A. I.; Mireles, J.; Choudhuri, A.; Lin, Y.; Wicker, R. B., Fabrication of smart parts using powder bed fusion additive manufacturing technology. *Addit Manuf* **2016,** *10*, 58-66.
131. Love, L. J.; Lind, R. F.; Jansen, J. F. In *Mesofluidic actuation for articulated finger and hand prosthetics*, Intelligent Robots and Systems, 2009. IROS 2009. IEEE/RSJ International Conference on, IEEE: 2009; pp 2586-2591.
132. Luong, D. X.; Subramanian, A. K.; Silva, G. A. L.; Yoon, J.; Cofer, S.; Yang, K.; Owuor, P. S.; Wang, T.; Wang, Z.; Lou, J.; Ajayan, P. M.; Tour, J. M., Laminated Object Manufacturing of 3D-Printed Laser-Induced Graphene Foams. *Adv Mater* **2018**, e1707416.
133. Blasco, E.; Muller, J.; Muller, P.; Trouillet, V.; Schon, M.; Scherer, T.; Barner-Kowollik, C.; Wegener, M., Fabrication of Conductive 3D Gold-Containing Microstructures via Direct Laser Writing. *Adv Mater* **2016,** *28* (18), 3592-5.
134. Hu, Q.; Sun, X. Z.; Parmenter, C. D. J.; Fay, M. W.; Smith, E. F.; Rance, G. A.; He, Y.; Zhang, F.; Liu, Y.; Irvine, D.; Tuck, C.; Hague, R.; Wildman, R., Additive manufacture of complex 3D Au-containing nanocomposites by simultaneous two-photon polymerisation and photoreduction. *Sci Rep* **2017,** *7* (1), 17150.
135. Staudinger, U.; Zyla, G.; Krause, B.; Janke, A.; Fischer, D.; Esen, C.; Voit, B.; Ostendorf, A., Development of electrically conductive microstructures based on polymer/CNT nanocomposites via two-photon polymerization. *Microelectron Eng* **2017,** *179*, 48-55.
136. Ahn, B. Y.; Duoss, E. B.; Motala, M. J.; Guo, X.; Park, S. I.; Xiong, Y.; Yoon, J.; Nuzzo, R. G.; Rogers, J. A.; Lewis, J. A., Omnidirectional printing of flexible, stretchable, and spanning silver microelectrodes. *Science* **2009,** *323* (5921), 1590-3.
137. Cummins, G.; Desmulliez, M. P. Y., Inkjet printing of conductive materials: a review. *Circuit World* **2012,** *38* (4), 193-213.
138. Cui, X.; Dean, D.; Ruggeri, Z. M.; Boland, T., Cell damage evaluation of thermal inkjet printed Chinese hamster ovary cells. *Biotechnol Bioeng* **2010,** *106* (6), 963-9.
139. Ko, S. H.; Pan, H.; Grigoropoulos, C. P.; Luscombe, C. K.; Fréchet, J. M. J.; Poulikakos, D., All-inkjet-printed flexible electronics fabrication on a polymer substrate by low-temperature high-resolution selective laser sintering of metal nanoparticles. *Nanotechnology* **2007,** *18* (34), 345202.
140. Van Osch, T. H. J.; Perelaer, J.; de Laat, A. W. M.; Schubert, U. S., Inkjet printing of narrow conductive tracks on untreated polymeric substrates. *Adv Mater* **2008,** *20* (2), 343-345.
141. Ko, S. H.; Chung, J.; Hotz, N.; Nam, K. H.; Grigoropoulos, C. P., Metal nanoparticle direct inkjet printing for low-temperature 3D micro metal structure fabrication. *J Micromech Microeng* **2010,** *20* (12), 125010.
142. Kim, J. H.; Chang, W. S.; Kim, D.; Yang, J. R.; Han, J. T.; Lee, G. W.; Kim, J. T.; Seol, S. K., 3D printing of reduced graphene oxide nanowires. *Adv Mater* **2015,** *27* (1), 157-61.
143. Singh, M.; Haverinen, H. M.; Dhagat, P.; Jabbour, G. E., Inkjet printing—process and its applications. *Adv Mater* **2010,** *22* (6), 673-685.
144. Saunders, R. E.; Gough, J. E.; Derby, B., Delivery of human fibroblast cells by piezoelectric drop-on-demand inkjet printing. *Biomaterials* **2008,** *29* (2), 193-203.
145. de Gans, B. J.; Duineveld, P. C.; Schubert, U. S., Inkjet printing of polymers: state of the art and future developments. *Adv Mater* **2004,** *16* (3), 203-213.

146. Magliulo, M.; Mulla, M. Y.; Singh, M.; Macchia, E.; Tiwari, A.; Torsi, L.; Manoli, K., Printable and flexible electronics: from TFTs to bioelectronic devices. *J Mater Chem C* **2015,** *3* (48), 12347-12363.
147. Derby, B., Inkjet printing of functional and structural materials: fluid property requirements, feature stability, and resolution. *Annu Rev Mater* **2010,** *40*, 395-414.
148. Cummins, G.; Desmulliez, M. P., Inkjet printing of conductive materials: a review. *Circuit World* **2012,** *38* (4), 193-213.
149. Calvert, P., Inkjet printing for materials and devices. *Chem Mater* **2001,** *13* (10), 3299-3305.
150. Öhlund, T.; Örtegren, J.; Forsberg, S.; Nilsson, H. E., Paper surfaces for metal nanoparticle inkjet printing. *Appl Surf Sci* **2012,** *259*, 731-739.
151. Van Osch, T. H.; Perelaer, J.; de Laat, A. W.; Schubert, U. S., Inkjet printing of narrow conductive tracks on untreated polymeric substrates. *Adv Mater* **2008,** *20* (2), 343-345.
152. Sirringhaus, H.; Kawase, T.; Friend, R.; Shimoda, T.; Inbasekaran, M.; Wu, W.; Woo, E., High-resolution inkjet printing of all-polymer transistor circuits. *Science* **2000,** *290* (5499), 2123-2126.
153. Kordas, K.; Mustonen, T.; Toth, G.; Jantunen, H.; Lajunen, M.; Soldano, C.; Talapatra, S.; Kar, S.; Vajtai, R.; Ajayan, P. M., Inkjet printing of electrically conductive patterns of carbon nanotubes. *Small* **2006,** *2* (8-9), 1021-5.
154. Huang, L.; Huang, Y.; Liang, J.; Wan, X.; Chen, Y., Graphene-based conducting inks for direct inkjet printing of flexible conductive patterns and their applications in electric circuits and chemical sensors. *Nano Res* **2011,** *4* (7), 675-684.
155. Chen, Y.; Chen, G.; Cui, Y.; Yang, Y., Preparation and Performance Study of Paper-Based Resin Nano-silver Inkjet Conductive Ink. In *Adv Graph Comm PackTechnol Mater*, Springer: 2016; pp 1001-1010.
156. Nie, X.; Wang, H.; Zou, J., Inkjet printing of silver citrate conductive ink on PET substrate. *Appl Surf Sci* **2012,** *261*, 554-560.
157. Shim, Y. B.; Won, M. S.; Park, S. M., Electrochemistry of conductive polymers VIII in situ spectroelectrochemical studies of polyaniline growth mechanisms. *J Electrochem Soc* **1990,** *137* (2), 538-544.
158. Balint, R.; Cassidy, N. J.; Cartmell, S. H., Conductive polymers: Towards a smart biomaterial for tissue engineering. *Acta Biomater* **2014,** *10* (6), 2341-2353.
159. Hu, L.; Hecht, D. S.; Gruner, G., Carbon nanotube thin films: fabrication, properties, and applications. *Chem Rev* **2010,** *110* (10), 5790-844.
160. Bhuian, B.; Winfield, R. J.; O'Brien, S.; Crean, G. M., Pattern generation using axicon lens beam shaping in two-photon polymerisation. *Appl Surf Sci* **2007,** *254* (4), 841-844.
161. Wu, S.; Serbin, J.; Gu, M., Two-photon polymerisation for three-dimensional micro-fabrication. *J Photochem Photobiol A Chem* **2006,** *181* (1), 1-11.
162. Ushiba, S.; Shoji, S.; Masui, K.; Kuray, P.; Kono, J.; Kawata, S., 3D microfabrication of single-wall carbon nanotube/polymer composites by two-photon polymerization lithography. *Carbon* **2013,** *59*, 283-288.
163. Ushiba, S.; Shoji, S.; Masui, K.; Kono, J.; Kawata, S., Direct laser writing of 3D architectures of aligned carbon nanotubes. *Adv Mater* **2014,** *26* (32), 5653-7.
164. Xiong, W.; Liu, Y.; Jiang, L. J.; Zhou, Y. S.; Li, D. W.; Jiang, L.; Silvain, J. F.; Lu, Y. F., Laser-Directed Assembly of Aligned Carbon Nanotubes in Three Dimensions for Multifunctional Device Fabrication. *Adv Mater* **2016,** *28* (10), 2002-9.
165. Wildman, R.; Hu, Q.; Liu, Y.; Tuck, C.; Hague, R. *Combining Two-Photon Polymerisation and Photoreduction to Enable the Manufacture of Metamaterials at the Nanosale*; University of Nottingham Nottingham 2016.
166. Marino, A.; Filippeschi, C.; Mattoli, V.; Mazzolai, B.; Ciofani, G., Biomimicry at the nanoscale: current research and perspectives of two-photon polymerization. *Nanoscale* **2015,** *7* (7), 2841-2850.
167. Koroleva, A.; Deiwick, A.; Nguyen, A.; Schlie-Wolter, S.; Narayan, R.; Timashev, P.; Popov, V.; Bagratashvili, V.; Chichkov, B., Osteogenic differentiation of human mesenchymal

stem cells in 3-D Zr-Si organic-inorganic scaffolds produced by two-photon polymerization technique. *PLoS One* **2015,** *10* (2), e0118164.
168. Worthington, K. S.; Wiley, L. A.; Kaalberg, E. E.; Collins, M. M.; Mullins, R. F.; Stone, E. M.; Tucker, B. A., Two-photon polymerization for production of human iPSC-derived retinal cell grafts. *Acta Biomater* **2017,** *55*, 385-395.
169. Lvov, S. N., *Introduction to Electrochemical Science and Engineering*. USA, 2014.
170. Elgrishi, N.; Rountree, K. J.; McCarthy, B. D.; Rountree, E. S.; Eisenhart, T. T.; Dempsey, J. L., A Practical Beginner's Guide to Cyclic Voltammetry. *J Chem Educ* **2017,** *95* (2), 197-206.
171. Huggins, R. A., *Energy Storage: Fundamentals, Materials and Applications*. 2nd ed.; USA, 2015.
172. Mabbott, G. A., An introduction to Cyclic Voltammetry. *J Chem Educ* **1983,** *60* (9), 697-702.
173. Frumkin, A., The double layer in electrochemistry. *J Electrochem Soc* **1960,** *107* (5), 461-472.
174. Vetter, K. J., *Electrochemical kinetics: theoretical aspects*. Elsevier: 2013.
175. Adamson, A. W.; Gast, A. P., Phys Chem Surf. **1967**.
176. Pera, M.-C.; Hissel, D.; Gualous, H., *Electrochemical Components*. Somerset, NJ, USA, 2013.
177. Buck, R. P., Kinetics of Bulk and Interfacial Ionic Motion: Microscopic Bases and Limits for the Nernst-Plank Equation Applied to Membrane Systems. *J Memb Sci* **1984,** *17*, 1-62.
178. Maex, R.; Jaeger, D.; Jung, R., *Encyclopedia of Computational Neuroscience*. USA, 2014.
179. Kissinger, P. T.; Heineman, W. R., Cyclic Voltammetry. *J Chem Educ* **1983,** *60* (9), 702-706.
180. Heinze, J., Cyclic Voltammetry - "Electrochemical Spectroscopy". *Ang Chem Inter Ed Eng* **1984,** *23* (11), 831-918.
181. Barsoukov, E.; Macdonald, J. R., *Impedance spectroscopy: theory, experiment, and applications*. John Wiley & Sons: 2018.
182. Orazem, M. E.; Tribollet, B., *Electrochemical impedance spectroscopy*. John Wiley & Sons: 2011; Vol. 48.
183. Loget, G.; Kuhn, A., Shaping and exploring the micro- and nanoworld using bipolar electrochemistry. *Anal Bioanal Chem* **2011,** *400* (6), 1691-1704.
184. Fosdick, S. E.; Knust, K. N.; Scida, K.; Crooks, R. M., Bipolar electrochemistry. *Angew Chem Intern Ed* **2013,** *52* (40), 10438-10456.
185. Bouffier, L.; Arbault, S.; Kuhn, A.; Sojic, N., Generation of electrochemiluminescence at bipolar electrodes: concepts and applications. *Analytical and Bioanalytical Chemistry* **2016**, 1-9.
186. Bouffier, L.; Arbault, S.; Kuhn, A.; Sojic, N., Generation of electrochemiluminescence at bipolar electrodes: concepts and applications. *Anal Bioanal Chem* **2016**, 1-9.
187. Gupta, C. K.; Sathiyamoorthy, D., *Fluid bed technology in materials processing*. CRC Press: 1998.
188. Loget, G.; Roche, J.; Kuhn, A., True bulk synthesis of Janus objects by bipolar electrochemistry. *Advanced Materials* **2012,** *24* (37), 5111-5116.
189. Fleischmann, M.; Ghoroghchian, J.; Pons, S., Electrochemical behavior of dispersions of spherical ultramicroelectrodes. 1. Theoretical considerations. *J Phys Chem* **1985,** *89* (25), 5530-5536.
190. Fleischmann, M.; Ghoroghchian, J.; Rolison, D.; Pons, S., Electrochemical behavior of dispersions of spherical ultramicroelectrodes. *J Phys Chem* **1986,** *90* (23), 6392-6400.
191. Fattah, Z.; Loget, G.; Lapeyre, V.; Garrigue, P.; Warakulwit, C.; Limtrakul, J.; Bouffier, L.; Kuhn, A., Straightforward single-step generation of microswimmers by bipolar electrochemistry. *Electrochim Acta* **2011,** *56* (28), 10562-10566.
192. Pumera, M., Electrochemically powered self-propelled electrophoretic nanosubmarines. *Nanoscale* **2010,** *2* (9), 1643-9.
193. Gao, W.; Feng, X.; Pei, A.; Kane, C. R.; Tam, R.; Hennessy, C.; Wang, J., Bioinspired Helical Microswimmers Based on Vascular Plants. *Nano Lett* **2014,** *14* (1), 305-310.

194. Wang, J., Can man-made nanomachines compete with nature biomotors? *ACS Nano* **2009,** *3* (1), 4-9.
195. Mei, Y.; Solovev, A. A.; Sanchez, S.; Schmidt, O. G., Rolled-up nanotech on polymers: from basic perception to self-propelled catalytic microengines. *Chem Soc Rev* **2011,** *40* (5), 2109-19.
196. Patra, D.; Sengupta, S.; Duan, W.; Zhang, H.; Pavlick, R.; Sen, A., Intelligent, self-powered, drug delivery systems. *Nanoscale* **2013,** *5* (4), 1273-83.
197. Wang, J.; Gao, W., Nano/microscale motors: biomedical opportunities and challenges. *ACS nano* **2012,** *6* (7), 5745-5751.
198. Xiao, Y.; Xu, L.; Qi, L.-W., Electrochemiluminescence bipolar electrode array for the multiplexed detection of glucose, lactate and choline based on a versatile enzymatic approach. *Talanta* **2017,** *165*, 577-583.
199. Chow, K. F.; Mavre, F.; Crooks, R. M., Wireless electrochemical DNA microarray sensor. *J Am Chem Soc* **2008,** *130* (24), 7544-5.
200. Chow, K.-F.; Chang, B.-Y.; Zaccheo, B. A.; Mavré, F.; Crooks, R. M., A sensing platform based on electrodissolution of a Ag bipolar electrode. *J Am Chem Soc* **2010,** *132* (27), 9228-9229.
201. Mavre, F.; Anand, R. K.; Laws, D. R.; Chow, K. F.; Chang, B. Y.; Crooks, J. A.; Crooks, R. M., Bipolar electrodes: a useful tool for concentration, separation, and detection of analytes in microelectrochemical systems. *Anal Chem* **2010,** *82* (21), 8766-74.
202. Wu, S.; Zhou, Z.; Xu, L.; Su, B.; Fang, Q., Integrating bipolar electrochemistry and electrochemiluminescence imaging with microdroplets for chemical analysis. *Biosens Bioelectron* **2014,** *53*, 148-53.
203. Wu, M. S.; Qian, G. S.; Xu, J. J.; Chen, H. Y., Sensitive electrochemiluminescence detection of c-Myc mRNA in breast cancer cells on a wireless bipolar electrode. *Anal Chem* **2012,** *84* (12), 5407-14.
204. Carlsen, R. W.; Edwards, M. R.; Zhuang, J.; Pacoret, C.; Sitti, M., Magnetic steering control of multi-cellular bio-hybrid microswimmers. *Lab on a Chip* **2014,** *14* (19), 3850-3859.
205. Yim, S.; Sitti, M., Design and rolling locomotion of a magnetically actuated soft capsule endoscope. *IEEE Trans Robot* **2012,** *28* (1), 183-194.
206. Liu, H.; Zhou, X.; Liu, W.; Yang, X.; Xing, D., based bipolar electrode electrochemiluminescence switch for label-free and sensitive genetic detection of pathogenic bacteria. *Anal Chem* **2016,** *88* (20), 10191-10197.
207. Särkkä, H.; Bhatnagar, A.; Sillanpää, M., Recent developments of electro-oxidation in water treatment—a review. *J Electroanal Chem* **2015,** *754*, 46-56.
208. Arjmand, M. M.; Rezaee, A.; Nasseri, S.; Eshraghi, S. S., Removing Bacillus subtilis spores from drinking water using a bipolar electrochemical method. *Inter J Electrochem Sci* **2016,** *11* (12), 10080-10086.
209. Anand, R. K.; Johnson, E. S.; Chiu, D. T., Negative dielectrophoretic capture and repulsion of single cells at a bipolar electrode: The impact of faradaic ion enrichment and depletion. *J Am Chem Soc* **2015,** *137* (2), 776-783.
210. Fortney, L. R., *Principles of electronics: analog and digital*. Oxford University Press: 1987.
211. Frenzel, L. E., *Electronics explained: the new systems approach to learning electronics*. Newnes: 2010.
212. Brindley, K., *Starting electronics*. Elsevier: 2011.
213. McDermott, L. C.; Shaffer, P. S., Research as a guide for curriculum development: An example from introductory electricity. Part I: Investigation of student understanding. *Am J Phys* **1992,** *60* (11), 994-1003.
214. Gates, E., *Introduction to Basic Electricity and Electronics Technology*. 2013.
215. Martin, R. M., *Electronic structure: basic theory and practical methods*. Cambridge University Press Cambridge, United Kingdom: 1999.
216. Hopfield, J. J.; Tank, D. W., Computing with neural circuits: A model. *Science* **1986,** *233* (4764), 625-633.

217. Plant, A. L.; Gueguetchkeri, M.; Yap, W., Supported phospholipid/alkanethiol biomimetic membranes: insulating properties. *Biophys J* **1994,** *67* (3), 1126-33.
218. Johnston, D.; Wu, S. M.-S., *Foundations of cellular neurophysiology*. MIT press: 1994.
219. Joyner, R. W.; Westerfield, M.; Moore, J. W.; Stockbridge, N., A numerical method to model excitable cells. *Biophys J* **1978,** *22* (2), 155-70.
220. Beeman, D., Hodgkin-Huxley model. *E Comput Neurosci* **2015**, 1389-1399.
221. Hodgkin, A. L.; Huxley, A. F.; Katz, B., Measurement of current-voltage relations in the membrane of the giant axon of Loligo. *J Physiol* **1952,** *116* (4), 424-448.
222. Grattarola, M.; Martinoia, S., Modeling the neuron-microtransducer junction: from extracellular to patch recording. *IEEE Trans Biomed Eng* **1993,** *40* (1), 35-41.
223. Alea-Reyes, M. E.; Soriano, J.; Mora-Espi, I.; Rodrigues, M.; Russell, D. A.; Barrios, L.; Perez-Garcia, L., Amphiphilic gemini pyridinium-mediated incorporation of Zn(II)meso-tetrakis(4-carboxyphenyl)porphyrin into water-soluble gold nanoparticles for photodynamic therapy. *Colloid Surf B Biointerf* **2017,** *158*, 602-609.
224. Mosqueira, D.; Mannhardt, I.; Bhagwan, J. R.; Lis-Slimak, K.; Katili, P.; Scott, E.; Hassan, M.; Prondzynski, M.; Harmer, S. C.; Tinker, A., CRISPR/Cas9 editing in human pluripotent stem cell-cardiomyocytes highlights arrhythmias, hypocontractility, and energy depletion as potential therapeutic targets for hypertrophic cardiomyopathy. *Eur Heart J* **2018**.
225. McGee, E. M., Bioelectronics and Implanted Devices. In *Medical enhancement and posthumanity*, Springer: 2008; pp 207-224.
226. Misra, N.; Martinez, J. A.; Huang, S.-C. J.; Wang, Y.; Stroeve, P.; Grigoropoulos, C. P.; Noy, A., Bioelectronic silicon nanowire devices using functional membrane proteins. *Proc Nat Acad Sci* **2009,** *106* (33), 13780-13784.
227. Smela, E., Conjugated polymer actuators for biomedical applications. *Adv Mater* **2003,** *15* (6), 481-494.
228. Ehret, R.; Baumann, W.; Brischwein, M.; Schwinde, A.; Stegbauer, K.; Wolf, B., Monitoring of cellular behaviour by impedance measurements on interdigitated electrode structures. *Biosens Bioelectron* **1997,** *12* (1), 29-41.
229. Lee, J.-Y.; An, J.; Chua, C. K., Fundamentals and applications of 3D printing for novel materials. *Appl Mater Tod* **2017,** *7*, 120-133.
230. Fosdick, S. E.; Knust, K. N.; Scida, K.; Crooks, R. M., Bipolar electrochemistry. *Angew Chem Int Ed* **2013,** *52* (40), 10438-10456.
231. Sanjuan-Alberte, P.; Saleh, E.; Shaw, A. J.; Lacalendola, N.; Willmott, G.; Vaithilingam, J.; Alexander, M. R.; Hague, R. J. M.; Rawson, F. J., Remotely Controlled in Situ Growth of Silver Microwires Forming Bioelectronic Interfaces. *ACS Appl Mater Interfaces* **2019,** *11* (9), 8928-8936.
232. **!!! INVALID CITATION !!! {}**.
233. Kim, Y.; Lee, B.; Yang, S.; Byun, I.; Jeong, I.; Cho, S. M., Use of copper ink for fabricating conductive electrodes and RFID antenna tags by screen printing. *Curr Appl Phys* **2012,** *12* (2), 473-478.
234. Cheng, K.; Yang, M. H.; Chiu, W. W.; Huang, C. Y.; Chang, J.; Ying, T. F.; Yang, Y., Ink-jet printing, self-assembled polyelectrolytes, and electroless plating: low cost fabrication of circuits on a flexible substrate at room temperature. *Macromol Rapid Comm* **2005,** *26* (4), 247-264.
235. He, Y.; Zhang, F.; Saleh, E.; Vaithilingam, J.; Aboulkhair, N.; Begines, B.; Tuck, C. J.; Hague, R. J.; Ashcroft, I. A.; Wildman, R. D., A tripropylene glycol diacrylate-based polymeric support ink for material jetting. *Addit Manuf* **2017,** *16*, 153-161.
236. Kızılel, S.; Pérez-Luna, V. H.; Teymour, F., Photopolymerization of poly (ethylene glycol) diacrylate on eosin-functionalized surfaces. *Langmuir* **2004,** *20* (20), 8652-8658.
237. Knolle, W.; Mehnert, R., Primary reactions in the electron-induced polymerization of acrylates. *Nucl Ins Meth Phys Res Sec B* **1995,** *105* (1-4), 154-158.
238. Perelaer, J.; De Laat, A. W.; Hendriks, C. E.; Schubert, U. S., Inkjet-printed silver tracks: low temperature curing and thermal stability investigation. *J Mater Chem* **2008,** *18* (27), 3209-3215.

239. Hyun, W. J.; Lim, S.; Ahn, B. Y.; Lewis, J. A.; Frisbie, C. D.; Francis, L. F., Screen printing of highly loaded silver inks on plastic substrates using silicon stencils. *ACS Appl Mater Interfaces* **2015,** *7* (23), 12619-12624.
240. Dearden, A. L.; Smith, P. J.; Shin, D. Y.; Reis, N.; Derby, B.; O'Brien, P., A low curing temperature silver ink for use in ink-jet printing and subsequent production of conductive tracks. *Macromol Rapid Comm* **2005,** *26* (4), 315-318.
241. Cheng, C.; Gonela, R. K.; Gu, Q.; Haynie, D. T., Self-assembly of metallic nanowires from aqueous solution. *Nano Lett* **2005,** *5* (1), 175-8.
242. Bradley, J. C.; Chen, H. M.; Crawford, J.; Eckert, J.; Ernazarova, K.; Kurzeja, T.; Lin, M. D.; McGee, M.; Nadler, W.; Stephens, S. G., Creating Electrical Contacts between Metal Particles using Directed Electrochemical Growth. *Nature* **1997,** *389* (6648), 268-271.
243. Birmingham, K.; Gradinaru, V.; Anikeeva, P.; Grill, W. M.; Pikov, V.; McLaughlin, B.; Pasricha, P.; Weber, D.; Ludwig, K.; Famm, K., Bioelectronic medicines: a research roadmap. *Nat Rev Drug Discov* **2014,** *13* (6), 399-400.
244. Sanjuán-Alberte, P.; Abayzeed, S. A.; Fuentes-Domínguez, R.; Alea-Reyes, M. E.; Clark, M.; Hague, R.; Alexander, M.; Pérez-García, L.; Rawson, F. J., *Wireless Bioelectronic Nanosystems for Intracellular Communication*. 2018.
245. Actis, P.; Tokar, S.; Clausmeyer, J.; Babakinejad, B.; Mikhaleva, S.; Cornut, R.; Takahashi, Y.; Lopez Cordoba, A.; Novak, P.; Shevchuck, A. I.; Dougan, J. A.; Kazarian, S. G.; Gorelkin, P. V.; Erofeev, A. S.; Yaminsky, I. V.; Unwin, P. R.; Schuhmann, W.; Klenerman, D.; Rusakov, D. A.; Sviderskaya, E. V.; Korchev, Y. E., Electrochemical nanoprobes for single-cell analysis. *ACS Nano* **2014,** *8* (1), 875-84.
246. Wang, Y.; Noel, J. M.; Velmurugan, J.; Nogala, W.; Mirkin, M. V.; Lu, C.; Guille Collignon, M.; Lemaitre, F.; Amatore, C., Nanoelectrodes for determination of reactive oxygen and nitrogen species inside murine macrophages. *Proc Natl Acad Sci U S A* **2012,** *109* (29), 11534-9.
247. Liu, J.; Wen, J.; Zhang, Z. R.; Liu, H. J.; Sun, Y., Voyage inside the cell: Microsystems and nanoengineering for intracellular measurement and manipulation. *Microsyst Nanoeng* **2015,** *1*, 15020.
248. Lee, D.; Lee, D.; Won, Y.; Hong, H.; Kim, Y.; Song, H.; Pyun, J. C.; Cho, Y. S.; Ryu, W.; Moon, J., Insertion of Vertically Aligned Nanowires into Living Cells by Inkjet Printing of Cells. *Small* **2016,** *12* (11), 1446-1457.
249. Loget, G.; Kuhn, A., Electric field-induced chemical locomotion of conducting objects. *Nature communications* **2011,** *2*, 535.
250. Loget, G.; Roche, J.; Kuhn, A., True Bulk Synthesis of Janus Objects by Bipolar Electrochemistry. *Adv Mater* **2012,** *24* (37), 5111-5116, 5144.
251. Bradley, J. C.; Ma, Z., Contactless Electrodeposition of Palladium Catalysts. *Angew Chem Int Ed Engl* **1999,** *38* (11), 1663-1666.
252. Roche, J.; Loget, G.; Zigah, D.; Fattah, Z.; Goudeau, B.; Arbault, S.; Bouffier, L.; Kuhn, A., Straight-forward synthesis of ringed particles. *Chem Sci* **2014,** *5* (5), 1961-1966.
253. Warakulwit, C.; Nguyen, T.; Majimel, J.; Delville, M. H.; Lapeyre, V.; Garrigue, P.; Ravaine, V.; Limtrakul, J.; Kuhn, A., Dissymmetric carbon nanotubes by bipolar electrochemistry. *Nano Lett* **2008,** *8* (2), 500-4.
254. Casal-Dujat, L.; Rodrigues, M.; Yague, A.; Calpena, A. C.; Amabilino, D. B.; Gonzalez-Linares, J.; Borras, M.; Perez-Garcia, L., Gemini imidazolium amphiphiles for the synthesis, stabilization, and drug delivery from gold nanoparticles. *Langmuir* **2012,** *28* (5), 2368-81.
255. Connor, E. E.; Mwamuka, J.; Gole, A.; Murphy, C. J.; Wyatt, M. D., Gold nanoparticles are taken up by human cells but do not cause acute cytotoxicity. *Small* **2005,** *1* (3), 325-327.
256. Penon, O.; Patino, T.; Barrios, L.; Nogues, C.; Amabilino, D. B.; Wurst, K.; Perez-Garcia, L., A new porphyrin for the preparation of functionalized water-soluble gold nanoparticles with low intrinsic toxicity. *ChemistryOpen* **2015,** *4* (2), 127-36.
257. Alkilany, A. M.; Thompson, L. B.; Boulos, S. P.; Sisco, P. N.; Murphy, C. J., Gold nanorods: their potential for photothermal therapeutics and drug delivery, tempered by the complexity of their biological interactions. *Adv Drug Deliv Rev* **2012,** *64* (2), 190-9.

258. Dreaden, E. C.; Alkilany, A. M.; Huang, X.; Murphy, C. J.; El-Sayed, M. A., The golden age: gold nanoparticles for biomedicine. *Chem Soc Rev* **2012,** *41* (7), 2740-79.
259. Giljohann, D. A.; Seferos, D. S.; Daniel, W. L.; Massich, M. D.; Patel, P. C.; Mirkin, C. A., Gold nanoparticles for biology and medicine. *Angew Chem Int Ed Engl* **2010,** *49* (19), 3280-94.
260. Fosdick, S. E.; Knust, K. N.; Scida, K.; Crooks, R. M., Bipolar electrochemistry. *Angewandte Chemie International Edition* **2013,** *52* (40), 10438-10456.
261. Loget, G.; Kuhn, A., Shaping and exploring the micro- and nanoworld using bipolar electrochemistry. *Analytical and Bioanalytical Chemistry* **2011,** *400* (6), 1691-1704.
262. Di Martino, G.; Turek, V. A.; Lombardi, A.; Szabó, I.; de Nijs, B.; Kuhn, A.; Rosta, E.; Baumberg, J. J., Tracking nanoelectrochemistry using individual plasmonic nanocavities. *Nano Lett* **2017,** *17* (8), 4840-4845.
263. Rasmussen, M.; Serov, A.; Artyushkova, K.; Chen, D.; Rose, T. C.; Atanassov, P.; Harris, J.; Minteer, S., Enhancement of Electrocatalytic Oxidation of Glycerol by Plasmonics. *Chem ElectroChem* **2018**.
264. Perrin, D. D.; Dempsey, B.; Serjeant, E. P., *pKa prediction for organic acids and bases*. Chapman and Hall: London; New York, 1981; Vol. 1.
265. Jing, C.; Rawson, F. J.; Zhou, H.; Shi, X.; Li, W. H.; Li, D. W.; Long, Y. T., New Insights into Electrocatalysis Based on Plasmon Resonance for the Real-Time Monitoring of Catalytic Events on Single Gold Nanorods. *Anal Chem* **2014,** *86* (11), 5513-5518.
266. Zhou, H.; Liu, Q.; Rawson, F. J.; Ma, W.; Li, D. W.; Li, D.; Long, Y. T., Optical monitoring of faradaic reaction using single plasmon-resonant nanorods functionalized with graphene. *Chem Comm* **2015,** *51* (15), 3223-3226.
267. Abayzeed, S. A.; Smith, R. J.; Webb, K. F.; Somekh, M. G.; See, C. W., Sensitive detection of voltage transients using differential intensity surface plasmon resonance system. *Opt Express* **2017,** *25* (25), 31552-31567.
268. Huang, Y.; Pitter, M. C.; Somekh, M. G., Morphology-dependent voltage sensitivity of a gold nanostructure. *Langmuir* **2011,** *27* (22), 13950-61.
269. Hasheminejad, M.; Fang, Y.; Li, M.; Jiang, Y.; Wang, W.; Chen, H. Y., Plasmonic Imaging of the Interfacial Potential Distribution on Bipolar Electrodes. *Angew Chem Int Ed Engl* **2017,** *56* (6), 1629-1633.
270. Huang, Y.; Pitter, M. C.; Somekh, M. G., Time-dependent scattering of ultrathin gold film under potential perturbation. *ACS Appl Mater Interfaces* **2012,** *4* (8), 3829-36.
271. Xiao, X. W.; Xu, W.; Zhang, D. Q.; Xu, H.; Lu, H. Y.; Zhu, D. B., A new fluorescence-switch based on supermolecular dyad with (tetraphenylporphyrinato) zinc(II) and tetrathiafulvalene units. *J Mater Chem* **2005,** *15* (26), 2557-2561.
272. Lahav, M.; Gabriel, T.; Shipway, A. N.; Willner, I., Assembly of a Zn (II)-Porphyrin–Bipyridinium Dyad and Au-Nanoparticle Superstructures on Conductive Surfaces. *J Am Chem Soc* **1999,** *121* (1), 258-259.
273. Apanasovich, V.; Novikov, E.; Yatskov, N.; Koehorst, R.; Schaafsma, T.; Van Hoek, A., Study of the Zn-porphyrin structure by fluorescence spectroscopy methods. *J Appl Spectrosc* **1999,** *66* (4), 613-616.
274. Tominaga, H.; Ishiyama, M.; Ohseto, F.; Sasamoto, K.; Hamamoto, T.; Suzuki, K.; Watanabe, M., A water-soluble tetrazolium salt useful for colorimetric cell viability assay. *Anal Commun* **1999,** *36* (2), 47-50.
275. Rochford, J.; Rooney, A. D.; Pryce, M. T., Redox control of meso-zinc(II) ferrocenylporphyrin based fluorescence switches. *Inorg Chem* **2007,** *46* (18), 7247-9.
276. Norel, L.; Tourbillon, C.; Warnan, J.; Audibert, J. F.; Pellegrin, Y.; Miomandre, F.; Odobel, F.; Rigaut, S., Redox-driven porphyrin based systems for new luminescent molecular switches. *Dalton Trans* **2018,** *47* (25), 8364-8374.
277. Goldman, D. E., Potential, Impedance, and Rectification in Membranes. *J Gen Physiol* **1943,** *27* (1), 37-60.
278. Gavet, O.; Pines, J., Progressive activation of CyclinB1-Cdk1 coordinates entry to mitosis. *Dev Cell* **2010,** *18* (4), 533-43.

279. Nunes, S. S.; Miklas, J. W.; Liu, J.; Aschar-Sobbi, R.; Xiao, Y.; Zhang, B.; Jiang, J.; Massé, S.; Gagliardi, M.; Hsieh, A., Biowire: a platform for maturation of human pluripotent stem cell–derived cardiomyocytes. *Nat Meth* **2013,** *10* (8), 781.
280. Burridge, P. W.; Keller, G.; Gold, J. D.; Wu, J. C., Production of de novo cardiomyocytes: human pluripotent stem cell differentiation and direct reprogramming. *Cell Stem Cell* **2012,** *10* (1), 16-28.
281. Saini, H.; Navaei, A.; Van Putten, A.; Nikkhah, M., 3D cardiac microtissues encapsulated with the co-culture of cardiomyocytes and cardiac fibroblasts. *Adv Healthc Mater* **2015,** *4* (13), 1961-71.
282. Aung, A.; Bhullar, I. S.; Theprungsirikul, J.; Davey, S. K.; Lim, H. L.; Chiu, Y.-J.; Ma, X.; Dewan, S.; Lo, Y.-H.; McCulloch, A., 3D cardiac μtissues within a microfluidic device with real-time contractile stress readout. *Lab on a Chip* **2016,** *16* (1), 153-162.
283. Au, H. T. H.; Cheng, I.; Chowdhury, M. F.; Radisic, M., Interactive effects of surface topography and pulsatile electrical field stimulation on orientation and elongation of fibroblasts and cardiomyocytes. *Biomaterials* **2007,** *28* (29), 4277-4293.
284. Ribeiro, M. C.; Tertoolen, L. G.; Guadix, J. A.; Bellin, M.; Kosmidis, G.; D'Aniello, C.; Monshouwer-Kloots, J.; Goumans, M.-J.; Wang, Y.-l.; Feinberg, A. W., Functional maturation of human pluripotent stem cell derived cardiomyocytes in vitro–correlation between contraction force and electrophysiology. *Biomaterials* **2015,** *51*, 138-150.
285. Robertson, C.; Tran, D. D.; George, S. C., Concise review: Maturation phases of human pluripotent stem cell-derived cardiomyocytes. *Stem cells* **2013,** *31* (5), 829-837.
286. Ribeiro, A. J.; Ang, Y. S.; Fu, J. D.; Rivas, R. N.; Mohamed, T. M.; Higgs, G. C.; Srivastava, D.; Pruitt, B. L., Contractility of single cardiomyocytes differentiated from pluripotent stem cells depends on physiological shape and substrate stiffness. *Proc Natl Acad Sci U S A* **2015,** *112* (41), 12705-10.
287. Ruan, J.-L.; Tulloch, N. L.; Razumova, M. V.; Saiget, M.; Muskheli, V.; Pabon, L.; Reinecke, H.; Regnier, M.; Murry, C. E., Mechanical stress conditioning and electrical stimulation promote contractility and force maturation of induced pluripotent stem cell-derived human cardiac tissue. *Circulation* **2016**, CIRCULATIONAHA. 114.014998.
288. Denning, C.; Borgdorff, V.; Crutchley, J.; Firth, K. S.; George, V.; Kalra, S.; Kondrashov, A.; Hoang, M. D.; Mosqueira, D.; Patel, A.; Prodanov, L.; Rajamohan, D.; Skarnes, W. C.; Smith, J. G.; Young, L. E., Cardiomyocytes from human pluripotent stem cells: From laboratory curiosity to industrial biomedical platform. *Biochim Biophys Acta* **2016,** *1863* (7 Pt B), 1728-48.
289. Patel, A. K.; Celiz, A. D.; Rajamohan, D.; Anderson, D. G.; Langer, R.; Davies, M. C.; Alexander, M. R.; Denning, C., A defined synthetic substrate for serum-free culture of human stem cell derived cardiomyocytes with improved functional maturity identified using combinatorial materials microarrays. *Biomaterials* **2015,** *61*, 257-265.
290. Xing, J. F.; Zheng, M. L.; Duan, X. M., Two-photon polymerization microfabrication of hydrogels: an advanced 3D printing technology for tissue engineering and drug delivery. *Chem Soc Rev* **2015,** *44* (15), 5031-9.
291. Xu, R. H.; Chen, X.; Li, D. S.; Li, R.; Addicks, G. C.; Glennon, C.; Zwaka, T. P.; Thomson, J. A., BMP4 initiates human embryonic stem cell differentiation to trophoblast. *Nat Biotechnol* **2002,** *20* (12), 1261-4.
292. Minami, I.; Yamada, K.; Otsuji, T. G.; Yamamoto, T.; Shen, Y.; Otsuka, S.; Kadota, S.; Morone, N.; Barve, M.; Asai, Y., A small molecule that promotes cardiac differentiation of human pluripotent stem cells under defined, cytokine-and xeno-free conditions. *Cell Rep* **2012,** *2* (5), 1448-1460.
293. Wang, H.; Hao, J.; Hong, C. C., Cardiac induction of embryonic stem cells by a small molecule inhibitor of Wnt/β-catenin signaling. *ACS Chem Biol* **2010,** *6* (2), 192-197.
294. Bedada, F. B.; Chan, S. S.; Metzger, S. K.; Zhang, L.; Zhang, J.; Garry, D. J.; Kamp, T. J.; Kyba, M.; Metzger, J. M., Acquisition of a quantitative, stoichiometrically conserved ratiometric marker of maturation status in stem cell-derived cardiac myocytes. *Stem Cell Rep* **2014,** *3* (4), 594-605.

295. LaFratta, C. N.; Baldacchini, T., Two-photon polymerization metrology: Characterization methods of mechanisms and microstructures. *Micromachines* **2017,** *8* (4), 101.
296. Schuster, M.; Turecek, C.; Mateos, A.; Stampfl, J.; Liska, R.; Varga, F., Evaluation of biocompatible photopolymers II: further reactive diluents. *Monatsh Chem* **2007,** *138* (4), 261-268.
297. Ovsianikov, A.; Malinauskas, M.; Schlie, S.; Chichkov, B.; Gittard, S.; Narayan, R.; Löbler, M.; Sternberg, K.; Schmitz, K.-P.; Haverich, A., Three-dimensional laser micro-and nano-structuring of acrylated poly (ethylene glycol) materials and evaluation of their cytoxicity for tissue engineering applications. *Acta Biomater* **2011,** *7* (3), 967-974.
298. Jia, G.; Wang, H.; Yan, L.; Wang, X.; Pei, R.; Yan, T.; Zhao, Y.; Guo, X., Cytotoxicity of carbon nanomaterials: single-wall nanotube, multi-wall nanotube, and fullerene. *Environ Sci Technol* **2005,** *39* (5), 1378-83.
299. Hanson, J.; Lowy, J., The structure of F-actin and of actin filaments isolated from muscle. *J Mol Biol* **1963,** *6* (1), 46-IN5.
300. Chowrashi, P. K.; Pepe, F. A., The Z-band: 85,000-dalton amorphin and alpha-actinin and their relation to structure. *J Cell Biol* **1982,** *94* (3), 565-573.
301. Koivumäki, J. T.; Naumenko, N.; Tuomainen, T.; Takalo, J.; Oksanen, M.; Puttonen, K. A.; Lehtonen, Š.; Kuusisto, J.; Laakso, M.; Koistinaho, J., Structural Immaturity of Human iPSC-Derived Cardiomyocytes: In Silico Investigation of Effects on Function and Disease Modeling. *Front Physiol* **2018,** *9*, 80.
302. Shin, S. R.; Jung, S. M.; Zalabany, M.; Kim, K.; Zorlutuna, P.; Kim, S. B.; Nikkhah, M.; Khabiry, M.; Azize, M.; Kong, J., Carbon-nanotube-embedded hydrogel sheets for engineering cardiac constructs and bioactuators. *ACS nano* **2013,** *7* (3), 2369-2380.
303. Chung, S.; Dzeja, P. P.; Faustino, R. S.; Perez-Terzic, C.; Behfar, A.; Terzic, A., Mitochondrial oxidative metabolism is required for the cardiac differentiation of stem cells. *Nat Rev Card* **2007,** *4* (S1), S60.
304. Lieu, D. K.; Liu, J.; Siu, C.-W.; McNerney, G. P.; Tse, H.-F.; Abu-Khalil, A.; Huser, T.; Li, R. A., Absence of transverse tubules contributes to non-uniform ca2+ wavefronts in mouse and human embryonic stem cell–derived cardiomyocytes. *Stem Cells Devel* **2009,** *18* (10), 1493-1500.
305. Maidhof, R.; Tandon, N.; Lee, E. J.; Luo, J.; Duan, Y.; Yeager, K.; Konofagou, E.; Vunjak-Novakovic, G., Biomimetic perfusion and electrical stimulation applied in concert improved the assembly of engineered cardiac tissue. *J Tissue Eng Regen Med* **2012,** *6* (10), e12-23.
306. Tandon, N.; Marsano, A.; Maidhof, R.; Wan, L.; Park, H.; Vunjak-Novakovic, G., Optimization of electrical stimulation parameters for cardiac tissue engineering. *J Tissue Eng Regen Med* **2011,** *5* (6), e115-25.
307. Sanjuan-Alberte, P.; Alexander, M. R.; Hague, R. J. M.; Rawson, F. J., Electrochemically Stimulating Developments in Bioelectronic Medicine. *Bioelec Med* **2018,** *4* (1), 1.
308. De Hemptinne, C.; Swann, N. C.; Ostrem, J. L.; Ryapolova-Webb, E. S.; San Luciano, M.; Galifianakis, N. B.; Starr, P. A., Therapeutic deep brain stimulation reduces cortical phase-amplitude coupling in Parkinson's disease. *Nature neuroscience* **2015,** *18* (5), 779.
309. Bihar, E.; Roberts, T.; Zhang, Y.; Ismailova, E.; Herve, T.; Malliaras, G. G.; De Graaf, J. B.; Inal, S.; Saadaoui, M., Fully Printed All-Polymer Tattoo/Textile Electronics for Electromyography. *Flex Print Electron* **2018,** *3* (3), 034004.
310. Zhu, Z.; Guo, S. Z.; Hirdler, T.; Eide, C.; Fan, X.; Tolar, J.; McAlpine, M. C., 3D Printed Functional and Biological Materials on Moving Freeform Surfaces. *Advanced Materials* **2018,** *30* (23), 1707495.
311. Gonzalez-Solino, C.; Lorenzo, M., Enzymatic Fuel Cells: Towards Self-Powered Implantable and Wearable Diagnostics. *Biosensors* **2018,** *8* (1), 11.
312. Williamson, A.; Rivnay, J.; Kergoat, L.; Jonsson, A.; Inal, S.; Uguz, I.; Ferro, M.; Ivanov, A.; Sjostrom, T. A.; Simon, D. T.; Berggren, M.; Malliaras, G. G.; Bernard, C., Controlling Epileptiform Activity with Organic Electronic Ion Pumps. *Adv Mater* **2015,** *27* (20), 3138-44.

313. Gu, T.; Wang, Y.; Lu, Y.; Cheng, L.; Feng, L.; Zhang, H.; Li, X.; Han, G.; Liu, Z., Platinum Nanoparticles to Enable Electrodynamic Therapy for Effective Cancer Treatment. *Advanced Materials* **2019**, 1806803.
314. Stupp, R.; Taillibert, S.; Kanner, A. A.; Kesari, S.; Steinberg, D. M.; Toms, S. A.; Taylor, L. P.; Lieberman, F.; Silvani, A.; Fink, K. L., Maintenance therapy with tumor-treating fields plus temozolomide vs temozolomide alone for glioblastoma: a randomized clinical trial. *Jama* **2015,** *314* (23), 2535-2543.
315. Buckner, C. A.; Buckner, A. L.; Koren, S. A.; Persinger, M. A.; Lafrenie, R. M., Inhibition of Cancer Cell Growth by Exposure to a Specific Time-Varying Electromagnetic Field Involves T-type Calcium Channels. *PLoS One* **2015,** *10* (4), e0124136.
316. Giladi, M.; Schneiderman, R. S.; Voloshin, T.; Porat, Y.; Munster, M.; Blat, R.; Sherbo, S.; Bomzon, Z.; Urman, N.; Itzhaki, A.; Cahal, S.; Shteingauz, A.; Chaudhry, A.; Kirson, E. D.; Weinberg, U.; Palti, Y., Mitotic Spindle Disruption by Alternating Electric Fields Leads to Improper Chromosome Segregation and Mitotic Catastrophe in Cancer Cells. *Sci Rep* **2015,** *5*, 18046.
317. Rick, J.; Chandra, A.; Aghi, M. K., Tumor Treating Fields: a New Approach to Glioblastoma Therapy. *J Neurooncol* **2018,** *137* (3), 447-453.
318. Nuccitelli, R., Application of Pulsed Electric Fields to Cancer Therapy. *Bioelectricity* **2018,** *1* (1), 24-28.
319. Sherman, H. G.; Jain, A.; Hicks, J.; Stolnik, S.; Alexander, C.; Rawson, F. J., Mammalian Cell-driven Polymerisation of Pyrrole. *ChemBioChem* **2018**.
320. Tonissen, K. F.; Di Trapani, G., Thioredoxin System Inhibitors as Mediators of Apoptosis for Cancer Therapy. *Molec Nutr Food Res* **2009,** *53* (1), 87-103.
321. Tseng, A.-S.; Beane, W. S.; Lemire, J. M.; Masi, A.; Levin, M., Induction of Vertebrate Regeneration by a Transient Sodium Current. *Journal of Neuroscience* **2010,** *30* (39), 13192-13200.
322. Fernandez-Yague, M. A.; Abbah, S. A.; McNamara, L.; Zeugolis, D. I.; Pandit, A.; Biggs, M. J., Biomimetic Approaches in Bone Tissue Engineering: Integrating Biological and Physicomechanical Strategies. *Adv Drug Deliv Rev* **2015,** *84*, 1-29.
323. Guerriero, F.; Ricevuti, G., Extremely Low Frequency Electromagnetic Fields Stimulation Modulates Autoimmunity and Immune Responses: a Possible Immuno-Modulatory Therapeutic Effect in Neurodegenerative Diseases. *Neural Regen Res* **2016,** *11* (12), 1888-1895.